



universität  
wien

# DISSERTATION

Titel der Dissertation

„First-principles Modeling  
of Thermoelectric Materials“

Verfasser

Mingxing Chen

angestrebter akademischer Grad

Doktor der Naturwissenschaften (Dr. rer. nat.)

Wien, 2012

Studienkennzahl lt. Studienblatt: A 091 411

Dissertationsgebiet lt. Studienblatt: Physik

Betreuerin / Betreuer: Ao. Univ.-Prof. tit. Univ.-Prof. Dr. Raimund Podlucky

---

# Zusammenfassung

Thermoelektrische Materialien sind für Stromerzeugung aus Abfallwärme, was physikalisch durch den Seebeck Effekt bewirkt wird, interessant. Dadurch kann die Abhängigkeit von fossilen Brennstoffen verringert werden. Die technologische Aufgabe ist es, geeignete Materialien mit einem hohen thermoelektrischen Wirkungsgrad (Figure of Merit”) zu erzeugen. Die Wissenschaft versucht nun die grundlegenden Materialeigenschaften -das heißt konkret die Transporteigenschaften, wie sie durch Elektronen und Gitterschwingungen vermittelt werden- zu verstehen und zu modellieren. Das Ziel der vorliegenden Arbeit ist es, ein Verständnis der thermoelektrische Eigenschaften ausgewählter Materialien von den tiefsten Grundlagen her zu entwickeln.

Die Grundzustandseigenschaften eines festen Materials wie strukturelle und thermodynamische Stabilität, elektronische Struktur und Gitterdynamik werden mit Hilfe der Dichtefunktionaltheorie, wie sie im Vienna *ab initio* Simulation Package (VASP) implementiert ist, untersucht. Thermoelektrische Eigenschaften wie Seebeck Tensor, elektrische Leitfähigkeit und elektronische thermische Leitfähigkeit werden unter Anwendung der Boltzmannschen Transport Theorie im Rahmen der Näherung konstanter Relaxationszeiten abgeleitet. Für die aktuellen Berechnungen der elektronischen Transporteigenschaften wird das Programmpaket BoltzTrap verwendet, das entsprechend adaptiert wurde um den VASP output zu übernehmen. Zwei Prototypen von thermoelektrischen Materialien, nämlich sogenannte Skutterudite und Clathrate, werden in enger Zusammenarbeit mit experimentellen Gruppen untersucht. In einem ersten Schritt werden Ge-basierte Skutterudite studiert. Das Auftreten von sogenannten Rasselmoden im Phononenspektrum, die für die thermische Gitterleitfähigkeit wichtig sein können, wird untersucht, indem die Phononenspektren berechnet werden. Zur Analyse der Resultate wird ein vereinfachtes Kraftkonstantenmodell entwickelt und angewendet. Der Hauptteil der Arbeit besteht in der Berechnung der elektronischen Struktur von strukturell voll relaxierten Verbindungen. Diese Information wird dann für die Berechnung des Seebeck Tensors des jeweiligen Materials verwendet. Die erste Materialklasse, die betrachtet wird, sind Skutterudite. Die gerechneten Resultate für die Ge-basierten Skutterudite  $\text{MPt}_4\text{Ge}_{12}$  ( $M = \text{Ba}, \text{La}$  and  $\text{Th}$ ) zeigen ziemlich niedrige Seebeckkoeffizienten, was recht ungewöhnlich für die üblichen Pniktid-Skutterudite ist. Tight binding Analysen weisen darauf hin, daß eine offene d-Schale ausschlaggebend für das Auftreten von elektronischen Bandlücken ist, die für das Optimieren thermoelektrischer Eigenschaften wichtig sind. Sogenanntes ”band engineering” wird gemacht, indem die Ergebnisse der tight binding Analyse mit der Mottschen Beziehung für den Seebeckkoeffizienten bei niedrigen Temperaturen vereinigt werden. Damit kann man die Ladungsträgerkonzentration, die durch die elektronische Struktur nahe der Fermi energy bestimmt wird, einstellen. Es stellt sich heraus, daß der Seebeckkoeffizient der  $\text{MPt}_4\text{Ge}_{12}$  Skutterudite um 2 Größenordnungen verbessert werden kann, wenn man das Ge-Untergitter mit Sb Atomen dotiert.

---

Die zweite Klasse von thermoelektrischen Materialien, die untersucht werden, sind Clathrate. Die hier vorgestellte First-Principles Methode wird erfolgreich angewendet, um die experimentellen Ergebnisse für  $\text{Ba}_8\text{M}_x\text{Ge}(\text{Si})_{46-x}$  ( $\text{M} = \text{Ni}, \text{Cu}, \text{Ag}, \text{Au}$ ) Clathrate zu verstehen. Von besonderer Wichtigkeit für die Transporteigenschaften ist die Änderung der Stöchiometrie der Proben, für die sorgfältige und ausführliche Untersuchungen insbesondere mit der sogenannten rigid-band Näherung gemacht werden. Diese Methode wird kritisch getestet und es stellt sich heraus, daß die atomare Größe eine wichtige Rolle spielt. Im Falle der elektronischen thermischen Leitfähigkeit wird die Lorenzzahl berechnet, um die Gültigkeit des Wiedemann-Franz'schen Gesetzes für Metalle auszutesten. Die Lorenzzahl wird üblicherweise dazu verwendet um die thermische Leitfähigkeit von Elektronen und Phononen zu trennen. Es stellt sich heraus, daß die Lorenzzahl sehr stark von Temperatur und Ladungsdichtekonzentration abhängen kann.

Die Ergebnisse dieser Dissertation, was sowohl berechnete Eigenschaften als auch die Analyse der Ergebnisse anbelangt, zeigen die Wichtigkeit und Leistungsfähigkeit einer First-Principles Computermethode für das computerunterstützte Entwerfen von Materialeigenschaften.

---

# Abstract

Thermoelectric materials have potential applications in power generation devices that convert waste heat into electric current by the so-called Seebeck effect thus providing an alternative energy technology to reduce the dependence on traditional fossil fuels. Technologically, the task is to fabricate suitable materials with high efficiency (the so-called figure-of-merit). From a scientific point of view one aims to model the underlying materials properties and in particular the transport phenomena as mediated by electrons and lattice vibrations. The goal of the present work is to develop an understanding of the thermoelectric properties of selected materials at a fundamental level.

The ground state properties of a solid material such as structural and thermodynamic stability, electronic structure and lattice dynamics are investigated by means of first-principles concepts within the framework of density functional theory as implemented in the Vienna *ab initio* Simulation Package (VASP). Thermoelectric properties such as Seebeck tensor, electrical conductivity and electronic thermal conductivity are derived by making use of Boltzmann's transport theory incorporating the constant relaxation time approximation. For the actual calculations of the electronic transport properties, the program package BoltzTrap is adapted to incorporate the necessary output from the VASP calculations. Two prototypical classes of thermoelectric materials, namely so-called skutterudites and clathrates are studied in close collaboration with experimental groups. In a first step vibrational properties of some Ge-based skutterudites are studied. The appearance of so-called phonon rattling modes, which are of importance for the lattice thermal conductivity, is investigated by calculating phonon spectra for these materials. For analyzing the results, a simplified force constant model is developed and applied. The main part of the work consists in calculating electronic structures of geometrically fully relaxed compounds which then is used for deriving the Seebeck tensor. The first materials' class studied are skutterudites. The calculated results for the Ge-based skutterudites  $\text{MPt}_4\text{Ge}_{12}$  ( $M = \text{Ba}, \text{La}$  and  $\text{Th}$ ) reveal rather low Seebeck coefficients, which are anomalous for traditional pnictide skutterudites. Tight binding analysis indicate that an open d shell is crucial for the appearance of gaps, which are important for optimizing thermoelectric properties. Combining this analysis with Mott's relation for the Seebeck coefficient at low temperatures "band engineering" is employed for tuning the charge carrier concentration which is reflected by the electronic structure close to Fermi energy. It is found that that the Seebeck coefficients of  $\text{MPt}_4\text{Ge}_{12}$  skutterudites can be improved by two orders of magnitude by appropriate doping the Ge-sublattice by Sb. The second large class of thermoelectric materials under investigation are clathrates. The present first-principles approach is successfully applied to understand the experimental findings for  $\text{Ba}_8\text{M}_x\text{Ge}(\text{Si})_{46-x}$  ( $M = \text{Ni}, \text{Cu}, \text{Ag}, \text{Au}$ ) clathrates. Of particular importance for the transport properties is the variation of stoichiometry of the samples, for which careful

---

and elaborate studies are made in particular in terms in of the rigid band approximation. This approach is critically tested and it is found furthermore that the atomic sizes play an important role. Considering the electronic thermal conductivity, the Lorenz number is also determined to examine the validity of the Wiedemann-Franz law in the metallic limit, which is used traditionally to separate thermal conductivities of electrons and phonons based on the measured electrical conductivity. It is found that the Lorenz number may depend strongly on the charge carrier density and temperatures. The results of the thesis in terms of numbers and analysis manifest the importance and capabilities of first-principles computational materials design.



# *Acknowledgements*

One can imagine how tough it is for a person pursuing his PhD degree in a strange country with language and culture different from his own. This thesis could not have been finished without the help and support of many people who are gratefully acknowledged here.

Foremost, I thank my advisor Raimund Podloucky for his education, guidance, support and encouragement throughout my PhD studies. He opened the door of a new academic field for me and initiated the topic of my PhD research. He has always been willing to share his knowledge and discuss ideas with me as well as give insightful comments when I go to him. He taught me a lot about working attitudes and research philosophy by guiding me figure out physical pictures out of calculations. I would also like to greatly appreciate his great effort on helping me through the thesis writing. I acknowledge him for his patience, willingness to help me in any regard.

I would like to thank Jürgen Hafner for his wonderful lecture on theory of solid states. I would also like to thank Cesare Franchini for teaching me a lot about VASP. I benefited a lot from his lecture, computational quantum mechanics. His easy-going personality has made our discussions enjoyable. It is my great pleasure to join Michael Weinert's lecture that gave me the knowledge base of relativistic effect in solids. I also benefited a lot from Robert Stadler's lecture about quantum transport.

I would like to thank my colleagues in institute for chemical physics at University of Vienna for their great help on my work and life in Vienna, especially David Reith, Marcel Hieckel, Martin Leitner and Claudia Blaas-Schenner. I thank David Reith for providing not only his fphon code but also selfless help on my course studies and life. I appreciate help from Marcel Hieckel, Martin Leitner and Claudia Blaas-Schenner, who taught me German and helped me on dealing with German documents. I would like to thank Markus for his patient technique support. I thank Xinlin Yan for his constant and reliable help.

I want to express special thanks to my wife Can Liu for her endless support. She has made my life wonderful, and I hope I can do the same for her. Finally, my deepest gratitude goes to my father Wenwu Chen and my mother Wushang Jiang for their continuous love and support.

Last but not least, I would like to thank FWF within the Science College W4 Computational Materials Science for its financial support to my Ph.D research study.





# Contents

<b>Abstract (German)</b>	<b>i</b>
<b>Abstract</b>	<b>iii</b>
<b>Acknowledgements</b>	<b>vi</b>
<b>List of Figures</b>	<b>xiii</b>
<b>List of Tables</b>	<b>xix</b>
<b>Abbreviations</b>	<b>xxi</b>
<b>1 Introduction</b>	<b>1</b>
1.1 Motivation . . . . .	1
1.2 Objective and Scope of Thesis . . . . .	3
1.3 Thermoelectric Effects . . . . .	3
1.4 Figure of Merit . . . . .	5
<b>2 Electronic Ground State and Lattice Dynamics</b>	<b>9</b>
2.1 Density Functional Theory . . . . .	11
2.2 Approximations to the exchange-correlation Functional . . . . .	12
2.3 Methods . . . . .	13
2.3.1 The Pseudo-potential Approach: VASP . . . . .	13
2.3.2 Tight-binding Method . . . . .	14
2.3.2.1 Slater-Koster Scheme . . . . .	14
2.3.2.2 Calculating TB parameters . . . . .	15
2.4 Theory of Lattice Dynamics . . . . .	16
2.4.1 Harmonic approximation . . . . .	16
2.4.2 Born-von Kármán model . . . . .	17
2.4.3 Direct method . . . . .	18
<b>3 Modeling Thermoelectric Materials</b>	<b>21</b>
3.1 Preliminaries . . . . .	21
3.2 Transport Coefficients . . . . .	23
3.3 Implementation Techniques . . . . .	24

3.3.1	Band Interpolation . . . . .	24
3.3.2	Electron Velocities . . . . .	28
3.3.3	Constant Relaxation Time Approximation . . . . .	29
3.3.4	Symmetry Properties . . . . .	30
3.3.5	Rigid Band Approximation . . . . .	31
3.3.6	Calculation of the transport properties by program V2Boltz . . . . .	32
3.4	Benchmark Calculations . . . . .	33
3.4.1	k-convergence . . . . .	33
3.4.2	Effects of exchange-correlation approximations . . . . .	36
<b>4</b>	<b>Ge-based Skutterudites</b>	<b>39</b>
4.1	Overview . . . . .	39
4.2	Structural Properties . . . . .	41
4.3	Lattice Dynamics of Ge-skutterudites . . . . .	42
4.3.1	Born-von Kármán Model Calculations . . . . .	42
4.3.2	First-principles Lattice dynamics of $\text{MPt}_4\text{Ge}_{12}$ . . . . .	44
4.3.2.1	Phonons of $\text{Pt}_4\text{Ge}_{12}$ . . . . .	45
4.3.2.2	Phonons of $\text{MPt}_4\text{Ge}_{12}$ . . . . .	45
4.3.2.3	Atomic Displacement Parameters . . . . .	53
4.3.2.4	Specific Heat . . . . .	54
4.3.3	Summary . . . . .	56
4.4	Thermoelectric Properties of Ge-skutterudites . . . . .	56
4.4.1	Electronic Structures of $\text{MPt}_4\text{Ge}_{12}$ . . . . .	56
4.4.2	Seebeck Coefficients of $\text{MPt}_4\text{Ge}_{12}$ . . . . .	58
4.4.2.1	Model Calculations . . . . .	58
4.4.2.2	Full Calculations . . . . .	59
4.4.3	Band Engineering for Optimization of Thermoelectric Properties . . . . .	60
4.4.3.1	Band Engineering by Chemical Doping . . . . .	61
4.4.3.2	Seebeck Coefficients of $\text{MPt}_4(\text{Sb}_x\text{Ge}_{12-x})$ . . . . .	65
<b>5</b>	<b>Group-IV-based Clathrates</b>	<b>69</b>
5.1	Introduction . . . . .	69
5.2	Unfilled Type-I and -II Clathrates: $\text{X}_{46}$ and $\text{X}_{34}$ . . . . .	70
5.2.1	Structural and Electronic properties . . . . .	70
5.2.2	Coordination and Bonding . . . . .	74
5.3	Structural Properties and Energetics of Doped and Filled Clathrates . . . . .	79
5.4	Gap and Doping . . . . .	83
5.5	Transport Properties of $\text{Ba}_8\text{Ag}_x\text{Ge}_{46-x}$ Clathrates . . . . .	89
5.5.1	Computational Details . . . . .	90
5.5.2	Seebeck Coefficient . . . . .	92
5.5.3	Electrical Resistivity . . . . .	94
5.6	Transport Properties of $\text{Ba}_8\text{M}_x\text{Si}_{46-x}$ ( $\text{M} = \text{Ni}, \text{Cu}, \text{Au}$ ) Clathrates . . . . .	96
5.6.1	$\text{Ba}_8\text{Au}_x\text{Si}_{46-x}$ Clathrates . . . . .	98

---

5.6.2	$\text{Ba}_8\text{Cu}_x\text{Si}_{46-x}$ Clathrates . . . . .	99
5.6.3	$\text{Ba}_8\text{Ni}_x\text{Si}_{46-x}$ clathrates . . . . .	101
5.7	Lorenz Number and Electronic Thermal Conductivity . . . . .	103
<b>6</b>	<b>Summary and Outlook</b>	<b>109</b>
<b>A</b>	<b>V2Boltz Manual</b>	<b>113</b>
A.1	Files Used by V2Boltz . . . . .	113
A.2	INPUT . . . . .	113
A.3	SYMOP . . . . .	116
A.4	STRUCT . . . . .	117
A.5	EIGENVAL . . . . .	117
<b>B</b>	<b>Mott's Relation and Its Simplified Version</b>	<b>119</b>
B.1	Mott's Relation . . . . .	119
B.2	Simplified Mott's Relation . . . . .	120
<b>C</b>	<b>Atomic Displacement Parameters</b>	<b>123</b>
<b>D</b>	<b>An Approximation to The Electronic Thermal Conductivity</b>	<b>127</b>
	<b>Bibliography</b>	<b>129</b>
	<b>List of Publications and Manuscripts</b>	<b>137</b>
	<b>Curriculum Vitae</b>	<b>139</b>



# List of Figures

1.1	Illustration of thermoelectric modules. Power generation (a) and refrigeration (b) modules. . . . .	4
3.1	Illustration of doping two atoms (in blue) onto six equivalent sites. (a) Because of the sample preparation at higher temperatures, experimentally the dopants are more or less statistically distributed. (b) - (d) Three possible configurations for modeling with a unit cell in which each site is either completely substituted by a dopant or not. . . . .	30
3.2	Calculated Fermi levels of $\text{Ba}_8\text{Au}_6\text{Si}_{40}$ (black solid line) and $\text{Ba}_8\text{Au}_{5.9}\text{Si}_{40.1}$ (red dashed line) at 0 K. The Fermi level of $\text{Ba}_8\text{Au}_{5.9}\text{Si}_{40.1}$ was derived by Eq. 3.49 taking $\text{Ba}_8\text{Au}_6\text{Si}_{40}$ as the reference. . . . .	31
3.3	Flow-chart depicting a generic calculation of components of the Seebeck tensor. . . . .	33
3.4	$\mathbf{k}$ -mesh convergence of calculations of the Seebeck coefficient of $\text{Ba}_8\text{Au}_6\text{Si}_{40}$ at $T = 600$ K for two different input $\mathbf{k}$ -meshes: $5 \times 5 \times 5$ (black line) and $25 \times 25 \times 25$ (red line). Interpolations were done over several Monkhorst-Pack grids using VASP eigenvalues. Seebeck coefficients were calculated using the interpolated eigenvalues. . . . .	34
3.5	Calculated $S(T)$ of $\text{Ba}_8\text{Au}_6\text{Si}_{40}$ using interpolated eigenvalues on a $\mathbf{k}$ -grid of $40 \times 40 \times 40$ ( $K'$ ) with VASP eigenvalues on grids of $5 \times 5 \times 5$ (black line) and $25 \times 25 \times 25$ (red line), respectively. . . . .	34
3.6	Comparisons in DOS of $\text{Ba}_8\text{Au}_6\text{Si}_{40}$ between the one from eigenvalues on a $25 \times 25 \times 25$ grid (red) directly derived by VASP and those from eigenvalues on a $40 \times 40 \times 40$ grid ( $K'$ ) interpolated from VASP eigenvalues on a $5 \times 5 \times 5$ grid (green line) and on a $25 \times 25 \times 25$ (blue line) grid, respectively. . . . .	35
3.7	$S(\mu)$ of $\text{Ba}_8\text{Au}_6\text{Si}_{40}$ at 300 K derived from LDA (black line) and GGA (red line) eigenvalues. Interpolations were performed over a $40 \times 40 \times 40$ grid based on VASP eigenvalues on a grid of $25 \times 25 \times 25$ points. The DOS from both LDA (green) and GGA (red line) calculations are shown in the inset. The LDA calculation produces a narrower gap than the GGA calculations. . . . .	36
3.8	$S(T)$ of $\text{Ba}_8\text{Au}_6\text{Si}_{40}$ derived from LDA (black line) and GGA (red line) eigenvalues. Interpolations were done over a grid of $40 \times 40 \times 40$ based on VASP eigenvalues on a grid of $25 \times 25 \times 25$ . . . . .	36

4.1	Crystal structures of (a) perovskite $ABC_3$ with empty A site and (b) an unfilled skutterudite. Large cyan and small red balls denote transition metals and nonmetal ligands, respectively. . . . .	41
4.2	(a)Structure of the filled skutterudite, (b)sketch of a 3 dimensional spring model for body-centered cubic structure, corresponding to the unit cell of a B2 structure. The symbols $m$ and $M$ are the masses for the framework atoms and the filler, respectively' $k_1$ represents spring constants between framework atoms, while $k_2$ is the spring konstant between framework and filler. . . . .	42
4.3	Phonon spectrum derived from the Born-von Kármán model with respect to relative masses $m'$ and spring constants $k'$ . . . . .	44
4.4	DFT derived Phonon spectrum and atom-projected PHDOS of $MPt_4Ge_{12}$ . Phonon bands are colored to show contributions of the filler. . . . .	46
4.5	Sketch of vibrating atoms of the lowest optical mode at $\Gamma$ for (a) $Pt_4Ge_{12}$ , (b) $BaPt_4Ge_{12}$ , (c) $LaPt_4Ge_{12}$ and (d) $ThPt_4Ge_{12}$ . Filler atoms: large balls, Pt: small gray balls, Ge: small magenta balls. . . . .	48
4.6	Atom-projected PHDOS of Ba with respect to scaling in FCs between Ba and Ge, and atomic mass of Ba. . . . .	52
4.7	Potential energy of the filler atoms ( Ba, La and Th) in the skutterudite. Calculations were performed by moving the fillers away from the center of the cage (static equilibrium position) along the x axis . . . . .	53
4.8	Calculated averaged ADPs $U_{iso}$ vs temperature for (a) $BaPt_4Ge_{12}$ , (b) $LaPd_4Ge_{12}$ (c) $ThPt_4Ge_{12}$ using Eq.(4.8). . . . .	54
4.9	Comparison of calculated temperature-dependence of specific heat $C_v$ (red solid line) of $ThPt_4Ge_{12}$ plotted as $C_v/T^3$ vs $\ln T$ with experiment (red diamonds) Ref. [90]. Black dotted line labels the spectral function of Einstein-like separated modes from the experimental model, black solid line labels calculated function $F(\omega)_{ThPt_4Ge_{12}}$ , blue dashed line represents the calculated function $F(\omega)_{BaPt_4Ge_{12}}$ . $F(\omega) = g(\omega)/\omega^2$ with $g(\omega)$ the PHDOS from first-principles lattice dynamics calculations. . . . .	55
4.10	Electronic structures of (a) $Pt_4Ge_{12}$ , (b) $BaPt_4Ge_{12}$ , (c) $LaPt_4Ge_{12}$ , (d) $ThPt_4Ge_{12}$ . Energy scale relative to the Fermi level. Solid lines label scalar-relativistic results and the dashed red ones denote results including spin-orbit coupling. . . . .	57
4.11	Comparison of the Seebeck coefficients from Eq.(4.13) (black solid line), Eq.(4.11) (red dashed line), and Eq.(4.12) (blue dotted line) . . . . .	59
4.12	DFT derived Seebeck coefficients as a function of chemical potential, i.e., temperature dependent Fermi level, at $T = 300$ K for $BaPt_4Ge_{12}$ (a), $LaPt_4Ge_{12}$ (b) and $ThPt_4Ge_{12}$ (c), respectively. The energy shifting for placing the Fermi level in the middle of the pseudogap (gap) is translated into $\Delta n$ , the change of the valence electron number. . . . .	59

4.13	VASP derived electronic structures (black lines) of $\text{Pt}_4\text{Ge}_{12}$ (left-top panel) and $\text{Au}_4\text{Ge}_{12}$ (right-top panel), and TB bands (red dashed lines). Illustration of on-site parameters as Ge 4p and Pt/Au 5d,6s levels (left-bottom panel) and DOS of $\text{Au}_4\text{Ge}_{12}$ derived from TB calculations (right-bottom panel) with several shifts of the $\varepsilon_{5d}$ level of Au. . . . .	65
4.14	Electronic structures of $\text{LaPt}_4(\text{Sb}_5\text{Ge}_7)$ and $\text{ThPt}_4(\text{Sb}_4\text{Ge}_8)$ at $T = 300$ K.	66
4.15	DFT derived Seebeck coefficient $S(\mu)$ for 300K as a function of varying chemical potential $\mu$ , i.e. number of valence electrons. The chemical potentials represents the Fermi energy for 300K within a rigid band model, and $\mu = 0$ corresponds to the Fermi level of undoped $\text{LaPt}_4(\text{Sb}_5\text{Ge}_7)$ and $\text{ThPt}_4(\text{Sb}_4\text{Ge}_8)$ . . . . .	66
4.16	DFT derived Seebeck coefficients of $\text{LaPt}_4(\text{Sb}_{5-\delta}\text{Ge}_{7+\delta})$ and $\text{ThPt}_4(\text{Sb}_{4-\delta}\text{Ge}_{8+\delta})$ ( $\delta = \pm 0.1$ ). . . . .	67
5.1	(a) Structure of filler-free type I clathrate $\text{X}_{46}$ . There are three types of Wyckoff positions, 6d, 16i, and 24k, which are shown in different colors. There are two types of polyhedras (20-atom dodecahedras and 24-atom tetrakaidecahedras) as structural units (b), which are also shown by including some of the atoms from neighboring cells (a). . . . .	71
5.2	(a) Structure of filler-free type II clathrate. There are three types of Wyckoff positions, 8a, 32e, and 96g, which are shown in different colors. There are two types of polyhedras (20-atom dodecahedras and 28-atom tetrakaidecahedras) as structural units (b), which are also shown by including some of atoms from neighboring cells (a). . . . .	72
5.3	Illustration of counting the second-nearest neighbors in clathrate structures. (a) Neighbors of an atoms in a tetrakaidecahedra which consists of pentagons and hexagons. For each atom, ways of choosing its second-nearest neighbors are illustrated in (b) and (c). The way of choosing the third-nearest neighbors are shown in (d). . . . .	74
5.4	Band structures of (a) $\text{Ge}_{46}$ and (b) $\text{Ge}_{34}$ as derived by VASP and LCPAO calculations. A basis set including one s orbital, three p orbitals and one zeta function $s^*$ was used in the LCPAO calculation. . . . .	75
5.5	(a) Structure of doped Ba-filled type-I clathrate $\text{Ba}_8\text{M}_x\text{Si}(\text{Ge})_{46-x}$ ( $x \leq 6$ ). M can be transition metals, noble metals, zinc group and group-III elements. When M are transition metals and noble metals, $x$ is not larger than 6 and M substitutes Si(Ge) atoms on 6d sites. When M are zinc group and group-III elements, $x$ can be larger than 6 and thus besides 6d sites, M substitute Si(Ge) atoms at other sites such as 16i and 24k sites. The two cages show schematically the environments of two different types of Ba, i.e., 2a (0,0,0) and 6c (0.25,0.5,0) sites. . . . .	80
5.6	Calculated formation energies $\Delta H$ $\text{Ba}_8\text{M}_x\text{Ge}_{46-x}$ ( $M = \text{Au}, \text{Ag}, \text{Pd}$ and $\text{Zn}$ ) as a function of doping $x$ . Also shown is the result for the unfilled and undoped cage solid $\text{Ge}_{46}$ . Calculations were done using VASP within LDA.	83

5.7	DFT derived formation energies $\Delta H$ $\text{Ba}_8\text{M}_x\text{Si}_{46-x}$ ( $\text{M} = \text{Au}, \text{Ag}, \text{Cu},$ and $\text{Ni}$ ) as a function of $x$ . The figure also shows the result for the unfilled cage solid $\text{Si}_{46}$ . Both GGA and LDA results are given. As expected, LDA predicts stronger stabilization than GGA. . . . .	84
5.8	VASP derived total DOS of $\text{Ge}_{46}$ and $\text{Ba}_8\text{Ge}_{46}$ . . . . .	85
5.9	VASP derived total and partial DOS of $\text{Ba}_8\text{Pd}_x\text{Ge}_{46-x}$ ( $x = 1 - 6$ ). Fermi energy is at $E = 0$ . Black lines denote the total DOS. Red, green and blue lines represent Ba-, Pd- and Ge-projected DOS. . . . .	86
5.10	VASP derived total and partial DOS of $\text{Ba}_8\text{Ag}_x\text{Ge}_{46-x}$ ( $x = 1 - 6$ ). Fermi energy is at $E = 0$ . Black lines denote the total DOS. Red, green and blue lines represent Ba-, Ag- and Ge-projected DOS. . . . .	87
5.11	Total DOS of $\text{Ba}_8\text{Zn}_x\text{Ge}_{46-x}$ ( $x = 1 - 8$ ). Fermi energy is at $E = 0$ . . . . .	88
5.12	VASP derived total and partial DOS of $\text{Si}_{46}$ , $\text{Ba}_8\text{Si}_{46}$ and $\text{Ba}_8\text{Au}(\text{Cu})_x\text{Si}_{46-x}$ ( $x = 5$ and $6$ ). Fermi energy is at $E = 0$ . Black lines denote the total DOS. Red, green and blue lines represent Ba-, Ag- and Ge-projected DOS. . . . .	89
5.13	VASP derived total and partial DOS of $\text{Ba}_8\text{Ni}_x\text{Si}_{46-x}$ ( $x = 1 - 6$ ). Fermi energy is at $E = 0$ . Black lines denote the total DOS. Red, green and blue lines represent Ba-, Ag- and Ge-projected DOS. . . . .	90
5.14	Measured temperature-dependent (a) Seebeck coefficients and (b) resistivities of $\text{Ba}_8\text{Ag}_x\text{Ge}_{46-x-y}\square_y$ . $\square$ represents a vacancy (Ref. [121]). Resistivity of $\text{Ba}_8\text{Ag}_5\text{Ge}_{42}$ has almost the same curve as $\text{Ba}_8\text{Ag}_{4.8}\text{Ge}_{41.2}$ (not shown by experimentalists). Data for $\text{Ba}_8\text{Ag}_{5.3}\text{Ge}_{40.7}$ and $\text{Ba}_8\text{Ag}_6\text{Ge}_{40}$ refer to the right axis. . . . .	91
5.15	DFT derived Seebeck coefficient at 300 K for $\text{Ba}_8\text{Ag}_5\text{Ge}_{41}$ and $\text{Ba}_8\text{Ag}_6\text{Ge}_{40}$ as a function of electron doping $\Delta n$ . A negative value corresponds to hole doping. . . . .	92
5.16	DFT derived temperature dependent Seebeck coefficient for $\text{Ba}_8\text{Ag}_x\text{Ge}_{46-x}$ (a) with $x = 5.0 - 5.4$ . (b) A finer scan in a narrower range of $x = 5.20 - 5.26$ . Calculations were carried out within the rigid band approximation by taking $\text{Ba}_8\text{Ag}_5\text{Ge}_{41}$ as reference. . . . .	93
5.17	DFT derived temperature dependent resistivity for $\text{Ba}_8\text{Ag}_x\text{Ge}_{46-x}$ ( $x = 5.20 - 5.26$ ). The reference compound is $\text{Ba}_8\text{Ag}_5\text{Ge}_{41}$ from which the values for the selected compositions were derived within the rigid band approximation by adjusting the Fermi energy according to the change in $\Delta n$ (from $-0.22$ to $-0.40$ , i.e. hole doping). . . . .	94
5.18	Temperature dependent resistivities for $\text{Ba}_8\text{Ag}_{5.24}\text{Ge}_{40.76}$ as calculated directly from Eq.(3.16) and from the approximation in Eq.(5.6). . . . .	95
5.19	DFT derived temperature dependent resistivities for $\text{Ba}_8\text{Ag}_{5.24}\text{Ge}_{40.76}$ for different artificial gap sizes. The gap for the reference compound $\text{Ba}_8\text{Ag}_5\text{Ge}_{41}$ (see Fig.5.10) was enlarged by shifting the valence band edge down by $\Delta\text{Gap}$ . 96	
5.20	Measured Seebeck coefficient and resistivity of $\text{Ba}_8\text{Au}_x\text{Si}_{46-x}$ Ref. [128]. $\text{Ba}_8\text{Au}_{5.4}\text{Si}_{41.6}$ and $\text{Ba}_8\text{Au}_{5.9}\text{Si}_{41.1}$ are from Ref. [127]. . . . .	97
5.21	Measured Seebeck coefficient and resistivity of $\text{Ba}_8\text{Cu}_x\text{Si}_{46-x}$ (Ref. [123]).	97
5.22	DFT derived Seebeck coefficients of $\text{Ba}_8\text{Au}_x\text{Si}_{46-x}$ . . . . .	98

5.23	DFT derived electrical resistivities of $\text{Ba}_8\text{Au}_x\text{Si}_{46-x}$ with $x = 5.07, 5.10$ and $5.13$ . . . . .	99
5.24	DFT derived Seebeck coefficient at 300 K for $\text{Ba}_8\text{Cu}_5\text{Si}_{41}$ and $\text{Ba}_8\text{Cu}_6\text{Si}_{40}$ as a function of doping $\Delta n$ . A negative value corresponds to hole doping.	100
5.25	DFT derived $S(T)$ for $\text{Ba}_8\text{Cu}_x\text{Si}_{46-x}$ with (a) $x = 5.0 - 5.9$ and (b) $x = 4.8 - 5.1$ for fine scan as calculated within the rigid band approximation taking frozen- $\text{Ba}_8\text{Cu}_5\text{Si}_{41}$ as the reference. For $\text{Ba}_8\text{Cu}_5\text{Si}_{41}$ the Seebeck coefficient derived by taking $\text{Ba}_8\text{Cu}_6\text{Si}_{40}$ as the reference is also shown for comparison(dotted line). . . . .	101
5.26	Experimental (a) and DFT derived (b) Seebeck coefficients of $\text{Ba}_8\text{Ni}_x\text{Si}_{46-x}$ . Inset shows locations of the Fermi level of $\text{Ba}_8\text{Ni}_{3.3}\text{Si}_{42.7}$ at 200 K and 1000 K, respectively. The arrow denoting the shifting direction of the Fermi level as temperature increases from 200 K and 1000 K. . . . .	102
5.27	Experimental (a) and DFT derived (b) electrical resistivities of $\text{Ba}_8\text{Ni}_x\text{Si}_{46-x}$ .	103
5.28	Lorenz number vs. charge doping for $\text{Ba}_8\text{Au}_6\text{Ge}_{40}$ at 300 K. Negative(positive) values correspond to hole(electron) dopings. $N = 2$ corresponds to a doping of 2 electrons that places the Fermi level into the middle of the gap according to the counting rule in Eq.(5.3). . . . .	105
5.29	Lorenz number as a function of temperature for $\text{Ba}_8\text{Au}_6\text{Ge}_{40}$ with doping of 0.0 (black solid line) and 0.8 electrons (blue dashed line), respectively. 0.8 electrons corresponds to $N = 0.8$ in Fig.5.28. The reason for choosing the doping of 0.8 electrons is that the calculated Seebeck coefficient (inset) agrees well with the experiment for $\text{Ba}_8\text{Au}_6\text{Ge}_{40}$ within the limits of the experimental error. . . . .	105
5.30	Temperature dependencies of $\frac{K_2}{T}$ and $\frac{\pi^2}{3}(\frac{k_B}{e})^2 T \sigma$ for $\text{Ba}_8\text{Au}_6\text{Ge}_{40}$ for zero doping. . . . .	106
5.31	Electronic thermal conductivities $\kappa_{el}$ for $\text{Ba}_8\text{Au}_6\text{Ge}_{40}$ with a doping of 0.8 electrons. from the Wiedemann-Franz law using a constant Lorenz number $L_0$ and a temperature-dependent Lorenz number derived from Eq.(5.13). . . . .	107
B.1	Illustration of the density of states and location of the Fermi level which favor a high Seebeck coefficient. . . . .	122



# List of Tables

4.1	Lattice constants ( $a$ ), bond lengths ( $R_{M,Ge}$ ), bonding energies ( $E_b(M)$ ) between the filler and Ge atoms on the cage framework, and formation energy per atom $\Delta H$ for $MPt_4Ge_{12}$ ( $M = Ba, La, \text{ and } Th$ ). $R_{Ge,Ge}$ represent the distance between the first nearest neighbors on a $PtGe_6$ octahedron. $E_b(M)$ is defined by $E_b(M) = E(MPt_4Ge_{12}) - E(Pt_4Ge_{12}) - E_{bulk}(M)$ , $E$ being total energies of the corresponding systems. . . . .	45
4.2	Force constants $\phi_{i\beta}^{(i'\alpha)}$ and $\phi'_{i\beta}^{(i'\alpha)}$ ( $\alpha, \beta = x, y, z$ , $i'$ and $i$ represent atoms in primitive cell) in unit of ( $eV/\text{\AA}^2u$ ), which are obtained from first-principles phonon calculations using the program <i>fPHON</i> . Ge1 and Ge2 (see Table 4.1) are first nearest neighbors in the $PtGe_6$ octahedron, located at $(0, y, z)$ and $(-z, 0, -y)$ , respectively. . . . .	50
4.3	On-site $\phi'_{Ba}^{(Ba)}$ with respect to scalings in filler-framework interaction $\phi_{Ba}^{(Ge)}$ and atomic mass of the filler. . . . .	52
4.4	Tight-binding hopping $V$ and on-site $\epsilon$ parameters (in eV) generated using the LCAPO method with interaction up to the fifth-nearest neighbors . .	62
4.5	Tight-binding overlap parameters generated using the LCAPO method with interaction up to the fifth-nearest neighbors . . . . .	63
5.1	Structural parameters of type I and II clathrates. Wyckoff positions $x, y, z$ dependent on the particular material. . . . .	73
5.2	Band gaps (eV) of diamond structure, type-I and -II clathrates structure. First line of each item: present VASP calculation, second line: other data	73
5.3	The number of nearest neighbors for each type of atoms in the three phases. Distances (in $\text{\AA}$ ) between neighbors are given in brackets. The ways of choosing 2NNs and 3NNs are illustrated in Fig.5.3. . . . .	75
5.4	Hopping parameters $V$ and $\epsilon$ (in eV) are generated using the LCAPO method with interaction up to fourth-nearest neighbors. The hopping parameters for each neighbor are generated at the atom-atoms distance for the neighbors very close to the averaged distance which are given in brackets (in $\text{\AA}$ ). . . . .	76
5.5	Overlap parameters as generated by the LCAPO method with interaction up to the third-nearest neighbors. Overlap parameters for each neighbor are generated at the atom-atoms distance for the neighbors very close to the averaged distance, which are given in brackets (in $\text{\AA}$ ). . . . .	77

5.6	Hamiltonian matrix elements $H_{m,n}(\mathbf{K})$ between one pair neighbors at $\Gamma$ for the three structures. A basis set consists of one s orbital, three p orbitals and one zeta function is used. For the diamond structure, $m$ represents orbitals of the atom at (0,0,0) and $n$ denotes orbitals of the atom at $(\frac{1}{4}, \frac{1}{4}, \frac{1}{4})$ . For $\text{Ge}_{46}$ , $m$ and $n$ label orbitals of the atoms at $(\frac{1}{4}, \frac{1}{2}, 0)$ and $(-y, z, 0)$ , respectively. For $\text{Ge}_{34}$ , $m$ and $n$ represent orbitals of the atoms at $(\frac{1}{8}, \frac{1}{8}, \frac{1}{8})$ and $(x_1, x_1, x_1)$ . Numbers 1 and 2 in brackets represent atoms involved in the Hamiltonian matrix, e.g., the atoms at $(\frac{1}{8}, \frac{1}{8}, \frac{1}{8})$ and $(x_1, x_1, x_1)$ . . . . .	79
5.7	Lattice constant $a$ (in $\text{\AA}$ ) and structural parameters for $\text{Ba}_8\text{Ag}_x\text{Ge}_{46-x}$ ( $x = 0 - 6$ ). . . . .	81
5.8	Lattice constant $a$ (in $\text{\AA}$ ) and structural parameters for $\text{Ba}_8\text{Au}_x\text{Si}_{46-x}$ and $\text{Ba}_8\text{Cu}_x\text{Si}_{46-x}$ ( $x = 0 - 6$ ). . . . .	82
5.9	Solubility limits of doping of $\text{Ba}_8\text{M}_x\text{Si}(\text{Ge})_{46-x}$ . . . . .	84

# Abbreviations

<b>TE</b>	Thermo <b>E</b> lectric
<b>ZT</b>	Figure-of-merit
<b>DFT</b>	Density <b>F</b> unctional <b>T</b> heory
<b>LDA</b>	Local <b>D</b> ensity <b>A</b> pproximation
<b>GGA</b>	Generalised <b>G</b> radient <b>A</b> pproximation
<b>PBE</b>	GGA, parametrisations according to <b>P</b> erdew, <b>B</b> urke and <b>E</b> rnzerhof
<b>PAW</b>	<b>P</b> rojector <b>A</b> ugmented <b>W</b> ave
<b>VASP</b>	Vienna <i><b>A</b>b <b>i</b>n<b>i</b>tio</i> <b>S</b> imulation <b>P</b> ackage
<b>DOS</b>	Density <b>O</b> f <b>S</b> tates
<b>PHDOS</b>	<b>P</b> Honon <b>D</b> ensity <b>O</b> f <b>S</b> tates
<b>BZ</b>	first <b>B</b> rillouin <b>Z</b> one
<b>TB</b>	Tight <b>B</b> inding
<b>TBA</b>	Tight <b>B</b> inding <b>A</b> pproximation
<b>LCPAO</b>	Linear <b>C</b> ombination of <b>P</b> seudo <b>A</b> tomical <b>O</b> rbital
<b>ADP</b>	Atomic <b>D</b> isplacement <b>P</b> arameter
<b>FCs</b>	Force <b>C</b> onstants
<b>1NNs</b>	First- <b>N</b> earest <b>N</b> eighbors
<b>2NNs</b>	Second- <b>N</b> earest <b>N</b> eighbors
<b>3NNs</b>	Third- <b>N</b> earest <b>N</b> eighbors



# Chapter 1

## Introduction

### 1.1 Motivation

While enjoying the conveniences offered by modern technologies relying on electricity, mankind has to face growing awareness regarding energy production, energy consumption and environment because of diminishing natural resources and global warming. Solutions to the energy problem should ensure sustainable development, including renewable energy to reduce the dependence on fossil fuels. Thermoelectric materials and their applications provide an option of improving the sustainability of electricity which are generated from the waste heat by means of thermoelectric generators. Likewise, a thermoelectric refrigerator uses power to drive a current of charge carriers which results in cooling. The thermoelectric refrigerator is environmentally friendly and has a long life, and therefore has the potential to replace traditional air conditioning.

The efficiency of thermoelectric devices is determined by the dimensionless figure-of-merit  $ZT$ , which depends on transport properties of the material such as the Seebeck coefficient, the electrical and thermal conductivities [1],

$$ZT = S^2\sigma T/\kappa. \quad (1.1)$$

Thus, a high  $ZT$  requires a large Seebeck coefficient,  $S$  and electrical conductivity,  $\sigma$  and a low thermal conductivity,  $\kappa$ . Over the past decades, most of efforts pursuing a high  $ZT$  concentrate on synthesizing and designing materials with a significantly reduced thermal conductivity accomplished by making use of their structural and electronic properties. Among them, superlattices and filled cage structures exhibit promising thermoelectric performances [2–6, 6, 7, 7–20]. The low thermal conductivity of superlattice structures is attributed to phonon scatterings between the interface, whereas the low thermal conductivity of caged structures, which can accommodate fillers in voids of the structure,

originates from incoherent phonon scatterings between the fillers and the framework. The basic idea is Slack's conjecture that the fillers are loosely bound to the surrounding cage atoms and therefore they "rattle". The rattling modes should strongly scatter the host phonons, leading to a dramatic reduction in the mean free path of phonons, resulting in a glass-like thermal conductivity while the electrical transport properties are less affected[1]. For this reason, skutterudites and clathrates become ideal candidates for promising thermoelectric materials since they contain large voids. Up to now, values of ZT larger than 1.6 for both filled-skutterudites and -clathrates have been reported[6, 7]. However, comparing with traditional thermoelectric materials, the relatively low efficiencies of the thermoelectric modules put them in a unfavorable competing position.

Further improvement of thermoelectric performance relies on the understanding of the transport properties. On one hand, mechanisms for the thermal conductivity are conflicting. Recent study reveal that phonons of skutterudites are in a crystal state rather than glass behavior as conjectured by Slack[21]. Moreover, it was also demonstrated that rather than the incoherent scatterings, the filler modes and host phonons are in a coherent scattering state, leading to longer phonon lifetimes[21]. Furthermore, the the Seebeck effect yet remains understood rather incompletely. For instance, FeSb<sub>2</sub> was found to display a giant Seebeck coefficient up to 45 mV/K at 12 K, over one hundred times those of conventional TE materials [22]. Although various mechanism have been proposed, none of them successfully could explain the remarkably high Seebeck coefficient [23–29].

Therefore, well-defined approaches and a deep analysis of their results are highly desirable. On the other hand, methods which can provide a microscopic understanding on a quantum mechanical level, so-called first-principles methods, become more and more feasible and popular. During the past decades, transport properties of electrons and phonons have been discussed extensively within the semi-classic Boltzmann transport theory, which allows us to describe macroscopic quantities in a microscopic concept. Basically, the Boltzmann theory treats electrons and phonons as particles whose motions are limited by various scattering mechanism described by relaxation times. Thus the accurate determination of the electronic structure and lattice dynamics of materials on a quantum mechanical level are prerequisites for a fundamental understanding of subsequent transport properties.

First-principles methods based on the density functional theory (DFT) in the local (spin-) density approximation (LDA) or in the generalized gradient approximation (GGA) emerged as very powerful approaches for such demanding tasks. They have made considerable successes in describing ground state properties of materials including crystal structure, electronic structure, lattice dynamics, elasticity, magnetism and other materials properties related to the total energy. Contrary to its extensive applications in descriptions of the ground properties, there are, however, only a small -but increasing-

number of attempts pioneered by Singh *et al* [30–36] to model thermoelectric properties. The present thesis deals with this subject.

## 1.2 Objective and Scope of Thesis

Equation 1.1 indicates that one can evaluate the thermoelectric performance of a material with the knowledge of the Seebeck coefficient  $S$ , the electric conductivity  $\sigma$  and the thermal conductivity  $\kappa$ . Both  $S$  and  $\sigma$  are transport properties of electrons, whereas  $\kappa$  is usually decoupled as  $\kappa_{el}$  and  $\kappa_{ph}$  relating to electron and phonon transports, respectively. Transport properties of electrons and phonons have been extensively discussed within the scopes of the Green-Kubo theory [37, 38] and Boltzmann transport theory [39, 40]. The latter is utilized for investigating electronic transport properties of thermoelectric materials throughout this thesis. For this purpose, electronic structures and lattice dynamics are prerequisites, for which first-principles methods are employed.

The main objective of this thesis is to develop an understanding of the thermoelectric properties of materials at the quantum mechanic level. This task is achieved by employing a comprehensive approach that merges the Boltzmann transport theory with a first-principles DFT method. This framework is used to explain a variety of experiments and to predict (or optimize) thermoelectric properties by means of band engineering.

This dissertation focuses on the electronic structure, lattice dynamics and electronic transport properties including electrical conductivity, Seebeck coefficient and electronic thermal conductivity. It is organized as follows. The rest of Chapter 1 attempts an overview of the thermoelectric phenomena and figure of merit that determines the efficiency of a thermoelectric material. Chapter 2 briefly reviews concepts for deriving ground state properties within density functional theory. Chapter 3 presents a powerful method combining the Boltzmann transport equations and first-principles electronic structures for calculating thermoelectric properties of materials. Technical details of code implementation are described and discussed. Applications of the methods are presented in Chapter 4 and 5 for two prototypical systems, namely skutterudites and clathrates. Both the theoretical results and experimental observations are included in this two chapters. Chapter 6 summarizes the work and provides a brief outlook for further efforts.

## 1.3 Thermoelectric Effects

Thermoelectric devices are based on two fundamental thermoelectric effects namely the Seebeck effect and the Peltier effect. The Seebeck effect was observed by Seebeck in

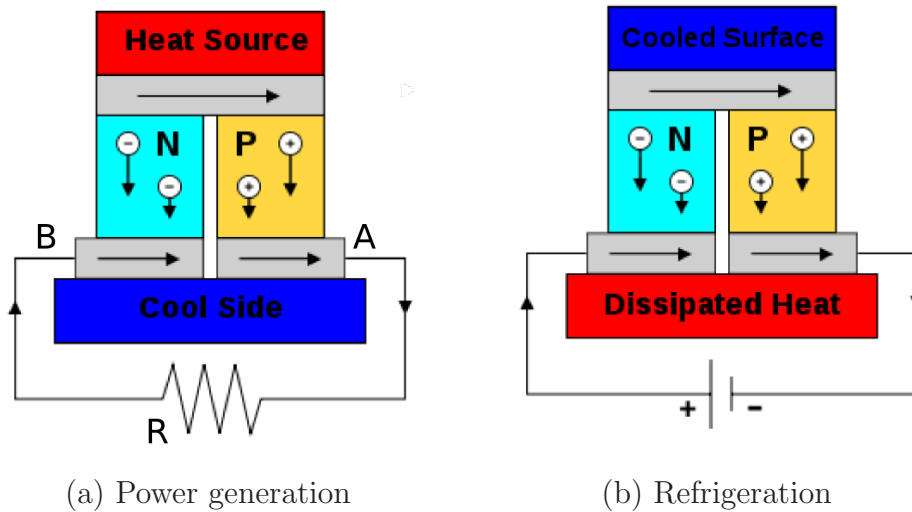


FIGURE 1.1: Illustration of thermoelectric modules. Power generation (a) and refrigeration (b) modules.

the early 1800s. As shown in Fig.1.1(a), if two dissimilar conductors, for instance n- and p-type semiconductors, are joined together and a temperature difference is applied to the two junctions, then a voltage difference ( $\Delta V$ ) between A and B proportional to the temperature difference ( $\Delta T$ ) is built up. The ratio of the voltage to the temperature difference ( $\Delta V/\Delta T$ ) is related to an intrinsic property of the materials historically termed as the thermopower which is now referred to as the Seebeck coefficient ( $S$ ). The differential Seebeck coefficient,  $S_{ab}$  being the difference in the Seebeck coefficients between a and b, is defined by

$$S_{ab} = \frac{\Delta V}{\Delta T} \quad (1.2)$$

The Peltier effect (Fig.1.1(b)) is the inverse of the Seebeck effect: when a current  $I$  is passed through a thermocouple between two different conductors, depending on the direction of the current absorption or generation  $Q$  of heat occurs at the two junctions. The Peltier coefficient is defined as

$$\pi_{ab} = \frac{Q}{I} \quad (1.3)$$

The Seebeck and Peltier coefficients are related by the Kelvin relationship:

$$S_{ab} = \frac{\pi_{ab}}{T} \quad (1.4)$$

which can be derived by applying irreversible thermodynamics. Their validity has been demonstrated for many thermoelectric materials and it is assumed that they hold for all materials used in thermoelectric applications.

## 1.4 Figure of Merit

For any technological application, efficiency is always the issue of highest concern. It should be noted that the basis physics behind thermoelectric phenomena is the diffusion of energy and charge transported by by carriers -electrons or holes- under a temperature gradient and an electric field. At this point some assumptions are made. First, the electrical and thermal conductivities and Seebeck coefficients of the two conductors, the arms of the thermoelectric generator, are constant for the whole material. Second, the contacts are ideal so that their resistances at the hot and cold junctions are negligible compared to those of the arms. The electrical power  $P$ , the power output, delivered to the load ( $R$  shown in Fig.1.1(a))is given as,

$$P = I^2 R_0, \quad (1.5)$$

where  $I$  is the electric current and  $R_0$  is the serial resistivity of the load. The current  $I$  is induced by the Seebeck effect

$$I = \frac{(S_p - S_n)(T_h - T_c)}{R_0 + R_p + R_n} \quad (1.6)$$

where,  $S_i$  and  $R_i$  ( $i$  stands for  $p$  or  $n$  conductors ) represent the Seebeck coefficients and resistivity of the two legs of the thermoelectric module, respectively. The temperatures  $T_h$  and  $T_c$  stand for the temperatures at the hot and cold sites, respectively. The quantity  $P$  is a function of the ratio of the load resistivity to the sum of the resistivities of the two legs. For maximizing  $P$ , it is required that  $R_0 = R_p + R_n$ .

The heat flow into the hot side consists of three components. First, the heat flow through the thermoelectric material due to the thermal conductance of the material,

$$Q_t = K(T_h - T_c) \quad (1.7)$$

where  $\kappa$  is the thermal conductivity of the two conductors in parallel,

$$\kappa = \frac{K_p K_n}{K_p + K_n} \quad (1.8)$$

The absorbed heat at the hot junction due to the Peltier effect, is

$$Q_p = (S_p - S_n)IT_h. \quad (1.9)$$

where, the Kelvin relation Eq.(1.4) has been used. The heat that arrives at the hot side due to Joule heating of the thermoelectric materials under the assumption that half of

this heat goes to the hot side and half to the cold side of the module, is now

$$Q_j = \frac{1}{2}I^2(R_p + R_n). \quad (1.10)$$

The efficiency  $\eta$  of a thermoelectric generation device is measured as the ratio of electrical power delivered to the load ( $R$  in Fig.1.1(a)) over the heat flow into the hot side of the module[41].

$$\eta = \frac{P}{Q_t + Q_p + Q_j}. \quad (1.11)$$

In the case of maximum of power output and substituting Eq.(1.7) to (1.10)  $\eta$  can be expressed as

$$\eta = \frac{T_h - T_c}{\frac{3T_h + T_c}{2} + \frac{4}{Z}} \quad (1.12)$$

where  $Z$  is given by

$$Z = \frac{(S_p - S_n)^2}{(R_p + R_n)K}. \quad (1.13)$$

The quantity  $Z$  is intrinsically determined by the physical properties of the materials. However,  $R_L = R_p + R_n$  is not the condition for maximizing efficiency. If one denotes  $m = \frac{R_L}{R_p + R_n}$ , then  $\eta$  is generally expressed as

$$\eta = \frac{T_h - T_c}{T_h} \frac{\frac{m}{1+m}}{1 + \frac{K(R_h + R_n)}{(S_p - S_n)^2} \frac{1+m}{T_h} - \frac{1}{2} \frac{T_h - T_c}{T_h} \frac{1}{1+m}} \quad (1.14)$$

Now,  $\eta$  is a function of the temperatures at the hot and cold junctions, of  $Z$ , and of  $m$ . Maximizing  $\eta$  with respect to  $m$  requires

$$\frac{\partial \eta}{\partial m} = 0 \quad (1.15)$$

which results in

$$m_0 = (1 + ZT_M)^{\frac{1}{2}} \quad (1.16)$$

where  $T_M$  is the average temperature of the hot and cold side:

$$T_M = \frac{T_h + T_c}{2} \quad (1.17)$$

The unit of  $Z$  is (1/K), the commonly used combined quantity  $ZT$  is the dimensionless. It is named the figure-of-merit, which can be rewritten as

$$ZT = \frac{S^2 \sigma}{K} \quad (1.18)$$

where  $\sigma$  is the electrical conductivity of a thermoelectric material.

Substituting  $m_0$  back to Eq.(1.14) yields the maximum efficiency as

$$\eta = \frac{T_h - T_c}{T_h} \frac{m_0 - 1}{m_0 + \frac{T_c}{T_h}} \quad (1.19)$$

One realizes that the larger  $m_0$  is, the higher is then efficiency.

Now the two limiting cases,  $ZT_M \ll 1$  and  $ZT_M \gg 1$ , are considered. When  $ZT_M \ll 1$ ,

$$\lim_{ZT_M \ll 1} \eta = \frac{T_h - T_c}{T_h} \frac{ZT_M}{2(1 + \frac{ZT_M}{2} + \frac{T_h}{T_c})}. \quad (1.20)$$

Therefore, an efficiency of much less than unity is obtained even when the temperatures fit the condition of  $(T_h - T_c)/T_h \rightarrow 1$ , which is not interesting for thermoelectrical applications. On the other hand, when  $ZT_M \gg 1$ , then  $\eta \rightarrow (T_h - T_c)/T_h$  becomes the ideal thermodynamic efficiency. In general,  $ZT_M$  is in the order of unity at most temperatures of interest. If  $ZT_M = 1$ , then  $\eta$  can never exceed the limit  $\frac{m-1}{m} \approx 0.29$ . The value  $\eta = 0.5$  is the upper boundary when  $ZT_M = 3$ .



## Chapter 2

# Electronic Ground State and Lattice Dynamics

For the calculation of a physical quantity of a material at the quantum level, the many-body Schrödinger equation that involves both nuclei and electrons has to be solved for the many-body eigenfunctions  $\Psi(\mathbf{R}_1, \mathbf{R}_2, \dots, \mathbf{R}_N; \mathbf{r}_1, \mathbf{r}_2, \dots, \mathbf{r}_n)$  with  $\mathbf{R}$  and  $\mathbf{r}$  labeling the positions of nuclei and electrons, respectively. The many-body Hamiltonian has the form of

$$\hat{H} = \hat{T}_e + \hat{T}_n + \hat{V}_{ee} + \hat{V}_{en} + \hat{V}_{nn} \quad (2.1)$$

where  $\hat{T}_e$  and  $\hat{T}_n$  are the operators of the kinetic energy of the electrons and nuclei, respectively,  $\hat{V}_{ee}$ ,  $\hat{V}_{en}$  and  $\hat{V}_{nn}$  are electron-electron, electron-nuclei and nuclei-nuclei Coulomb interactions, respectively. Writing them explicitly,

$$\hat{T}_e = -\frac{\hbar^2}{2m_e} \sum_{i=1}^N \nabla_i^2 \quad (2.2)$$

$$\hat{T}_n = -\frac{\hbar^2}{2M_n} \sum_{n=1}^M \nabla_n^2 \quad (2.3)$$

$$\hat{V}_{ee} = \frac{1}{4\pi\epsilon_0} \frac{1}{2} \sum_{i,j=1;i \neq j}^N \frac{e^2}{|\mathbf{r}_i - \mathbf{r}_j|} \quad (2.4)$$

$$\hat{V}_{en} = -\frac{1}{4\pi\epsilon_0} \sum_{n=1}^M \sum_{i=1}^N \frac{Z_n e^2}{|\mathbf{r}_i - \mathbf{R}_n|} \quad (2.5)$$

$$\hat{V}_{nn} = \frac{1}{4\pi\epsilon_0} \frac{1}{2} \sum_{n,m=1;n \neq m}^M \frac{Z_n Z_m e^2}{|\mathbf{R}_n - \mathbf{R}_m|} \quad (2.6)$$

where  $m_e$  and  $M_n$  are the electron and nucleus mass respectively,  $Z_n$  is the nuclear number of the  $n$ -th atom,  $e$  is the electronic charge, and  $\hbar$  is the reduced Planck constant.

Because nuclei are much heavier than electrons i.e.,  $M_n \gg m_e$ , one can often treat the nuclei as if they are static (Born-Oppenheimer approximation)[42]. Therefore one separates the electronic degrees of freedom from those of the nuclei by separating the ion kinetic energy from Eq.(2.1) and treat the atomic positions  $R_n$  as external parameters in the electronic Hamiltonian. Therefore, the decoupling of the electronic and nuclei degrees leads to  $\Psi = \psi\Phi$  with  $\psi$  and  $\Phi$  denoting wavefunctions of electrons and nuclei, respectively. The electronic Hamiltonian is given by

$$\hat{H}_e = \hat{T}_e + \hat{V}_{ee} + \hat{V}_{en} \quad (2.7)$$

By solving Eq.(2.7), one obtains the total energy of the ground state of the system

$$E_0 = \langle \psi_0 | H_e | \psi_0 \rangle + V_{nn} \quad (2.8)$$

where  $\psi_0$  is the eigenfunction of the electronic ground state and  $E_0$  is the ground total energy of the system. However, for realistic systems the resultant electronic Hamiltonian Eq.(2.7) is far too complicated for a direct solution of Schrödinger's equation because of the large number of electrons. Instead of solving for the many-body wavefunctions, density functional theory (DFT) deals with this problem in terms of the electronic density distribution  $\rho(\mathbf{r})$  and moves all complications such as the electron exchange-correlation functional as a universal function of the density  $E_{xc}[\rho(\mathbf{r})]$  into an effective potential energy term. The total energy functional  $E[\rho]$  is minimized for the ground state density, which yields the ground state energy.

During the past decades, *ab initio* or first-principles methods based on the DFT developed by Kohn and Sham, [43, 44] became the "standard model" in computational material science. The term "ab initio" or "first-principles" means to calculate material properties directly from fundamental quantum mechanics without any empirical parameters. On the other hand, the tight binding method is a method that parametrizes the Hamiltonian in terms of matrix elements built up by atom-like orbitals. In the sense of bonding described by atomic orbitals, the tight binding concept provides an illustrative physical insight. In this chapter, the framework of an *ab initio* and the tight binding method are briefly sketched, which are used in this thesis.

## 2.1 Density Functional Theory

The basic formulation of the DFT are the Hohenberg-Kohn theorems. According to the Hohenberg-Kohn theorems the total energy of the electronic Hamiltonian is a functional of the electron density  $E = E[\rho(\mathbf{r})]$ , which is minimized for the ground state density  $\rho_0(\mathbf{r})$ [43]. In the spirit of this theory, the total energy functional of a many-electron system under an external potential  $v_{ext}$  (the potential energy generated by the nuclei) is given by

$$E[n] = \int v_{ext}[\rho(\mathbf{r})]d\mathbf{r} + F[\rho(\mathbf{r})] \quad (2.9)$$

where  $F[\rho(\mathbf{r})]$  is a universal functionak of the electronic density, which consists of the kinetic energy of electrons  $T[\rho(\mathbf{r})]$ , the classic Coulomb interaction (Hartree interaction) between the electrons,  $E_H[\rho(\mathbf{r})]$  and the remaining term  $E_{xc}[\rho(\mathbf{r})]$  containing all the complications of the non-classical electron exchange-correlation interactions. The ground state energy is derived by applying the variational principle

$$\left. \frac{\delta E[\rho(\mathbf{r})]}{\delta \rho(\mathbf{r})} \right|_{\rho=\rho_0} = 0 \quad (2.10)$$

with the constraint that the number of electrons  $N$  remains constant during the variational process:

$$\int \rho_0(\mathbf{r})d\mathbf{r} = N \quad (2.11)$$

The Hohenberg-Kohn theory arrives at an equation which only involves functional or derivatives of functionals of the density alone. However, this equation could not be solved (at least up to now) with the required accuracy.

Therefore, another scheme was suggested partially going back to a wavefunction-like description. Kohn and Sham remedied the Hohenberg-Kohn problem by mapping the fully interacting electronic system onto a fictitious system of noninteracting quasi particles moving in an effective potential[44]. The kinetic energy functional  $T$  is split into a single particle term  $T_s$  and the remainder ( $T - T_s$ ) is merged into the many-body exchange-correlation functional. The problem of finding the many-body Schrödinger equation is now replaced by solving single particle equations

$$\left[-\frac{1}{2}\nabla^2 + V_{eff}(\mathbf{r})\right]\psi_i = \varepsilon_i\psi_i \quad (2.12)$$

where  $\psi(\mathbf{r})$  are so-called Kohn-Sham (KS) orbitals, which have no direct physical meaning but only server for building up the true ground state density by summing over an

appropriate number of states (one usually takes occupied states),

$$\rho_0(\mathbf{r}) = \sum_{i=1}^{occ.} |\psi_i(\mathbf{r})|^2 \quad (2.13)$$

The density  $\rho_0(\mathbf{r})$  is subject to the constraint condition Eq.(2.11). The resulting effective potential consists of the external potential  $V_{ext}$ , the Hartree potential  $V_H$ , and the exchange-correlation potential  $V_{xc}$ :

$$\begin{aligned} V_{eff} &= V_{ext} + V_H + V_{xc} \\ V_{ext} &= -\frac{1}{4\pi\epsilon_0} \sum_{n=1}^M \frac{Z_n e^2}{|\mathbf{r}_i - \mathbf{R}_n|} \\ V_H &= \frac{1}{4\pi\epsilon_0} \int \frac{e^2 \rho[\mathbf{r}_j]}{|\mathbf{r}_i - \mathbf{r}_j|} d\mathbf{r}_j \\ V_{xc} &= \frac{\delta E_{xc}[\rho]}{\delta[\rho]} \end{aligned} \quad (2.14)$$

Consequently, the ground state total energy for a given configuration  $\{\mathbf{R}_1, \dots, \mathbf{R}_N\}$  of atoms is given by

$$E_0(\mathbf{R}_1, \dots, \mathbf{R}_N) = \sum \varepsilon_i - \frac{1}{2} E_H[\rho_0] + E_{xc}[\rho_0] - \int V_{xc} \rho_0 d\mathbf{r} + V_{nn}(\mathbf{R}_1, \dots, \mathbf{R}_N) \quad (2.15)$$

with the the ground state energy  $E_0$ . Correspondingly, the force  $\mathbf{F}_I$  acting on atom  $I$  is defined as

$$\mathbf{F}_I(\mathbf{R}_I) = \frac{\partial E_0(\mathbf{R}_1, \dots, \mathbf{R}_N)}{\partial \mathbf{R}_I} \quad (2.16)$$

exploiting the total energy being dependent on the atomic positions.

## 2.2 Approximations to the exchange-correlation Functional

The quality of the results of actual calculations for real systems depends on the approximation one has to make for  $E_{xc}$ . There are two well-known and widely used approximations: the local density approximation (LDA) and the generalized gradient approximation (GGA). Within LDA, the exchange-correlation energy is given by[44]

$$E_{xc}^{LDA}[\rho(\mathbf{r})] = \int d\mathbf{r} \rho(\mathbf{r}) \epsilon_{xc}^{LDA}[\rho(\mathbf{r})] \quad (2.17)$$

where  $\epsilon_{xc}^{LDA}$  is the exchange-correlation energy per electron for a homogeneous gas of interacting electrons. The GGA treats  $\epsilon_{xc}$  as a function of  $n(\mathbf{r})$  and its gradient  $\nabla n(\mathbf{r})$  [45, 46],

$$\epsilon_{xc}^{GGA}[\rho(\mathbf{r})] = f[\rho(\mathbf{r}), \nabla\rho(\mathbf{r})] \quad (2.18)$$

by that taking into account also the local change of the functional. LDA and in particular GGA are often successful in calculating various ground states properties. It is, however, well known that LDA overestimates the binding energy, while GGA works well for smaller atoms (e.g. 3d and 4d transition elements) but underestimates the bonding for large atoms (such as 5d transition elements).

## 2.3 Methods

### 2.3.1 The Pseudo-potential Approach: VASP

The KS orbitals used to construct the electron density as defined in Eq.(2.13) are expanded in convenient basis sets. For crystals with periodic boundary conditions, the KS orbitals must obey the Bloch theorem and are therefore labeled in terms of the wave vector  $\mathbf{k}$  and band index  $n$ ,  $\psi_{n,\mathbf{k}}(\mathbf{r})$ . For the boundary condition, plane waves are natural choices,

$$\psi_{n,\mathbf{k}}(\mathbf{r}) = \sum_{\mathbf{G}} c_{n,\mathbf{k}}^{\mathbf{G}} e^{i(\mathbf{k}+\mathbf{G})\cdot\mathbf{r}} \quad (2.19)$$

where  $\mathbf{G}$  is a reciprocal lattice vector.

The main disadvantage of a plane wave basis set is that the number of basis functions required to accurately describe atomic wavefunctions close to a nucleus would be enormous because of the rapid change of the potential and wavefunction near the nuclei. To make calculations feasible and trustable, one replaces the bare nuclei by ions for the construction of so-called pseudo-potentials. The argument for that is that only the outer-shell electronic states of atoms are involved in the bonding.

The practical implementation of DFT, used throughout this thesis, is the Vienna *ab initio* Simulation Package (VASP)[47, 48], which adopts the plane wave basis set and Blöchl's projector-augmented wave (PAW) method for constructing the pseudo-potentials [49, 50]. For the actual calculations in this thesis, either the LDA parametrization of Ceperley and Alder[51] or the GGA parametrization of Perdew, Burke and Ernzerhof[52] GGA are chosen for the exchange-correlation functional, depending on the specific material under study.

## 2.3.2 Tight-binding Method

### 2.3.2.1 Slater-Koster Scheme

Besides plane waves, one may use localized orbitals such as atomic orbitals as basis sets, for which the Bloch sum is constructed by

$$\phi_{n,\mathbf{k}}(\mathbf{r}) = \frac{1}{\sqrt{N}} \sum_{\mathbf{R}_i} e^{i\mathbf{R}_i \cdot \mathbf{k}} \varphi_n(\mathbf{r} - \mathbf{R}_i) \quad (2.20)$$

where the sum extends over atomic coordinates in all the unit cells of the solid. The function  $\varphi_n(\mathbf{r} - \mathbf{R}_i)$  denotes an atomic orbital centered at  $\mathbf{R}_i$  with  $n$  labeling atomic quantum numbers of the orbital. The orbital  $\phi_{n,\mathbf{k}}(\mathbf{r})$  must satisfy the Bloch theorem. Generally, several types of atomic orbitals are involved, therefore one uses the Bloch sum of each orbital as basis to construct the wavefunction which is the eigenfunction of the Schrödinger equation as given by Eq.(2.12).

$$\psi_{i,\mathbf{k}}(\mathbf{r}) = \sum_n C_n^i(\mathbf{k}) \phi_{n,\mathbf{k}}(\mathbf{r}) \quad (2.21)$$

Substituting Eq.(2.21) and multiplying Eq.(2.7) on the left by the complex conjugate of  $\phi_m(\mathbf{k})$ , one arrives at

$$\sum_n H_{m,n}(\mathbf{k}) C_n^i(\mathbf{k}) = \varepsilon_i(\mathbf{k}) \sum_n S_{m,n}(\mathbf{k}) C_n^i(\mathbf{k}) \quad (2.22)$$

where

$$H_{m,n}(\mathbf{k}) = \frac{1}{N} \sum_{\mathbf{R}_i, \mathbf{R}_j} e^{i\mathbf{k} \cdot (\mathbf{R}_j - \mathbf{R}_i)} \int \varphi_m^*(\mathbf{r} - \mathbf{R}_i) H \varphi_n(\mathbf{r} - \mathbf{R}_j) = \sum_{\mathbf{R}} e^{i\mathbf{k} \cdot \mathbf{R}} h_{m,n}(\mathbf{R}) \quad (2.23)$$

$$S_{m,n}(\mathbf{k}) = \frac{1}{N} \sum_{\mathbf{R}_i, \mathbf{R}_j} e^{i\mathbf{k} \cdot (\mathbf{R}_j - \mathbf{R}_i)} \int \varphi_m^*(\mathbf{r} - \mathbf{R}_i) \varphi_n(\mathbf{r} - \mathbf{R}_j) = \sum_{\mathbf{R}} e^{i\mathbf{k} \cdot \mathbf{R}} s_{m,n}(\mathbf{R}) \quad (2.24)$$

The Slater-Koster concept uses orthogonal orbitals. There are four types of integrals involved in Eq.(2.23): on-site, two-center, three-center and four-center integrals depending on the center of atomic orbitals  $\varphi$  and  $H$ . In the Slater-Koster scheme[53], it is assumed that three-center and four-center integrals are negligible compared to two-center integrals. The two-center  $h$  and  $s$  are generally referred to as hopping and overlap parameters, respectively. By the Slater-Koster method, an energy integral between two orbitals located at two different atoms is a function of bond integrals and direction cosines between the two atoms,

$$h_{m,n} = f(V_i, \alpha, \beta, \gamma) \quad (i = \sigma, \pi, \delta) \quad (2.25)$$

where  $\alpha, \beta, \gamma$  are the direction cosines and  $V_i$  are bond integrals. The Slater-Koster table lists complete energy integrals for s, p, and d orbitals [53]

### 2.3.2.2 Calculating TB parameters

The fitting procedure in principle is quite simple. One performs the TB calculations starting from a set of guess TB parameters and then compares the TB bands with those derived from *ab initio* calculations. One then needs to adjust the TB parameters in order to minimize the deviation of TB bands from the *ab initio* bands. By applying a loop of such operations, one obtains a set of reasonable parameters. There exists standard nonlinear optimization algorithms for the fitting procedure. The procedure is straightforward and works for systems with a few atoms per unit cell. However, the number of the TB parameters grows significantly as the size of the system grows. Correspondingly, the number of parameters used during the minimizing procedure grows significantly, consequently resulting in an extremely expensive fitting. Moreover, the quality of the returned TB parameters depends on the number of bands used in the fitting, which further adds difficulties to derive physically meaningful TB parameters.

Instead, one may extract TB parameters directly from an *ab initio*-like method using localized orbitals which could be Gaussian-type orbitals[54], maximally localized Wannier orbitals [55] and so on. Andersen *et al* pioneered the attempts using a linear combination of muffin-tin orbital (LMTO) method[56, 57]. Although the resulting hopping parameters usually vanish rapidly as a function of distance between the atoms, they strongly depend on the atomic spheres approximation which causes uncertainties for the fitting. In the thesis, a linear combination of pseudo-atomic orbital (LCPAO) as implemented in the OpenMX package is used to obtain the two-center hopping parameters[58, 59]. Non-orthogonal basis are used. The pseudo-atomic orbitals (PAO) are derived from wavefunction of the atomic Kohn-Sham equations with a confinement pseudo-potential

$$V(r) = \begin{cases} -\frac{Z}{r} & r \leq r_1 \\ \sum_{n=0}^3 b_n r^n & r_1 \leq r \leq r_c \\ h & r_c < r \end{cases} \quad (2.26)$$

where  $b_n$  are determined to ensure the radial wave function and its first derivative are continuous at both  $r_1$  and  $r_c$ . This controls the slope and tail of the radial function. Then the atomic orbitals are constructed by combining the radial wave function with spherical harmonics. The generated radial function has the same number of nodes as the full potential atomic orbital. However, in contrast to the long range full potential atomic orbital, it can have a much shorter tail which facilitates tight binding fitting. In this thesis a cutoff radii of 7.0 a.u. for Pt, Au and Ge is used.

One then constructs wavefunctions for the KS equation using Eqs.(2.20) and (2.21), and then builds the charge density utilizing Eq.(2.13). The resulting Hamiltonian and overlap matrices of the KS equation are given by Eqs.(2.23) and (2.24). Thus, the parameters  $h_{m,n}$  and  $s_{m,n}$  can be extracted directly from such a calculation and tight binding parameters are derived using the Slater-Koster table in Ref.[53].

## 2.4 Theory of Lattice Dynamics

The basic theory of the harmonic lattice dynamics of solids is formulated in the textbook of Born and Huang[60], in which motions of atoms follow Newton's second law. In the Born-von Kármán model[60, 61], the chemical bond between atoms is simulated by forces of a spring without considering the electronic structure that actually determine them. For this concept, the spring constants are needed which might be extracted from experimental informations. In contrast to this empirical approach, *ab initio* or first-principles approaches have to take the electronic structure fully into account for calculating forces and the phonon spectrum is derived without any empirical information. The *ab initio* approaches to harmonic vibration properties are generally divided into two categories based on the different ways of constructing the dynamical matrix, namely the linear response theory and the direct method. In the linear response approach, the dynamical matrix is expressed in terms of the dielectric matrix which describes the response of the electronic system to the perturbations of lattice distortion. On the other hand, in the direct method often referred as the supercell method, the dynamical matrix is constructed by force fields generated by small displacements of atoms in a supercell [62, 63]. In this section, the Born-von Kármán model and the direct method are introduced, which are used to investigate the lattice dynamics of the proposed materials in the harmonic approximation.

### 2.4.1 Harmonic approximation

In solids, atoms vibrate about their equilibrium positions and their motions follow Newton's second law.

$$M_i \ddot{u}_{li\alpha} = F_{li\alpha} = -\frac{\partial V}{\partial u_{li\alpha}} \quad (2.27)$$

The potential energy  $V$  can be written in increasing power of the displacement  $s_{li\alpha}$  about the equilibrium positions

$$V = V_0 + \sum_{\substack{li\alpha \\ l'i'\beta}} \frac{\partial^2 V}{\partial u_{li\alpha} \partial u_{l'i'\beta}} + \frac{1}{3!} \sum_{\substack{li\alpha \\ l'i'\beta \\ l''i''\gamma}} \frac{\partial^3 V}{\partial u_{li\alpha} \partial u_{l'i'\beta} \partial u_{l''i''\gamma}} + \dots \quad (2.28)$$

By the harmonic approximation, the expansion is terminated at the second order. Substituting Eq.(2.28) into Eq.(2.27), one arrives at

$$M_i \ddot{u}_{i\alpha} = - \sum_{l'j'\beta} \phi \begin{pmatrix} l'j'\beta \\ lj\alpha \end{pmatrix} u_{l'j'\beta} \quad (2.29)$$

where  $\phi \begin{pmatrix} l'j'\beta \\ lj\alpha \end{pmatrix} = \frac{\partial^2 V}{\partial u_{i\alpha} \partial u_{l'j'\beta}}$ .

Because of the periodicity of the solid the solutions to Eq.(2.29) must be periodic in space, and the ansatz for the time dependency comes from differential equation according to Newton's second law,

$$s_{li\alpha} = \frac{1}{\sqrt{M_i}} c_{i\alpha} e^{(i\mathbf{q} \cdot \mathbf{R}_i - \omega t)} \quad (2.30)$$

Inserting Eq.(2.30) into Eq.(2.29), one finally obtains

$$D_{i\alpha}^{i'\beta}(\mathbf{q}) = \sum_{l'} \frac{1}{\sqrt{m_i m_{i'}}} \phi \begin{pmatrix} l'i'\beta \\ li\alpha \end{pmatrix} e^{i\mathbf{q} \cdot (\mathbf{R}_{l'i'} - \mathbf{R}_{li})} \quad (2.31)$$

The frequencies are derived by solving the eigenequations

$$\omega^2 c_{i\alpha} = \sum_{i'\beta} D_{i\alpha}^{i'\beta}(q) c_{i'\beta} \quad (2.32)$$

In principle, phonon dispersion  $\omega(q)$  can be obtained by solving Eq.(2.32) once given  $\phi \begin{pmatrix} l'j'\beta \\ lj\alpha \end{pmatrix}$ .

Finally, the equations have to be quantized properly in order to fulfill the Bose-Einstein statistics of the quantized levels of the harmonic oscillators. After that, one speaks about phonons, the quantized energies of the spectrum, and also the zero point vibration energy arises.

## 2.4.2 Born-von Kármán model

Within the Born-von Kármán model, chemical bond between atoms is simulated by spring constants[60, 61]. The  $\alpha$  component of the acting force on atom  $j$  in cell  $l$  is induced by atom  $j'$  in cell  $l'$ , which is expressed in general as

$$\phi \begin{pmatrix} l'j'\beta \\ lj\alpha \end{pmatrix} = -k e_\alpha e_\beta \quad (l'j' \neq lj) \quad (2.33)$$

where  $k$  is the spring constant and  $e_\alpha$  and  $e_\beta$  are direction cosines of the vector from  $i$  to  $i'$ . The so-called self force constants (SFCs) (sometimes referred to on-site force constants)

are constructed by

$$\phi \begin{pmatrix} li\beta \\ li\alpha \end{pmatrix} = - \sum_{\substack{l',i' \\ l'i' \neq li}} \phi \begin{pmatrix} l'i'\beta \\ li\alpha \end{pmatrix} \quad (2.34)$$

With the knowledge of the force constants, the dynamical matrix is constructed by Eq.(2.32) and diagonalized.

### 2.4.3 Direct method

From Eq.(2.27) and (2.29), one writes

$$F_{li\alpha} = - \sum_{l'i'\beta} \phi \begin{pmatrix} l'j'\beta \\ lj\alpha \end{pmatrix} u_{l'i'\beta} \quad (2.35)$$

If only one of the atoms is displaced while all others are frozen, forces on the atoms are only induced by the displaced one. In other words,  $u_s$  are zero except for  $u_{l'i'\beta}$ . Consequently, the force constant  $\phi \begin{pmatrix} l'j'\beta \\ lj\alpha \end{pmatrix}$  can be simply formulated as

$$\phi \begin{pmatrix} l'j'\beta \\ lj\alpha \end{pmatrix} = \frac{F_{li\alpha}}{u_{l'i'\beta}} \quad (2.36)$$

Now, the force constants (or force constant matrix, rather) can be set up based on forces on atoms induced by displaced atoms.

Accurate force calculations can be done using a first-principles method. The force on ion  $i$  along  $\alpha$  direction is given by

$$F_{i\alpha} = - \frac{\partial}{\partial u_{i\alpha}} \langle \Psi | H_e | \Psi \rangle - \frac{\partial E_{ion}}{\partial u_{i\alpha}} \quad (2.37)$$

where  $H_e$  is the electronic Hamiltonian as given by Eq.2.7, and  $E_{ion}$  is the energy of interaction between the ions.

The Hellmann-Feynman theorem states that if  $\Psi$  is an eigenstate of the Hamiltonian, then

$$\frac{\partial}{\partial u_{i\alpha}} \langle \Psi | H_e | \Psi \rangle = \langle \Psi | \frac{\partial H_e}{\partial u_{i\alpha}} | \Psi \rangle \quad (2.38)$$

Substituting this to Eq.(2.37) gives

$$F_{i\alpha} = - \langle \Psi | \frac{\partial H_e}{\partial u_{i\alpha}} | \Psi \rangle - \frac{\partial E_{ion}}{\partial u_{i\alpha}} \quad (2.39)$$

The direct method has been implemented in the *f*PHON program package <sup>1</sup>.

---

<sup>1</sup>*f*PHON, written by David Reith, which is a strongly modified and generalized version of the package PHON[64, 65]



# Chapter 3

## Modeling Thermoelectric Materials

Transport theory deals with flow of charges or heat flow through a solid material under external fields, such as an electric field and/or a temperature gradient. The motions of carriers (electrons or phonons) are driven by the external fields but resisted by internal scattering processes between them and other (quasi)particles. There are energy and momentum exchanges within the interactions resulting in finite electric or thermal conductivity. On the other hand, the interactions have the consequence that the conducted carriers are not in their equilibrium states. There are two approaches to such a non-equilibrium transport, namely the Green-Kubo theory theory[38] and the semi-classical Boltzmann transport theory[39]. The former relates transport coefficients to the correlation function of the current or heat flux. The latter treats effects of various scattering mechanisms on transport properties in terms of relaxation times. The Boltzmann transport theory has proven its validity in numerous applications where calculated transport coefficients can be readily be compared with experimental results. In this section it is shown how to merge the electronic structure -as derived from a first-principles approach- into the Boltzmann transport theory for deriving the electronic transport coefficients .

### 3.1 Preliminaries

The Boltzmann theory describes the electron system by introducing a distribution function, which is given by the Fermi function when electrons are in equilibrium states. It is explicitly dependent on the band index  $n$  and wavevector  $\mathbf{k}$ , which are the quantum numbers of the electronic states. When deviating from equilibrium, the distribution function may depend on spatial coordinates  $\mathbf{r}$  and time  $t$ , characterized by  $f_n(\mathbf{r}, \mathbf{k}, t)$ . The distribution  $f_n(\mathbf{r}, \mathbf{k}, t)$  in the neighborhood of  $\mathbf{r}$  may change as a result of the following mechanisms:

1. Diffusion: electrons with velocities  $\mathbf{v}(\mathbf{k})$  flow into the vicinity of  $\mathbf{r}$  from adjacent regions meanwhile others leave, because of diffusion.
2. external fields: electrons are driven by forces generated by external fields, which in the present case is the electric field and the temperature gradient.
3. Collisions: electrons are scattered from state to state by various interactions including electron-phonon, electron-electron, electron-impurity interactions and so on.

The total rate of change of the distribution function is then

$$\dot{f} = \dot{f}_{diff} + \dot{f}_{field} + \dot{f}_{coll}. \quad (3.1)$$

In the steady state  $\dot{f}$  vanish. Thus one arrives at

$$\dot{f}_{diff} + \dot{f}_{field} = -\frac{df}{dt_{coll}}. \quad (3.2)$$

If one introduces a relaxation time  $\tau(\mathbf{k})$  to describe scattering effects and assumes that  $f_n(\mathbf{r}, \mathbf{k}, t)$  approaches the equilibrium distribution  $f^0(\mathbf{k})$ , then

$$\frac{\partial f}{\partial t_{coll}} = -\frac{f(\mathbf{k}) - f^0(\mathbf{k})}{\tau(\mathbf{k})}. \quad (3.3)$$

As  $f$  is a function of  $(\mathbf{r}, \mathbf{k}, t)$ , the rate of change of the distribution due to diffusion and external field can be written as

$$-\dot{f}_{diff+field} = \frac{\partial f}{\partial \mathbf{r}} \frac{\mathbf{r}}{dt} + \frac{\partial f}{\partial \mathbf{k}} \frac{e\mathcal{E}}{\hbar}, \quad (3.4)$$

where

$$\frac{\mathbf{r}}{dt} = \mathbf{v}(\mathbf{k}) \frac{1}{\hbar} \frac{\partial E}{\partial \mathbf{k}} \quad (3.5)$$

Since  $f$  deviates only slightly from  $f^0$ ,  $f$  is replaced by  $f^0$  for the above equation. One obtains easily the relation  $\frac{\partial f}{\partial \mathbf{r}}$  from the definition of  $f^0$

$$\frac{\partial f}{\partial \mathbf{r}} = -\frac{\partial f^0}{\partial E} \left( \nabla \mu + \frac{E - \mu}{T} \right) \nabla T. \quad (3.6)$$

Substituting Eq.(3.6) back into Eq.(3.4) and then substituting Eqs.(3.3) and (3.4) into Eq.(3.2), the distribution function is then written as

$$f(\mathbf{k}) = f^0(\mathbf{k}) + \left( -\frac{\partial f^0}{\partial E} \right) \mathbf{v}(\mathbf{k}) \tau(\mathbf{k}) \left\{ e\mathcal{E} - \left( \frac{\partial \mu}{\partial T} + \frac{E - \mu}{T} \right) \nabla T \right\}. \quad (3.7)$$

## 3.2 Transport Coefficients

The flowing of charges under electric field leads to an electric current, of which the density is

$$\mathbf{J}_e = \frac{2e}{8\pi^3} \int \mathbf{v}(\mathbf{k}) f(\mathbf{k}) d\mathbf{k} \quad (3.8)$$

where  $f(\mathbf{k})$  is given by Eq.(3.7). Similarly for the heat current density produced by the electrons, one gets

$$\mathbf{J}_Q = \frac{2}{8\pi^3} \int \mathbf{v}(\mathbf{k}) [E - \mu] f(\mathbf{k}) d\mathbf{k} \quad (3.9)$$

in which  $\mu$  is the chemical potential. Substituting Eq.(3.7) into Eqs.(3.8) and (3.9) and neglecting the term  $f^0$  in Eq.(3.7) one arrives at

$$\begin{aligned} \mathbf{J}_e &= \frac{2e}{8\pi^3} \int \mathbf{v}(\mathbf{k}) \mathbf{v}(\mathbf{k}) \tau(\mathbf{k}) \left(-\frac{\partial f^0}{\partial E}\right) \left[ e\varepsilon - \nabla\mu + \frac{E - \mu}{T} (-\nabla T) \right] d\mathbf{k} \\ &= \frac{e^2}{4\pi^3} \int \mathbf{v}(\mathbf{k}) \mathbf{v}(\mathbf{k}) \tau(\mathbf{k}) \left(-\frac{\partial f^0}{\partial E}\right) \left[ \varepsilon - \frac{1}{e} \nabla\mu \right] d\mathbf{k} \\ &\quad + \frac{e}{4\pi^3 \hbar} \int \mathbf{v}(\mathbf{k}) \mathbf{v}(\mathbf{k}) \tau(\mathbf{k}) \left[ \frac{E - \mu}{T} \right] (\nabla T) d\mathbf{k} \end{aligned} \quad (3.10)$$

$$\begin{aligned} \mathbf{J}_Q &= \frac{2}{8\pi^3} \int \mathbf{v}(\mathbf{k}) \mathbf{v}(\mathbf{k}) \tau(\mathbf{k}) \left(-\frac{\partial f^0}{\partial E}\right) \left[ e\varepsilon - \nabla\mu + \frac{E - \mu}{T} (-\nabla T) \right] (E - \mu) d\mathbf{k} \\ &= \frac{e}{4\pi^3} \int \mathbf{v}(\mathbf{k}) \mathbf{v}(\mathbf{k}) \tau(\mathbf{k}) \left[ \varepsilon - \frac{1}{e} \nabla\mu \right] (E - \mu) \left(-\frac{\partial f^0}{\partial E}\right) d\mathbf{k} \\ &\quad + \frac{1}{4\pi^3} \int \mathbf{v}(\mathbf{k}) \mathbf{v}(\mathbf{k}) \tau(\mathbf{k}) \frac{E - \mu}{T} (-\nabla T) \left(-\frac{\partial f^0}{\partial E}\right) d\mathbf{k} \end{aligned} \quad (3.11)$$

By defining now the integral

$$K_n = \frac{1}{4\pi^3 \hbar} \int \mathbf{v}(\mathbf{k}) \mathbf{v}(\mathbf{k}) \tau(\mathbf{k}) (E - \mu)^n \left(-\frac{\partial f^0}{\partial E}\right) d\mathbf{k} \quad (3.12)$$

Eqs.(3.10) and (3.11) can be expressed in terms of  $K_n$ ,

$$\mathbf{J}_e = e^2 K_0 \varepsilon + \frac{e K_1}{T} (-\nabla T), \quad (3.13)$$

$$\mathbf{J}_Q = e K_1 \varepsilon + \frac{K_2}{T} (-\nabla T). \quad (3.14)$$

When there is no temperature gradient, i.e.,  $\nabla T = 0$  in Eq.(3.13), one obtains

$$\mathbf{J}_e = \sigma \varepsilon \quad (3.15)$$

where  $\sigma$  is the electrical conductivity, which is of the form

$$\sigma = e^2 K_0 \quad (3.16)$$

When the electric field is absent and only a temperature gradient exists, one might be tempted to think that the thermal conductivity is obtained simply by taking it as a coefficient of the thermal gradient in Eq.(3.14), i.e., under the conditions that an external electric field is zero. It is a straightforward matter to ensure that no electric current passes through the sample. In this case the relation  $\mathbf{j}_e = 0$  in Eq.(3.13) is valid. Substituting Eq.(3.13) into Eq.(3.14) for eliminating the electric field yields

$$\mathbf{J}_Q = \kappa(-\nabla T) \quad (3.17)$$

where  $\kappa$  is the electronic thermal conductivity

$$\kappa = \frac{1}{T} \left[ K_2 - \frac{K_1^2}{K_0} \right]. \quad (3.18)$$

If it is assumed that there is a temperature gradient across a sample which is in an open-circuit condition, then there is no electric current but an electric field

$$\varepsilon = \frac{K_1}{eTK_0} \nabla T \quad (3.19)$$

is produced. From the definition of the Seebeck coefficient, one obtains then

$$S = \frac{K_1}{eTK_0} \quad (3.20)$$

## 3.3 Implementation Techniques

### 3.3.1 Band Interpolation

Integration of Eqs.(3.16), (3.18) and (3.20) involves a delta-like function, namely the energy derivative of the Fermi function, which requires eigenvalues on a dense  $\mathbf{k}$ -mesh for an accurate evaluation. For example, Yao et al used  $2 \times 10^6$   $\mathbf{k}$ -points in order to get a converged value of the intrinsic anomalous Hall conductivity[66]. Direct calculations via the a first-principles method are too cumbersome for such an enormous  $\mathbf{k}$ -point mesh. Thus, an efficient and accurate interpolation method is therefore required for this type of calculations.

Shankland introduced a Fourier-based interpolation method involve least squares fitting[67]. In this method a periodic function known at discrete set of points is represented by a

Fourier series which passes exactly through the given points and yet remains smooth. Suppose one has a set of  $N$  data points to be fitted with a Fourier series

$$f(\mathbf{k}) = \sum_{i=1}^N a_i e^{i\mathbf{k}\mathbf{R}_i} \quad (3.21)$$

where  $\mathbf{R}_i$  denotes a real-space lattice translation. The interpolation requires that the resulting function passes exactly the  $N$  points. If the expansion is truncated at  $M > N$ , then interpolation is underdetermined. A good interpolation requires a smooth interpolation and avoiding oscillations in between the  $N$  data points. To fit the requirements, Shankland introduced an auxiliary roughness function, which is the integrated square of the deviation of the expanded function from its mean value, plus the integrated square of the derivative of the function, the second derivative, and so on,

$$\begin{aligned} \mathfrak{R} &= \frac{1}{2} \int_0^{2\pi} [C_0 f^2(k) + C_1 f'^2(k) + \dots] dx \\ &= \sum_{m=1}^M |a_m|^2 (C_0 + C_1 |\mathbf{R}_m|^2 + C_2 |\mathbf{R}_m|^4 + \dots) \end{aligned} \quad (3.22)$$

Since energy bands have the symmetry of the crystal, a natural choice of the expansion are symmetrized plane waves or star functions,

$$S_m(\mathbf{k}) = \frac{1}{n_r} \sum_{\alpha=1}^{n_r} e^{i\alpha \mathbf{R}_m \cdot \mathbf{k}} \quad (3.23)$$

where the sum runs over all operations of the point group of the crystal. The interpolation function is written as

$$\tilde{\varepsilon}(\mathbf{k}) = \sum_{m=1}^M \varepsilon_m S_m(\mathbf{k}) \quad (3.24)$$

with the idea to use more expansion coefficients  $\varepsilon_m$ , namely  $M$ , than the given number of data points  $N$ , i.e.  $M > N$ . Substituting Eq.(3.23) into Eq.(3.43) and then substituting the latter in Eq.(3.22), the roughness function  $\mathfrak{R}$  can be expressed as

$$\mathfrak{R} = \sum_{m=1}^M |\varepsilon_m|^2 \varphi(\mathbf{R}_m) \quad (3.25)$$

in which  $\varphi$  is given by

$$\varphi(\mathbf{R}_m) = C_0 + C_1 |\mathbf{R}_m|^2 + C_2 |\mathbf{R}_m|^4 + \dots \quad (3.26)$$

There, the coefficients  $C_m$  have to be chosen suitably. The problem of the interpolation

consists now in minimizing the roughness function, subject to the constraint that the interpolating function passes through the given  $N$  data points. In other words,

$$\tilde{\varepsilon}(\mathbf{k}_i) = E(\mathbf{k}_i) \quad (i = 1, 2, \dots, N), \quad (3.27)$$

where  $E(\mathbf{k}_i)$  represent the  $N$  data points.

Introducing the Lagrange multipliers

$$\wp^* = \wp(\mathbf{R}_m) + \sum_{i=1}^N \lambda_i (E(\mathbf{k}_i) - \tilde{\varepsilon}(\mathbf{k}_i)), \quad (3.28)$$

minimizing  $\wp^*$  with respect to the coefficient  $\varepsilon_i^*$  and the  $\lambda_i$ , one obtains

$$\frac{\delta \wp^*}{\delta \varepsilon_i^*} = \varepsilon_i \wp(\mathbf{R}_m) - \sum_{i=1}^N \lambda_i S_m^*(\mathbf{k}_i) = 0 \quad (3.29)$$

for which  $\tilde{\varepsilon}(\mathbf{k}_i) = \tilde{\varepsilon}^*(\mathbf{k}_i)$  has been used.

$$\frac{\delta \wp^*}{\delta \lambda_i} = E(\mathbf{k}_i) - \sum_{m=1}^M \varepsilon_m S_m(\mathbf{k}_i) \quad (3.30)$$

Substituting Eq.(3.29) into Eq.(3.30) one gets

$$E(\mathbf{k}_j) = \sum_{i=1}^N H_{ij} \lambda_i \quad (3.31)$$

with

$$H_{ij} = \sum_{m=1}^M S_m^*(\mathbf{k}_i) S_m(\mathbf{k}_j) / \wp(\mathbf{R}_m) \quad (3.32)$$

One realizes that once the formulation of the roughness is given, the  $\lambda_i$ 's can be calculated from the linear equations Eq.(3.31). With the knowledge of  $\lambda_i$ , the expansion coefficients  $\varepsilon_m$  are derived from Eq.(3.29) and then the interpolation can be proceeded via Eq.(3.43).

The problem left to be solved is how to choose a proper set of  $C_m$  in Eq.(3.26). It seems there are many uncertainties of the choice of  $C_m$ . However one should bear in mind that the fit should be insensitive to the choice. Actually the situation becomes clear, if one realizes that the interpolation is constrained to pass through all the given  $N$  data points. In other words, different sets  $\wp(\mathbf{R}_m)$  may result in different avlues of  $H$ , but no matter what they are, the resulting  $\lambda_i$  must guarantee Eqs.(3.29) and (3.31). Therefore, the quality of the fit is insensitive to the choice of  $C_m$ . Indeed, tests of Koelling and Wood support this argument as long as all the coefficients  $C_m$  are nonzero[68].

Pickett noticed that the expression in Eq.(3.25) has the undesired effect of minimizing deviations of  $\tilde{\varepsilon}(\mathbf{k})$  from zero and emphasize that the more physical restriction is to minimize the deviations of  $\tilde{\varepsilon}(\mathbf{k})$  from its mean value[69]. As suggested by Pickett, a more reasonable way is to omit the  $m = 1$  term

$$\mathfrak{R} = \sum_{m=2}^M |\varepsilon_m|^2 \wp(\mathbf{R}_m). \quad (3.33)$$

Applying the minimizing procedure that as described above, one gets

$$\varepsilon_i^* \wp(\mathbf{R}_m) = \sum_{i=1}^N \lambda_i S_m(\mathbf{k}_i) \quad (m > 1) \quad (3.34)$$

In addition, the quantities  $\lambda_i$  are subject to the condition

$$\sum_{i=1}^N \lambda_i = 0. \quad (3.35)$$

Substituting Eq.(3.35) into Eq.(3.34), one obtains

$$\varepsilon_i^* \wp(\mathbf{R}_m) = \sum_{i=1}^{N-1} \lambda_i [S_m(\mathbf{k}_i) - S_m(\mathbf{k}_N)] \quad (3.36)$$

Multiplying the complex conjugate of Eq.(3.36) by  $[S_m(\mathbf{k}_j) - S_m(\mathbf{k}_N)]/\wp(\mathbf{R}_m)$  and then summing  $m$  from 2 to  $M$ , one arrives at

$$E(\mathbf{k}_j) - E(\mathbf{k}_N) = \sum_{i=1}^{N-1} H_{ij} \lambda_i^*, \quad (3.37)$$

where

$$H_{ij} = \sum_{m=2}^M \frac{[S_m^*(\mathbf{k}_i) - S_m^*(\mathbf{k}_N)][S_m(\mathbf{k}_j) - S_m(\mathbf{k}_N)]}{\wp(\mathbf{R}_m)} \quad (3.38)$$

Solving Eq.(3.37) for  $\lambda_i$  and substituting them into the complex conjugate of Eq.(3.36), ends up with the expansion coefficients

$$\varepsilon_m = \sum_{i=1}^{N-1} \frac{\lambda_i^* [S_m^*(\mathbf{k}_i) - S_m^*(\mathbf{k}_N)]}{\wp(\mathbf{R}_m)} \quad (m > 1) \quad (3.39)$$

The coefficients  $\varepsilon_1$  can be obtained from Eq.(3.27),

$$\varepsilon_1 = E(\mathbf{k}_N) - \sum_{m=2}^M \varepsilon_m S_m(\mathbf{k}_N) \quad (3.40)$$

Also, Pickett proposed a form for  $\wp(\mathbf{R}_m)$ ,

$$\wp(\mathbf{R}_m) = (1 - C_1(R'_m)^2)^2 + C_2(R'_m)^6 \quad (3.41)$$

where  $R'_m = R_m/R_{min}$  and  $R_{min}$  is the smallest nonzero lattice vector. As regards to the initial coefficients,  $C_1$  and  $C_2$ , they were fixed to be 0.75.

Although already having electron eigenvalues  $E_n(\mathbf{k})$  on a dense  $m\mathbf{k}$  mesh by employing the interpolating scheme to  $E_n(\mathbf{k})$  over a relative coarse  $k$ -mesh from ab initio methods, one is still far from practical computations of transport coefficients given by Eqs.(3.16), (3.18) and (3.20). One has to calculate the integrals  $K_n$  as given by Eq.(3.12), which are present in all the transport coefficients. The calculation of  $K_n$  involves computations of the electron velocity  $\mathbf{v}(\mathbf{k})$  and relaxation time  $\tau(\mathbf{k})$ . In the rest of this section, techniques of computing  $K_n$  and related transport coefficients are presented. Moreover, the rigid band approximation and symmetry properties of transport tensors are discussed, which are used in the thesis to simulate experiments.

### 3.3.2 Electron Velocities

The velocity of electronic bands is given as

$$\mathbf{v}_n(\mathbf{k}) = \frac{1}{\hbar} \frac{\partial E_n(\mathbf{k})}{\partial \mathbf{k}} \quad (3.42)$$

with the quantum numbers  $n$ , the band index, and the  $\mathbf{k}$  vector. It should be noted, that Eq.(3.42) is exactly the same as Eq.(3.5). In principle, one can use a finite difference method to calculate the derivative, but such methods are cumbersome. Rather than following this brute force concept, a Fourier transformation algorithm is used for the present purpose, because it can be made stable and fast. Remembering that  $E_n(\mathbf{k})$  is given by Eq.(3.43) the derivative can be easily calculated, rewriting it

$$\tilde{\varepsilon}_n(\mathbf{k}) = \sum_{m=1}^M \frac{1}{n_r} \sum_{\alpha}^{n_r} \varepsilon_m^n e^{i\alpha \mathbf{R}_m \cdot \mathbf{k}}. \quad (3.43)$$

The derivative of  $\tilde{\varepsilon}_n(\mathbf{k})$  with respect to  $\mathbf{k}$  is

$$\frac{\partial \tilde{\varepsilon}_n(\mathbf{k})}{\partial \mathbf{k}} = \sum_{m=1}^M \frac{1}{n_r} \sum_{\alpha}^{n_r} \varepsilon_m^n(i\alpha \mathbf{R}_m) e^{i\alpha \mathbf{R}_m \cdot \mathbf{k}}. \quad (3.44)$$

Calculation of Eq.(3.44) can be easily accomplished by employing well-established Fast-Fourier-Transform (FFT) techniques, such as used in the subroutine C3FFT from Math Kernel Library of Intel.

### 3.3.3 Constant Relaxation Time Approximation

With the velocities at hand, one can now proceed by evaluating the integrals  $K_n$ , but the relaxation times  $\tau(\mathbf{k})$  are not directly accessible. As stated in Sec.3.1, the relaxation times of electrons  $\tau$  describe various scattering effects in Boltzmanns' theory. There are numerous scatterings events for the electrons including electron-electron, electron-phonon, electron-magnon, boundary scatterings and so on. These scattering effects are complicated to formulate and may interplay with each other. In Matthiessen's rule, the scattering effects are independent of each other and then an effective relaxation time  $\tau(M)$  is given by

$$\frac{1}{\tau_M} = \sum_i \frac{1}{\tau_i} \quad (3.45)$$

where the sum runs over all independent scattering events for a given state with energy  $E_n(\mathbf{k})$ . Although the rule simplifies our problem, relaxation times remain difficult to calculate for technical reasons. For instance, up to now the electron-phonon coupling can in principle be computed on a DFT level by using linear response theory. However, the calculations are extremely demanding time-consuming. Thus a first-principles calculation of  $\tau_{el-ph}$  is not feasible at the moment for systems with a larger numbers of atoms per unit cell. Instead of the full calculation of  $\tau$ , it is treated here as a an empirical constant. Then, the electrical conductivity and Seebeck coefficient are given as

$$\frac{\sigma}{\tau} = \frac{e^2}{4\pi^3 \hbar} \int \mathbf{v}(\mathbf{k}) \mathbf{v}(\mathbf{k}) \left(-\frac{\partial f^0}{\partial E}\right) d\mathbf{k}, \quad (3.46)$$

$$S = \frac{\int \mathbf{v}(\mathbf{k}) \mathbf{v}(\mathbf{k}) (E - \mu) \left(-\frac{\partial f^0}{\partial E}\right) d\mathbf{k}}{eT \int \mathbf{v}(\mathbf{k}) \mathbf{v}(\mathbf{k}) \left(-\frac{\partial f^0}{\partial E}\right) d\mathbf{k}}. \quad (3.47)$$

In fact, relaxation time  $\tau$  appears in both the numerator and denominator of Eq.(3.20) and it cancels. Thus the Seebeck coefficient is much less sensitive to scattering events included in  $\tau$  than the conductivity. In practical calculations of  $\sigma$ , one firstly calculates  $\frac{\sigma}{\tau}$  by Eq.(3.46) and then treat  $\tau$  as an empirical parameter by fitting  $\sigma$  to experiments.

This was done also in this work by deriving  $\tau$  by fitting to *one* value of the experimental conductivity. This worked surprisingly well, as will be shown later on.

### 3.3.4 Symmetry Properties

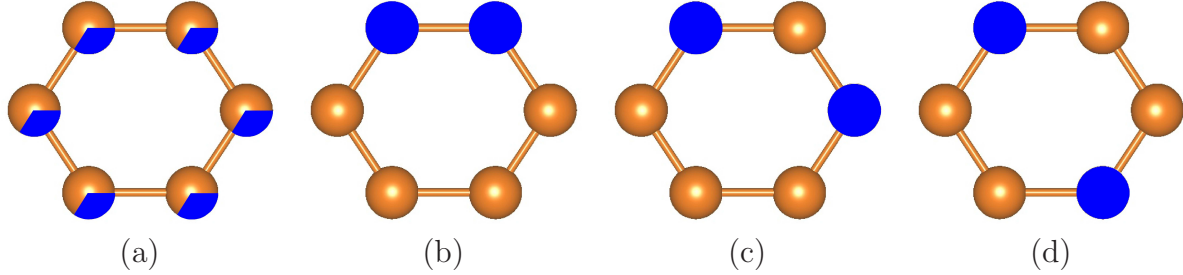


FIGURE 3.1: Illustration of doping two atoms (in blue) onto six equivalent sites. (a) Because of the sample preparation at higher temperatures, experimentally the dopants are more or less statistically distributed. (b) - (d) Three possible configurations for modeling with a unit cell in which each site is either completely substituted by a dopant or not.

Difference in crystal symmetry between theoretical modeling and experimental samples may occur when one has to deal with doping. Experimentally, the crystal symmetry of the undoped compound may be maintained upon doping because the dopants are -more or less- statistically distributed on the sites. While the dopants are at specific crystallographic site according to the ordered arrangements of atoms needed for the DFT modeling, the symmetry inherent to the undoped case may be broken upon doping. Fig.3.1 illustrates the differences in understanding doping between the experimental situation and theoretical modeling.

Conductivity  $\sigma$  and Seebeck coefficient  $S$  are second-rank tensors with  $\sigma$  being symmetric according to  $\sigma_{ij} = \sigma_{ji}$ . However,  $S$  is not necessarily symmetric when the symmetry of the solid does not enforce this property. A high crystal symmetry reduces the number of independent tensor elements. In particular,  $\sigma$  and  $S$  become isotropic in solids with cubic symmetries, which means that the only non-zero elements are in the diagonal, and these elements have the same value. Using a different symmetry in the theoretical modeling as compared to the experimental sample leads to differences in the transport coefficients. To mimic the experimental situation of maintaining the high symmetry of the undoped case, this full symmetry can be enforced to the Seebeck and conductivity tensors by symmetrization,

$$\bar{T} = \sum_{\alpha} \Lambda_{\alpha}^{-1} \bar{T} \Lambda_{\alpha} \quad (3.48)$$

where  $\Lambda_{\alpha}$  represent point group operations of the crystal, and  $\bar{T}$  denotes a transport tensor.

### 3.3.5 Rigid Band Approximation

Many of theoretical efforts are try to explain experimental results. Difficulties include various temperature and doping effects inherent in the experimental, which arise due to complex circumstances forced by nature. Therefore, reasonable modelings have to be made. As a prototypical problem, experimental fractional compositions cannot be directly simulated because this would require enormously large super cells.

A simple way out of this problem is the rigid band approximation. In the present case it was employed to model experimental compositions by taking a reference composition, for which full first-principles calculations can be made. The composition of this reference system should be chosen as close as possible to the experimental conditions. Suppose  $\Delta n$  is the changed number of valence electrons with respect to the reference compound with  $N_0$  valence electrons, the chemical potential of the doped system is calculated from

$$N_e = \int_{-\infty}^{\infty} N(E)f(T; \mu)dE \quad (3.49)$$

where  $\mu$  is the chemical potential (i.e. temperature dependent Fermi energy) for the doped system with  $N_e = N_0 + \Delta n$  electrons. By that ansatz it is assumed, that the small change in valence electron numbers does not alter the electronic structure (i.e. the density of states) at all, the bands are kept rigid.

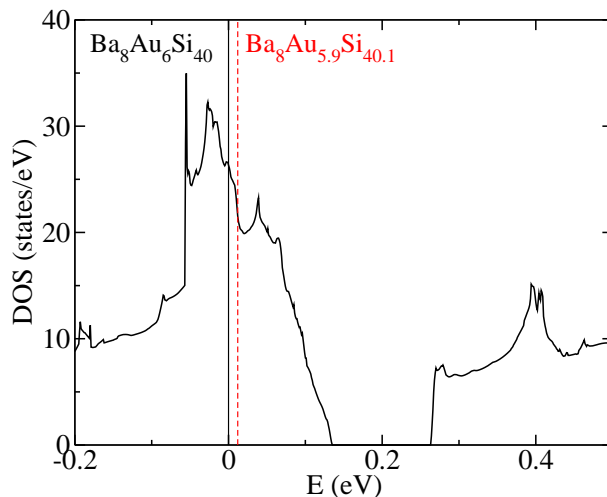


FIGURE 3.2: Calculated Fermi levels of  $\text{Ba}_8\text{Au}_6\text{Si}_{40}$  (black solid line) and  $\text{Ba}_8\text{Au}_{5.9}\text{Si}_{40.1}$  (red dashed line) at 0 K. The Fermi level of  $\text{Ba}_8\text{Au}_{5.9}\text{Si}_{40.1}$  was derived by Eq. 3.49 taking  $\text{Ba}_8\text{Au}_6\text{Si}_{40}$  as the reference.

As an example, the clathrates  $\text{Ba}_8\text{Au}_x\text{Si}_{46-x}$  are taken. Then,  $\text{Ba}_8\text{Au}_6\text{Si}_{40}$  is chosen as the reference compound to simulate the experimental compound Bath a small doping  $\text{Ba}_8\text{Au}_{5.9}\text{Si}_{40.1}$ . The change in valence electron numbers  $\Delta n$  is now counted assuming that

Au and Si contribute 1 and 4 valence electrons to the system, respectively. The Fermi level of  $\text{Ba}_8\text{Au}_{5.9}\text{Si}_{40.1}$  is shown in Fig.3.2.

### 3.3.6 Calculation of the transport properties by program V2Boltz

The above techniques were implemented in the program V2Boltz <sup>2</sup>, which has following features.

- Originally BoltzTraP has only an interface to WIEN2K. Based on the consideration of popularity of VASP, program V2Boltz is made available for using VASP output and symmetry.
- V2Boltz is able to calculate temperature-dependent transport coefficients for any electron doping within the rigid band approximation. This was done by implementing Eq.3.49, with which one derives the chemical potential for a given doping at any temperature.
- V2Boltz is able to symmetrize transport tensors by implementation of Eq.3.48.
- As a byproduct of solving Eq.3.42 the Fermi velocity is accessible by V2Boltz:

$$\mathbf{v}_n(E_F) = \sum_{\mathbf{k}} v_n(k) \delta(\tilde{\epsilon}_n(\mathbf{k}) - E_F) \quad (3.50)$$

The Fermi velocities are important for spin polarization transport, for which the spin polarization  $P$  is defined by[71]

$$P = \frac{N_{\uparrow}(E_F)v_{\uparrow}(E_F) - N_{\downarrow}(E_F)v_{\downarrow}(E_F)}{N_{\uparrow}(E_F)v_{\uparrow}(E_F) + N_{\downarrow}(E_F)v_{\downarrow}(E_F)} \quad (3.51)$$

where  $N_{\sigma}(E_F)$  and  $v_{\sigma}(E_F)$  ( $\sigma = \uparrow, \downarrow$ ) represent the majority and minority spin DOS and Fermi velocities, respectively. The application was recently demonstrated in investigation of half-metallic ferromagnetic systems by the author and his co-workers[72].

- V2Boltz is able also to calculates Lorenz numbers for evaluating thermal conductivity of phonons (see Sec. 5.7).
- V2Boltz was modified for a convenient usage. It uses namelist to read in the desired information and restarts calculations using existing DOS and velocity files.

A manual of V2Boltz is added in Appendix.A. A schematic flow chart of calculating

---

<sup>2</sup>V2Boltz, written by Mingxing Chen, is a substantial developments and extensions of BoltzTrap developed by G. K. H. Madsen and D. J. Singh[70]

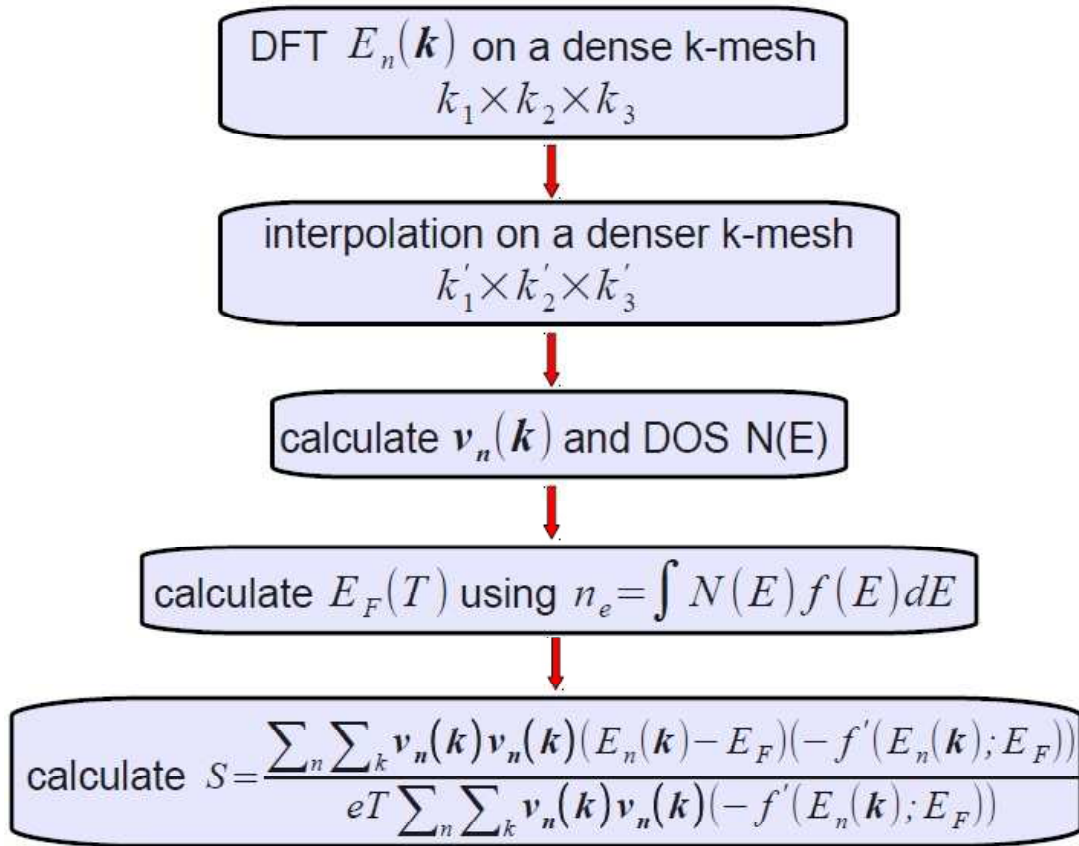


FIGURE 3.3: Flow-chart depicting a generic calculation of components of the Seebeck tensor.

Seebeck coefficients is depicted in Fig.3.3.

## 3.4 Benchmark Calculations

### 3.4.1 $\mathbf{k}$ -convergence

There are numerical issues, which needs to be addressed and checked out: how dense should the interpolated  $\mathbf{k}$ -mesh be to produce a convergent Seebeck coefficients: and how dense should the  $\mathbf{k}$ -mesh of the DFT input be for the interpolation?

The  $\mathbf{k}$ -mesh convergence was first tested for Seebeck coefficient of  $\text{Ba}_8\text{Au}_6\text{Si}_{40}$ . Interpolations were performed on various Monkhorst-Pack grids using VASP eigenvalues on meshes of  $5 \times 5 \times 5$  (black line) and  $25 \times 25 \times 25$  (red line), respectively (see Fig.3.4). It is shown that if one starts with a rather coarse grid, say  $5 \times 5 \times 5$ , a grid at least as

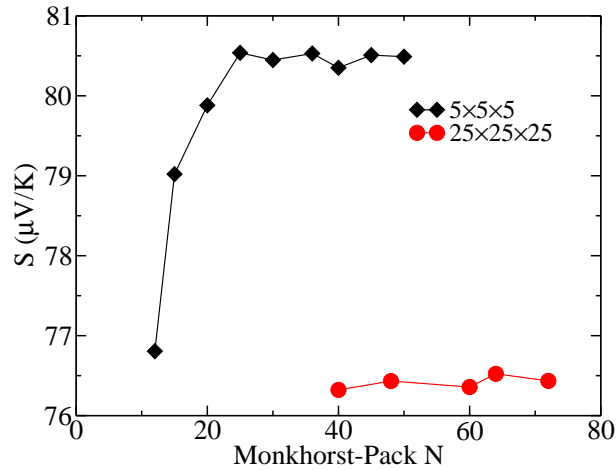


FIGURE 3.4:  $\mathbf{k}$ -mesh convergence of calculations of the Seebeck coefficient of  $\text{Ba}_8\text{Au}_6\text{Si}_{40}$  at  $T = 600$  K for two different input  $\mathbf{k}$ -meshes:  $5 \times 5 \times 5$  (black line) and  $25 \times 25 \times 25$  (red line). Interpolations were done over several Monkhorst-Pack grids using VASP eigenvalues. Seebeck coefficients were calculated using the interpolated eigenvalues.

dense as  $25 \times 25 \times 25$  for the interpolation is required to obtain converged values. Fig.3.4 also shows that differences occur between two converged calculations derived from VASP eigenvalues on different  $\mathbf{k}$ -meshes for interpolations. For instance, interpolations on a grid of  $40 \times 40 \times 40$  using both sets of VASP eigenvalues resulted in converged Seebeck coefficients, but there is a difference of  $4 \mu\text{V}/\text{K}$  in the resulting Seebeck coefficients at 300 K, which is an error of about 5%.

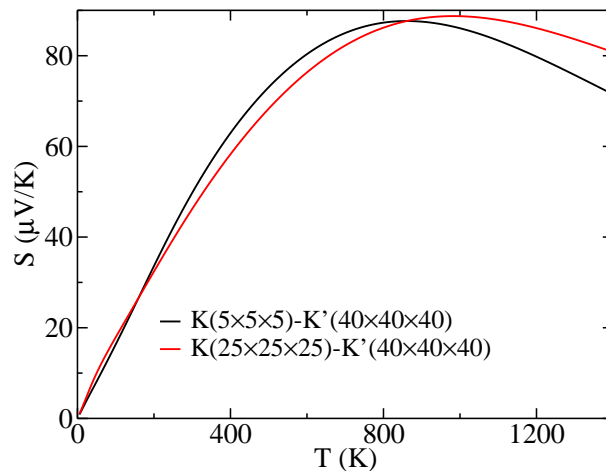


FIGURE 3.5: Calculated  $S(T)$  of  $\text{Ba}_8\text{Au}_6\text{Si}_{40}$  using interpolated eigenvalues on a  $\mathbf{k}$ -grid of  $40 \times 40 \times 40$  ( $K'$ ) with VASP eigenvalues on grids of  $5 \times 5 \times 5$  (black line) and  $25 \times 25 \times 25$  (red line), respectively.

Figure 3.5 shows  $S(T)$  of  $\text{Ba}_8\text{Au}_6\text{Si}_{40}$  derived from interpolated eigenvalues on a  $40 \times 40 \times 40$  grid with VASP eigenvalues on the two different grids, namely  $5 \times 5 \times 5$  (black line) and  $25 \times 25 \times 25$ . Although the trends are very similar, some differences are produced. The most noticeable difference is the position of the maximum appearing in the Seebeck coefficient. When using VASP eigenvalues on the grid of  $5 \times 5 \times 5$  for the interpolation, the maximum appears around 800 K. However, it occurs about 1000 K if the VASP eigenvalues for a grid of  $25 \times 25 \times 25$  is used.

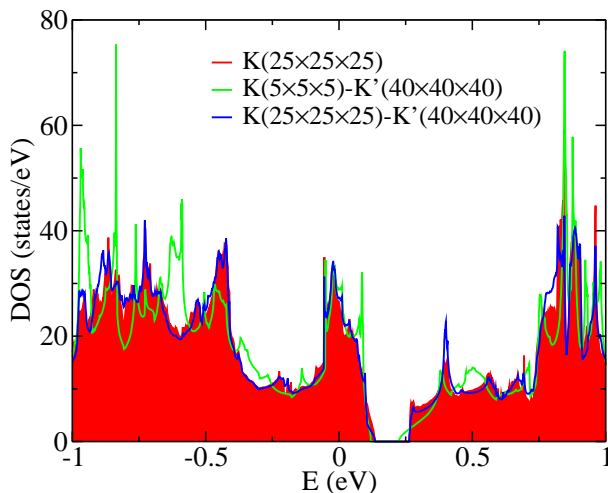


FIGURE 3.6: Comparisons in DOS of  $\text{Ba}_8\text{Au}_6\text{Si}_{40}$  between the one from eigenvalues on a  $25 \times 25 \times 25$  grid (red) directly derived by VASP and those from eigenvalues on a  $40 \times 40 \times 40$  grid ( $K'$ ) interpolated from VASP eigenvalues on a  $5 \times 5 \times 5$  grid (green line) and on a  $25 \times 25 \times 25$  (blue line) grid, respectively.

The differences originate from the interpolation procedure which strongly relies on the density of the input grids, on which VASP eigenvalues are generated. Fig.3.6 displays effects of input (i.e., VASP)  $\mathbf{k}$  grids on the density of states as calculated from the interpolated eigenvalues. The density of states derived from eigenvalues on a grid of  $25 \times 25 \times 25$  almost remains unchanged as compared that from interpolated eigenvalues on a grid of  $40 \times 40 \times 40$ . The resulting densities of states agree well between with each other between them. However, if the interpolation is performed starting with eigenvalues on a coarse grid of  $5 \times 5 \times 5$ , the discrepancy in the DOS is significant. The reason is that if the grid for the interpolation is too far from the one of the input eigenvalues, there are too many points between two input data points needed to fit. The growing of the number of the fitting points leads to a growing of the deviation from their exact values. Therefore, input eigenvalues should be calculated on a mesh as dense as possible for a high accuracy. It should be noted that the accuracy behavior can be different for different systems, depending on the specific properties of the electronic bands.

### 3.4.2 Effects of exchange-correlation approximations

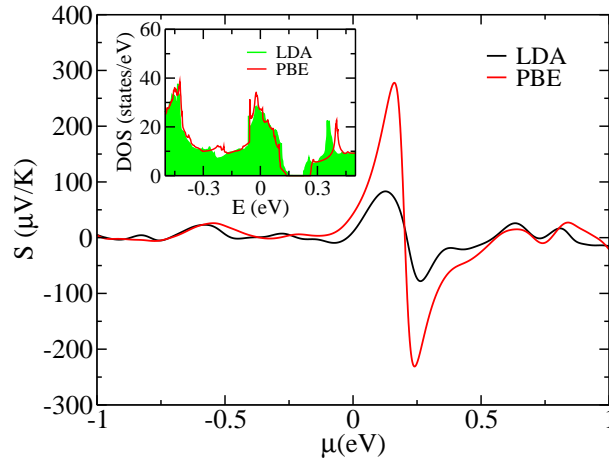


FIGURE 3.7:  $S(\mu)$  of  $\text{Ba}_8\text{Au}_6\text{Si}_{40}$  at 300 K derived from LDA (black line) and GGA (red line) eigenvalues. Interpolations were performed over a  $40 \times 40 \times 40$  grid based on VASP eigenvalues on a grid of  $25 \times 25 \times 25$  points. The DOS from both LDA (green) and GGA (red line) calculations are shown in the inset. The LDA calculation produces a narrower gap than the GGA calculations.

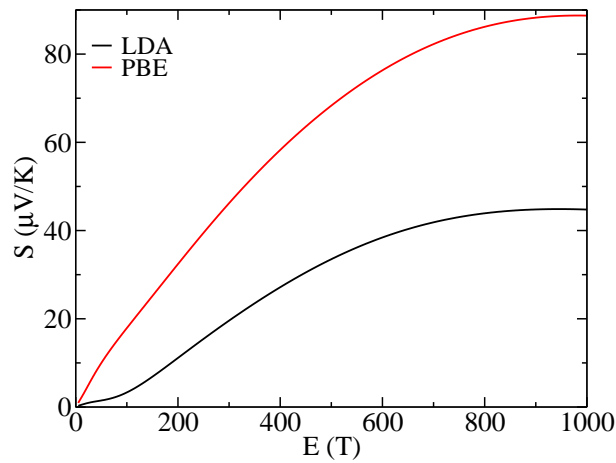


FIGURE 3.8:  $S(T)$  of  $\text{Ba}_8\text{Au}_6\text{Si}_{40}$  derived from LDA (black line) and GGA (red line) eigenvalues. Interpolations were done over a grid of  $40 \times 40 \times 40$  based on VASP eigenvalues on a grid of  $25 \times 25 \times 25$ .

It is well known that the bonding and consequently the ground state properties such as volume depend on the actual approximation to the exchange-correlation functional, such as the difference in gap size of the diamond structure of Si between LDA and GGA. Since Seebeck coefficients are derived from energy eigenvalues, different choices of the electron exchange-correlation function certainly lead to differences in the Seebeck coefficients for the same systems at their respective equilibrium volumes. Figs.3.7 and 3.8 depict  $S(\mu)$  and

$S(T)$  at 300 K of  $\text{Ba}_8\text{Au}_6\text{Si}_{40}$  as derived from LDA and GGA eigenvalues at their respective equilibrium volumes. The Differences between the two approximations are clearly visible. LDA produces a smaller gap and a much smaller magnitude of the Seebeck coefficient especially when  $\mu$  is close to the gap. The  $S(T)$  as derived from GGA calculations is over two times larger than that from LDA calculations at 1000 K.



# Chapter 4

## Ge-based Skutterudites

### 4.1 Overview

During the past two decades, filled pnictide skutterudites have experienced substantial attention due to their promising thermoelectric performance as controlled by their unique structures [6, 8–15, 73–78]. As first proposed by Slack [79] filling the voids in the skutterudite structure would reduce the lattice thermal conductivity significantly and thus meets the requirements for a high thermoelectric performance. Slack’s conjecture is that phonons of the framework are strongly scattered by the filler and thus produces a glass-like lattice thermal conductivity is produced while the electrical conductivity of a crystalline material is preserved: the concept of phonon-glass and electron crystal (PGEC)[1]. This paradigm has been challenged in recent investigations. Koza *et al* showed by neutron-scattering experiments on  $(\text{La,Ce})\text{Fe}_4\text{Sb}_{12}$  [21] that filler vibrations are coherently coupled with the host’s lattice dynamics. Moreover, Christensen *et al* argued that the effect of the rattler is to flatten the phonon bands rather than providing a strong phonon scattering mechanism [80].

The debate on the effect of the filling on the thermal conductivity is associated with the occurrence and properties of rattling modes. There were numerous attempts to understand rattling modes in skutterudites and clathrates. [81–86] Both theoretical calculations and experimental measurements of vibrational properties demonstrated that a well-defined localized peak in the low frequency regime of the phonon density of states (PHDOS), which is dominated by the vibrating filler atoms, appears when the material is doped by heavy elements are doped. This localization feature is accompanied by an anti-crossing or avoided anti-crossing behavior of optical and acoustic modes due to a weak bonding between the filler atoms and the framework [83, 84] However, such a localized peak is missing in some skutterudites. For instance, the localized peak was not detected for

CeOs<sub>4</sub>Sb<sub>12</sub> by inelastic neutron scattering experiments [87]. localized phonon peak is also missing for MFe<sub>4</sub>Sb<sub>12</sub> (M=Ca, Sr and Ba) [88]. The filler-framework interaction and the atomic mass of the filler certainly play a role for the properties of the rattling modes, but the effect is not yet fully understood. This particular point is one of the subjects which is studied from first principles in the present thesis.

Recently a new family of purely Ge-based skutterudites without any pnictogen element has been synthesized [89–95], which is unique in several respects: (i) different to their mostly investigated pnictogen-based relatives the caged-framework is entirely built by Ge atoms. (ii) the bonding in the cages is different from other Ge-caged compounds because Ge atoms are four-fold coordinated concerning its nearest neighbors; (iii) the transition temperatures of superconductivity are unexpectedly high but the Seebeck coefficients are unexpectedly low as compared to pnictogen-based skutterudites [91, 96, 97]. For the Seebeck effect is a result of the mobility of electrons, the significant difference in thermoelectric properties between pnictogen- and Ge-skutterudites originates from differences of the electronic structures.

Efforts have been devoted to combine the thermoelectric properties and electronic structures for the purpose of optimizing the thermoelectric performance. For instance, Mahan *et al* proposed that a delta-function shaped electronic density of states (DOS) at the Fermi level is required to maximize the ZT, [98], which was recently demonstrated experimentally in terms of band engineering [99]. However, the required singularity of the DOS around the Fermi level is not fulfilled in many cases. For instance, many thermoelectric materials miss the localized d (f) and pinning states but still exhibit promising thermoelectric properties [100–103]. These observations certainly motivate a search for a general rule for band engineering towards optimized thermoelectric properties.

In the chapter the lattice dynamics of the newly discovered family of skutterudites MPt<sub>4</sub>Ge<sub>12</sub> (M = Ba, La and Th) is investigated by using a direct method based for the first-principles calculations of the phonon spectrum and DOS, aiming at the understanding of the nature of filler or guest atom vibrational modes in caged materials. As for the TE properties, a strategy for optimizing the TE performance is developed, which may guide band engineering, which is based on the characteristics of electronic structures. A rule for doping of MPt<sub>4</sub>Ge<sub>12</sub> to improve thermoelectric properties is proposed. As a result of this investigation, Enhanced Seebeck coefficients are predicted for LaPt<sub>4</sub>(Ge<sub>7+δ</sub>Sb<sub>5-δ</sub>) and ThPt<sub>4</sub>(Ge<sub>8+δ</sub>Sb<sub>4-δ</sub>).

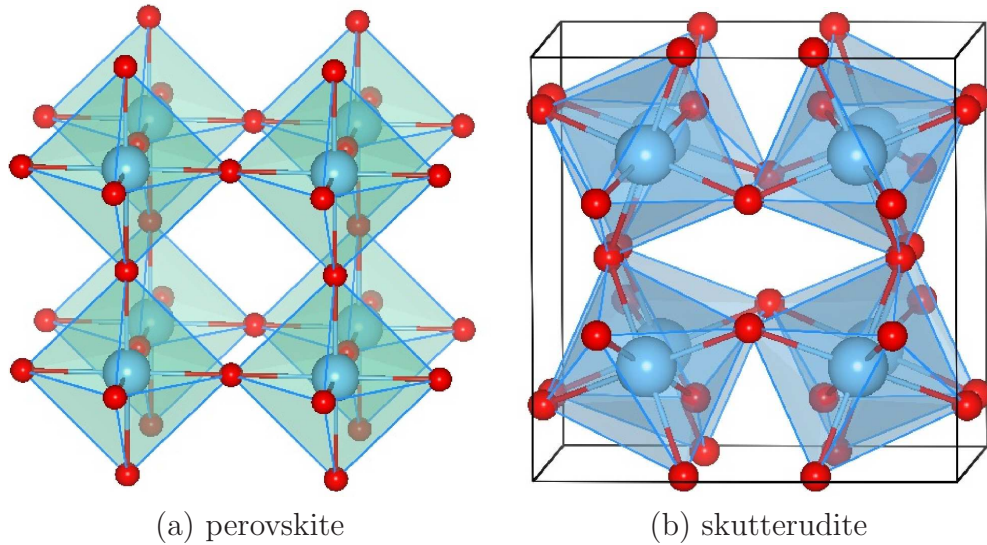


FIGURE 4.1: Crystal structures of (a) perovskite  $ABC_3$  with empty A site and (b) an unfilled skutterudite. Large cyan and small red balls denote transition metals and nonmetal ligands, respectively.

## 4.2 Structural Properties

The skutterudites of composition  $MP_3$  (M transition metal, P pnictogen element) received their name because of the place where they were found first, namely in Skutterud, Norway. Skutterudites crystallize in a body-centered cubic (bcc) structure with space group  $Im\bar{3}$  (No.204). The conventional unit cell contains eight  $MP_3$  units, with the M atoms occupying the 8c sites  $(\frac{1}{4}, \frac{1}{4}, \frac{1}{4})$  and the P atoms located on the 24g sites  $(0, y, z)$  as shown in Fig.4.1, where the exact values of y and z depend on the particular compound. M is octahedrally coordinated by P, forming a distorted  $MP_6$  octahedra. There is a great similarity between the skutterudites and the  $ReO_3$  structure as well as the perovskite structure  $\square MP_3$  ( $\square$  denotes an empty A site). In the ideal perovskite  $\square MP_3$  the eight octahedra are not tilted which results in eight voids. The skutterudite structure can be deduced from the perovskite structure by tilting the octahedra [104, 105]. During the tilting the octahedra keep connected and the volume of six of the eight voids are reduced and become the centers of rectangularly ordered pnictogen atoms. The remaining two voids are significantly enlarged, which can accommodate various fillers. A filled skutterudite has the chemical formula  $AM_4P_{12}$  with a primitive cell of a body-centered cubic type (Fig.4.2(a)). The main differences between both structures are that the  $MP_6$  octahedra are distorted in the skutterudite.

As noted by Smith *et al*[106], the skutterudite structure is related to the perovskite structure by the transformation

$$y' = \frac{1}{2} + s(y - \frac{1}{2}) \quad z' = \frac{1}{2} + s(z - \frac{1}{2}) \quad (4.1)$$

The perovskite structure ( $s = 0$ ) is transformed into the skutterudite structure when  $s = 1$ .

## 4.3 Lattice Dynamics of Ge-skutterudites

### 4.3.1 Born-von Kármán Model Calculations

The essential structural characteristics of skutterudites is that it contains cages formed by framework atoms which are filled by heavy guest atoms. To model the structural properties, a B2 structure is constructed, which is shown in Fig.4.2(b). To investigate the effect of the filler atom's mass and bonding to the framework on the vibrational properties, a simplified model is constructed as shown in Fig.4.2(b). For the filler the first nearest

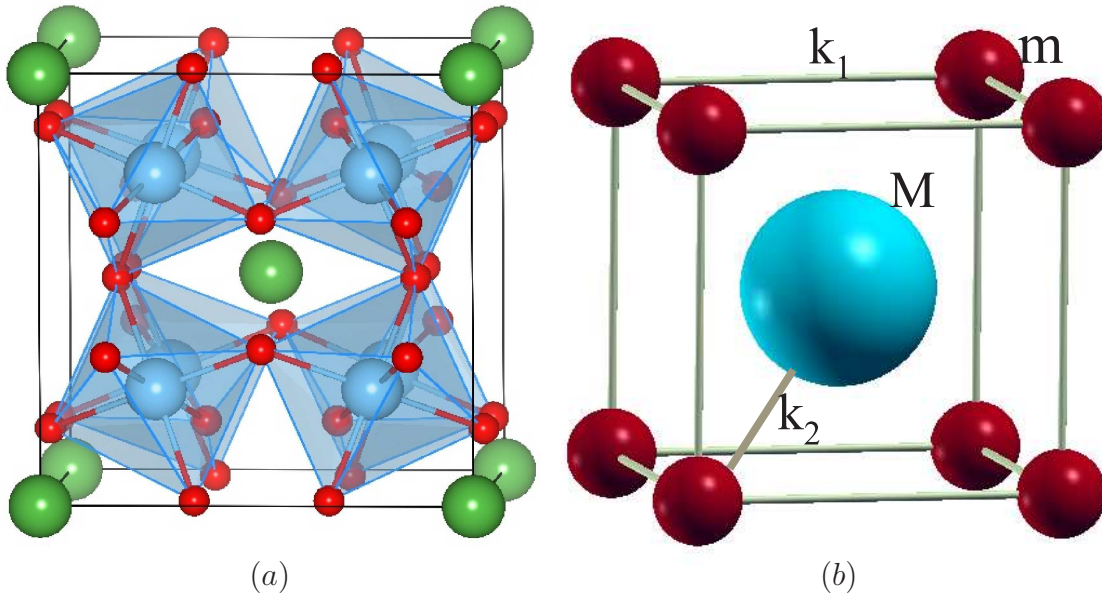


FIGURE 4.2: (a)Structure of the filled skutterudite, (b)sketch of a 3 dimensional spring model for body-centered cubic structure, corresponding to the unit cell of a B2 structure. The symbols  $m$  and  $M$  are the masses for the framework atoms and the filler, respectively'  $k_1$  represents spring constants between framework atoms, while  $k_2$  is the spring konstant between framework and filler.

neighbor approximation is imposed and for the framework atoms interactions up to the second nearest neighbors are taken into account. Relative spring constant and atomic

mass are introduced by defining  $k'=k_1/k_2$  and  $m'=m/M$ . In the present calculations  $m'$  is chosen for masses of framework atoms (red balls in Fig.4.2) and 1 is defined for the filler (green ball Fig.4.2). Spring constants between framework  $k_1$  are set to 1 and  $k_2$  is represented by  $k'$ .

Within the Born-von Kármán theory, a force constant matrix is assigned to each of the neighbors of a particular atom, whose properties are related to the direction cosines for the two neighboring atoms. In the B2 lattice the force constant matrix, i.e. the  $\alpha$  component of force acting on atom  $j$  in cell  $l$  induced by atom  $j'$  in cell  $l'$ , expressed for on atoms sitting at  $(0,0,0)$  and the neighbor sitting at  $a(0.5, 0.5, 0.5)$  is

$$\phi \begin{pmatrix} l'j'\beta \\ lj\alpha \end{pmatrix} = \begin{pmatrix} \zeta_1 & \eta_1 & \eta_1 \\ \eta_1 & \zeta_1 & \eta_1 \\ \eta_1 & \eta_1 & \zeta_1 \end{pmatrix} \quad (4.2)$$

For the neighbor atom at  $a(1, 0, 0)$  it is

$$\phi \begin{pmatrix} l'j'\beta \\ lj\alpha \end{pmatrix} = \begin{pmatrix} \zeta_2 & 0 & 0 \\ 0 & \eta_2 & 0 \\ 0 & 0 & \eta_2 \end{pmatrix} \quad (4.3)$$

In Madelung's method, the chemical bond between atoms is simulated by forces of a spring. For the central case, the force constant matrix elements can be related to the spring constant by

$$\phi \begin{pmatrix} l'j'\beta \\ lj\alpha \end{pmatrix} = -ke_\alpha e_\beta \quad (l'j' \neq lj) \quad (4.4)$$

where  $k$  is the spring constant and  $e_\alpha$  and  $e_\beta$  are direction cosines of the vector from  $i$  to  $i'$ . It turns out that for real systems with B2 structure, (e.g. NiAl)  $\eta_1$  is different from but very close to  $\zeta_1$  and  $\eta_2$  is relatively small but can not be neglected when compared to  $\zeta_2$ . In the present calculations,  $\eta_1$  is set to 95% of  $\zeta_1$  and  $\eta_2$  is set to 20%  $\zeta_2$ , which are close to those for NiAl as from ab initio calculations[107]. Relative spring constant and atomic mass are introduced by defining  $k'=k_1/k_2$  and  $m'=m/M$ . Here  $m'$  is set for masses of framework atoms (red balls in Fig.4.2) and 1 is for the mass of the filler (green ball Fig.4.2), and  $k_1$  is set to 1 and  $k_2$  equals  $k'$ . Phonon spectra derived from Born-von Kármán model calculations with respect to different  $m'$  and  $k'$  are shown in Fig.4.3. Two important features can be observed that are relevant for the appearance of rattling modes. One is the involvement of acoustic modes around the boundary of the Brillouin Zone (BZ). Acoustic modes tend to be flattened as  $q$  comes close to the boundary of BZ for small  $k'$ , for which one can see exactly flat bands along X-P and  $\Gamma$ -P directions with  $k' = 0.3$ . This means that peaks appear in the phonon DOS in the low frequency energy regime.

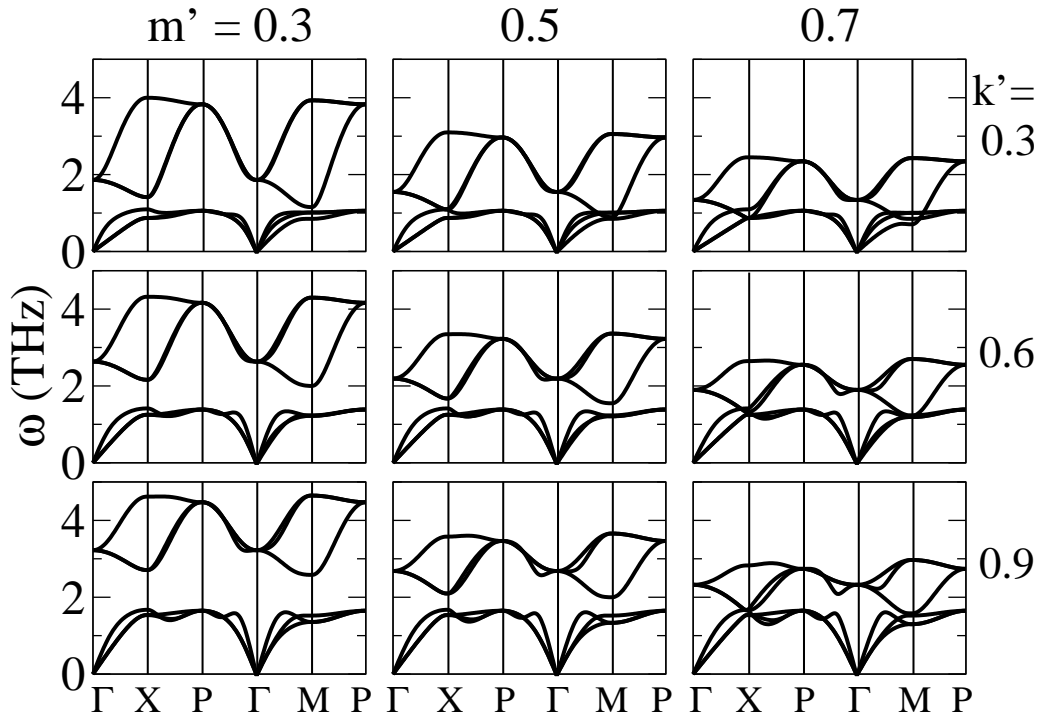


FIGURE 4.3: Phonon spectrum derived from the Born-von Kármán model with respect to relative masses  $m'$  and spring constants  $k'$ .

### 4.3.2 First-principles Lattice dynamics of $\text{MPt}_4\text{Ge}_{12}$

For phonon calculations with *ab initio* method, force constant matrix are constructed based on forces on atoms with respect to a small displacement of a particular atom. [65] Density functional theory (DFT) calculations for the  $\text{MPt}_4\text{Ge}_{12}$  ( $M = \text{Ba}, \text{La}$  and  $\text{Th}$ ) compounds were carried out by applying the Vienna Ab initio Simulation Package (VASP). [47, 48] The generalized gradient approximation is used for the exchange correlation functional using the parametrization of Perdew, Burke, and Ernzerhof, [52] and the pseudopotential is treated within the framework of Blchls projector augmented wave method. [49, 50] The valence states configuration for the construction of the pseudopotentials included  $5s^25p^66s^2$  for Ba,  $5s^25p^66s^25d^1$  for La,  $5s^25p^66s^25d^2$  for Th,  $6s^15d^9$  for Pt, and  $3d^{10}4s^24p^2$  for Ge. A  $5 \times 5 \times 5$  Monkhorst grid was used to sample the Brillouin zone for force calculations in skutterudites with a  $2 \times 2 \times 2$  supercell.

Table 4.1 lists lattice constants, distances, bonding energies between fillers and Ge on cage framework and formation energies for  $\text{MPt}_4\text{Ge}_{12}$ . A structural contraction can be seen from the decreasing lattice constants and bond length between the fillers and Ge atoms, which means there probably is a enhanced bonding as the filler from Ba to Th. The bonding energy between the filler and  $\text{Pt}_4\text{Ge}_{12}$  framework for  $\text{ThPt}_4\text{Ge}_{12}$  is in a moderate strength among all the compounds. From the point of view of energetics, a

system	$a$ (Å)	$R_{M,Ge}$ (Å)	$R_{Pt,Ge}$ (Å)	$R_{Ge,Ge}$ (Å)	$E_b(M)$ (eV)	$\Delta H$ (kJ/mol)
BaPt <sub>4</sub> Ge <sub>12</sub>	8.81	3.42	2.54	3.31	-3.63	-35.90
LaPt <sub>4</sub> Ge <sub>12</sub>	8.75	3.37	2.53	3.31	-4.41	-40.33
ThPt <sub>4</sub> Ge <sub>12</sub>	8.70	3.35	2.51	3.30	-3.97	-37.84

TABLE 4.1: Lattice constants ( $a$ ), bond lengths ( $R_{M,Ge}$ ), bonding energies ( $E_b(M)$ ) between the filler and Ge atoms on the cage framework, and formation energy per atom  $\Delta H$  for MPt<sub>4</sub>Ge<sub>12</sub> (M = Ba, La, and Th).  $R_{Ge,Ge}$  represent the distance between the first nearest neighbors on a PtGe<sub>6</sub> octahedron.  $E_b(M)$  is defined by  $E_b(M) = E(\text{MPt}_4\text{Ge}_{12}) - E(\text{Pt}_4\text{Ge}_{12}) - E_{\text{bulk}}(M)$ ,  $E$  being total energies of the corresponding systems.

weak bonding is characterized by a small bonding energy. It is shown here, however, that this point of view is invalidated for the studied compounds.

#### 4.3.2.1 Phonons of Pt<sub>4</sub>Ge<sub>12</sub>

As acoustic modes carry most of heat during phonon transport, modes in the low energy regime are of interest in thermal transport. To investigate effect of the filling on lattice dynamics of skutterudites, phonons of empty Pt<sub>4</sub>Ge<sub>12</sub> are first investigated. Figure 4.4.a shows phonon dispersion curves along high symmetry directions and atom-projected phonon density of states (PHDOS) for empty Pt<sub>4</sub>Ge<sub>12</sub> skutterudite. Modes in low energy regime are dominated by Ge atoms and no flat bands are observed that yield a localized peak in the low energy regime of PHDOS.

#### 4.3.2.2 Phonons of MPt<sub>4</sub>Ge<sub>12</sub>

Phonon dispersions and density of states for the three proposed compounds are shown in Fig.4.4(b)-(d), which demonstrate different effects on the lattice dynamics from different fillers. For BaPt<sub>4</sub>Ge<sub>12</sub>, no distinctive filler peak can be found at low frequencies. A rather broad peak of the total PHDOS as composed by all three local PHDOS arises above 2.2 THz. This implies significant hybridization between Ba and the unfilled framework. The situation changes drastically, when Ba is substituted by La: then the mentioned broad peak is split into two peaks: the upper peak remaining at 2.2 THz is dominated by Pt and Ge modes, while the lower one at 1.5 THz is dominated by La modes, which can be considered as localized modes. However, at 1.5 THz there still exists a substantial hybridization between the filler La and the framework. In the case of ThPt<sub>4</sub>Ge<sub>12</sub>, the

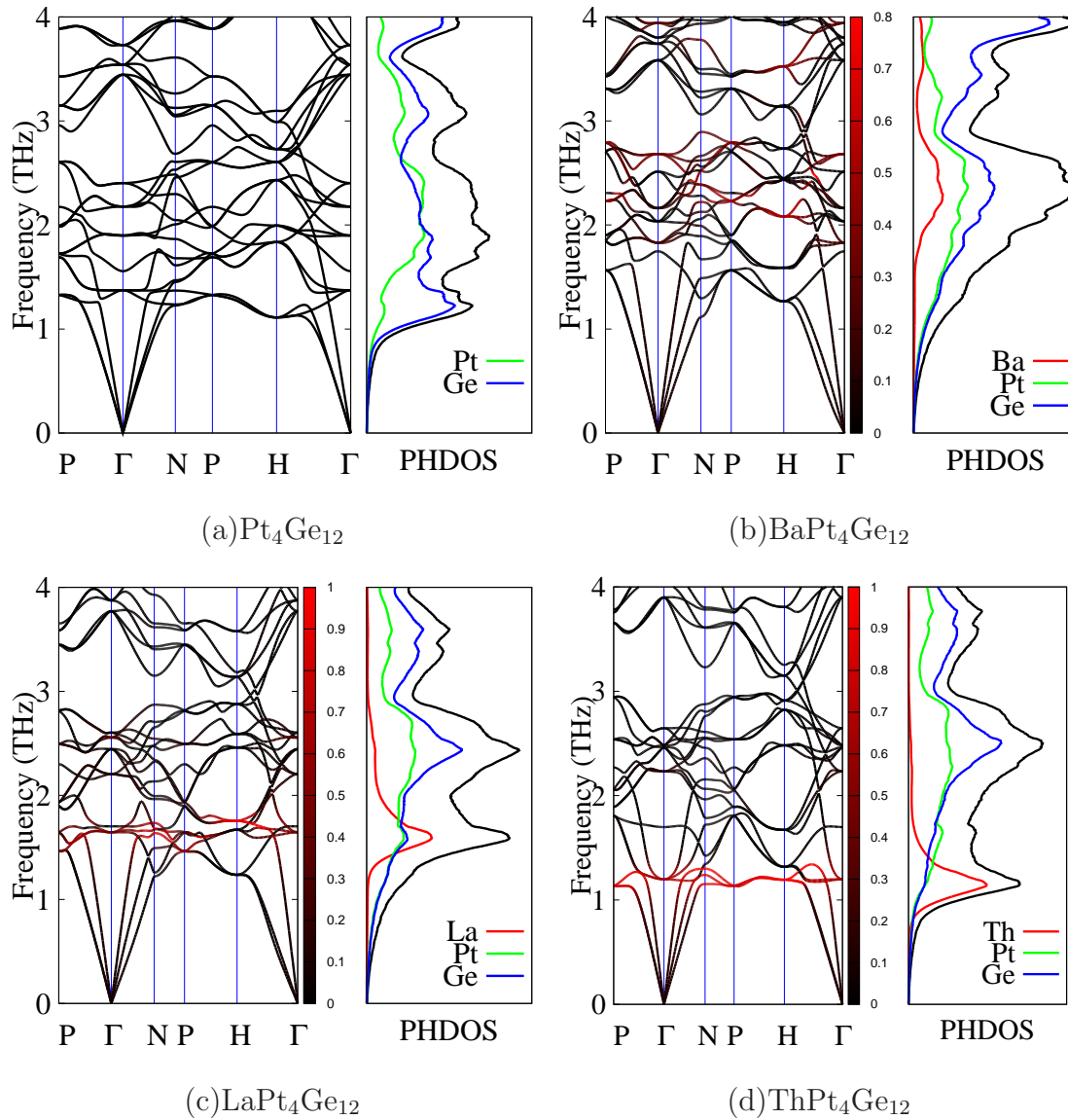


FIGURE 4.4: DFT derived Phonon spectrum and atom-projected PHDOS of  $\text{MPt}_4\text{Ge}_{12}$ . Phonon bands are colored to show contributions of the filler.

filler peak is lowered to 1 THz and the hybridization between the filler and framework is weakened and the localization feature is enhanced.

The differences in modes from different fillers can be seen more clearly by taking a closer view on the phonon dispersions, which are colored red for the local filler contribution. For  $\text{BaPt}_4\text{Ge}_{12}$ , the contributions of Ba reach through a wide range of frequencies indicating delocalized characteristics of the filler modes. In the case of  $\text{LaPt}_4\text{Ge}_{12}$ , La dominated bands are mostly optical modes which are confined in a narrow frequency window between 1.5 and 1.8 THz, consequently producing a localized peak in the PHDOS. In particular, La-dominated modes at  $\Gamma$  and H are lowered when compared to  $\text{BaPt}_4\text{Ge}_{12}$ . For

ThPt<sub>4</sub>Ge<sub>12</sub>, the filler modes are significantly different from the former two compounds. Th-dominated modes are localized acoustic bands close to the BZ boundary and optical modes at  $\Gamma$ . Most notably, acoustic modes along the direction P-H are almost flattened. The behavior of the Th-filler modes can be understood in terms of the heavy mass of Th compared to Ba and La: in a rough estimate (assuming constant spring constants in all cases), the frequency is inverse proportional to the square root of the mass. However, comparing the results for Ba and La, the masses are rather equal, but the La filler produces localized modes in contrast to Ba. This difference can be attributed to the difference in bonding, because La provides three valence electrons but Ba only two.

The behavior of the low-lying optical filler modes can be compared to filled-pnictide-skutterudites, such as CeRu<sub>4</sub>Sb<sub>12</sub>[83], SmRu<sub>4</sub>P<sub>12</sub>[84], and LaRu<sub>4</sub>P<sub>12</sub>[86], in which an avoided anti-crossing behavior of the lowest optical mode and the acoustic modes occurs. Such an anti-crossing behavior is usually accompanied by a tendency of localization of optical modes around  $\Gamma$  and acoustic branches at the BZ boundary. As shown in Fig.4.4(a) there is an anti-crossing between the lowest optical and highest acoustic branches along the directions P- $\Gamma$  and  $\Gamma$ -H. However, flat bands arise neither at  $\Gamma$  for optical modes nor around the BZ boundary for acoustic modes. For LaPt<sub>4</sub>Ge<sub>12</sub> flat optical modes appear around  $\Gamma$  but lost the avoided anti-crossing behavior which becomes pronounced in LaPt<sub>4</sub>Ge<sub>12</sub> along P- $\Gamma$ . The reasons for that will be discussed below.

The differences in phonons from different fillers for the lowest optical mode at  $\Gamma$  is shown in Fig.4.5 sketching the vibrations of the corresponding eigenvectors of the dynamical matrix. For Pt<sub>4</sub>Ge<sub>12</sub>, the mode is dominated by vibrating Ge atoms. In the case of BaPt<sub>4</sub>Ge<sub>12</sub> the mode is contributed by both vibrating Ge and Pt atoms, but dominated by Pt vibrations. For La(Th)Pt<sub>4</sub>Ge<sub>12</sub>, the mode is dominated by filler vibrations but has little contributions from Ge atoms, according to the PHDOS and dispersion as shown in Fig.4.4.

To understand the differences in filler modes, an analysis of force constants has been carried out. Rewriting the dynamical matrix, Eq.(2.32).

$$D_{i\alpha}^{i'\beta}(\mathbf{q}) = \sum_l \phi' \begin{pmatrix} li'\beta \\ i\alpha \end{pmatrix} e^{-i\mathbf{q}\cdot\mathbf{R}_l} \quad (4.5)$$

where one re-defines

$$\phi' \begin{pmatrix} li'\beta \\ i\alpha \end{pmatrix} = \frac{1}{\sqrt{m_i m_{i'}}} \phi \begin{pmatrix} li'\beta \\ i\alpha \end{pmatrix} \quad (4.6)$$

with  $\phi \begin{pmatrix} li' \\ i \end{pmatrix}$  being the force constant matrix between atom  $i$  in the primitive cell at the origin and atom  $i'$  in the  $l$ th cell. From Eq. (4.5), for two systems with the same structure, the difference in phonon spectra originate from  $\phi'$ . There are basically two types of  $\phi'$ : one is for a pair of atoms which are different and referred as off-site  $\phi'$ . Another one is

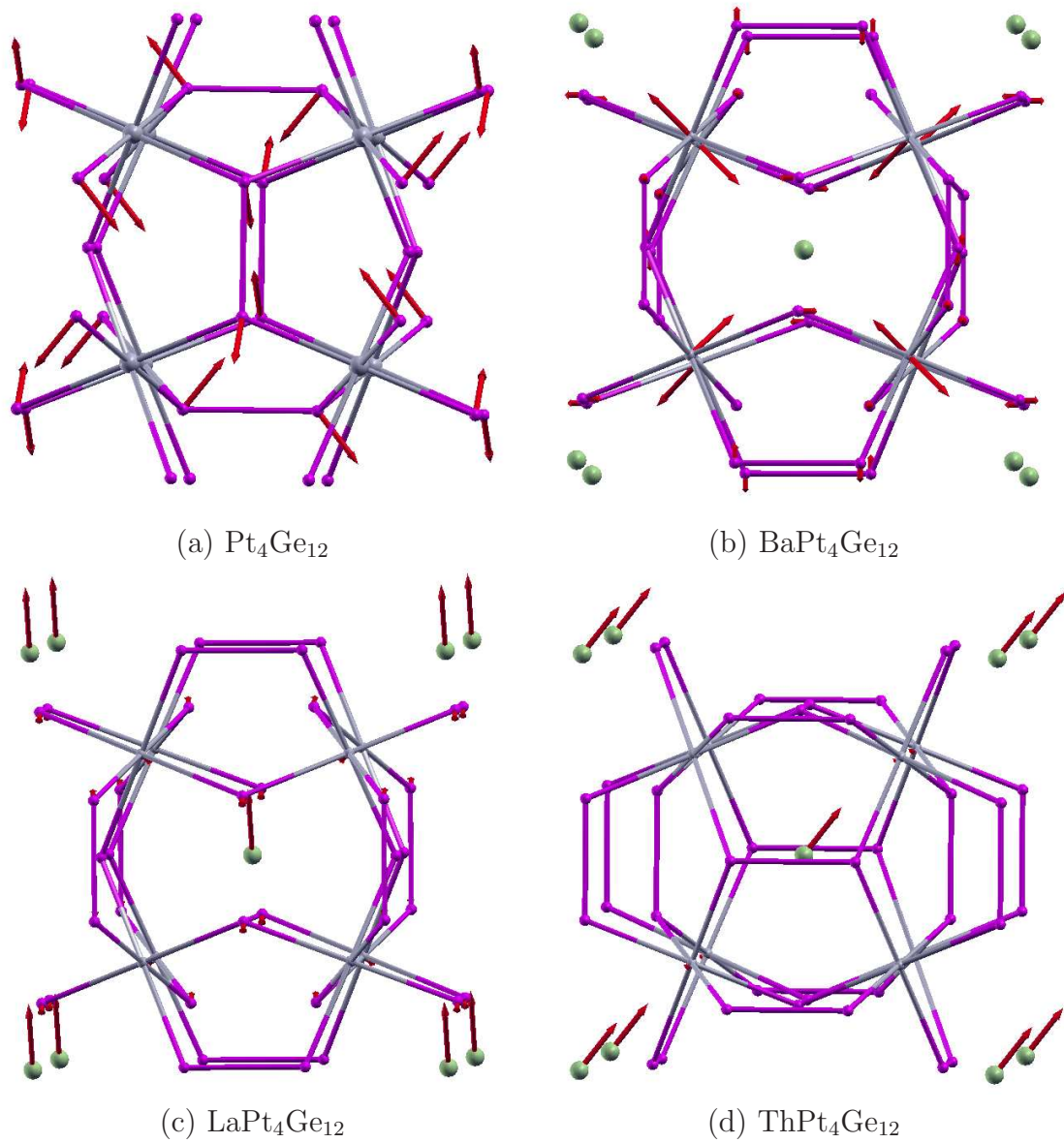


FIGURE 4.5: Sketch of vibrating atoms of the lowest optical mode at  $\Gamma$  for (a)  $\text{Pt}_4\text{Ge}_{12}$ , (b)  $\text{BaPt}_4\text{Ge}_{12}$ , (c)  $\text{LaPt}_4\text{Ge}_{12}$  and (d)  $\text{ThPt}_4\text{Ge}_{12}$ . Filler atoms: large balls, Pt: small gray balls, Ge: small magenta balls.

for an atom and itself in the same cell, i.e.,  $\phi'_{i\alpha}{}^{(i\beta)}$  ( $\alpha, \beta = x, y, z$ ), which is referred to as on-site  $\phi'$ . The elements of  $\phi'$  can be interpreted as hopping parameters in TB method. The difference is that they are intrinsically related to each other through the relation for force constants:

$$\sum_{l,i} \phi'_{i\alpha}{}^{(li'\beta)} = 0 \quad (4.7)$$

Correspondingly, there are two types of force constants: off-site  $\phi$  and on-site  $\phi$ . Atomic masses play their role via Eq.(4.6).

Among the three fillers, Ba has almost the same atomic mass as La. Th is much heavier, because its mass is about 1.7 times larger than Ba. The remarkable differences between the phonon spectrum of BaPt<sub>4</sub>Ge<sub>12</sub> and LaPt<sub>4</sub>Ge<sub>12</sub> suggest different filler-framework force constants between two compounds, or in other words the bonding is significantly different.

Neigh.	system	$\phi(x)$	$\phi(y)$	$\phi(z)$	$\phi(x_y)$	$\phi(x_z)$	$\phi(y_z)$	$\phi'(x)$	$\phi'(y)$	$\phi'(z)$	$\phi'(x_y)$	$\phi'(x_z)$	$\phi'(y_z)$
$(\begin{smallmatrix} Ge1 \\ Ge2 \end{smallmatrix})$	BaPt <sub>4</sub> Ge <sub>12</sub>	0.026	-0.317	0.041	-0.165	-0.055	-0.044	0.0	-0.004	0.001	-0.002	-0.001	-0.001
	LaPt <sub>4</sub> Ge <sub>12</sub>	0.023	-0.331	0.042	-0.189	-0.069	-0.038	0.0	-0.005	0.001	-0.003	-0.001	-0.001
	ThPt <sub>4</sub> Ge <sub>12</sub>	0.022	-0.387	0.073	-0.247	-0.055	-0.044	0.0	-0.005	0.001	-0.003	-0.001	-0.001
$(\begin{smallmatrix} Ge1 \\ Pt \end{smallmatrix})$	BaPt <sub>4</sub> Ge <sub>12</sub>	-2.746	-0.450	-0.740	1.042	-1.036	0.480	-0.023	-0.004	-0.006	0.009	-0.009	0.004
	LaPt <sub>4</sub> Ge <sub>12</sub>	-3.160	-0.582	-0.740	1.235	-1.198	0.568	-0.027	-0.005	-0.006	0.010	-0.010	0.005
	ThPt <sub>4</sub> Ge <sub>12</sub>	-3.559	-0.695	-0.814	1.384	-1.387	0.648	-0.029	-0.006	-0.007	0.012	-0.012	0.005
$(\begin{smallmatrix} M \\ Ge1 \end{smallmatrix})$	BaPt <sub>4</sub> Ge <sub>12</sub>	0.068	-0.103	-1.019	0.0	0.0	-0.413	0.001	-0.001	-0.010	0.0	0.0	-0.004
	LaPt <sub>4</sub> Ge <sub>12</sub>	0.023	-0.062	-0.665	0.0	0.0	-0.335	0.0	-0.001	-0.007	0.0	0.0	-0.003
	ThPt <sub>4</sub> Ge <sub>12</sub>	0.066	-0.028	-0.617	0.0	0.0	-0.371	0.0	0.0	-0.005	0.0	0.0	-0.003
$(\begin{smallmatrix} Ge1 \\ Ge1 \end{smallmatrix})$	BaPt <sub>4</sub> Ge <sub>12</sub>	7.750	3.377	7.534	0.0	0.0	-0.766	0.107	0.046	0.104	0.0	0.0	-0.010
	LaPt <sub>4</sub> Ge <sub>12</sub>	8.721	4.544	7.250	0.0	0.0	-0.012	0.120	0.063	0.100	0.0	0.0	-0.012
	ThPt <sub>4</sub> Ge <sub>12</sub>	9.746	5.696	7.649	0.0	0.0	-1.050	0.134	0.078	0.105	0.0	0.0	-0.014
$(\begin{smallmatrix} Pt \\ Pt \end{smallmatrix})$	BaPt <sub>4</sub> Ge <sub>12</sub>	9.769	$\phi(x)$	$\phi(x)$	1.011	$\phi(x_y)$	$-\phi(x_y)$	0.050	$\phi'(x)$	$\phi'(x)$	0.005	$\phi'(y)$	$-\phi'(y)$
	LaPt <sub>4</sub> Ge <sub>12</sub>	10.933	$\phi(x)$	$\phi(x)$	1.375	$\phi(x_y)$	$-\phi(x_y)$	0.056	$\phi'(x)$	$\phi'(x)$	0.007	$\phi'(y)$	$-\phi'(y)$
	ThPt <sub>4</sub> Ge <sub>12</sub>	12.077	$\phi(x)$	$\phi(x)$	1.731	$\phi(x_y)$	$-\phi(x_y)$	0.062	$\phi'(x)$	$\phi'(x)$	0.009	$\phi'(y)$	$-\phi'(y)$
$(\begin{smallmatrix} M \\ M \end{smallmatrix})$	BaPt <sub>4</sub> Ge <sub>12</sub>	4.600	$\phi(x)$	$\phi(x)$	0.0	0.0	0.0	0.033	$\phi'(x)$	$\phi'(x)$	0.0	0.0	0.0
	LaPt <sub>4</sub> Ge <sub>12</sub>	2.320	$\phi(x)$	$\phi(x)$	0.0	0.000	0.0	0.017	$\phi'(x)$	$\phi'(x)$	0.0	0.0	0.0
	ThPt <sub>4</sub> Ge <sub>12</sub>	2.058	$\phi(x)$	$\phi(x)$	0.0	0.0	0.0	0.009	$\phi'(x)$	$\phi'(x)$	0.0	0.0	0.0

TABLE 4.2: Force constants  $\phi(i'_{i\beta})$  and  $\phi'(i'_{i\beta})$  ( $\alpha, \beta = x, y, z$ ,  $i'$  and  $i$  represent atoms in primitive cell) in unit of (eV/Å<sup>2</sup>u), which are obtained from first-principles phonon calculations using the program *fPHON*. Ge1 and Ge2 (see Table 4.1) are first nearest neighbors in the PtGe<sub>6</sub> octahedron, located at (0,y,z) and (-z,0,-y), respectively.

As the force constants fall off rapidly with the distance between the atoms, the interactions between first-nearest neighbors are the most important. In particular, the fillers reside in very large voids, and therefore the second-nearest-neighbor interactions can be neglected, which means  $\phi_{(Ge)}^{(M)}$  (M is the filler) between the filler and its first-nearest neighbors dominating the on-site terms of M, i.e.,  $\phi_{(M)}^{(M)}$ . Here indices for unit cell and components of  $\phi$  are omitted. For Pt, its first-nearest neighbors are six Ge atoms on the  $\text{PtGe}_6$  octahedron. Therefore  $\phi_{(Pt)}^{(Ge)}$  between Pt and the first-nearest neighboring Ge, dominate the on-site terms  $\phi_{(Pt)}^{(Pt)}$ . While for Ge the main contributions to on-site  $\phi_{(Ge)}^{(Ge)}$  come from  $\phi_{(Ge')}^{(Ge)}$  (Ge' represents neighbors of Ge) and  $\phi_{(Ge)}^{(Pt)}$ . Contributions of  $\phi_{(Pt)}^{(M)}$  and  $\phi_{(Ge)}^{(M)}$  are relatively less important for on-site  $\phi_{(Pt)}^{(Pt)}$  and on-site  $\phi_{(Ge)}^{(Ge)}$ .

Table 4.2 lists  $\phi_{(Ge1)}^{(M)}$ ,  $\phi_{(Ge1)}^{(Pt)}$  and  $\phi_{(Ge2)}^{(Ge1)}$  and corresponding elements of  $\phi'$  with M being the fillers at (0.0, 0.0, 0.0), Pt at (0.25,0.25,0.25) and Ge at (0,y,z) and (-z,0,-y) referred to as Ge1 and Ge2, respectively. Ge1 and Ge2 are the nearest neighbors on a  $\text{PtGe}_6$  octahedron.

First  $\phi$  and  $\phi'$  between two different atoms are examined. Matrix elements of  $\phi_{(Ge2)}^{(Ge1)}$  and  $\phi'_{(Pt)}^{(Ge1)}$  undergo slight increases as the filler changes from Ba, La to Th. This is due to nearly constant  $R_{Ge1,Ge2}$  and  $R_{Pt,Ge}$  (see Table 4.1) which yield almost unchanged inter-atomic interactions. Consequently, corresponding matrix elements of  $\phi'$  are almost constant with only a slight growth. In contrast, significant changes occur in  $\phi$  and  $\phi'$  between the filler M and Ge1 atom. From Table 4.2, one sees that  $\phi_{(Ge1,z)}^{(M,z)}$  has the largest value, thus playing the most important role among all matrix elements of  $\phi_{(Ge1)}^{(M)}$ . Note, that the off-diagonal elements of  $\phi_{(Ge1)}^{(M)}$  almost remain unchanged. However, the diagonal elements, i.e.,  $\phi_{(Ge1,\alpha)}^{(M,\alpha)}$  ( $\alpha = x, y, z$ ) decrease dramatically as the filler changes from Ba, La to Th. For instance,  $\phi_{(Ge1,z)}^{(La,z)}$  is only about 70% of  $\phi_{(Ge1,z)}^{(Ba,z)}$ , which implies much weaker interaction between La and Ge1 than that between Ba and Ge1. Substituting La by Th results in a little change in  $\phi_{(Ge1,z)}^{(M,z)}$ . As for corresponding  $\phi'$ , because Ba has nearly the same atomic mass as La, resultant  $\phi'_{(Ge1,z)}^{(La,z)}$  is about 70% of  $\phi'_{(Ge1,z)}^{(Ba,z)}$ . Thus, phonon modes of La are less affected by the framework atoms than those of Ba. Although  $\phi_{(Ge1,z)}^{(La,z)}$  is appropriately the same as  $\phi_{(Ge1,z)}^{(Th,z)}$ , the heavy Th leads to considerably smaller  $\phi'_{(Ge1,z)}^{(Th,z)}$ , which is only half of  $\phi'_{(Ge1,z)}^{(Ba,z)}$ . This implies that modes of Th are more independent than those of La.

Now turns to the discussions on-site  $\phi$  and  $\phi'$ . Because of small increases in matrix elements  $\phi_{(Ge1)}^{(Ge1)}$  and  $\phi_{(Ge1)}^{(Pt)}$  as the filler changes from Ba, La to Th, a slight strengthening of on-site  $\phi_{(Ge)}^{(Ge)}$  and  $\phi_{(Pt)}^{(Pt)}$  as well as the corresponding on-site  $\phi'$  can be expected. Indeed, Table 4.2 supports this expectation. The most interesting case is on-site  $\phi_{(M)}^{(M)}$  and  $\phi'_{(M)}^{(M)}$ , which decrease significantly as M changes from Ba to La. For instance,  $\phi_{(La,x)}^{(La,x)}$  is only about 50% of  $\phi_{(Ba,x)}^{(Ba,x)}$  and  $\phi_{(Th,x)}^{(Th,x)}$  is less than half of  $\phi_{(Ba,x)}^{(Ba,x)}$ . The trend in  $\phi_{(M)}^{(M)}$  coincides with that in  $\phi_{(Ge1)}^{(M)}$ , because the later determines the former. When  $\phi_{(M)}^{(M)}$  is multiplied

by the inverse of atomic mass of M, the  $\phi'_{(La,x)}$  is about half of  $\phi'_{(Ba,x)}$ . The heavy atomic mass of Th significantly lowers  $\phi'_{(Th)}$ , of which  $\phi'_{(Th,x)}$  is only half of  $\phi'_{(La,x)}$ . It is worth noting that differences between on-site  $\phi'_{(M)}$  and  $\phi'_{(Pt)}$  are more close to those of  $\phi'_{(M)}$  than  $\phi'_{(Ge1)}$ . For  $BaPt_4Ge_{12}$ ,  $\phi'_{(Ba)}$  is comparable to  $\phi'_{(Pt)}$ . However, for  $LaPt_4Ge_{12}$  diagonal elements of  $\phi'_{(La)}$  are much smaller than those of  $\phi'_{(Pt)}$ . The differences are further enhanced when replacing La by Th. Together with the much weaker filler-framework interaction, i.e.,  $\phi'_{(Ge)}$ , the much larger differences between  $\phi'_{(M)}$  and  $\phi'_{(Pt)}$  for Th than those for Ba and La suggests that modes of Th are more localized and separated from those of Pt and Ge.

x	scaled FCs			scaled mass		
	0.75	0.50	0.35	1.3	1.6	2.0
$\phi'_{(Ba)}$	0.026	0.018	0.014	0.026	0.021	0.017

TABLE 4.3: On-site  $\phi'_{(Ba)}$  with respect to scalings in filler-framework interaction  $\phi_{(Ba)}$  and atomic mass of the filler.

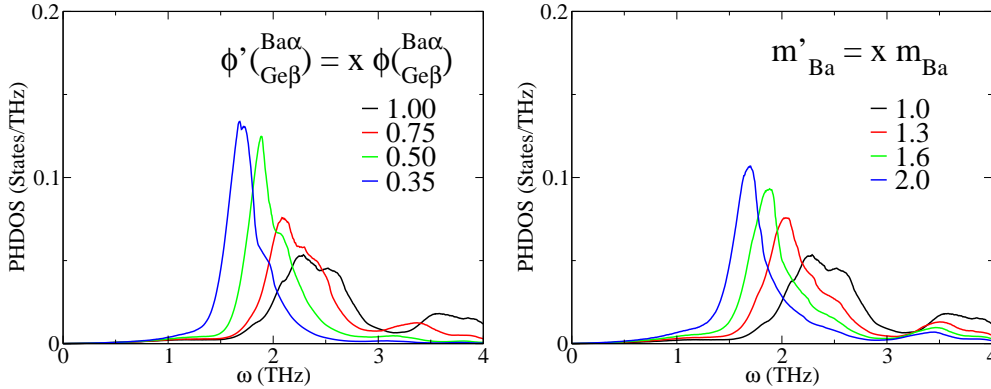


FIGURE 4.6: Atom-projected PHDOS of Ba with respect to scaling in FCs between Ba and Ge, and atomic mass of Ba.

To investigate effect of the interplay between FCs and atomic mass on rattling modes, The PHDOS are calculated with respect to changes in  $\phi_{(Ge)}$  between Ba and its twelve nearest neighbor Ge atoms and atomic mass of Ba, respectively. Fig.4.6 depicts the evolution of phonon modes of Ba with respect to scaling in FCs and atomic mass of Ba. As  $\phi_{(Ge)}$  decreases, the Ba-mode shifts toward lower energy regime and gradually become localized. Likewise, the Ba-mode lost delocalization as its mass is enhanced. The results suggest that the rattling modes can be manipulated by altering filler-framework interaction and atomic mass of the filler, for instance, substituting Ba with much more heavy elements. Both decreasing filler-framework FCs and increasing the atomic mass lower on-site  $\phi'_{(Ba)}$  and thus produces a large difference between  $\phi'_{(Ba)}$  and  $\phi'_{(Pt)}$ . Table 4.3 shows how  $\phi'_{(Ba)}$

reduces with respect to scalings in  $\phi_{Ge}^{(Ba)}$  and  $m_{Ba}$ . In particular,  $\phi_{Ba}^{(Ba)}$  is comparable to  $\phi_{La}^{(La)}$  when  $\phi_{Ge}^{(Ba)}$  is reduced to 35% and  $m_{Ba}$  is doubled. Correspondingly, the position of the peak of filler mode agrees with that of La (see Fig.4.4).

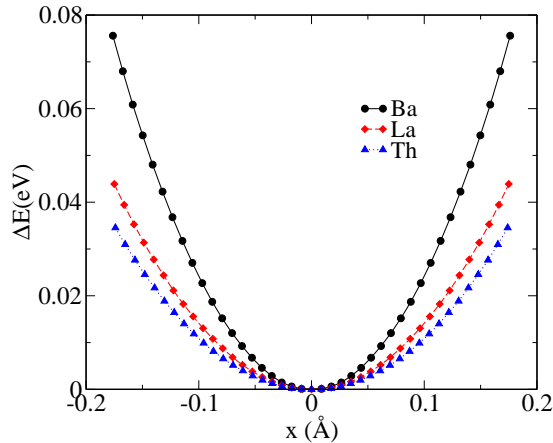


FIGURE 4.7: Potential energy of the filler atoms ( Ba, La and Th) in the skutterudite. Calculations were performed by moving the fillers away from the center of the cage (static equilibrium position) along the x axis

The significant difference in filler-framework FCs between Ba and La implies different potentials of the fillers. The potential energies of the fillers was calculated by displacing the filler in the primitive cell while keeping all other atoms fixed. Fig.4.7 shows Ba has the strongest potential energy and Th has the weakest potential energy, which is consistent with the trend in filler-framework FCs. Fitting the potential energy with the harmonic expression  $E = kx^2$  ( $k$  is the spring constant), one obtains a decreasing  $k$  that is 2.42, 1.42 and 1.12 (in unit of eV/(Å<sup>2</sup>)) for Ba-, La- and Th-filled Pt<sub>4</sub>Ge<sub>12</sub>, respectively. The difference between  $k_{Ba}$  and  $k_{La}$  is significant whereas  $k_{La}$  and  $k_{Th}$  are more or less at the same level. With fitted  $k$ , one further qualitatively estimates trend of the filler vibration frequency within the harmonic oscillator model  $\omega = \sqrt{\frac{k}{m}}$ . One obtains a lowering of filler mode for decreasing  $k$  as the filler varies from Ba to Th. Considering the large difference in potential and small difference in atomic mass between Ba and La, one may argue that bonding between the filler and framework plays an important role in determining the potential energy of the filler. That is attributed to the effect of the atomic size of the filler as shown in in previous studies for Group-IIA-element-doped skutterudites and Group-IA-element-doped clathrates. [88, 108]

#### 4.3.2.3 Atomic Displacement Parameters

Atomic displacement parameters (ADPs) measure the mean-square displacement amplitude of an atom about its equilibrium position in a crystal, of which the value can be due

to the vibration of the atom. Thus, the differences in vibrations of constituted elements can be detected by ADPs. In the isotropic case, ADPs  $U_{iso}$  is given by

$$U_{iso}(T) = \frac{1}{3} \langle \mathbf{u}_l^2(T) \rangle = \frac{1}{3} \sum_{\alpha=1}^3 \langle \mathbf{u}_{l\alpha}^2(T) \rangle \quad (4.8)$$

where  $\langle \mathbf{u}_l^2(T) \rangle$  is the mean-square displacement of  $l$ th atom, which is given by

$$\langle \mathbf{u}_l^2 \rangle = \frac{3\hbar}{2M_l} \int \frac{g_l(\omega)}{\omega} \coth\left(\frac{\hbar\omega}{2k_B T}\right) \quad (4.9)$$

$g_l(\omega)$  is the atom-projected PHDOS of  $l$ th atom. Details about the derivation are given in Appendix C.

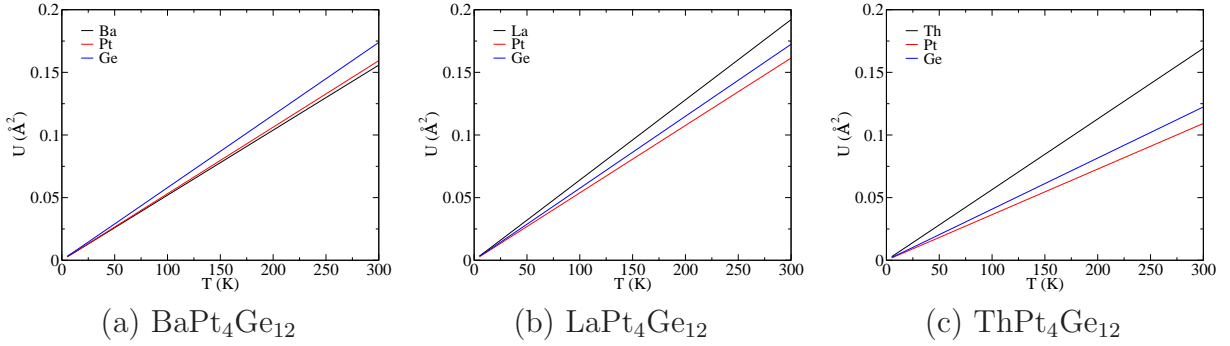


FIGURE 4.8: Calculated averaged ADPs  $U_{iso}$  vs temperature for (a)  $\text{BaPt}_4\text{Ge}_{12}$ , (b)  $\text{LaPt}_4\text{Ge}_{12}$  (c)  $\text{ThPt}_4\text{Ge}_{12}$  using Eq.(4.8).

Figure 4.8 show calculated  $U_{iso}$  of each type of atoms vs temperature for  $\text{MPd}_4\text{Ge}_{12}$ , which reflect essential features of guest modes as observed in corresponding phonon spectrum. In  $\text{BaPd}_4\text{Ge}_{12}$ , Ba shows a little smaller  $U_{iso}$  than those of framework atoms resulting from its delocalized phonon DOS. That implies Ba may not be in a rattling motions. La shows a different behavior from Ba because its  $U_{iso}$  is little large than those framework atoms, which can be understood from the difference in phonon DOS (Fig.4.4). Th exhibits a distinguish rattling behavior for its  $U_{iso}$  is larger than those of Pt and Ge by about 40%. Our calculations are in good agreement with experimental measurements.

#### 4.3.2.4 Specific Heat

The rattling modes play an important role in thermal properties. Recent experiment shows that  $\text{ThPt}_4\text{Ge}_{12}$  has a complicated specific heat that can not be explained by the Debye model [90]. A model was applied to explain the measured specific heat. It assumes that besides a Debye DOS, there exists two energetically separated Einstein-type modes

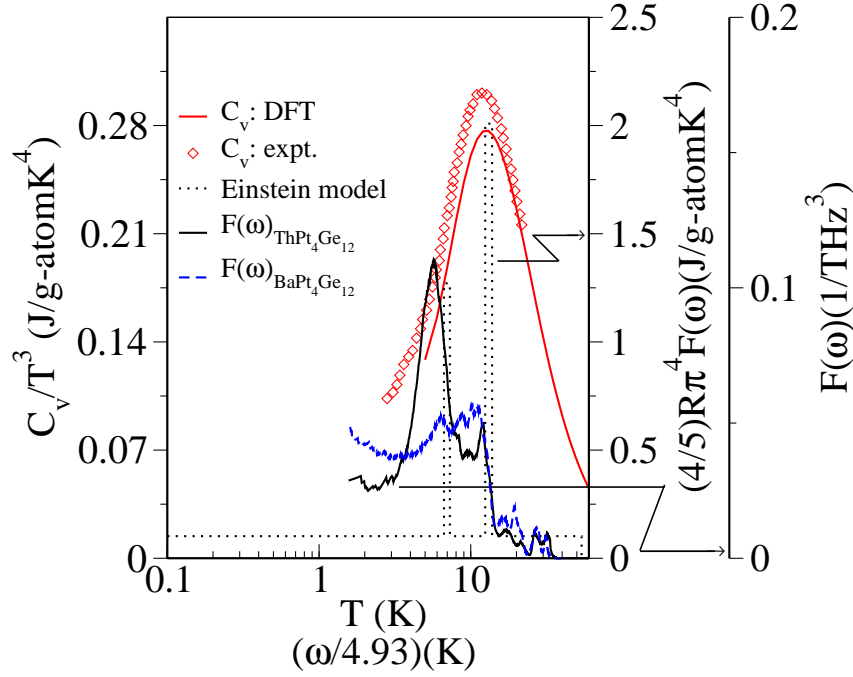


FIGURE 4.9: Comparison of calculated temperature-dependence of specific heat  $C_v$  (red solid line) of  $\text{ThPt}_4\text{Ge}_{12}$  plotted as  $C_v/T^3$  vs  $\ln T$  with experiment (red diamonds) Ref. [90]. Black dotted line labels the spectral function of Einstein-like separated modes from the experimental model, black solid line labels calculated function  $F(\omega)_{\text{ThPt}_4\text{Ge}_{12}}$ , blue dashed line represents the calculated function  $F(\omega)_{\text{BaPt}_4\text{Ge}_{12}}$ .  $F(\omega) = g(\omega)/\omega^2$  with  $g(\omega)$  the PHDOS from first-principles lattice dynamics calculations.

$\omega_1$  and  $\omega_2$  in the system. However, these modes are assumed to have a width  $\Delta\omega$ , which are somehow different from the standard Einstein ones.

$$C_V(T) = 3R \int_a g(\omega) \frac{\left(\frac{\omega}{2T}\right)^2}{\sinh^2\left(\frac{\omega}{2T}\right)} d\omega \quad (4.10)$$

with  $\omega$  the phonon frequency,  $g(\omega)$  phonon density of states and  $R$  the gas constant. The most common assumptions on  $g(\omega)$  are  $g(\omega) = \delta(\omega)$  and  $g(\omega) \sim \omega^2$  up to a cut-off frequency  $\omega_D$ , corresponding to the well-known Einstein and Debye model, respectively. Junod *et al*[109]. demonstrated that certain functionals of the phonon specific heat take the form of convolutions of the phonon spectrum. In particular,  $(5/4)R^4 C_{ph} T^3$  is an image of the spectrum  $g(\omega)/\omega^2$  for  $\omega = 4.93 T$ , where  $\omega$  is expressed in degrees Kelvin. One may suspect that one of the Einstein may corresponds to the rattling modes for both Einstein-like mode and low-lying optical mode have the localized feature. According to this model, the phonon features of the model can be derived from DFT phonon DOS, defining  $F(\omega) = g(\omega)/\omega^2$  where  $g(\omega)$  is the phonon DOS from lattice dynamics calculations. Fig.4.9 show comparison of our calculations with experiments and fitting of the model. For the specific heat our calculation is in a good agreement with the experiment. For  $\text{ThPt}_4\text{Ge}_{12}$  the calculated function,  $F(\omega)$ , has a structure of two separated peaks, of which the positions

are comparable to that of Einstein-like modes from the model. The lowest energy peak is contributed by the low lying peak in the phonon DOS dominated by Th modes. On the contrary, the two-peak structure is missing in  $F(\omega)$  for  $\text{BaPt}_4\text{Ge}_{12}$  in which guest phonon modes are delocalized. Our calculations support the validity of the model. Furthermore, our analysis indicates that localized guest mode can be dictated indirectly by specific heat experiments.

### 4.3.3 Summary

We have used an first-principles lattice dynamics method to investigate the lattice dynamics of a new family of filled-skutterudites,  $\text{MPt}_4\text{Ge}_{12}$  ( $M = \text{Ba}, \text{La}$  and  $\text{Th}$ ). The most significant result is the rattling modes undergo a delocalization-localization transition as the filler goes from Ba to Th, which is driven by filler-framework coupling and filler mass. The rattling modes can be manipulated either by suppression of filler-framework or enhancement of atomic mass of the filler toward improving thermoelectric performance of materials. Our calculations of specific heat reveal validity of the empirical model which introduces two Einstein-like modes besides the Debye phonon DOS. The implications of these results suggest that the localized rattling modes can be indirectly observed by specific heat experiments and the rattling modes can be controlled for thermoelectric applications.

## 4.4 Thermoelectric Properties of Ge-skutterudites

### 4.4.1 Electronic Structures of $\text{MPt}_4\text{Ge}_{12}$

Figure 4.10 depicts electronic structures of  $\text{MPt}_4\text{Ge}_{12}$  ( $M = \text{Ba}, \text{La}$ , and  $\text{Th}$ ). For the systems contain heavy elements, both non-relativistic and relativistic calculations were performed. It shows that for all compounds both calculations predict almost the same bands which means the relativistic effect only has little effects on the bands. For  $\text{BaPt}_4\text{Ge}_{12}$  (Fig.4.10(b)) there is small shift for the bands at about -3 eV. For  $\text{LaPt}_4\text{Ge}_{12}$  (Fig.4.10(c)) and  $\text{ThPt}_4\text{Ge}_{12}$  (Fig.4.10(d)) flat bands are observed at about 2 eV which are due to the localized  $f$  states of La and Th. Parabolic bands are observed around  $H$  for all the considered systems. As the filler goes from Ba, La to Th, the parabolic bands are down-shifted and finally a gap is formed of about 1 eV for  $\text{ThPt}_4\text{Ge}_{12}$ .

The relativistic effect has little influence on the DOS around the Fermi level and slight modification on those in the range of -5 to -3. A sharp peak in both  $\text{LaPt}_4\text{Ge}_{12}$  and  $\text{ThPt}_4\text{Ge}_{12}$  centered at 2 eV is observed, which is due to localized  $f$  electrons in La and

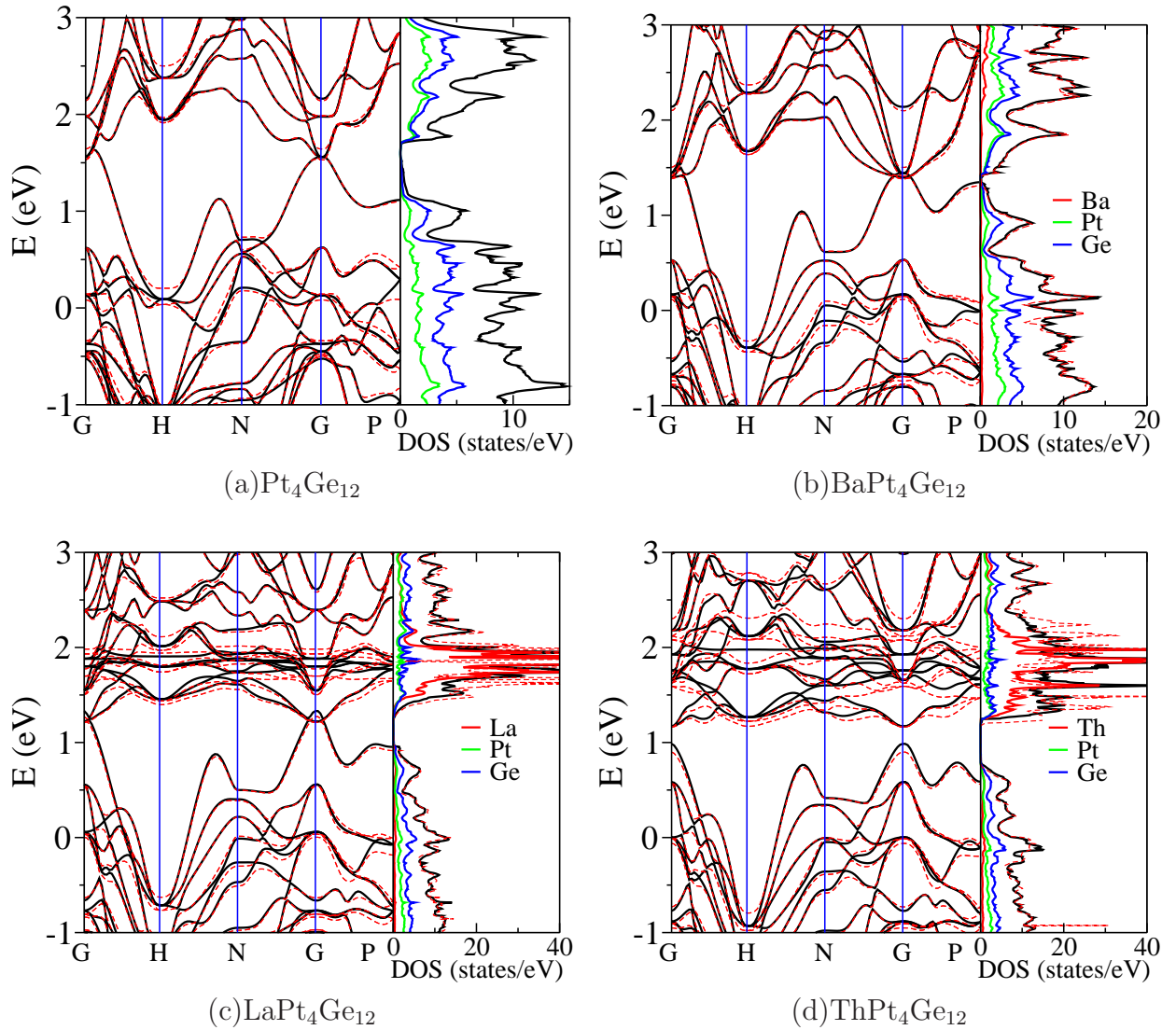


FIGURE 4.10: Electronic structures of (a)  $\text{Pt}_4\text{Ge}_{12}$ , (b)  $\text{BaPt}_4\text{Ge}_{12}$ , (c)  $\text{LaPt}_4\text{Ge}_{12}$ , (d)  $\text{ThPt}_4\text{Ge}_{12}$ . Energy scale relative to the Fermi level. Solid lines label scalar-relativistic results and the dashed red ones denote results including spin-orbit coupling.

Th. There is a gap away from the Fermi energy by about 1 to 1.5 eV and get more and more close to the Fermi level as nuclear charge increases. This shifting is due to band filling which is related to the valence electron configurations of the filler with Ba, La, Th having 2,3,4 valence electrons, respectively.

## 4.4.2 Seebeck Coefficients of $\text{MPt}_4\text{Ge}_{12}$

### 4.4.2.1 Model Calculations

We first investigate the applicability of the Mott's relation Eq.(B.9) and its simplified version Eq.(B.18) by comparing the results with that derived from full calculations, i.e., Eq.(3.20). For the sake of clarity, they are rewritten for the Mott's relation

$$S = \frac{\pi^2 k_B^2 T}{3e} \left[ \frac{\partial \ln \sigma(E)}{\partial E} \right]_{E=\mu} \quad (4.11)$$

for the simplified Mott's relation

$$S = -\frac{\pi^2 k_B^2 T}{3|e|} \left\{ \frac{1}{N(E)} \frac{dN(E)}{dE} \right\}_{E=\mu} \quad (4.12)$$

and for the full calculation

$$S = \frac{\int \mathbf{v}(\mathbf{k})\mathbf{v}(\mathbf{k})\tau(\mathbf{k})(E - \mu)\left(-\frac{\partial f^0}{\partial E}\right)d\mathbf{k}}{eT \int \mathbf{v}(\mathbf{k})\mathbf{v}(\mathbf{k})\tau(\mathbf{k})\left(-\frac{\partial f^0}{\partial E}\right)d\mathbf{k}} \quad (4.13)$$

Eq.(4.11) was implemented within the constant relaxation time approximation. The quantity  $\frac{\sigma(E)}{\tau}$ , the product of  $v^2(\varepsilon)$  and  $N(\varepsilon)$ , were derived from full calculations using V2Boltz. The scheme for such a calculation is illustrated by the flow-chart as shown in Fig.3.3. Input eigenvalues were derived from DFT calculations on a k-mesh of  $25 \times 25 \times 25$ . Then they were used to generate eigenvalues on a much denser k-mesh  $70 \times 70 \times 70$  in terms of Fourier interpolation. The electronic chemical potential  $\mu(T)$  was calculated using Eq.(3.49). Results are shown in Fig.4.11 for  $\text{BaPt}_4\text{Ge}_{12}$  without any doping. Mott's relation, Eq.(4.11), agrees well with the full calculation (Eq.(4.13)) at low temperatures region and tends to deviate at elevated temperatures. This is attributed to temperature-dependent property of the energy derivative of the Fermi function,  $\frac{\partial f^0}{\partial E}$ , appeared in Eq.(4.13).  $\frac{\partial f^0}{\partial E}$  has delta-like properties at low temperatures. Thus  $\mathbf{v}(\mathbf{k})\mathbf{v}(\mathbf{k})\tau(k)$  only contributes to the calculation of  $S$  within a few  $k_B T$  of  $E = \mu$ .  $[\mathbf{v}(\mathbf{k})\mathbf{v}(\mathbf{k})\tau(k)]|_{E_n(\mathbf{k})=\mu}$  has the largest weight, because  $[\frac{\partial f^0}{\partial E}]$  has the largest value at  $E_n(\mathbf{k}) = \mu$ . As  $T$  close to the zero limit,  $\mathbf{v}\mathbf{v}\tau$  at  $\mu$  dominates the contributions to  $S$ . The peak lowers and broadens with respect to an increasing temperature, which lowers the weight of  $\mathbf{v}\mathbf{v}\tau$  at  $\mu$  to  $S$ . However, this feature is not contained in Mott's relations which, in stead, simply uses either conductivity or DOS at the Fermi level. The simplified Mott's relation Eq.(4.12) produces a relatively larger discrepancy with Eq.(4.13). This means the second term at the right hand side of Eq.(4.11) is becoming important at higher temperatures because of the shift in chemical potential. Nevertheless, the three equations give the same sign of

the Seebeck coefficient. This implies the usefulness of Eq.(4.12) in estimating the sign of the Seebeck coefficient in terms of the derivative of the DOS.

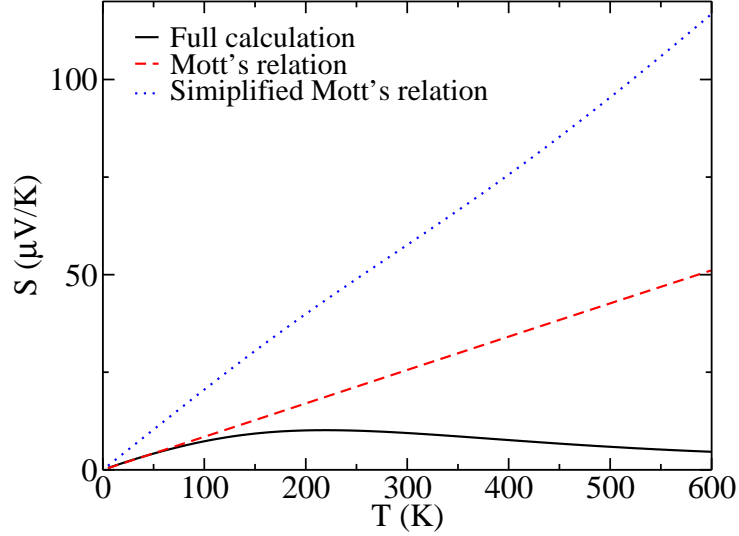


FIGURE 4.11: Comparison of the Seebeck coefficients from Eq.(4.13) (black solid line), Eq.(4.11) (red dashed line), and Eq.(4.12) (blue dotted line)

#### 4.4.2.2 Full Calculations

Calculated Seebeck coefficients of  $\text{MPt}_4\text{Ge}_{12}$  as a function of chemical potential, corresponding to shifting of the Fermi energy, at  $T=300\text{K}$  shown in Fig.4.12. Each compound

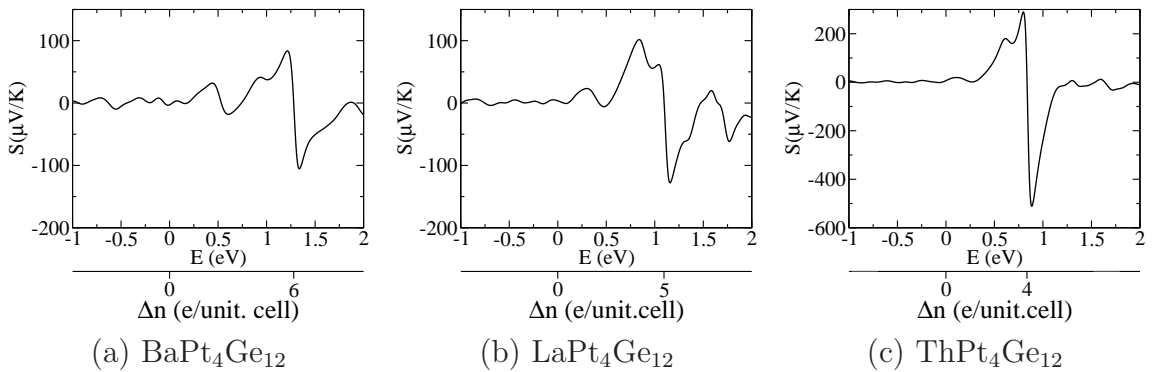


FIGURE 4.12: DFT derived Seebeck coefficients as a function of chemical potential, i.e., temperature dependent Fermi level, at  $T = 300\text{K}$  for  $\text{BaPt}_4\text{Ge}_{12}$  (a),  $\text{LaPt}_4\text{Ge}_{12}$  (b) and  $\text{ThPt}_4\text{Ge}_{12}$  (c), respectively. The energy shifting for placing the Fermi level in the middle of the pseudogap (gap) is translated into  $\Delta n$ , the change of the valence electron number.

exhibits a rather low Seebeck coefficient at  $\Delta n = 0$  (undoped case) consistent with experiments. For example, both experiment and calculation yield a Seebeck coefficient of about  $7.0 \mu\text{V}/\text{K}$  at  $T = 300 \text{ K}$  for  $\text{BaPt}_4\text{Ge}_{12}$  [96]. This is anomalous to pnictide skutterudites which have Seebeck coefficients with magnitudes over  $100 \mu\text{V}/\text{K}$  [11, 12, 14, 31]. The magnitude of the Seebeck coefficient increases significantly when the Fermi level of the undoped compounds is increased to about 1.25, 1.10, and 0.80 eV to fall in the gap. Crossing the gap the sign of  $S$  changes. In particular, in the case of  $\text{ThPt}_4\text{Ge}_{12}$  the negative peak has a surprisingly larger magnitude than the positive peak around the critical point. This feature can be understood with the help of simplified Mott's relation and the characteristics of the bands close to the gap. States above the gap are made of flat bands and thus result in a localized DOS which yields a significant slope of DOS, leading to a larger Seebeck coefficient. This fits the pattern shown in Fig.B.1 for optimizing TE properties. The results suggest that good thermoelectric properties are favorable when the Fermi level is shifted close to a gap or pseudogap.

### 4.4.3 Band Engineering for Optimization of Thermoelectric Properties

The concepts presented under the name band engineering of optimized thermoelectric  $\text{MPt}_4\text{Ge}_{12}$  skutterudites are based on the electronic properties of  $\text{CoSb}_3$ , which is a well known thermoelectric material [12]. The pioneering DFT study of D. Singh [30] revealed that there is a small gap around Fermi energy, which is the consequence of the hybridization of Sb-p and Co-d states. This hybridization gap is fundamentally different from the gap occurring in clathrates, which will be discussed in the next section. In clathrates the gap is formed by the pnictide framework, e.g.  $\text{Ge}_{46}$  for a clathrate of type I, whereas for skutterudites the mentioned p-d hybridization is mandatory. Returning to  $\text{CoSb}_3$  the magic number of valence electrons for placing the Fermi energy into the gap is 24, because Co provides 9 and  $\text{Sb}_3$  15 valence electrons. Assuming now, that substitution of Co and Sb by similar elements such as Pt and Ge, respectively, does not change significantly the gap formation properties, a simple electron counting rule is proposed for placing  $E_F$  into the gap. The  $\text{Pt}_4\text{Ge}_{12}$  backbone will be taken as a reference, and counting its number of valence electrons,  $N_1 = 4 + 12 \times 4 = 88$ ) one finds that 8 electrons are missing for reaching the number of valence electrons of  $\text{Co}_4\text{Sb}_{12}$ ,  $N_0 = 96$ . Therefore, if one wants to move  $E_F$  close to the gap a sufficient number of electrons have to be provided by a) filler atoms and/or b) suitable substitutions of the framework atoms Pt and Ge. This is the meaning of the term band engineering.

#### 4.4.3.1 Band Engineering by Chemical Doping

If the shifting of the Fermi level is transferred into electron doping within the rigid band approximation, 6, 5, and 4 e/u.c more are needed to place the Fermi level in the middle of the gap for Ba-, La-, and Th-Pt<sub>4</sub>Ge<sub>12</sub> compounds, respectively, which requires a proper doping. When the filler is chosen for doping, an element is needed which provides 8 valence electrons. That means the dopant must be a lanthanide or actinide with f-states as valence states. However, the f-states strongly disturb the electronic structure at the Fermi level, and their localisation properties (correlation and magnetism) can be quite complex. For example, a metal rather than a semiconducting behavior is predicted for SmPt<sub>4</sub>Ge<sub>12</sub> by previous calculations[94]. Therefore f states induce uncertainties of band engineering, which requires extensive search rather than simple electron counting.

		Hopping parameters									
		Ge-Ge				Ge-M					
	NN	$V_{4s4s,\sigma}$	$V_{4s4p,\sigma}$	$V_{4p4p,\sigma}$	$V_{4p4p,\pi}$	$V_{4s6s,\sigma}$	$V_{4s5d,\sigma}$	$V_{4p6s,\sigma}$	$V_{4p5d,\sigma}$	$V_{4p5d,\pi}$	
1stNN	Pt4Ge12	-3.19	4.88	3.78	-2.01	-4.33	-2.49	-4.36	-1.86	1.72	
	Au4Ge12	-3.11	4.74	3.60	-1.97	-4.31	-2.35	-4.36	-1.89	1.66	
2ndNN	Pt4Ge12	-1.15	2.35	3.07	-0.99	-0.52	-0.30	-1.09	-0.60	0.19	
	Au4Ge12	-1.15	2.34	2.97	-0.98	-0.51	-0.27	-1.08	-0.56	0.18	
3rdNN	Pt4Ge12	-0.74	1.67	2.48	-0.51	-0.05	-0.03	-0.18	-0.09	0.01	
	Au4Ge12	-0.72	1.63	2.53	-0.64	-0.05	-0.02	-0.17	-0.09	0.01	
4thNN	Pt4Ge12	-0.57	1.32	2.16	-0.42						
	Au4Ge12	-0.57	1.34	2.24	-0.39						
5thNN	Pt4Ge12	-0.25	0.65	1.36	-0.25						
	Au4Ge12	-0.25	0.66	1.33	-0.26						
6thNN	Pt4Ge12	-0.02	0.06	0.24	-0.02						
	Au4Ge12	-0.02	0.06	0.23	-0.01						
		On-site terms									
		Ge				M					
		$\epsilon_{4s}$	$\epsilon_{4p_x}$	$\epsilon_{4p_y}$	$\epsilon_{4p_z}$	$\epsilon_{6s}$	$\epsilon_{5d_{z^2}}$	$\epsilon_{5d_{x^2-y^2}}$	$\epsilon_{5d_{xy}}$	$\epsilon_{5d_{xz}}$	$\epsilon_{5d_{yz}}$
	Pt4Ge12	0.00	5.94	6.41	6.86	2.95	5.09	5.09	5.11	5.11	5.11
	Au4Ge12	0.00	5.65	6.40	6.86	2.07	2.64	2.64	2.66	2.66	2.66

TABLE 4.4: Tight-binding hopping  $V$  and on-site  $\epsilon$  parameters (in eV) generated using the LCAPO method with interaction up to the fifth-nearest neighbors

		Tight-binding overlap parameters								
		Ge-Ge				Ge-M				
	NN	$S_{4s4s,\sigma}$	$S_{4s4p,\sigma}$	$S_{4p4p,\sigma}$	$S_{4p4p,\pi}$	$S_{4s6s\sigma}$	$S_{4s5d,\sigma}$	$S_{4p6s,\sigma}$	$S_{4p5d,\sigma}$	$S_{4p5d,\pi}$
1stNN	Pt4Ge12	0.17	-0.31	-0.40	0.17	0.27	0.13	0.40	0.13	-0.13
	Au4Ge12	0.17	-0.31	-0.40	0.17	0.27	0.12	0.04	0.12	-0.12
2ndNN	Pt4Ge12	0.06	-0.14	-0.27	0.06	0.02	0.01	0.07	0.04	-0.01
	Au4Ge12	0.06	-0.14	-0.27	0.06	0.02	0.01	0.07	0.04	-0.01
3rdNN	Pt4Ge12	0.03	-0.09	-0.20	0.04					
	Au4Ge12	0.03	-0.09	-0.20	0.03					
4thNN	Pt4Ge12	0.03	-0.09	-0.18	0.03					
	Au4Ge12	0.03	-0.08	-0.18	0.03					
5thNN	Pt4Ge12	0.01	-0.03	-0.09	0.01					
	Au4Ge12	0.01	-0.03	-0.09	0.01					

TABLE 4.5: Tight-binding overlap parameters generated using the LCAPO method with interaction up to the fifth-nearest neighbors

The second recipe of doping refers to the doping of framework atoms corresponding to  $\text{Pt}_4\text{Ge}_{12}$ , which is more often applied. Most of doping of thermoelectric pnictogen-based skutterudites begin with the corresponding framework [11, 74]. As for Pt-site doping, noble metal elements are possible dopants providing one more electron than the latest transition elements Ni, Pd, Pt. The question is, how the electronic structure is affected and if the gap feature is preserved. Testing the replacement of Pt by Au, Fig.4.13 shows the electronic structures of  $\text{Pt}_4\text{Ge}_{12}$  and  $\text{Au}_4\text{Ge}_{12}$  (taking  $\text{Pt}_4\text{Ge}_{12}$  without any structural relaxation). The most significant difference is that a pseudo-gap is formed around 1.6 eV for  $\text{Pt}_4\text{Ge}_{12}$ , which is missing (or rather small) for  $\text{Au}_4\text{Ge}_{12}$ . A closer look at the bands of  $\text{Pt}_4\text{Ge}_{12}$  reveals that only around  $\Gamma$  do bands with strong dispersion cross the 1.6 eV energy line, which have a very small weight in the BZ sampling overall resulting in the pseudo-gap with a width of 0.6 eV. For  $\text{Au}_4\text{Ge}_{12}$ , however, the gap width is narrowed substantially because of the downshift of the 5d band according to Fig.4.13, as revealed directly from a tight-binding (TB) fit. The gap opens up if all hopping parameters are fixed, but only the 5d level is raised (bottom-right panel). The tight binding parameters are generated by using the OpenMX package[59] based on a linear combination of pseudoatomic orbital (LCPAO) method[110] (see Sec. 2.3.2.2). The interactions reach up to the fifth nearest neighbors for Ge-Ge and the third nearest neighbors for Ge-Au/Pt interactions. The LCPAO calculations are in reasonable agreement with the VASP calculations as shown in Fig.4.13, and the TB parameters are listed in Tables 4.4 and 4.5, showing that the overlap integrals are close to zero. As expected, the hopping (overlap) integrals are practically the same for the Pt- and Au-compound. A significant difference occurs, however, with respect to the positions of the 5d and 6s level of the metal, which are much closer together for Au than for Pt, as sketched in Fig.4.13 (bottom-left panel). To investigate the effect of the 5d-6s difference of the metal levels on the gap the corresponding on-site 5d parameter was shifted upwards by  $\varepsilon_{shift}(d)$  to increase the s-d difference. The bottom-left panel of Fig.4.13 depicts the DOS of  $\text{Au}_4\text{Ge}_{12}$  depending on  $\varepsilon_{shift}(d)$ . A gap clearly emerges around 1.0 eV as  $\varepsilon_{shift}(d)$  increases up to 2.0 eV, at which the 5d-6s difference of Au is comparable to that of Pt.

Of course, also substitution and related electron doping can also be done on the Ge-sublattice, for which pnictogen-elements such as Sb are suitable, provided the electronic structure around the gap region remains basically undisturbed. As elaborated at the very beginning of this subsection, the magic valence electron number is 96 for placing the Fermi energy into the gap. Filled skutterudites such as  $\text{LaPt}_4(\text{Sb}_5\text{Ge}_7)$  and  $\text{ThPt}_4(\text{Sb}_4\text{Ge}_8)$  have exactly this required number and confirming the counting rule a gap opens up at the Fermi energy as shown by Fig.4.14.

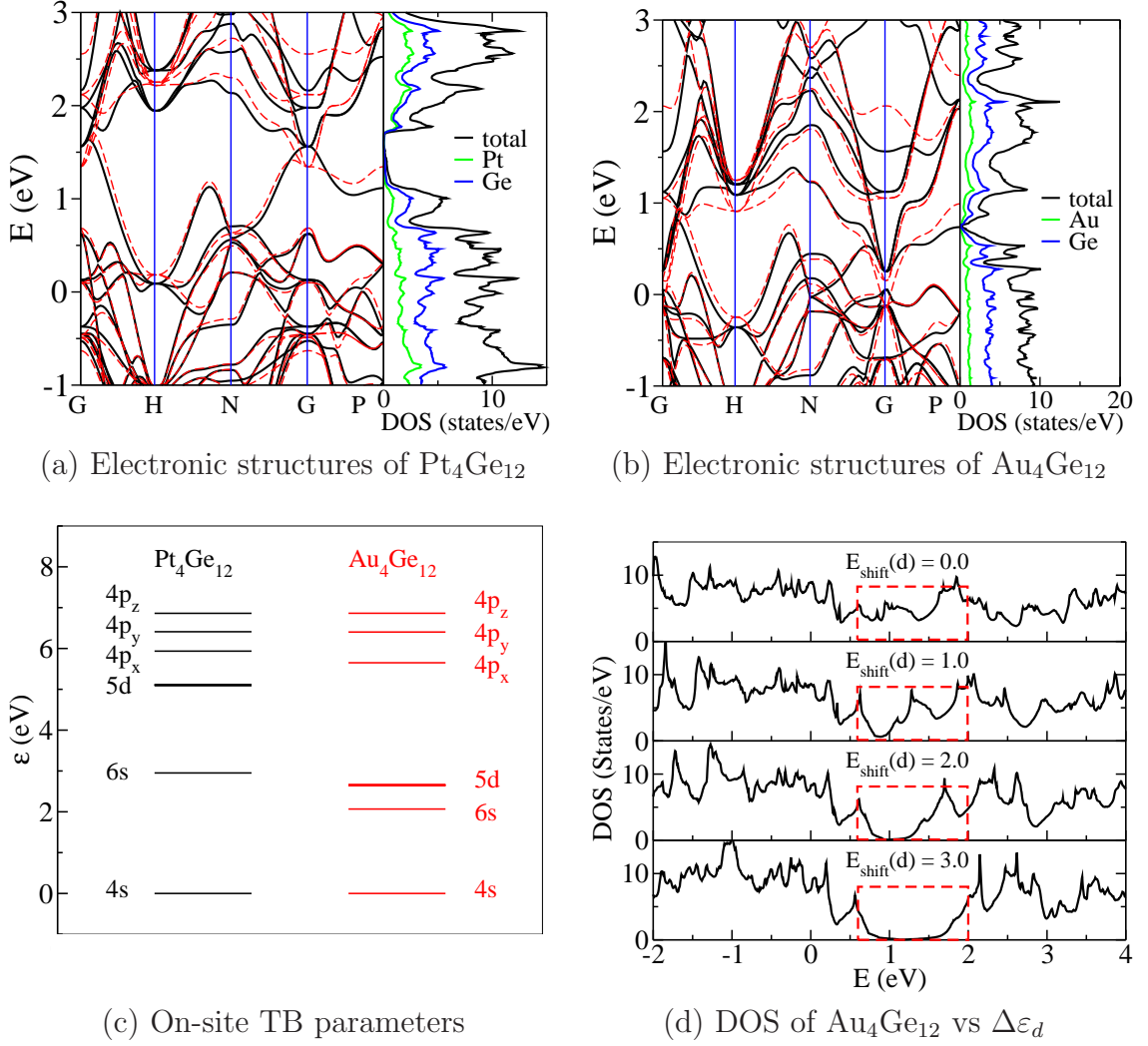


FIGURE 4.13: VASP derived electronic structures (black lines) of  $\text{Pt}_4\text{Ge}_{12}$  (left-top panel) and  $\text{Au}_4\text{Ge}_{12}$  (right-top panel), and TB bands (red dashed lines). Illustration of on-site parameters as Ge 4p and Pt/Au 5d,6s levels (left-bottom panel) and DOS of  $\text{Au}_4\text{Ge}_{12}$  derived from TB calculations (right-bottom panel) with several shifts of the  $\varepsilon_{5d}$  level of Au.

#### 4.4.3.2 Seebeck Coefficients of $\text{MPt}_4(\text{Sb}_x\text{Ge}_{12-x})$

Looking into the effects on TE properties by doping Ge-based skutterudites with Sb, as shown in Fig.4.15 at 300 K, it is indicated that Seebeck coefficients over  $100 \mu\text{V}/\text{K}$  can be obtained when the doping of Sb is very close to 5 for  $\text{LaPt}_4\text{Ge}_{12}$  and 4 for  $\text{ThPt}_4\text{Ge}_{12}$ , respectively. Varying the number of valence electrons in terms of shifting the Fermi energy within a rigid band model reveals that  $S(\mu)$  becomes significantly pronounced when the Fermi level falls close to the top of the gap, where bands are much flatter than those at the bottom of the gap. Fig.4.16 depicts temperature dependent Seebeck coefficients of  $\text{LaPt}_4(\text{Sb}_{5-\delta}\text{Ge}_{7+\delta})$  and  $\text{ThPt}_4(\text{Sb}_{4-\delta}\text{Ge}_{8+\delta})$  with  $\delta = \pm 0.1$ . Basically,

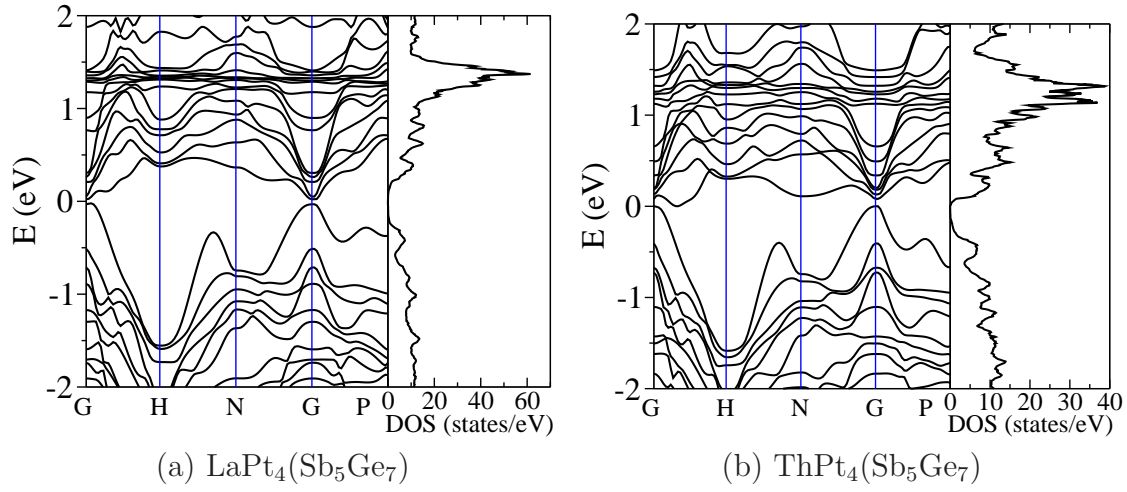


FIGURE 4.14: Electronic structures of  $\text{LaPt}_4(\text{Sb}_5\text{Ge}_7)$  and  $\text{ThPt}_4(\text{Sb}_4\text{Ge}_8)$  at  $T = 300$  K.

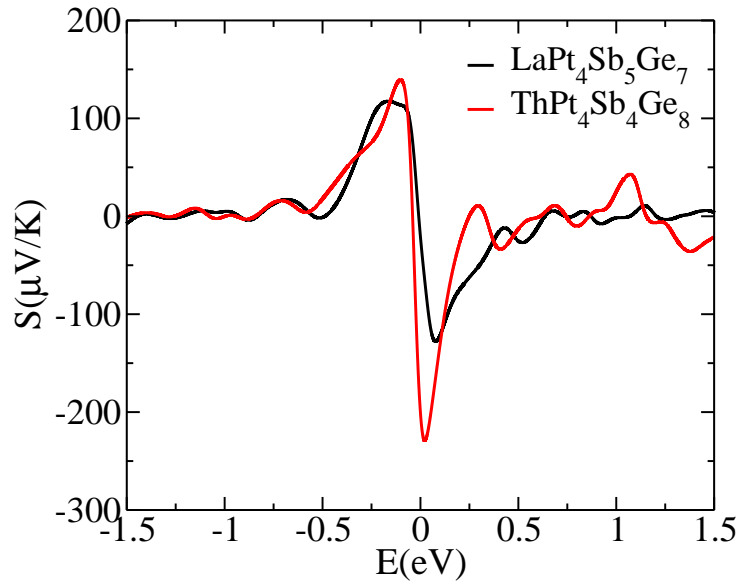


FIGURE 4.15: DFT derived Seebeck coefficient  $S(\mu)$  for 300K as a function of varying chemical potential  $\mu$ , i.e. number of valence electrons. The chemical potentials represents the Fermi energy for 300K within a rigid band model, and  $\mu = 0$  corresponds to the Fermi level of undoped  $\text{LaPt}_4(\text{Sb}_5\text{Ge}_7)$  and  $\text{ThPt}_4(\text{Sb}_4\text{Ge}_8)$ .

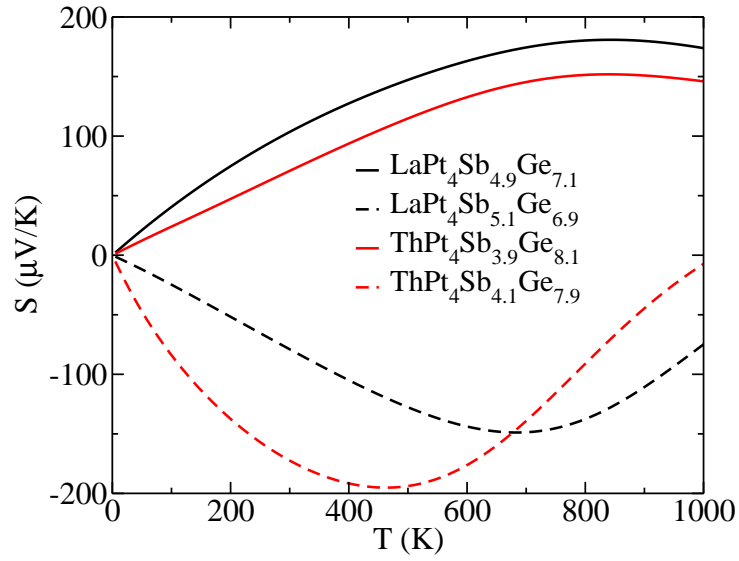


FIGURE 4.16: DFT derived Seebeck coefficients of  $\text{LaPt}_4(\text{Sb}_{5-\delta}\text{Ge}_{7+\delta})$  and  $\text{ThPt}_4(\text{Sb}_{4-\delta}\text{Ge}_{8+\delta})$  ( $\delta = \pm 0.1$ ).

each compound shows a Seebeck coefficient with values over  $100 \mu\text{V}/\text{K}$  at its maximum. Compared to corresponding pure Ge-based skutterudites whose values are less than  $10 \mu\text{V}/\text{K}$  for  $\text{BaPt}_4\text{Ge}_{12}$  (see Fig.4.11 and Ref.[96]) and  $\text{ThPt}_4\text{Ge}_{12}$ [97] one can conclude that an improvement of two orders of magnitude for the Seebeck coefficient is achieved for  $\text{LaPt}_4(\text{Sb}_{5-\delta}\text{Ge}_{7+\delta})$  and  $\text{ThPt}_4(\text{Sb}_{4-\delta}\text{Ge}_{8+\delta})$ . Based on this finding One may speculate that high Seebeck coefficients can be obtained with a proper doping of Sb in other Ge-based skutterudites.



# Chapter 5

## Group-IV-based Clathrates

### 5.1 Introduction

Clathrates have attracted considerable interest as thermoelectric materials. Most of the work done so far focused on group-IV based compounds with the type-I structure, [7, 16–20, 111, 112] making use of their structural properties to obtain a low lattice thermal conductivity. For thermoelectric applications, electronic transport properties such as the Seebeck coefficient and electrical conductivity were optimized by tuning the charge carrier concentration. The optimization can be achieved by void-filling elements, substitution, and/or doping of the occupied lattice sites. The search for high-performance TE material has yield exciting results for the group-IV-based clathrates: for instance, a figure of merit,  $ZT$ , over 1.6 at 1100 K was obtained with  $\text{Ba}_8\text{Ga}_{16}\text{Ge}_{30}$ [7].

Despite the developments, the highly desirable further improvement of  $ZT$  is still a demanding problem. Various chemical dopings have been tried, including noble metals, nickel- and zinc-group elements on the 6d sites of type-I clathrates. However, none of them shows a larger  $ZT$  than  $\text{Ba}_8\text{Ga}_{16}\text{Ge}_{30}$ . Thus, a fundamental understanding of correlations between TE properties and the electronic structure is necessary to possibly constitute a general rule of chemical doping for good TE properties.

Their parent compounds –the filler-free clathrates– have interesting electronic properties. For the Si and Ge backbone in the clathrate structures the gap is significantly larger than for the diamond ground state structure. DFT and post DFT calculations predict an increase of at least 0.7 eV of the band gap of  $\text{Si}_{34}$  and  $\text{Si}_{46}$  as compared to the diamond phase [113, 114].

In the case of  $\text{Ge}_{34}$  and  $\text{Ge}_{46}$  calculated gaps of type-I and -II clathrates are again significantly larger than for the diamond structure, for which the gap is zero by standard DFT calculations[114–116]. I should be noted, that standard DFT calculations grossly

underestimate gaps, but nevertheless reproduce the correct trend. By application of very expensive post DFT methods gaps can be fairly well reproduced and these calculations serve as benchmarks.

Little effort has been devoted to the understanding of the gap differences between these phases. Zhao *et al* suggested that the existence of pentagonal rings in  $\text{Ge}_{46}$  accounts for the differences[116]. However, the structures also exhibit a great deal of resemblances such as a nearest-neighbor fourfold coordination for all the isomers.

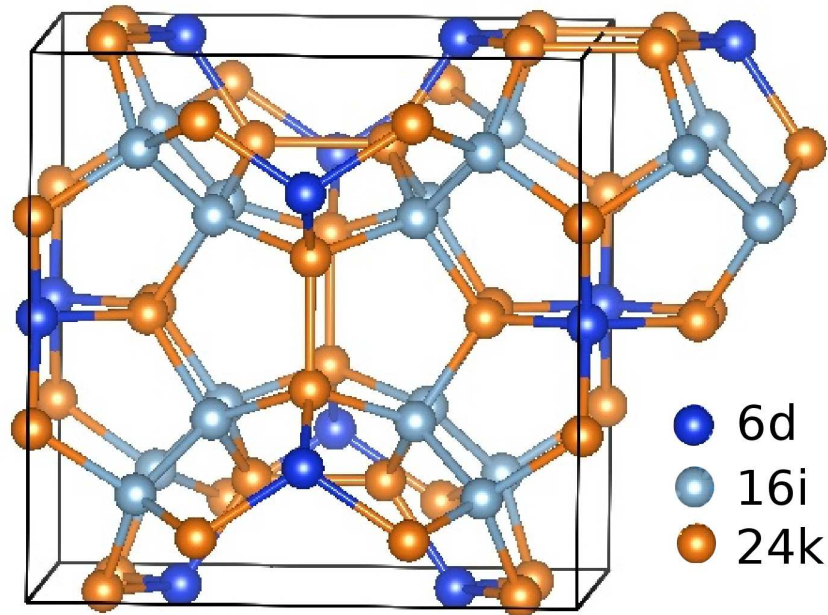
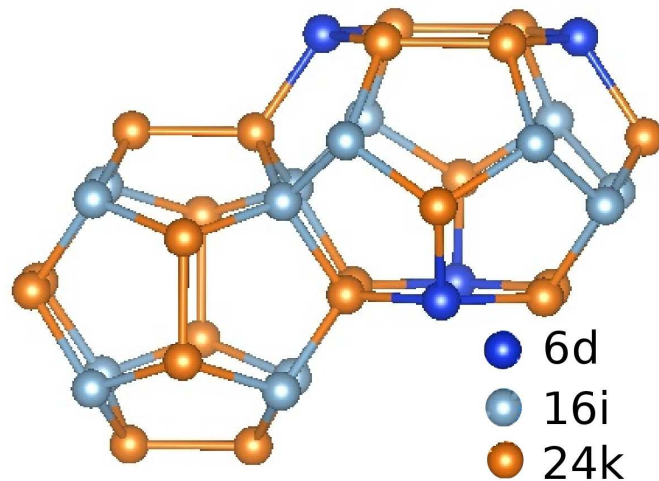
Moreover, experimentally electronic thermal conductivity is derived from measured electrical conductivity using the Wiedemann-Franz law in which a constant is used for the Lorenz number from the metallic limit. The Lorenz number is the ratio of the electronic thermal conductivity to the product of temperature and electrical conductivity. However, Eqs.(3.16) and (3.18) show that they have different temperature-dependences. Therefore, the ratio must be temperature-dependent rather than temperature-independent. Consequently, the assumption of the constant Lorenz number must lead to discrepancies from the true value. This law can only be trusted for simple metals, but is generally used anyway. Examining the validity of the Wiedemann-Franz law and proposing a effective evaluating the lattice thermal conductivity would no doubt benefit the field of thermoelectrics.

## 5.2 Unfilled Type-I and -II Clathrates: $\text{X}_{46}$ and $\text{X}_{34}$

The purpose of this chapter is to explain, by means of a first-principles approach combining with the tight binding approximation, the origin of gap differences between different isomers. The first subsection presents the structural and electronic structures of all the isomers, diamond structure, type-I and -II clathrates for each group IV member. The second subsection discusses the origin of the gap differences between the isomers based on TB analysis.

### 5.2.1 Structural and Electronic properties

The type-I clathrate referred to as  $\text{X}_{46}$ , has a simple cubic lattice with 46 atoms per unit cell and its space group is  $\text{Pm}\bar{3}\text{n}$  (No 223). The type-II clathrate, referred to as  $\text{X}_{34}$  or  $\text{X}_{136}$ , is based on a face-centered cubic lattice with 34 atoms in the primitive cell (or 136 atoms in the conventional cell) and its space group is  $\text{Fd}\bar{3}\text{m}$  (No 227). Coordinates for the type-I and -II clathrates are listed in Table 5.1. The main structural feature is that atoms in these phases are fourfold-coordinated forming  $\text{sp}^3$ -type covalent bonds and they form cages. There are two types of cages in type I clathrate, two pentagonal

(a) type-I clathrate  $X_{46}$ 

(b) structural units

FIGURE 5.1: (a) Structure of filler-free type I clathrate  $X_{46}$ . There are three types of Wyckoff positions, 6d, 16i, and 24k, which are shown in different colors. There are two types of polyhedras (20-atom dodecahedras and 24-atom tetrakaidecahedras) as structural units (b), which are also shown by including some of the atoms from neighboring cells (a).

dodecahedra (20-atom cage with 12 pentagons) and six tetrakaidecahedra (24-atom cage with 12 pentagons and 2 hexagons), of which the centers are on 2a and 6d Wyckoff sites, respectively. The pentagonal dodecahedra are not directly connected to each other but linked by tetrakaidecahedra. In the type-II clathrate structure, there are also two types of cages, eight pentagonal dodecahedra and sixteen hexakaidecahedra (12 pentagons and 4 hexagons) in the conventional unit cell, of which the centers are on 8b and 16c Wyckoff

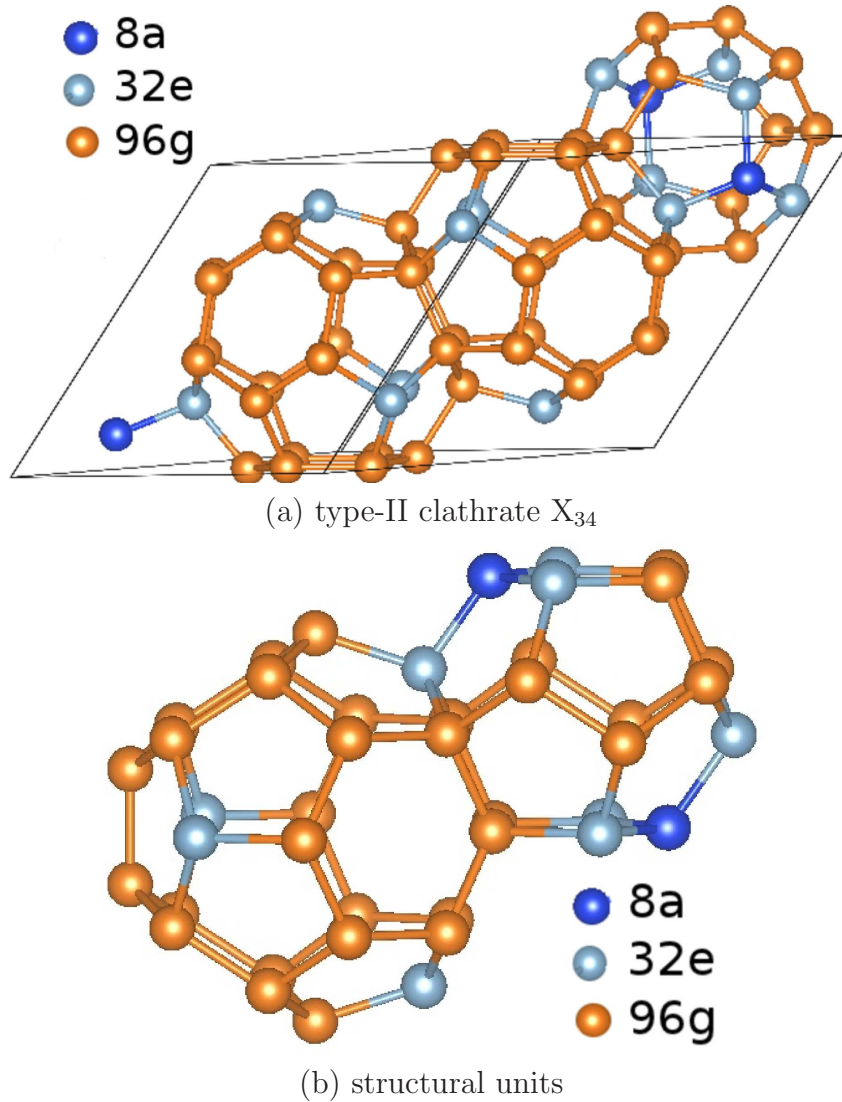


FIGURE 5.2: (a) Structure of filler-free type II clathrate. There are three types of Wyckoff positions, 8a, 32e, and 96g, which are shown in different colors. There are two types of polyhedras (20-atom dodecahedras and 28-atom tetrakaidecahedras) as structural units (b), which are also shown by including some of atoms from neighboring cells (a).

sites, respectively.

For calculations of the electronic structure of the pure, filler-free clathrates, the generalised gradient approximation (GGA) is used for the exchange-correlation functional using the parametrization of Perdew, Burke, and Ernzerhof (PBE). The electron-ion interaction is treated within the framework of Blöchl's projector augmented wave method (PAW). The valence state configurations for the construction of the pseudopotentials included  $2s^22p^2$  for C,  $3s^23p^2$  for Si, and  $4s^24p^2$  for Ge. A  $5 \times 5 \times 5$  Monkhorst and Pack [119] was used to sample the Brillouin zone. Table 5.2 summarizes the band gaps of C, Si,

type I (Pm $\bar{3}$ n: No 223)		type II (Fd $\bar{3}$ m: No 227)	
Wyckoff positions			
6d	$(\frac{1}{4}, \frac{1}{2}, 0)$	8a	$(\frac{1}{8}, \frac{1}{8}, \frac{1}{8})$
16i	$(x, x, x)$	32e	$(x_1, x_1, x_1)$
24k	$(0, y, z)$	96g	$(x_2, x_2, z)$

TABLE 5.1: Structural parameters of type I and II clathrates. Wyckoff positions  $x$ ,  $y$ ,  $z$  dependent on the particular material.

	diamond	type I	type II
C	4.11	3.87	4.05
	5.48 <sup>a</sup>	5.15 <sup>b</sup>	5.25 <sup>b</sup>
Si	0.62	1.34	1.39
	1.17 <sup>a</sup>	1.85 <sup>b</sup>	1.85 <sup>b</sup>
Ge	0.00	1.09	0.68
	0.74 <sup>a</sup>	1.21 <sup>c</sup>	0.75 <sup>c</sup>

<sup>a</sup>Experiment (Ref. [117])

<sup>b</sup>GW calculations (Ref. [118])

<sup>c</sup>LDA calculations (Ref. [115])

TABLE 5.2: Band gaps (eV) of diamond structure, type-I and -II clathrates structure. First line of each item: present VASP calculation, second line: other data

and Ge as calculated the ground state diamond structure as well as with the type-I and -II clathrate structures. The result of the present GGA-DFT calculation are compared to experiment as well as post DFT (GW) calculations and on LDA result. Before discussing the results it should be noted that -as is well known- standard DFT calculations give far too small gaps for C, Si, and Ge (and many other systems as well) but usually trends and pressure dependencies are described reasonably well. Post DFT applications such as GW may cure the problem but are very expensive, and not usable for larger and less symmetric systems.

Table 5.2 shows a significant decrease of the gap when going from C to Si and Ge, for all the structures. For C, the diamond phase has a slightly larger gap than for the clathrate structures, which is in contrast to Si and Ge. The Gaps of Si- and Ge-based unfilled clathrates are much larger than those of corresponding ground state diamond structure.

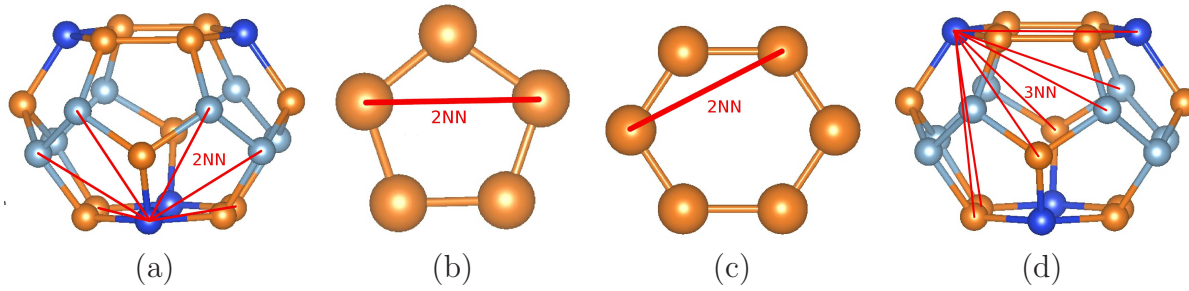


FIGURE 5.3: Illustration of counting the second-nearest neighbors in clathrate structures. (a) Neighbors of an atoms in a tetrakaidecahedra which consists of pentagons and hexagons. For each atom, ways of choosing its second-nearest neighbors are illustrated in (b) and (c). The way of choosing the third-nearest neighbors are shown in (d).

Most remarkable is the gaps of the Ge series, because standard DFT predicts a zero gap for the diamond structure, but produces a gap of 1.1 eV for the type-I clathrates and 0.7 eV for type II. The filler-free type-I and -II clathrates have so far not been successfully synthesized. Nevertheless, the features of their gaps make them promising materials for thermoelectric and optoelectronic applications.

The deviations between the standard DFT calculations and experiments and GW results are rather constant for the C and Si systems (see Table 5.2). For Ge the gap sizes obtained for the clathrate structures agree reasonably well with another DFT calculations applying the LDA approximation.

## 5.2.2 Coordination and Bonding

Although the three phases are differently structured, they do bear resemblances. In all the structures each atom is fourfold coordinated, because it has four first-nearest neighbors (1NNs). In both clathrates each atom has twelve second-nearest neighbors (2NNs) because each atom is shared by six polyhedrons. However, the number of third-nearest neighbors (3NNs) of an atom is different from type to type. The ways of identifying the 2NNs and 3NNs are illustrated in Fig.5.3. Table lists the number of neighbors and the range of atom-atom distances between the neighbors.

Bond lengths are rather similar for 1NNs and 2NNs, which are about 2.50 and 4.0 Å for 1NNs and 2NNs, respectively. It should be noted that in the diamond structure atoms of each nearest neighbor type are equivalent and therefore there is only one 1NN and one 2NN distance. In clathrates the symmetry is reduced: in the type-I clathrate the four 1NNs of an atom on the 6d site are 24k atoms (Fig.5.1), while those of an atom on the 16i site consists of one 16i atom and three 24k atoms, resulting in two different types of distances between 1NNs. Nevertheless, they are very close to each other. For both clathrates, the averaged distances between third-nearest neighbors (3NNs) are about

system	site	1NN	2NN	3NN	4NN
Ge <sub>2</sub>		4 (2.50)	12 (4.08)	12 (4.78)	6 (5.77)
	6d	4 (2.51)	12 (3.99 ~ 4.45)	18 (5.39 ~ 5.91)	
Ge <sub>46</sub>	16i	4 (2.47 ~ 2.48)	12 (3.99 ~ 4.01)	21 (5.58 ~ 5.85)	
	24k	4 (2.48 ~ 2.52)	12 (4.01 ~ 4.45)	16 (5.49 ~ 5.85)	
Ge <sub>34</sub>	8a	4 (2.46)	12 (4.00)	24 (5.61)	
	32e	4 (2.46 ~ 2.49)	12 (3.97 ~ 4.02)	18 (5.56 ~ 5.73)	
	96g	4 (2.49 ~ 2.52)	12 (3.97 ~ 4.31)	10 (5.61 ~ 5.79)	

TABLE 5.3: The number of nearest neighbors for each type of atoms in the three phases. Distances (in Å) between neighbors are given in brackets. The ways of choosing 2NNs and 3NNs are illustrated in Fig.5.3.

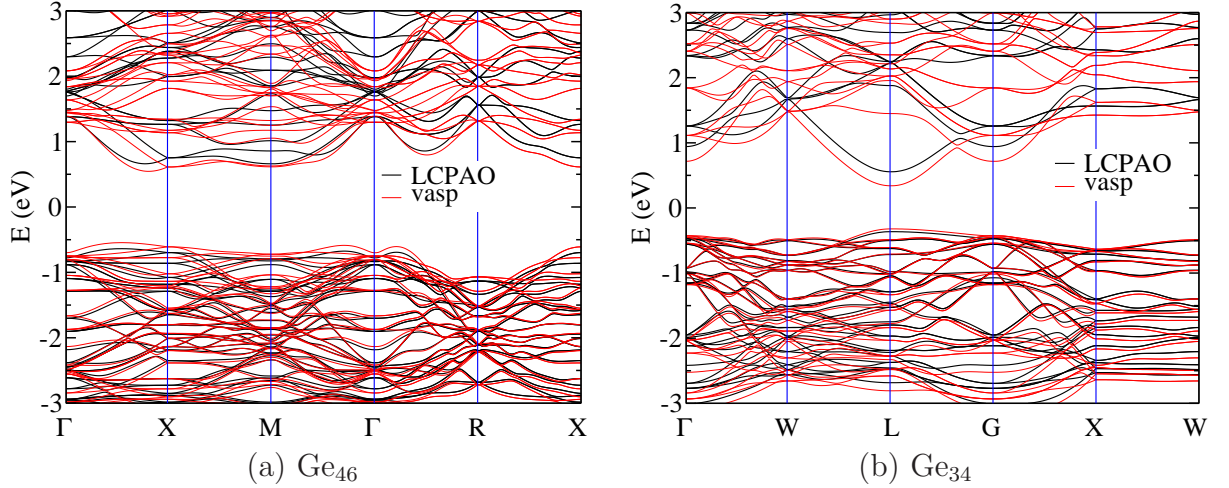


FIGURE 5.4: Band structures of (a) Ge<sub>46</sub> and (b) Ge<sub>34</sub> as derived by VASP and LCPAO calculations. A basis set including one s orbital, three p orbitals and one zeta function s\* was used in the LCPAO calculation.

5.60 Å, which is close to the atom-atom distances of 5.77 Å between the fourth-nearest neighbors for the diamond structure. For the diamond structure, the atom-atom distances between 3NNs are 4.78 Å.

TB parameters were generated using LCPAO method, which has been discussed in Sec. 2.3.2. A basis set consisting of one s, three p orbitals and one zeta function s\* are used in the LCPAO calculations. Fig.5.4 compares the results of the VASP and LCPAO calculations showing that the LCPAO method is in reasonable agreement with the high-quality calculation. In principle, better agreement can be made by including more zeta

		Hopping						
		$V_{ss,\sigma}$	$V_{sp,\sigma}$	$V_{pp,\sigma}$	$V_{pp,\pi}$	$V_{ss^*,\sigma}$	$V_{s^*s^*,\sigma}$	$V_{s^*p,\sigma}$
1stNN	Diamond (2.50)	-3.80	5.44	3.65	-2.09	3.83	-0.33	-0.12
	Ge <sub>46</sub> (2.48)	-3.76	5.37	3.71	-2.03	3.82	-0.26	-0.10
	Ge <sub>34</sub> (2.49)	-3.84	5.48	3.61	-2.09	3.82	-0.29	-0.10
2ndNN	Diamond (4.08)	-0.37	0.92	1.76	-0.30	1.17	-1.01	-1.59
	Ge <sub>46</sub> (4.01)	-0.38	0.95	1.85	-0.33	1.22	-1.18	-1.70
	Ge <sub>34</sub> (4.04)	-0.41	1.01	1.88	-0.33	1.28	-1.19	-1.74
3rdNN	Diamond (4.78)	-0.08	0.25	0.65	-0.09	0.37	-0.80	-0.75
	Ge <sub>46</sub> (5.55)	-0.02	0.06	0.21	-0.01	0.10	-0.49	-0.32
	Ge <sub>34</sub> (5.61)	-0.01	0.05	0.19	-0.01	0.09	-0.50	-0.32
4thNN	Diamond (5.77)	-0.01	0.03	0.11	-0.01	0.05	-0.32	-0.19
		On-site terms						
		$\epsilon_{4s}$	$\epsilon_{4p_x}$	$\epsilon_{4p_y}$	$\epsilon_{4p_z}$	$\epsilon_{s^*}$		
Diamond		0.00	6.61	6.61	6.61	10.64		
	6d	0.00	6.86	6.58	6.58	10.89		
	Ge <sub>46</sub>							
	16i	-0.06	6.61	6.61	6.61	10.47		
	24k	0.00	6.71	6.77	6.42	10.79		
Ge <sub>34</sub>	8a	0.00	6.52	6.52	6.52	10.48		
	32e	0.01	6.56	6.56	6.56	10.50		
	96g	-0.02	6.50	6.50	6.83	10.77		

TABLE 5.4: Hopping parameters  $V$  and  $\epsilon$  (in eV) are generated using the LCAPO method with interaction up to fourth-nearest neighbors. The hopping parameters for each neighbor are generated at the atom-atoms distance for the neighbors very close to the averaged distance which are given in brackets (in Å).

functions. However, to avoid a huge amount of TB parameters the basis set is made as small as possible.

The tight-binding parameters are summarized in Table 5.4 and 5.5. Except for those involving the zeta function, the absolute values of the hopping parameters significantly decrease with increasing atom-atom distances. For the 1NNs the hoppings are two to ten times larger than those of the 2NNs in magnitude. The 3NN interaction are rather

		Overlap						
		$S_{ss,\sigma}$	$S_{sp,\sigma}$	$S_{pp,\sigma}$	$S_{pp,\pi}$	$S_{ss^*,\sigma}$	$S_{s^*s^*,\sigma}$	$S_{s^*p,\sigma}$
1stNN	Diamond (2.50)	0.20	-0.36	-0.40	0.21	-0.31	0.17	0.15
	Ge <sub>46</sub> (2.48)	0.20	-0.36	-0.40	0.20	-0.31	0.17	0.15
	Ge <sub>34</sub> (2.49)	0.20	-0.36	-0.40	0.21	-0.31	0.17	0.15
2ndNN	Diamond (4.08)	0.02	-0.05	-0.12	0.02	-0.07	0.16	0.15
	Ge <sub>46</sub> (4.01)	0.02	-0.05	-0.12	0.02	-0.07	0.16	0.15
	Ge <sub>34</sub> (4.04)	0.02	-0.05	-0.13	0.02	-0.07	0.16	0.16
3rdNN	Diamond (4.78)	0.00	-0.01	-0.04	0.00	-0.02	0.09	0.06
	Ge <sub>46</sub> (5.55)	0.00	0.00	-0.01	0.02	0.00	0.03	0.02
	Ge <sub>34</sub> (5.61)	0.00	0.00	-0.01	0.00	0.00	0.02	0.01

TABLE 5.5: Overlap parameters as generated by the LCAPO method with interaction up to the third-nearest neighbors. Overlap parameters for each neighbor are generated at the atom-atoms distance for the neighbors very close to the averaged distance, which are given in brackets (in Å).

negligible because they are less than 10% of the 2NN interactions. Comparing the three structures, resemblances can be observed. For 1NNs and 2NNs the TB parameters are almost the same over all three different structures. Differences are observed for 3NNs between the diamond structure and the clathrates because the atom-atom distances for them are different. However, the TB parameters for the 3NNs of clathrates are very similar to those for the fourth-nearest neighbors of the diamond structure, since the atom-atom distances are similar.

From Eqs.(2.23) and (2.24), the band structure is determined by bond integrals and its structure. For the TB parameters are quantitatively similar to each other among the three structures, the differences concerning the gap comes from the differences in structure. Indeed besides structural similarities, there are significant differences between the three structures, which may account for the gap differences. In the diamond structure, there are two atoms in unit cell, labeled as A and B for clarity. If A is located at (0,0,0), the four 1NNs of A are B occupying

$$\frac{a}{4}, \frac{a}{4}, \frac{a}{4} \quad \frac{a}{4}, -\frac{a}{4}, -\frac{a}{4} \quad -\frac{a}{4}, \frac{a}{4}, -\frac{a}{4} \quad -\frac{a}{4}, -\frac{a}{4}, \frac{a}{4}$$

When constructing the Hamiltonian matrix elements between orbitals on atoms A and B using Eqs.(2.23) with interaction only up to 2NNs, these four neighbors are involved for

each pair of orbitals, namely,

$$H_{m,n}(\mathbf{k}) = \sum_{i=1}^4 e^{i\mathbf{k}\cdot\mathbf{R}_i} h_{m,n}(\mathbf{R}_i) \quad (5.1)$$

where  $m$  and  $n$  denote orbitals of A and B respectively. However, the situations in clathrates are totally different. Taking 6d sites in  $\text{Ge}_{46}$  as an example. The atoms on 6d sites with coordination of  $(\frac{1}{4}, \frac{1}{2}, 0)$  have the same distances from all the four 1NNs, but the four 1NNs neighbors are involved in four different constructions of  $H_{m,n}$ . Moreover, there are significant differences in direction cosines, which are used to construct  $h_{m,n}$ . In the diamond structure, the direction cosines between neighbors have special properties because of the high symmetry of the diamond structure. In  $\text{Ge}_{46}$  the 1NNs of atoms on 6d sites are 24k sites, of which coordinations are related to  $(0, y, z)$  by the space group of  $\text{Ge}_{46}$ . The direction cosines from 6d to 24k have no special properties as the diamond structure has, because  $y$  and  $z$  have to be determined for each specific material. In the case of  $\text{Ge}_{34}$ , atoms on 8a sites have the same distances (see Table 5.3) from their 1NNs neighbors like in diamond structure. For this type of atoms, their four 1NNs are atoms on 32e site, of which coordinations are related to  $(x_1, x_1, x_1)$  (See Table 5.3). Thus the direction cosines from an 8a atom to its four 1NNs are like  $(\frac{1}{\sqrt{3}}, \frac{1}{\sqrt{3}}, \frac{1}{\sqrt{3}})$  and  $(\frac{1}{\sqrt{3}}, -\frac{1}{\sqrt{3}}, -\frac{1}{\sqrt{3}})$  ... However, the four 1NNs of are not the same atom but different, which are entirely distinct from the diamond case. The four 1NNs of the 8a sites are some atoms on 32e sites but not translated by one atoms as in the diamond structure. For the other types of atoms, the distances from an atom to its four 1NNs are different. Thus these distinct structural properties lead to significant differences in Hamiltonian matrix elements between the three structures and therefore results in different band structures between them.

To show the resultant differences in Hamiltonian, Table 5.6 lists Hamiltonian matrix elements  $H_{m,n}(\mathbf{K})$  between one pair of neighbors at  $\Gamma$  for the three structures. For the diamond structure,  $m$  represents orbitals of the atom at  $(0,0,0)$  and  $n$  denotes orbitals of the atom at  $(\frac{1}{4}, \frac{1}{4}, \frac{1}{4})$ . For  $\text{Ge}_{46}$ ,  $m$  and  $n$  label orbitals of the atoms at  $(\frac{1}{4}, \frac{1}{2}, 0)$  and  $(-y, z, 0)$ , respectively. For  $\text{Ge}_{34}$ ,  $m$  and  $n$  represent orbitals of the atoms at  $(\frac{1}{8}, \frac{1}{8}, \frac{1}{8})$  and  $(x_1, x_1, x_1)$ . Since the basis set includes one s orbital, three p orbitals and one orbital zeta function. the Hamiltonian matrix between a pair neighbors is in the dimension of  $5 \times 5$ . Significant differences in the magnitude of Hamiltonian matrix elements between the diamond structure and each clathrate can be observed. However, those for both clathrates are more or less on the same size, which is consistent with the trend in the band gaps.

		s(2)	s*(2)	p <sub>x</sub> (2)	p <sub>y</sub> (2)	p <sub>z</sub> (2)
	Diamond	-16.34	20.01	0	0	0
s(1)	Ge <sub>46</sub>	-3.76	3.84	-3.11	0	4.43
	Ge <sub>34</sub>	-3.99	3.90	3.24	3.24	3.24
	Diamond		-13.14	0	0	0
s*(1)	Ge <sub>46</sub>		-0.26	0.31	0	0.05
	Ge <sub>34</sub>		-0.56	-0.05	-0.05	-0.05
	Diamond			1.27	0	0
p <sub>x</sub> (1)	Ge <sub>46</sub>			-0.14	0	-2.59
	Ge <sub>34</sub>			-0.26	1.96	1.96
	Diamond				1.27	0
p <sub>y</sub> (1)	Ge <sub>46</sub>				-2.09	0
	Ge <sub>34</sub>				-0.26	1.96
	Diamond					1.27
p <sub>z</sub> (1)	Ge <sub>46</sub>					1.79
	Ge <sub>34</sub>					-0.26

TABLE 5.6: Hamiltonian matrix elements  $H_{m,n}(\mathbf{K})$  between one pair neighbors at  $\Gamma$  for the three structures. A basis set consists of one s orbital, three p orbitals and one zeta function is used. For the diamond structure,  $m$  represents orbitals of the atom at  $(0,0,0)$  and  $n$  denotes orbitals of the atom at  $(\frac{1}{4}, \frac{1}{4}, \frac{1}{4})$ . For Ge<sub>46</sub>,  $m$  and  $n$  label orbitals of the atoms at  $(\frac{1}{4}, \frac{1}{2}, 0)$  and  $(-y, z, 0)$ , respectively. For Ge<sub>34</sub>,  $m$  and  $n$  represent orbitals of the atoms at  $(\frac{1}{8}, \frac{1}{8}, \frac{1}{8})$  and  $(x_1, x_1, x_1)$ . Numbers 1 and 2 in brackets represent atoms involved in the Hamiltonian matrix, e.g., the atoms at  $(\frac{1}{8}, \frac{1}{8}, \frac{1}{8})$  and  $(x_1, x_1, x_1)$ .

### 5.3 Structural Properties and Energetics of Doped and Filled Clathrates

As mentioned in Sec.5.2, for type-I clathrates there are two types of voids. By filling them, one obtains filled clathrates. The most common fillers are alkali- and alkali-earth metals and lanthanum group elements. The fully filling results in two fillers at 2a  $(0, 0, 0)$  and six filler at 6c  $(0.25, 0.5, 0)$  sites, respectively. For optimizing thermoelectric properties, dopants are introduced to change charge carrier density, which can be transition metals, noble metals, zinc group and group-III elements. When M are transition metals and

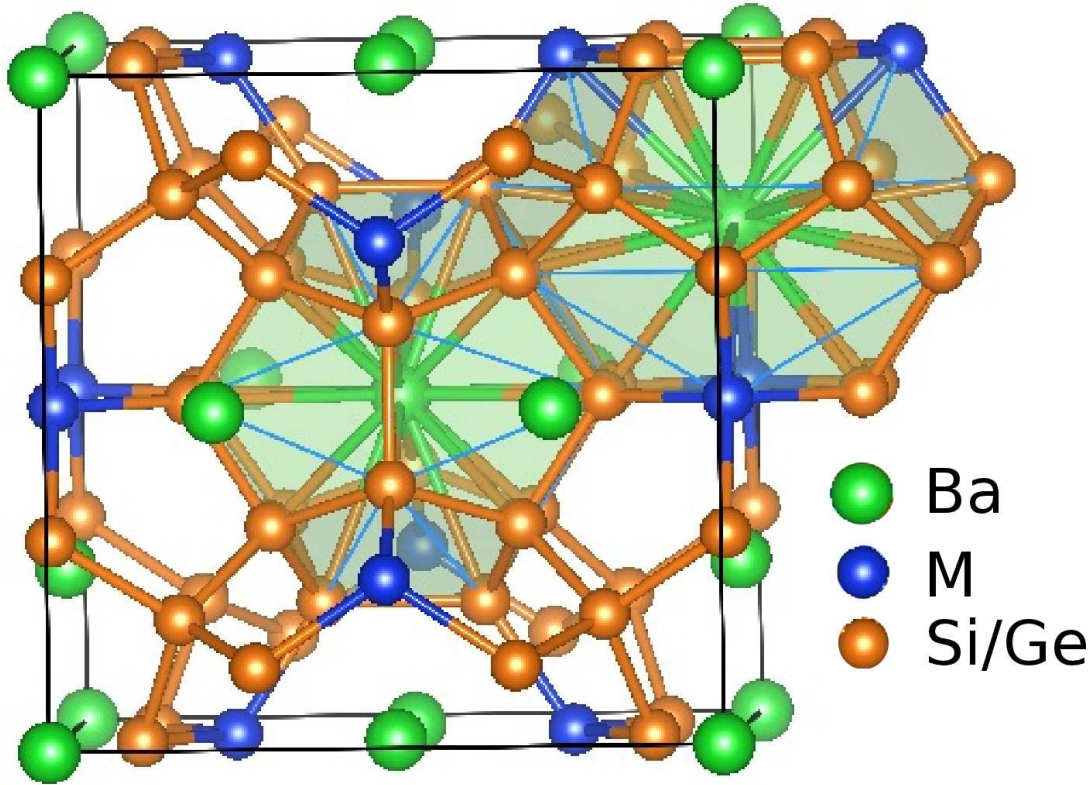


FIGURE 5.5: (a) Structure of doped Ba-filled type-I clathrate  $\text{Ba}_8\text{M}_x\text{Si}(\text{Ge})_{46-x}$  ( $x \leq 6$ ). M can be transition metals, noble metals, zinc group and group-III elements. When M are transition metals and noble metals,  $x$  is not larger than 6 and M substitutes Si(Ge) atoms on 6d sites. When M are zinc group and group-III elements,  $x$  can be larger than 6 and thus besides 6d sites, M substitute Si(Ge) atoms at other sites such as 16i and 24k sites. The two cages show schematically the environments of two different types of Ba, i.e., 2a (0,0,0) and 6c (0.25,0.5,0) sites.

noble metals,  $x$  is no more than 6 and M most likely substitute Si(Ge) atoms on 6d sites. When M are zinc group and group-III elements,  $x$  can be larger 6 and thus besides 6d sites, M substitute Si(Ge) atoms at other sites such as 16i and 24k sites. Fig.5.5 show schematically the structure of  $\text{Ba}_8\text{M}_x\text{Si}(\text{Ge})_{46-x}$  ( $x \leq 6$ ).

As discussed in Sec.3.3, because of the experimental preparation at higher temperatures dopants are more or less statistically distributed at the target doping sites, whereas they have to be placed on specific lattice sites in the theoretical modeling. The ordering may break crystal symmetry and lead to several possible structural configurations. For instance, there is only one configuration for  $\text{Ba}_8\text{Ag}_5\text{Ge}_{41}$  and  $\text{Ba}_8\text{Ag}_6\text{Ge}_{40}$  if all Ag atoms are located at 6d sites. However, there are two inequivalent structural configurations for  $\text{Ba}_8\text{Ag}_4\text{Ge}_{42}$ . In a case such as  $\text{Ba}_8\text{Ag}_4\text{Ge}_{42}$ , structural relaxations were performed for all the possible structural configurations. Formation energies were derived by using the lowest energy among them. Electronic structure calculations for the system were carried

out by taking the structural configuration with the lowest total energy. In general, in addition to the point-group symmetry, even the shape of the cubic unit cell including the length of the axes may change whereby the deviations from the ideal structure are, however, rather small. In all the present calculations, a cubic structure was assumed in accordance with experiment.

DFT calculations were performed by applying VASP. The pseudopotentials were constructed according to the projector augmented wave (PAW) method. Unless stated otherwise, for Ge-based clathrates, e.g.,  $\text{Ba}_8\text{M}_x\text{Ge}_{46-x}$ , the exchange-correlation functional was parametrized in terms of LDA according to Ceperley and Alder (CA), whereas for Si-based clathrates, e.g.,  $\text{Ba}_8\text{M}_x\text{Si}_{46-x}$ , it is approximated within GGA using the parametrization of Perdew, Burke, and Ernzerhof (PBE). The valence state configuration for the construction of the pseudopotentials included the 5s, 5p and 6s states for Ba, the 4s and 3d states for Ni, Cu and Zn, the 5s and 4d states for Pd and Ag, the 6s and 5d states for Au, 3s and 3p states for Si, and the 3d, 4s and 4p states for Ge. For structural relaxations and total energy calculations, a  $5 \times 5 \times 5$   $\mathbf{k}$  point grid according to Monkhorst and Pack grid was used to sample the Brillouin zone. For subsequent DOS calculations, a  $\mathbf{k}$ -mesh of  $11 \times 11 \times 11$  was used. For the purpose of TE calculations, a  $\mathbf{k}$ -mesh of  $25 \times 25 \times 25$  was used.

Property	a	Ge2 in 16i (x,x,x)	Ge3 in 24k (x,y,z)
$\text{Ge}_{46}$	10.51	0.184	0.117, 0.308
$\text{Ba}_8\text{Ge}_{46}$	10.90	0.185	0.118, 0.307
$\text{Ba}_8\text{Ag}_1\text{Ge}_{45}$	10.81	0.184	0.117, 0.306
$\text{Ba}_8\text{Ag}_2\text{Ge}_{44}$	10.78	0.185	0.121, 0.312
$\text{Ba}_8\text{Ag}_3\text{Ge}_{43}$	10.75	0.182	0.126, 0.302
$\text{Ba}_8\text{Ag}_4\text{Ge}_{42}$	10.72	0.183	0.123, 0.305
$\text{Ba}_8\text{Ag}_5\text{Ge}_{41}$	10.71 (10.84 <sup>a</sup> )	0.183 (0.182 <sup>a</sup> )	0.116, 0.312 (0.116, 0.307 <sup>a</sup> )
$\text{Ba}_8\text{Ag}_6\text{Ge}_{40}$	10.72	0.183	0.116, 0.308

<sup>a</sup>Experiment (Ref. [121])

TABLE 5.7: Lattice constant a (in Å) and structural parameters for  $\text{Ba}_8\text{Ag}_x\text{Ge}_{46-x}$  ( $x = 0 - 6$ ).

Tables 5.7 and 5.8 show lattice parameters for  $\text{Ba}_8\text{Ag}_x\text{Ge}_{46-x}$ ,  $\text{Ba}_8\text{Au}_x\text{Si}_{46-x}$  and  $\text{Ba}_8\text{Cu}_x\text{Si}_{46-x}$ , of which their TE properties will be discussed below. For each system, one finds that the DFT derived lattice constants are larger by about 1% or smaller by the same amount than available experimental data depending on the approximation for the exchange correlation functional. When comparing structural parameters to corresponding experiment results, usually rather good agreement can be found.

Property	a	Si2 in 16i (x,x,x)	Si3 in 24k (x,y,z)
Si <sub>46</sub>	10.25	0.181	0.116, 0.304
Ba <sub>8</sub> Si <sub>46</sub>	10.38	0.182	0.118, 0.303
Ba <sub>8</sub> Au <sub>1</sub> Si <sub>45</sub>	10.42	0.183	0.119, 0.306
Ba <sub>8</sub> Au <sub>2</sub> Si <sub>44</sub>	10.44	0.185	0.119, 0.307
Ba <sub>8</sub> Au <sub>3</sub> Si <sub>43</sub>	10.47	0.183	0.119, 0.303
Ba <sub>8</sub> Au <sub>4</sub> Si <sub>42</sub>	10.48 (10.40 <sup>a</sup> )	0.183 (0.183 <sup>a</sup> )	0.118, 0.304 (0.120, 0.308 <sup>a</sup> )
Ba <sub>8</sub> Au <sub>5</sub> Si <sub>41</sub>	10.49 (10.41 <sup>a</sup> )	0.183 (0.183 <sup>a</sup> )	0.119, 0.302 (0.116, 0.305 <sup>a</sup> )
Ba <sub>8</sub> Au <sub>6</sub> Si <sub>40</sub>	10.52 (10.42 <sup>a</sup> )	0.184 (0.185 <sup>a</sup> )	0.117, 0.304 (0.117, 0.306 <sup>a</sup> )
Ba <sub>8</sub> Cu <sub>1</sub> Si <sub>45</sub>	10.41	0.185	0.122, 0.309
Ba <sub>8</sub> Cu <sub>2</sub> Si <sub>44</sub>	10.41	0.185	0.117, 0.308
Ba <sub>8</sub> Cu <sub>3</sub> Si <sub>43</sub>	10.42	0.184	0.123, 0.309
Ba <sub>8</sub> Cu <sub>4</sub> Si <sub>42</sub>	10.43	0.184	0.120, 0.309
Ba <sub>8</sub> Cu <sub>5</sub> Si <sub>41</sub>	10.44 (10.33 <sup>b</sup> )	0.184 (0.185 <sup>b</sup> )	0.122, 0.308 (0.120, 0.309 <sup>b</sup> )
Ba <sub>8</sub> Cu <sub>6</sub> Si <sub>40</sub>	10.45	0.184	0.119, 0.311

<sup>a</sup>Experiment (Ref. [128]), <sup>b</sup>Experiment (Ref. [123])

TABLE 5.8: Lattice constant a (in Å) and structural parameters for Ba<sub>8</sub>Au<sub>x</sub>Si<sub>46-x</sub> and Ba<sub>8</sub>Cu<sub>x</sub>Si<sub>46-x</sub> ( $x = 0 - 6$ ).

The formation enthalpy  $\Delta H$  for Ba<sub>8</sub>M<sub>x</sub>Si(Ge)<sub>46-x</sub> as depicted in Figs. 5.6 and 5.7), are defined as:

$$\Delta H(Ba_8M_xSi(Ge)_{46-x}) = [E(Ba_8M_xSi(Ge)_{46-x}) - 8E_{bulk}(Ba) - xE_{bulk}(M) - (46-x)E_{bulk}(Ge)]/54 \quad (5.2)$$

where  $E(Ba_8M_xSi(Ge)_{46-x})$  represents the total energy of Ba<sub>8</sub>M<sub>x</sub>Si(Ge)<sub>46-x</sub>, and  $E_{bulk}$  denote total energies of the elemental bulks.

The enthalpy costs of forming the cage structure of Si<sub>46</sub> and Ge<sub>46</sub> are positive, indicating they are less stable than the diamond ground state structure. Filling Ba atoms into the voids of Si<sub>46</sub> or Ge<sub>46</sub> results in a significant gain in binding energy, which is about -17 kJ/mol for Si<sub>46</sub> or -20 kJ/mol for Ge<sub>46</sub>. The incorporation of M into the Ge(Si)-framework stabilizes the clathrate-I compound as evidenced by a decrease of the enthalpy of formation ( $\Delta H$ ). The stabilization as induced by incorporation of M into Ba<sub>8</sub>Si(Ge)<sub>46</sub> is interesting. For Ba<sub>8</sub>M<sub>x</sub>Ge<sub>46-x</sub> the enthalpies always decrease as  $x$  varies from 0 to 6 when Au and Pd serve as dopants. However, the decrease in the enthalpy end at  $x = 5$  for Ag and 8 for Zn, respectively. These first-principles findings are in line with the solubility limits estimated by the experiment (see Table 5.9), except for Pd.

Similar phenomena can be observed for Ba<sub>8</sub>M<sub>x</sub>Si<sub>46-x</sub>, for which calculations have been

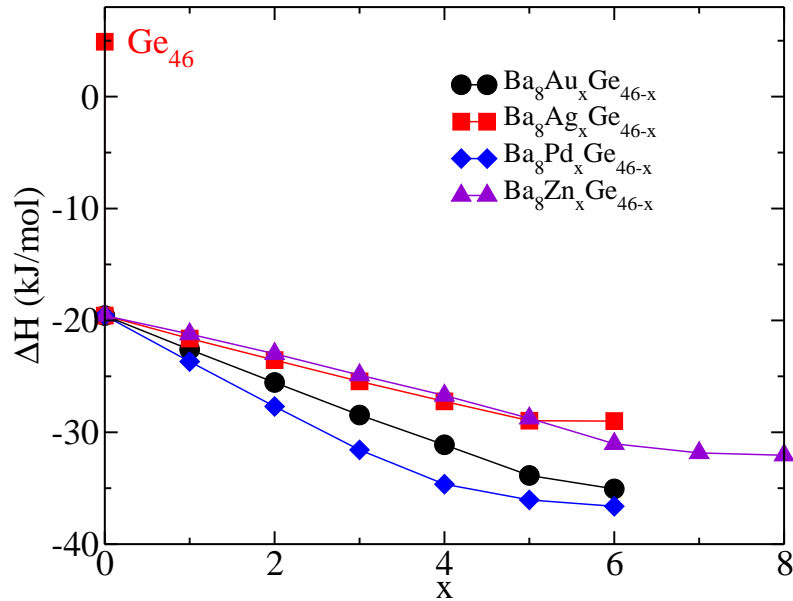


FIGURE 5.6: Calculated formation energies  $\Delta H$   $\text{Ba}_8\text{M}_x\text{Ge}_{46-x}$  ( $\text{M} = \text{Au}, \text{Ag}, \text{Pd}$  and  $\text{Zn}$ ) as a function of doping  $x$ . Also shown is the result for the unfilled and undoped cage solid  $\text{Ge}_{46}$ . Calculations were done using VASP within LDA.

done using both LDA and GGA. Like in  $\text{Ba}_8\text{M}_x\text{Ge}_{46-x}$ , Au has a much stronger stabilization effect than Cu and Ag. For instance, increasing the Cu content from  $x = 1$  to 5 (i.e. the minimum of  $\Delta H$ ) gives a rather small stabilization of -1.6 kJ/mol, whereas for the Au-based clathrate the gain in bonding (taking now  $\text{Ba}_8\text{Au}_6\text{Si}_{40}$  as the minimum) is significantly larger, namely -13.6 kJ/mol. For the Au-doped compounds the enthalpy of formation decreases (i.e. bonding is enhanced) with increasing Au content, which is very similar to the results for  $\text{Ba}_8\text{Ag}_x\text{Ge}_{46-x}$ . The trend for the Cu-doped compounds is quite different, because  $\Delta H$  remains rather constant with increasing  $x$ . A more careful examination reveals that  $\Delta H$  slightly increases for  $x > 5$  implying that a doping level exceeding 5 is unfavorable. The enthalpy of formation for  $\text{Ba}_8\text{Ni}_x\text{Si}_{46-x}$  also decreases from  $x = 0$  to 4 Ni. Further substitution of Ni up to  $\text{Ba}_8\text{Ni}_6\text{Si}_{40}$  does not further decrease  $\Delta H$ . This is consistent with the experimental fact that no samples with  $x$  larger 4 and 5 for Ni and Cu, respectively, can be synthesized, whereas the limiting doping of Au is 6 (see Table 5.9).

## 5.4 Gap and Doping

As elaborated previously, placing Fermi energy close to a gap in the electronic structure is an important concept for obtained large Seebeck coefficients. How to achieve this goal with a suitable chemical doping is the subject of this Section. For this purpose, a systematic DFT study of the electronic structure of  $\text{Ba}_8\text{M}_x\text{Ge}_{46-x}$  and  $\text{Ba}_8\text{M}_x\text{Si}_{46-x}$

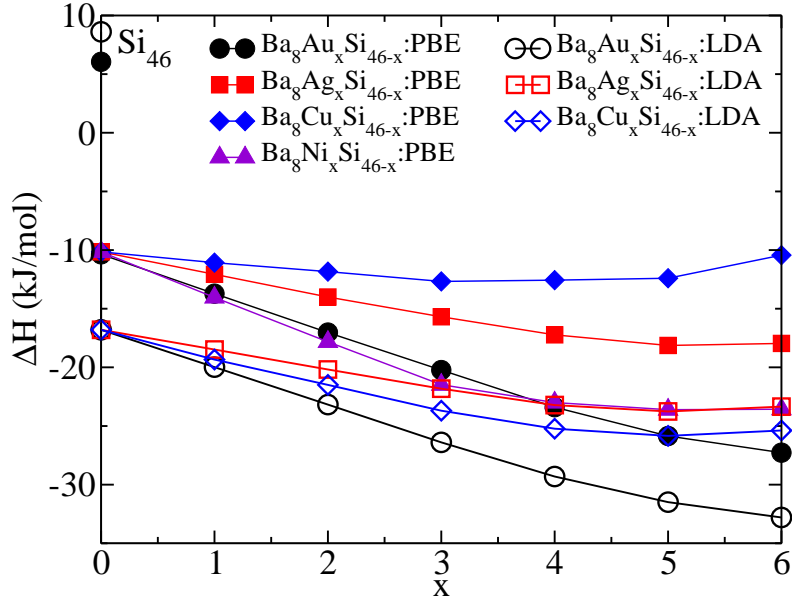


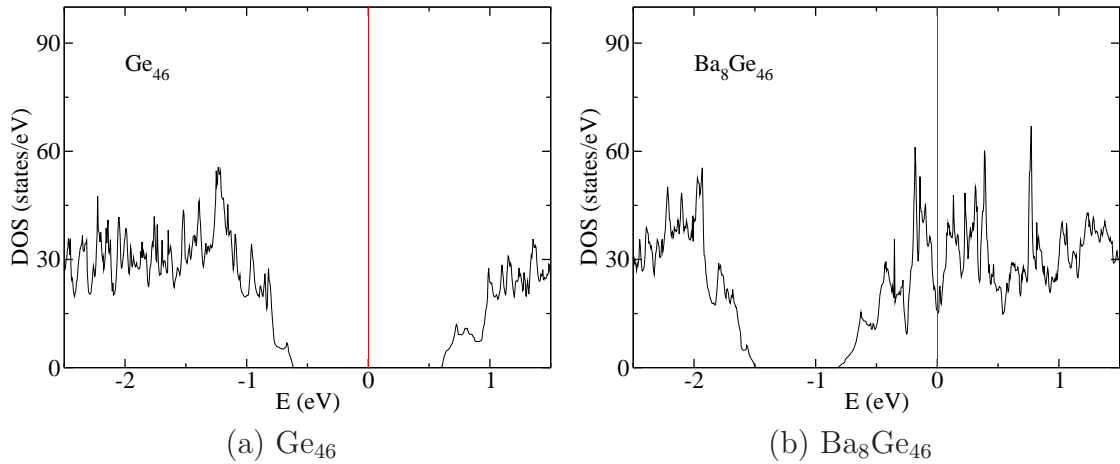
FIGURE 5.7: DFT derived formation energies  $\Delta H$   $\text{Ba}_8\text{M}_x\text{Si}_{46-x}$  ( $M = \text{Au}, \text{Ag}, \text{Cu},$  and  $\text{Ni}$ ) as a function of  $x$ . The figure also shows the result for the unfilled cage solid  $\text{Si}_{46}$ . Both GGA and LDA results are given. As expected, LDA predicts stronger stabilization than GGA.

systems		
dopants	$\text{Ba}_8\text{M}_x\text{Si}_{46-x}$	$\text{Ba}_8\text{M}_x\text{Ge}_{46-x}$
Au	5.9	6.0
Ag	5.4	5.3
Cu	4.9	6.0
Pd		3.8
Ni	3.8	
Zn	8.0	8.0

TABLE 5.9: Solubility limits of doping of  $\text{Ba}_8\text{M}_x\text{Si}(\text{Ge})_{46-x}$ .

clathrates is presented.  $M$  stands for late transition and noble metal elements such as  $\text{Ni}$ ,  $\text{Pd}$ ,  $\text{Pt}$ ,  $\text{Cu}$ ,  $\text{Ag}$ ,  $\text{Au}$ ,  $\text{Zn}$ .

For all the compounds, the calculated DOS of  $\text{Ba}_8\text{M}_x\text{Ge}_{46-x}$  ( $M = \text{Pd}, \text{Ag}, \text{Zn}$ ) in Figs.5.8 - 5.11 show a gap or gap-like features (i.e. very small value of DOS) in a certain energy region depending on the composition and number of valence electrons. Starting with the unfilled clathrates  $\text{Si}_{46}$  and  $\text{Ge}_{46}$  filling Ba into them conserves the gap (with a reduced size of 0.8 eV for  $\text{Ba}_8\text{Si}_{46}$  and 0.7 eV for  $\text{Ba}_8\text{Ge}_{46}$ ), but now Fermi energy  $E_F$  falls in the conduction band region, making the material metallic. In all cases, the gap size shrinks

FIGURE 5.8: VASP derived total DOS of  $\text{Ge}_{46}$  and  $\text{Ba}_8\text{Ge}_{46}$ .

significantly even more upon doping of M and continues to shrink as the doping increases, with the exception of  $\text{Ba}_8\text{M}_6\text{Ge}_{40}$  which is distinct from the others with smaller dopings  $x$  because of its high symmetry. As a general trend the gap sizes of  $\text{Ba}_8\text{M}_x\text{Ge}_{46-x}$  for a fixed doping  $x$  increase when M changes from Pd through Ag to Zn which can be roughly correlated to the atomic size.

For  $\text{Ba}_8\text{Pd}_x\text{Ge}_{46-x}$ , in combination with the reduced size of the gap new electronic states appear in the gap, which gradually merge into the valence bands as the doping of Pd grows. These in-gap states are missing for  $\text{Ba}_8\text{Ag}_x\text{Ge}_{46-x}$  and  $\text{Ba}_8\text{Zn}_x\text{Ge}_{46-x}$ . This is a consequence of the positions of the d-levels which is highest for Pd when compared to Ag and Zn. From Figs.5.9 and 5.10 it can be seen, that the d-states of Ag are lower in energy as compared to Pd in  $\text{Ba}_8\text{Pd}_x\text{Ge}_{46-x}$  for  $x \geq 4$ . There, part of the contributions of Pd-5d states to the DOS are visible. The differences in the gap sizes and in-gap states between different M elements can therefore be attributed to the relative positions of the d level, which is correlated to the number of valence electrons of the M element.

An important feature of the electronic structure is the position of the Fermi level relative to the gap. In general, the Fermi level moves from the conduction bands across the gap down to the valence bands as M increases, because replacement of Ge or Si by M reduces the total number of valence electrons. For  $\text{Ba}_8\text{Pd}_x\text{Ge}_{46-x}$ , the Fermi level falls into the gap for  $x = 4$ . While for  $\text{Ba}_8\text{Ag}_x\text{Ge}_{46-x}$   $x$  is in between 5 and 6 since the Fermi levels of  $\text{Ba}_8\text{Ag}_5\text{Ge}_{41}$  and  $\text{Ba}_8\text{Ag}_6\text{Ge}_{40}$  lie below above and below the gap, respectively. In the case of  $\text{Ba}_8\text{Zn}_x\text{Ge}_{46-x}$ , 8 Zn atoms are required to shift the Fermi level into the middle of the gap. For this observation, a simple but general electron counting rule will be presented later on.

Electronic DOS for  $\text{Ba}_8\text{M}_x\text{Si}_{46-x}$  ( $M = \text{Au}, \text{Cu}, \text{Ni}$ ) are shown in Figs. 5.12 and 5.13, which exhibit similar doping effects as observed for the Ge-based clathrates doped by the

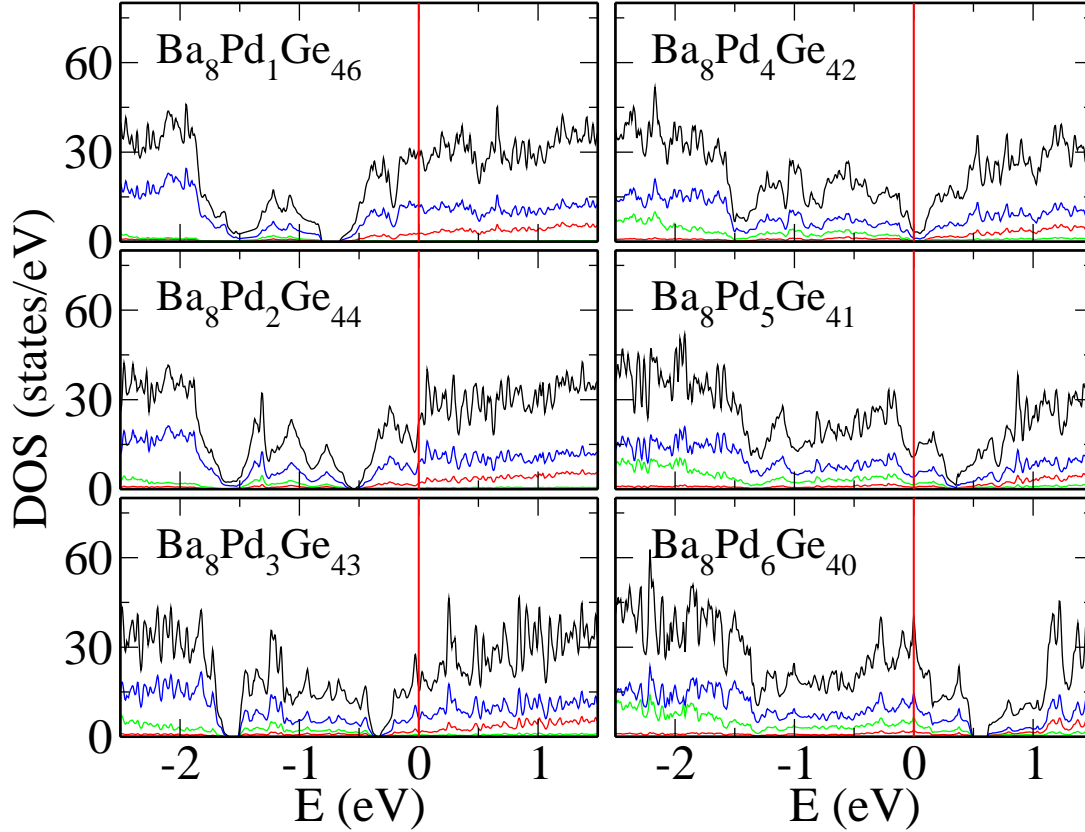


FIGURE 5.9: VASP derived total and partial DOS of  $\text{Ba}_8\text{Pd}_x\text{Ge}_{46-x}$  ( $x = 1 - 6$ ). Fermi energy is at  $E = 0$ . Black lines denote the total DOS. Red, green and blue lines represent Ba-, Pd- and Ge-projected DOS.

same group elements. The exception is  $\text{Ba}_8\text{Ni}_x\text{Si}_{46-x}$ , because the gap clearly present in  $\text{Ba}_8\text{Si}_{46}$  shrinks more and more by substituting Si by Ni. For  $\text{Ba}_8\text{Ni}_1\text{Si}_{45}$  two separated peaks, mainly of Ni-character, appear in the gap. The one with lower energy is localized and dominated by Ni d-states, whereas the second one with higher energy is broader. On one hand, as the doping of Ni increases, the sharper peak grows and gradually mixes with framework states. On the other hand, the peak at higher energy broadens and finally for  $\text{Ba}_8\text{Ni}_4\text{Si}_{42}$  it merges with the other one, which leads to the vanishing of the gap and left a narrow valley at the Fermi level. For further substitution by Ni up to  $x = 6$  second gap, very small gap appears at 0.45 eV. In this case the second gap is located above the Fermi-level. Current electronic structures are in good agreement with previous calculations [120]. It should be noted that a satellite peak located at -0.5 eV in the DOS of  $\text{Ba}_8\text{Si}_{46}$  is preserved upon doping by Ni. The Fermi level moves through the satellite peak with increased doping, which suggests that the rigid band approximation -needed for small changes in stoichiometry- may be applicable, when the Fermi level is in the vicinity of the satellite peak. However, the Ni-doping causes considerable changes of the

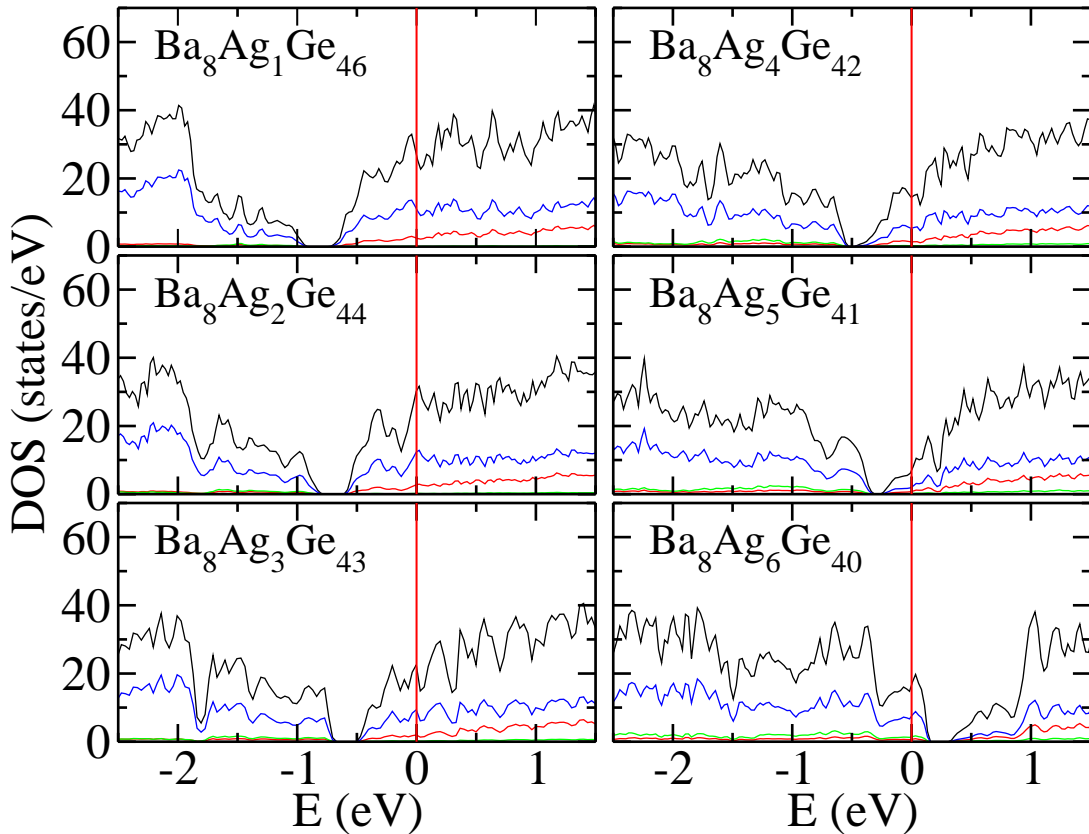


FIGURE 5.10: VASP derived total and partial DOS of  $\text{Ba}_8\text{Ag}_x\text{Ge}_{46-x}$  ( $x = 1 - 6$ ). Fermi energy is at  $E = 0$ . Black lines denote the total DOS. Red, green and blue lines represent Ba-, Ag- and Ge-projected DOS.

DOS in contrast to doping by elements with larger sizes, such as Pd, Pt, Ag, Au, which has to be considered carefully, when the rigid band approximation is applied.

All the DOS indicate that  $\text{Ba}_8\text{M}_x\text{Ge}(\text{Si})_{46-x}$  experiences a transition from a n-type semiconductor to a p-type semiconductor as  $x$  increases. Therefore, there must be a critical composition where the Fermi level falls into the gap. For estimating this critical composition  $x$  of a simple electron counting procedure is proposed and was tested to work properly: assuming that hybridized and delocalized states are present above the filled d-band of the metal and the Fermi energy is not pinned by localized states, a rigid band concept is applied. That means, that the basic features of the DOS are not too much changed upon doping and Fermi energy is shifted upwards or downwards according to the change of the number of valence electrons. It is further -safely- assumed that the transition metal elements want to have their d-band filled. On this basis the valency  $n$  of the M element is determined:  $n$  is the number of free electronic states provided by M. According to this idea, for e.g. Ni, Pd, Pt  $n$  is  $n=0$ , for Cu, Ag, Au it is  $n=1$  and for Zn it is  $n=2$ . For Co -not studied here- but of interest for doping it would be  $n=-1$ .

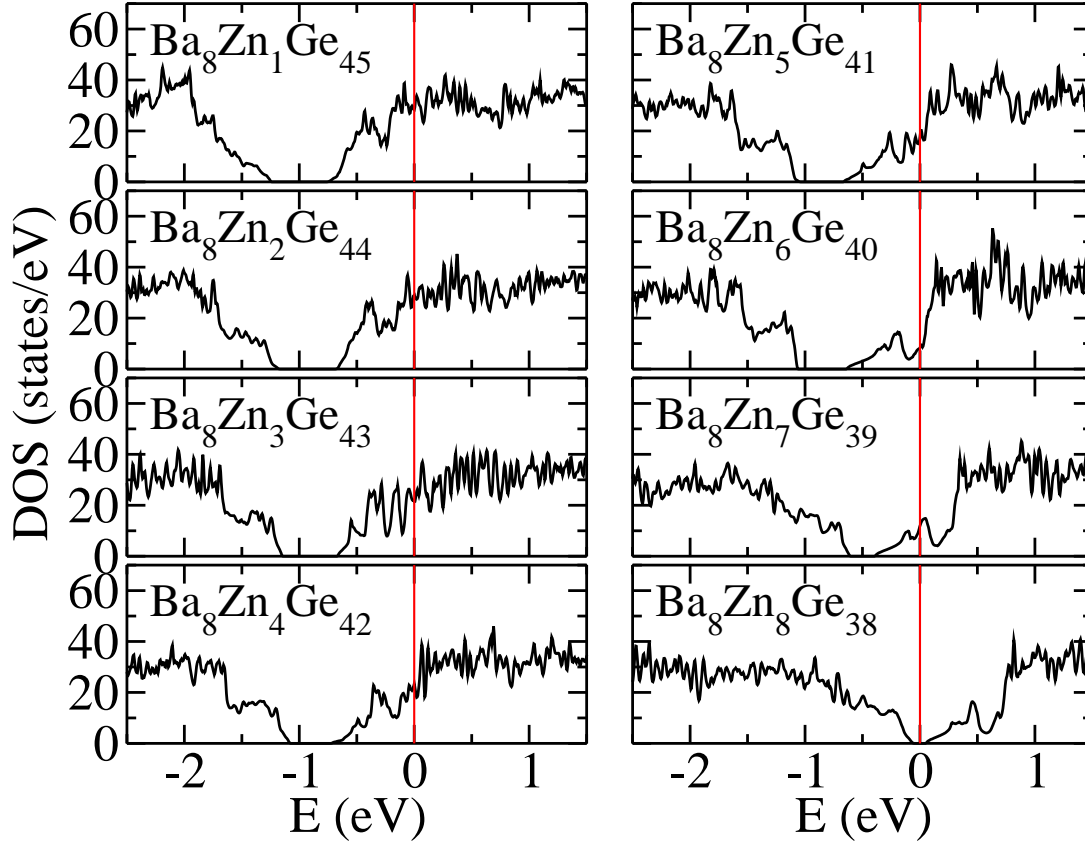


FIGURE 5.11: Total DOS of  $\text{Ba}_8\text{Zn}_x\text{Ge}_{46-x}$  ( $x = 1 - 8$ ). Fermi energy is at  $E = 0$ .

When M replaces Ge(Si) in  $\text{Ba}_8\text{M}_x\text{Ge}(\text{Si})_{46-x}$ ,  $4x$  electrons are lost but  $nx$  electrons ( $n$  is the valency of the dopant, as described) are gained, whereas  $\text{Ba}_8$  contributes 16 electrons. If these 16 electrons would be lost, then Fermi energy falls in the gap as generated by the unfilled  $\text{Ge}(\text{Si})_{46}$ . Therefore the losses upon doping must equal 16, which defines the condition for the critical doping  $x_{gap}$  (the doping, for which the Fermi energy falls into the gap), as

$$x_{gap} = \frac{16}{4 - n} \quad (5.3)$$

For  $M = \text{Cu}/\text{Ag}/\text{Au}$  (i.e. the valency  $n = 1$ ) the value of  $x_{gap} = 5.33$  is derived, which is perfectly full-filled by the above VASP calculations. For compounds with  $M = \text{Ni}/\text{Pd}$ ,  $x_{gap} = 4$  because  $n = 0$ . Although a real gap is absent at the Fermi level of  $\text{Ba}_8\text{Ni}_4\text{Si}_{42}$ , a rather narrow valley of the DOS occurs. According to the above assumption on the valency of Ni, the compound  $\text{Ba}_8\text{Ni}_6\text{Si}_{40}$  has 8 electrons less than  $\text{Ba}_8\text{Ni}_4\text{Si}_{42}$  and the Fermi level falls into energies lower than the gap. Indeed, integrating the DOS from the Fermi energy up to the gap yields exactly eight electrons. Likewise, for  $M = \text{Zn}$  one obtains  $x_{gap} = 8$  ( $n = 2$ ) and  $x_{gap} = 16$  for Ga/Al-doped compounds. Comparing with all the discussed DOS of  $\text{Ba}_8\text{M}_x\text{Ge}(\text{Si})_{46-x}$  the counting rule of Eq.(5.3) works perfectly.

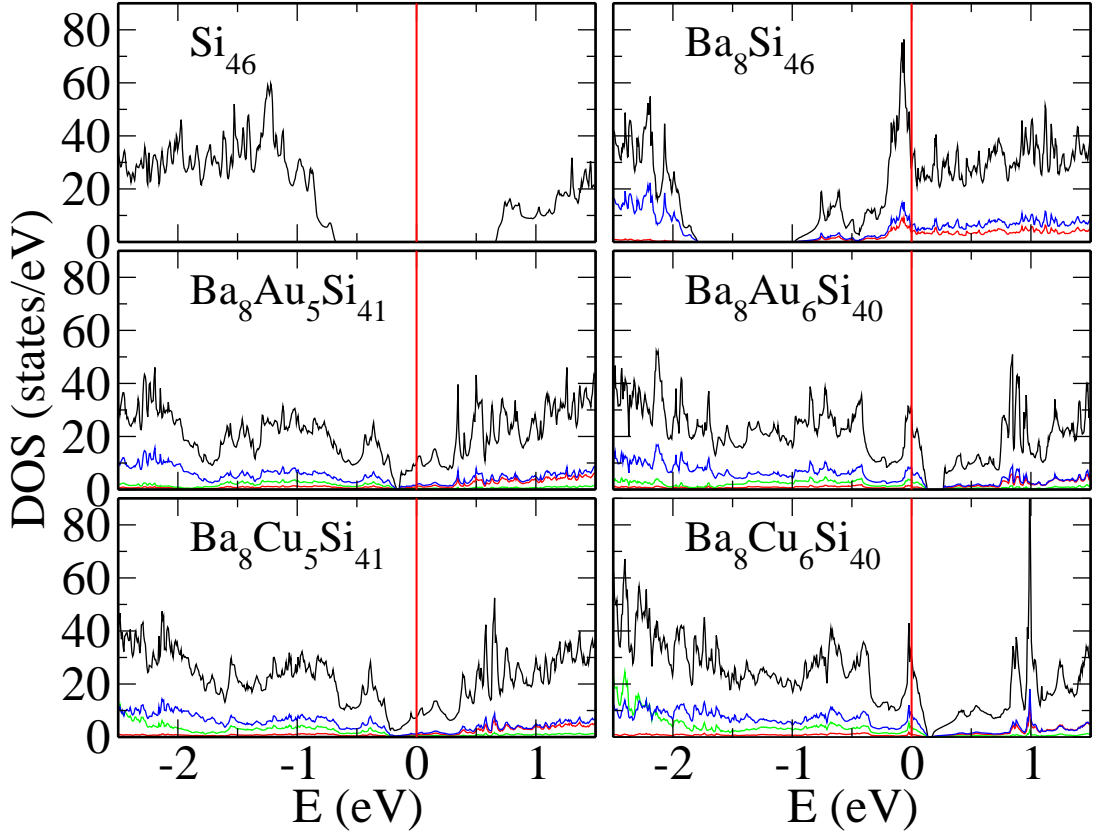


FIGURE 5.12: VASP derived total and partial DOS of  $\text{Si}_{46}$ ,  $\text{Ba}_8\text{Si}_{46}$  and  $\text{Ba}_8\text{Au}(\text{Cu})_x\text{Si}_{46-x}$  ( $x = 5$  and  $6$ ). Fermi energy is at  $E = 0$ . Black lines denote the total DOS. Red, green and blue lines represent Ba-, Ag- and Ge-projected DOS.

## 5.5 Transport Properties of $\text{Ba}_8\text{Ag}_x\text{Ge}_{46-x}$ Clathrates

This section is devoted to explore, calculate and analyse the TE properties  $\text{Ba}_8\text{Ag}_x\text{Ge}_{46-x}$  in combination with recent experimental investigations. This work was published in *Acta Materialia*, **59**, 2368 (2011) and demonstrates the usefulness of a combined experimental and theoretical DFT approach to understand materials properties. The measured temperature-dependent Seebeck coefficients  $S(T)$  for various concentrations  $x$  of  $\text{Ba}_8\text{Ag}_x\text{Ge}_{46-x-y}\square_y$  is displayed in Fig. 5.14[121]. It should be noticed, that also vacancies might play a role, as indicated by  $\square_y$  in the chemical formula. Basically, the experiments show that the Seebeck coefficient changes sign around the magical composition  $x = 5.3$ , as discussed in the previous Section. For each compound with  $x < 5.3$ , the Seebeck coefficients are negative, for which the position of the minimum shifts toward lower temperatures as  $x$  increases. At low temperatures with the exception of  $\text{Ba}_8\text{Ag}_6\text{Ge}_{40}$  and  $\text{Ba}_8\text{Ag}_{5.3}\text{Ge}_{40.7}$  the resistivity  $\rho(T)$  exhibits metallic behavior, which gradually changes

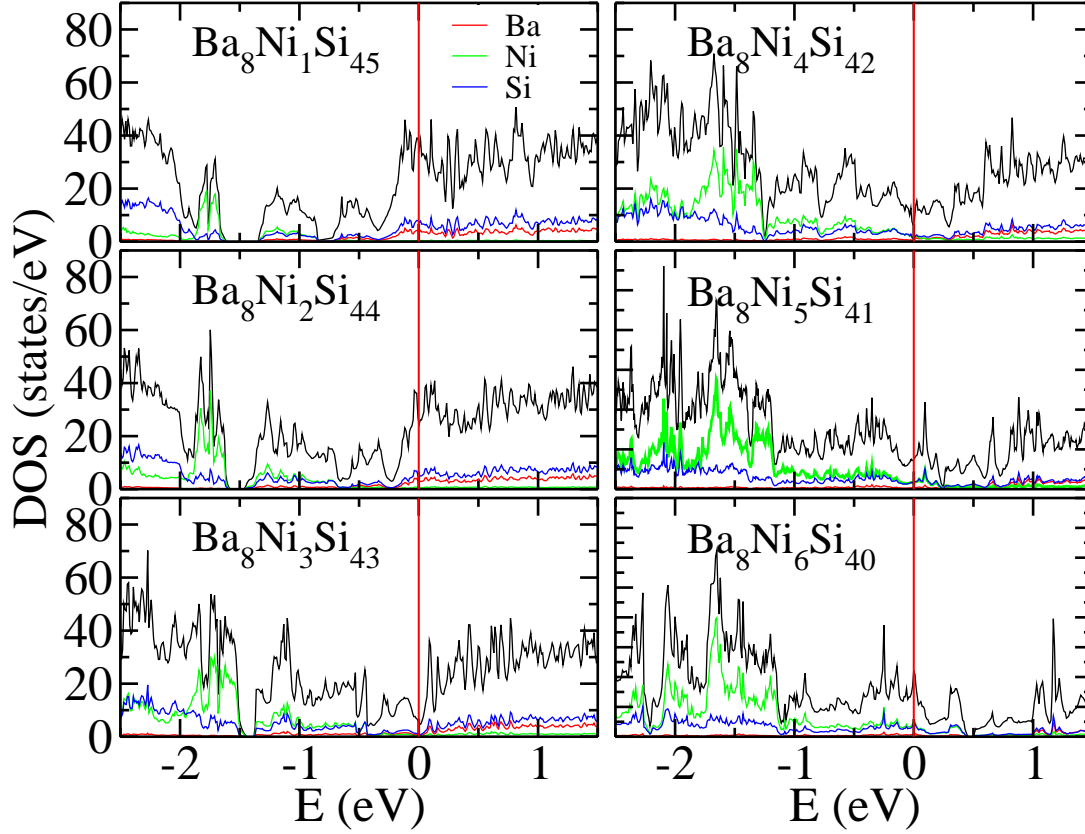


FIGURE 5.13: VASP derived total and partial DOS of  $\text{Ba}_8\text{Ni}_x\text{Si}_{46-x}$  ( $x = 1 - 6$ ). Fermi energy is at  $E = 0$ . Black lines denote the total DOS. Red, green and blue lines represent Ba-, Ag- and Ge-projected DOS.

at higher temperatures and at increased Ag content towards a more insulating character with the occurrence of a maximum. Focusing on  $\text{Ba}_8\text{Ag}_{2.1}\text{Ge}_{41.9}\square_{2.0}$ , the metallic behavior becomes evident. With increasing content of Ag the resistivity  $\rho(T)$  becomes qualitatively and quantitatively modified: (i) the overall absolute resistivity increases, (ii) is almost linear at low temperatures. and (iii) a maximum occurs at a high temperature, which becomes more pronounced and shifts towards lower temperature for increasing Ag content.

### 5.5.1 Computational Details

Electronic transport properties such as electrical resistivity and Seebeck coefficients of  $\text{Ba}_8\text{Ag}_5\text{Ge}_{41}$  and  $\text{Ba}_8\text{Ag}_6\text{Ge}_{40}$  are studied within the Boltzmann transport theory Eqs.(3.16) and (3.20) as implemented in V2Boltz. According to experiment the type-I clathrates -even when substitutions were made- have cubic symmetry with space group  $\text{Pm}\bar{3}\text{n}$ . This is -in principal- not the case for DFT calculations, when all structural degrees of freedom

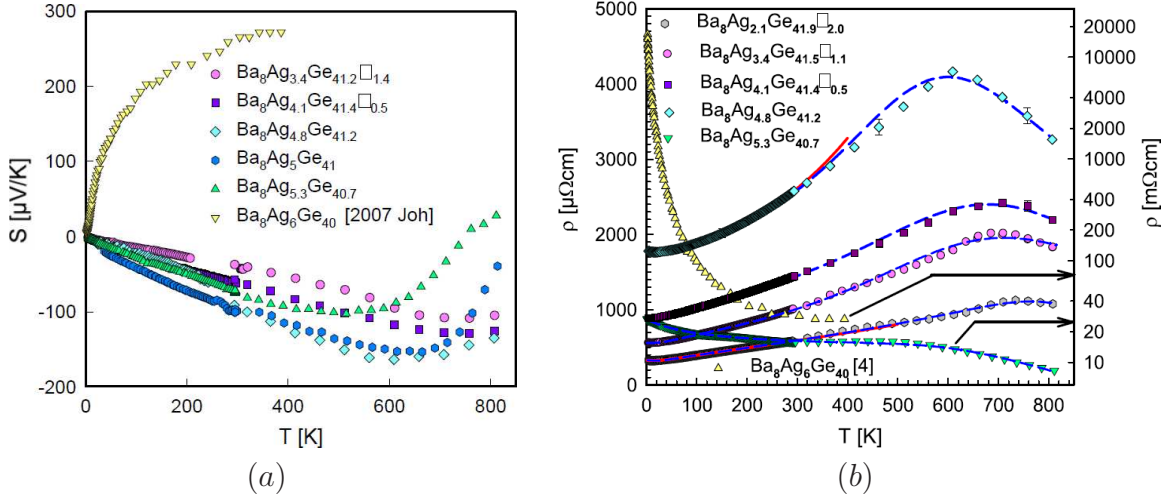


FIGURE 5.14: Measured temperature-dependent (a) Seebeck coefficients and (b) resistivities of  $\text{Ba}_8\text{Ag}_x\text{Ge}_{46-x-y}\square_y$ .  $\square$  represents a vacancy (Ref. [121]). Resistivity of  $\text{Ba}_8\text{Ag}_5\text{Ge}_{42}$  has almost the same curve as  $\text{Ba}_8\text{Ag}_{4.8}\text{Ge}_{41.2}$  (not shown by experimentalists). Data for  $\text{Ba}_8\text{Ag}_{5.3}\text{Ge}_{40.7}$  and  $\text{Ba}_8\text{Ag}_6\text{Ge}_{40}$  refer to the right axis.

are relaxed. Because the experimental samples are synthesized at higher temperature it seems plausible that some kind of random distribution of defects takes place and the samples maintain the full symmetry of the perfect, undoped composition. Thus, to be consistent with experiment the symmetry of  $\text{Pm}\bar{3}\text{n}$  is enforced on the coefficients of the transport tensors using Eq.(3.48) for symmetrization. Because of cubic symmetry, the symmetrized tensors are diagonal and all elements are equal,

$$\bar{T}_{x,x} = \bar{T}_{y,y} = \bar{T}_{z,z}. \quad (5.4)$$

,  $\bar{T}$  is then described as isotropic.

For compounds such as  $\text{Ba}_8\text{Ag}_x\text{Ge}_{46-x-y}\square_y$  ( $\square$  represents vacancy) the rigid band approximation is applied to adjust  $E_F$  for the correct number of valence electrons by taking  $\text{Ba}_8\text{Ag}_5\text{Ge}_{41}$  as reference when  $x$  should be very close to 5. The chemical potential  $\mu$  (i.e. temperature dependent Fermi energy) is derived by Eq.(3.49). The change in valence electrons as compared to the reference compound is derived within the rigid band model counting two valence electrons per Ba atom, one per Ag and four for each Ge. When taking  $\text{Ba}_8\text{Ag}_5\text{Ge}_{41}$  as the reference compound,  $\Delta n = -0.60, -0.63, -0.66, -0.72$  and  $-0.76$  corresponds to  $\text{Ba}_8\text{Ag}_{5.20}\text{Ge}_{40.80}$ ,  $\text{Ba}_8\text{Ag}_{5.21}\text{Ge}_{40.79}$ ,  $\text{Ba}_8\text{Ag}_{5.22}\text{Ge}_{40.78}$ ,  $\text{Ba}_8\text{Ag}_{5.24}\text{Ge}_{40.76}$  and  $\text{Ba}_8\text{Ag}_{5.26}\text{Ge}_{40.74}$ , respectively. However, one should be aware, that there is some experimental uncertainties for determining the correct composition, which is reflected in some uncertainty of the number of valence electrons, and hence the determination of the Fermi energy. For example, if the Ge composition has an uncertainty of  $\pm 0.1$  atoms (which

is within the experimental error bar), this would amount to  $\pm 0.4$  for the uncertainty in the number of valence electrons. Therefore, theory should always scan a certain range of number of electrons for a conclusive comparison with experiment.

### 5.5.2 Seebeck Coefficient

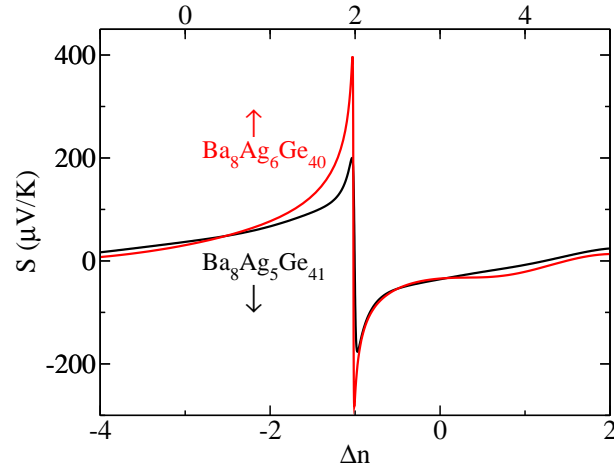


FIGURE 5.15: DFT derived Seebeck coefficient at 300 K for  $\text{Ba}_8\text{Ag}_5\text{Ge}_{41}$  and  $\text{Ba}_8\text{Ag}_6\text{Ge}_{40}$  as a function of electron doping  $\Delta n$ . A negative value corresponds to hole doping.

Figure 5.15 depicts the calculated Seebeck coefficients at 300 K vs. chemical doping for  $\text{Ba}_8\text{Ag}_5\text{Ge}_{41}$  and  $\text{Ba}_8\text{Ag}_6\text{Ge}_{40}$ . As the figure demonstrates, the rigid band approximation works rather well because the shapes of the curves agree very well with each other except for the absolute values nearby the gap where the Seebeck coefficient changes sign and fluctuates strongly. It should be noted, however, that the shift in  $E_F$  to accommodate two extra electrons for  $\text{Ba}_8\text{Ag}_6\text{Ge}_{40}$  is larger than for  $\text{Ba}_8\text{Ag}_5\text{Ge}_{41}$ , which has one more electron when compared to  $\text{Ge}_{46}$ . For  $\text{Ba}_8\text{Ag}_5\text{Ge}_{41}$  the crystal symmetry is reduced to such an extent that the Seebeck tensor has different components, if no symmetrization is done. Consequently, Fig. 5.15 shows the result after symmetrization, when the Seebeck tensor became diagonal.

Figure 5.16 depicts the DFT derived temperature dependent Seebeck coefficients for  $\text{Ba}_8\text{Ag}_x\text{Ge}_{46-x}$ , which are very sensitive to doping. Apparently,  $S(T)$  changes sign when the Ag concentration crosses the critical as expressed by the composition  $\text{Ba}_8\text{Ag}_{5.33}\text{Ge}_{40.67}$ . The DFT results for  $S(T)$  resemble the experimental trend rather well and for  $\text{Ba}_8\text{Ag}_5\text{Ge}_{41}$  even its magnitude compares favorably to the experiment (see Fig. 5.14) and the position of the minimum shifts toward lower temperature as  $x$  increases.

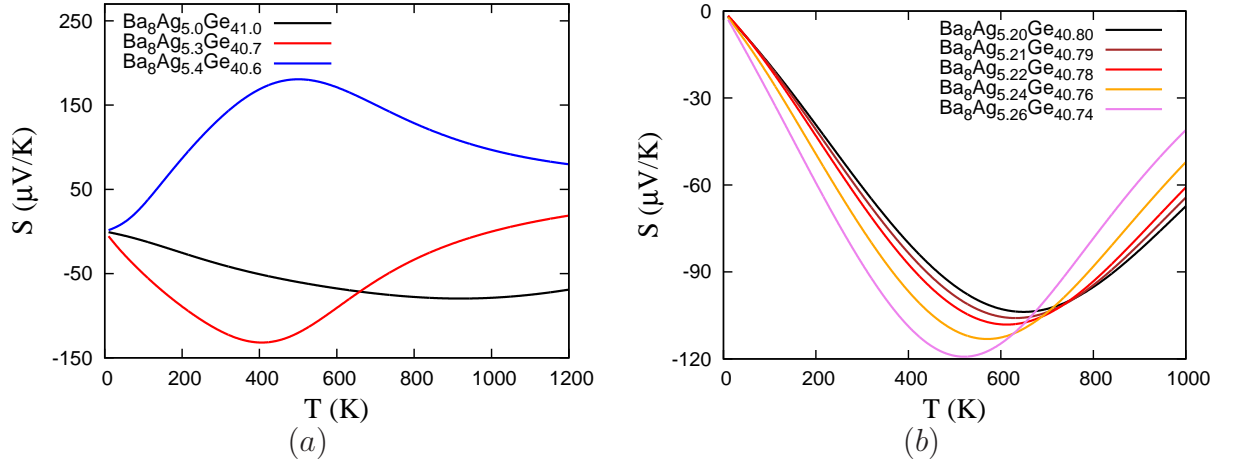


FIGURE 5.16: DFT derived temperature dependent Seebeck coefficient for  $\text{Ba}_8\text{Ag}_x\text{Ge}_{46-x}$  (a) with  $x = 5.0 - 5.4$ . (b) A finer scan in a narrower range of  $x = 5.20 - 5.26$ . Calculations were carried out within the rigid band approximation by taking  $\text{Ba}_8\text{Ag}_5\text{Ge}_{41}$  as reference.

The Seebeck coefficient for  $\text{Ba}_8\text{Ag}_x\text{Ge}_{46-x}$  at sufficiently low temperatures can be understood by the simplified Mott's relation according to Eq. (B.15) in which the sign and magnitude of the Seebeck coefficient is determined by the energy derivative of the DOS at the Fermi energy, which results in an opposite sign of Seebeck coefficient and slope of the DOS at  $E_F$ . One can also learn that a small value of the DOS together with a large slope may give rise to a large Seebeck coefficient, and for that purpose Fermi energy should be as close as possible to the gap. As temperature increases, the Fermi energy moves closer to or far away from the gap, with which a growing or decreasing  $S(T)$  is accompanied. According to the electron counting rule in Eq.(5.3) 5.33 Ag atoms per unit cell are required to place the Fermi energy in the gap.

For  $\text{Ba}_8\text{Ag}_x\text{Ge}_{46-x}$  ( $x = 5.20 - 5.26$ ), the Fermi level are somewhere between the bottom of the gap and the one for  $\text{Ba}_8\text{Ag}_5\text{Ge}_{41}$ . From Fig.5.10 one derives a positive derivative and consequently, a negative Seebeck coefficient, in accordance with experiment. The Fermi energy of  $\text{Ba}_8\text{Ag}_{5.26}\text{Ge}_{40.74}$  is closest to the gap, and as a consequence the Seebeck coefficient reaches its largest absolute value (of about  $120 \mu\text{V/K}$  at about 500 K) of all the compounds studied (Fig. 5.16). Increasing the number of valence electrons, or in other words moving  $E_F$  farther away from the gap, significantly reduces the absolute value of  $S(T)$  although the change in the number of valence electrons is rather small.

As elaborated above, one should be aware that rather small uncertainties in the stoichiometry which are inherent to the experiment result in significant fluctuations of the number of valence electrons, which concomitantly leads to substantial variations of the Seebeck coefficients-according to Eq.(B.1), as demonstrated by Fig.5.16.

### 5.5.3 Electrical Resistivity

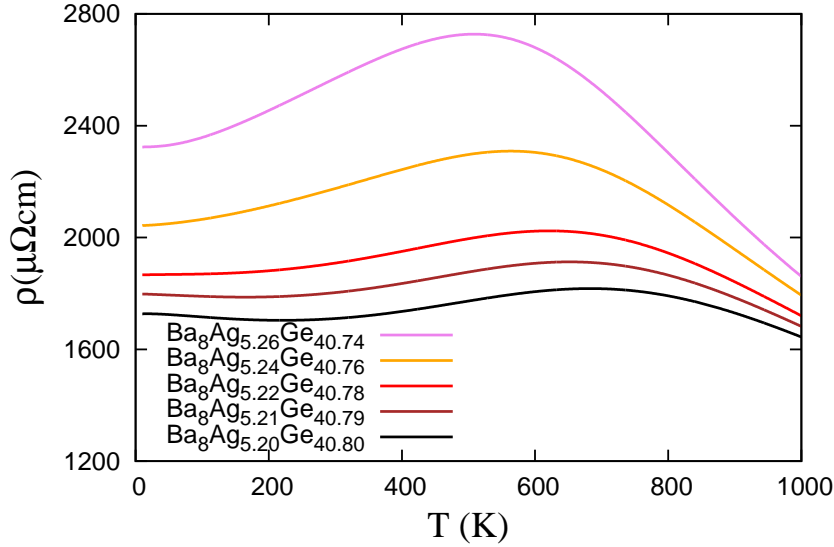


FIGURE 5.17: DFT derived temperature dependent resistivity for  $\text{Ba}_8\text{Ag}_x\text{Ge}_{46-x}$  ( $x = 5.20 - 5.26$ ). The reference compound is  $\text{Ba}_8\text{Ag}_5\text{Ge}_{41}$  from which the values for the selected compositions were derived within the rigid band approximation by adjusting the Fermi energy according to the change in  $\Delta n$  (from  $-0.22$  to  $-0.40$ , i.e. hole doping).

For deriving the resistivity of  $\text{Ba}_8\text{Ag}_5\text{Ge}_{41}$  within the constant-relaxation-time approximation,  $\tau = 1.5 \times 10^{-14}$  s was chosen in order to fit the calculated resistivity of  $\text{Ba}_8\text{Ag}_{5.22}\text{Ge}_{40.78}$  to one experimental value, namely the value of the high temperature maximum. The resistivity tensor  $\rho$  is the inverse of the electrical conductivity according to

$$\rho = \sigma^{-1} \quad (5.5)$$

The temperature dependent resistivity  $\rho(T)$  for the above mentioned Ag doping is shown in Fig.5.17. Obviously, the trend of the calculations matches rather well with the experimental data except for a small discrepancy in the low temperature regime. This discrepancy is due to the choice of the constant relaxation time, which is in fact energy and temperature dependent. As discussed for the experimental results, the resistivity  $\rho(T)$  increases with increasing temperature up to a maximum and then decreases at higher temperatures, which is the sure indication of a gap in the DOS. The reason, why resistivity increases with an increasing doping of Ag (i.e. decreasing Ge concentration), is, that the number of valence electrons, i.e., charge carrier density, is reduced and therefore  $E_F$  moves closer to the gap. This means that fewer states contribute to the conductivity, i.e. the resistivity is enhanced, as observed in Fig.5.17. Similar to experiment a peak is observed for all  $\text{Ba}_8\text{Ag}_x\text{Ge}_{46-x}$  compounds with  $x$  smaller than the critical value of 5.33. For  $\text{Ba}_8\text{Ag}_{5.22}\text{Ge}_{40.78}$  the peak occurs at about 700 K, which is close to the experimental peak for  $\text{Ba}_8\text{Ag}_5\text{Ge}_{41}$ .

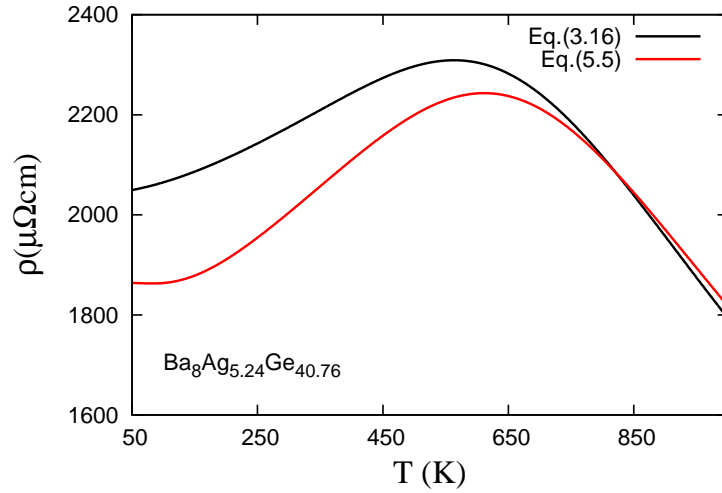


FIGURE 5.18: Temperature dependent resistivities for  $\text{Ba}_8\text{Ag}_{5.24}\text{Ge}_{40.76}$  as calculated directly from Eq.(3.16) and from the approximation in Eq.(5.6).

The resistivity peak is closely related to the location of the chemical potential  $\mu(T)$ , i.e. the temperature dependent Fermi energy. For instance, the calculations indicate that  $E_F$  of  $\text{Ba}_8\text{Ag}_{5.22}\text{Ge}_{40.78}$  slightly shifts towards lower energies as temperature increases, resulting in a small decrease in the DOS at the Fermi level. This leads to a reduction in the charge carrier density, which therefore leads to a decrease in the electrical conductivity, or enhancement of the resistivity. However, thermally excited states from below the gap contribute more and more to the charge carrier density with increasing temperature and cause a decrease in the resistivity. Thus there must be a critical temperature where a maximum of the resistivity occurs. In order to analyze the physical origin of the resistivity maximum, Eq.3.16 is approximated by assuming that the electron velocity  $v$  is constant, and thus can be moved out of the integral,

$$\sigma(T; \mu) = \frac{e}{4\pi^3} v^2 \tau \int N(E) \left(-\frac{\partial f}{\partial E}\right) dE. \quad (5.6)$$

If this equation works reasonably well, the features of  $\rho(T)$  and related quantities can be discussed in terms of the DOS and the universal function  $\frac{\partial f}{\partial E}$ , the energy derivative of the ferm-Dirac distribution, only. For  $\text{Ba}_8\text{Ag}_{5.24}\text{Ge}_{40.76}$  Fig.5.18 shows the calculated results according to Eqs.(3.16) and (5.6). For this purpose, Eq.(5.6) is fitted to the result of Eq.(3.16) at a selected temperature. It is obvious that the approximated expression of the resistivity in Eq.(5.6) closely resembles the full calculation.

To further illustrate how the gap affects the transport properties, the resistivity for different sizes of the gap was computed for  $\text{Ba}_8\text{Ag}_{5.24}\text{Ge}_{40.76}$ . The size of the gap was artificially modified by shifting the bands below the gap down in energy by a fixed amount. The

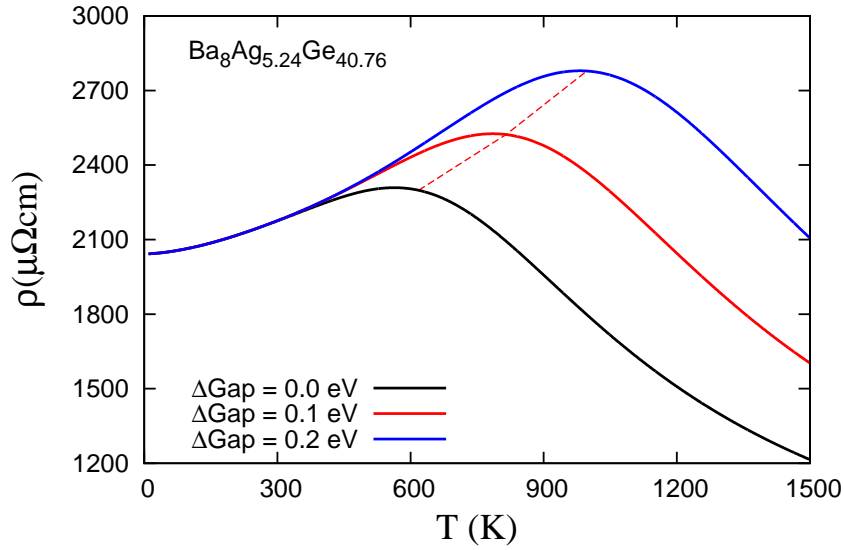


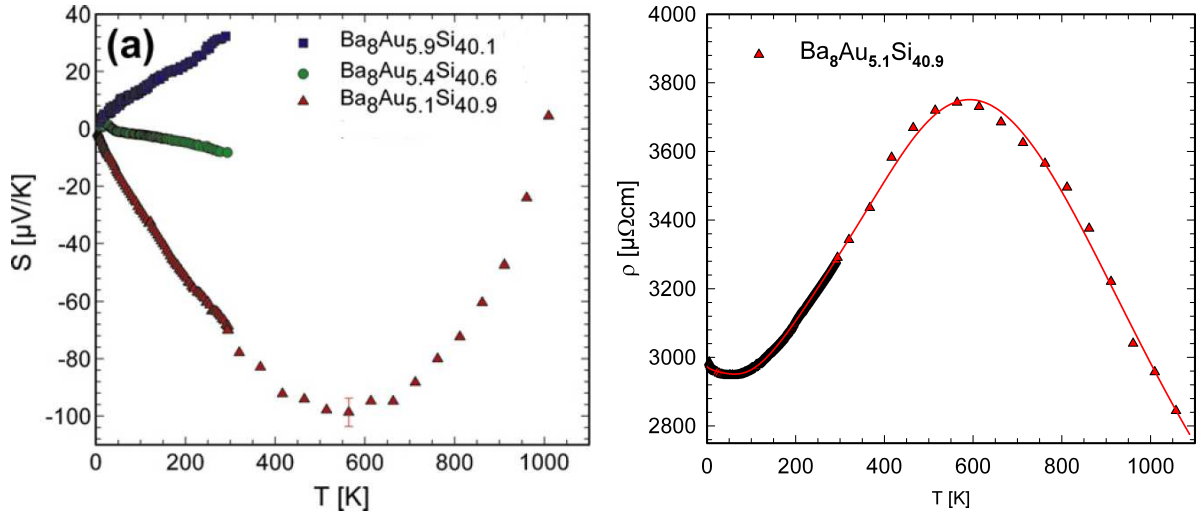
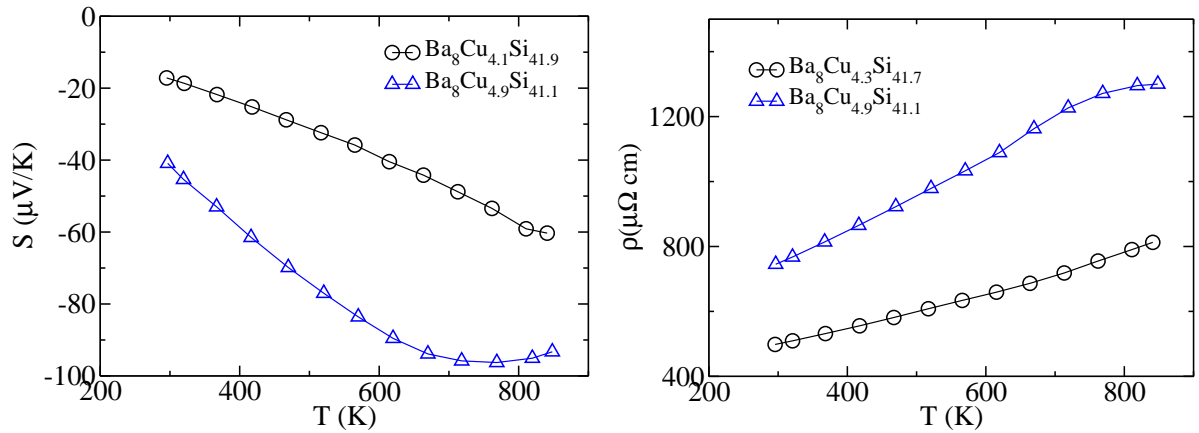
FIGURE 5.19: DFT derived temperature dependent resistivities for  $\text{Ba}_8\text{Ag}_{5.24}\text{Ge}_{40.76}$  for different artificial gap sizes. The gap for the reference compound  $\text{Ba}_8\text{Ag}_5\text{Ge}_{41}$  (see Fig.5.10) was enlarged by shifting the valence band edge down by  $\Delta\text{Gap}$ .

results as given in Fig.5.19, show a distinct gap-size dependent behavior of the resistivity. The maximum of  $\rho(T)$  is shifted towards higher temperature as the gap size is enlarged, and it finally disappears for a sufficiently large gap. This gap-size dependent behavior of the peak confirms the importance of thermal excitations of states below the gap in transport properties for the compounds studied.

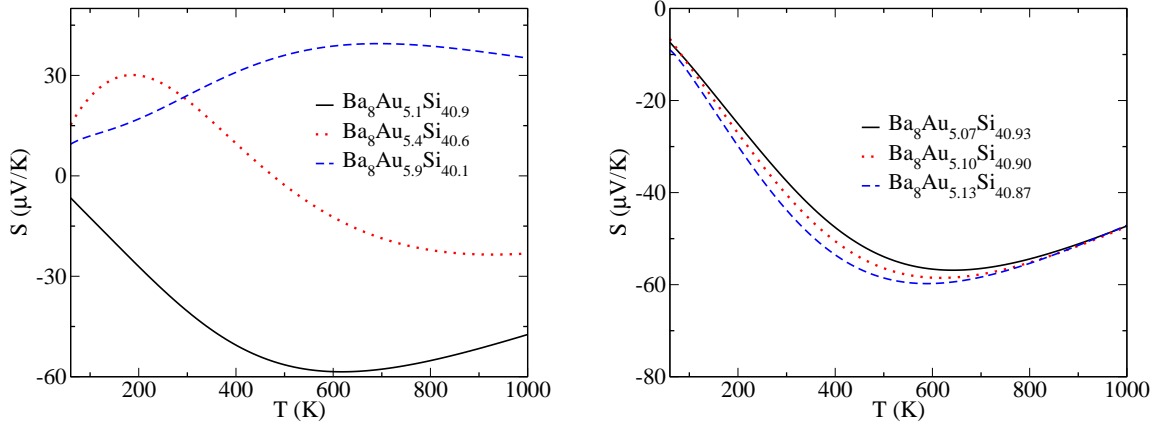
## 5.6 Transport Properties of $\text{Ba}_8\text{M}_x\text{Si}_{46-x}$ ( $\text{M} = \text{Ni}, \text{Cu}, \text{Au}$ ) Clathrates

Thermoelectric properties of Si-based clathrates have been extensively studied recently aiming at exploring their potential as TE materials. Up to now a maximum  $ZT$  of  $\sim 0.8$  at elevated temperatures was reported for the  $\text{Ba}_8\text{Ga}_x\text{Si}_{46-x}$  [18, 122], and very recently, Ni, Cu, Au were used to substitute Ga for further optimization [120, 123–127]. However, compared to the Ge related materials their relatively low  $ZT$ s make Si-based clathrates less attractive for TE applications. Nevertheless, Si-based materials are of technological interest, because Si is much cheaper than Ge, which becomes important for industrial fabrication on a large scale. Therefore, effort remains to find good TE materials based on Si-frameworks.

In this section the same approach will be used as for  $\text{Ba}_8\text{Ag}_x\text{Ge}_{46-x}$  to Si-based clathrates to analyze experimental findings and to possibly their TE properties.

FIGURE 5.20: Measured Seebeck coefficient and resistivity of  $\text{Ba}_8\text{Au}_x\text{Si}_{46-x}$  Ref. [128].FIGURE 5.21: Measured Seebeck coefficient and resistivity of  $\text{Ba}_8\text{Cu}_x\text{Si}_{46-x}$  (Ref. [123]).

The experimental information indicates that Seebeck coefficients of  $\text{Ba}_8\text{Au}_x\text{Si}_{46-x}$  are negative and positive when  $x$  is smaller or larger than 5.4 [127, 128] which is just around the critical limit of  $x = 5.33$  for the Fermi energy to ly in the gap. For  $\text{Ba}_8\text{Au}_{5.1}\text{Si}_{40.9}$  the Seebeck coefficient decreases as  $T$  increases until about 600 K and then turns to increase. Correspondingly, a maximum occurs in the electrical resistivity at 600 K according to Fig.5.20.  $\text{Ba}_8\text{Cu}_x\text{Si}_{46-x}$  shows a similar phenomenon except the minimum (maximum) in the Seebeck coefficient (resistivity) are shifted to higher temperatures for concentration of Cu lower 5[123].

FIGURE 5.22: DFT derived Seebeck coefficients of of  $\text{Ba}_8\text{Au}_x\text{Si}_{46-x}$ .

### 5.6.1 $\text{Ba}_8\text{Au}_x\text{Si}_{46-x}$ Clathrates

To compare the calculations with the most interesting experimental sample of composition  $\text{Ba}_8\text{Au}_{5.1}\text{Si}_{40.9}$ , the composition  $\text{Ba}_8\text{Au}_5\text{Si}_{41}$  was chosen as the reference as starting point for the rigid band application. The procedure of calculations is the same as for  $\text{Ba}_8\text{Ag}_5\text{Ge}_{41}$ , as given in Sec. 5.5.1. In the  $\text{BaAuSi}$  clathrates Ba, Au and Si contribute 2, 1 and 4 valence electrons to the system, respectively. Consequently,  $\Delta n = -0.3, -1.2$  and  $-2.7$ , namely hole doping, corresponds to  $\text{Ba}_8\text{Au}_{5.1}\text{Si}_{40.9}$ ,  $\text{Ba}_8\text{Au}_{5.4}\text{Si}_{40.6}$  and  $\text{Ba}_8\text{Au}_{5.9}\text{Si}_{40.1}$ , respectively. Fig.5.22 depicts the calculated temperature dependent Seebeck coefficient for the three compounds, which demonstrates that  $S(T)$  is very sensitive upon doping. For  $\text{Ba}_8\text{Au}_{5.1}\text{Si}_{40.9}$  a negative  $S(T)$  with a minimum around 600 K is obtained.  $S(T)$  changes sign when the Au concentration is increased from 5.1 to 5.4 at low temperature and becomes negative as the temperature is increased. The sign of  $S(T)$  for  $\text{Ba}_8\text{Au}_{5.4}\text{Si}_{40.6}$  at low temperature is different from the experimental measurement, as shown in Fig.5.20. It should be noted that  $\text{Ba}_8\text{Au}_{5.4}\text{Si}_{40.6}$  is very close the critical composition  $\text{Ba}_8\text{Au}_{5.33}\text{Si}_{40.67}$  around which the Seebeck coefficient changes sign. Rather small uncertainties in the stoichiometry -which are inherent to the experimental preparation- result in significant fluctuations of the number of valence electrons and therefore leads to a substantial variation of the Seebeck coefficient.  $\text{Ba}_8\text{Au}_{5.9}\text{Si}_{40.1}$  has a positive  $S(T)$  with a maximum around 700 K. Fig.5.22 shows  $ZT$  and Seebeck coefficient  $S(T)$  for  $\text{Ba}_8\text{Au}_x\text{Si}_{46-x}$  with variations in  $x$  close to the chemical composition of the experimental sample  $\text{Ba}_8\text{Au}_{5.1}\text{Si}_{40.9}$ . One realizes that the calculated  $S(T)$  for  $\text{Ba}_8\text{Au}_{5.1}\text{Si}_{40.9}$  is comparable with the experiment in terms of both the sign and position of the minimum.

The maximum in the electrical resistivity is also closely related to the position of the Fermi energy. As demonstrated for the  $\text{Ba}_8\text{Ag}_x\text{Ge}_{46-x}$  clathrates, the peak of the electrical

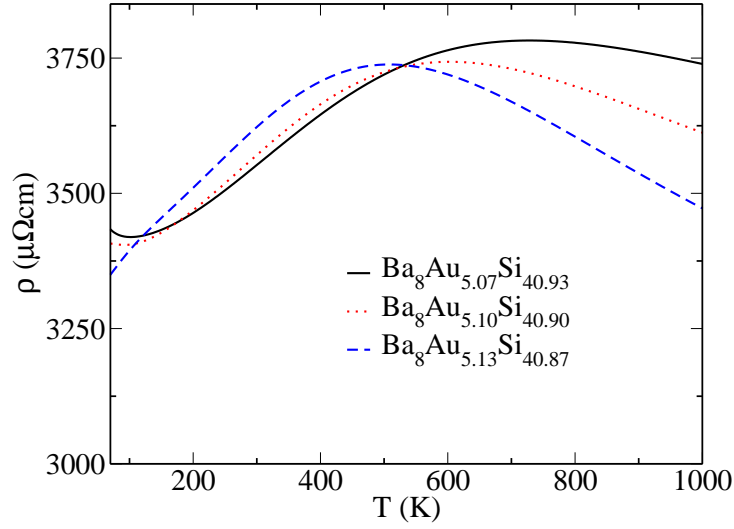


FIGURE 5.23: DFT derived electrical resistivities of  $\text{Ba}_8\text{Au}_x\text{Si}_{46-x}$  with  $x = 5.07, 5.10$  and  $5.13$ .

resistivity arises due to the placement of the Fermi energy close to a gap and the temperature dependence of the energy derivative of the Fermi function,  $f(E)$ . More specifically, if the Fermi energy is very close to the gap but at a higher energy, the states below the gap will involve electronic transport above a certain temperature due to the temperature broadening of  $f(E)$ . As the Fermi energy shifts closer to or further away from the gap, lower or higher temperatures are required for exiting states below the gap. Fig.5.23 shows the calculated electrical resistivity for three compounds with  $x$  equals 5.07, 5.10 and 5.13, respectively. A  $\tau = 7.96 \times 10^{-14}$  s was chosen for the relaxation time in order to fit the calculated resistivity of  $\text{Ba}_8\text{Ag}_{5.10}\text{Ge}_{40.90}$  to the corresponding experimental value at the high temperature maximum. From the discussion above, one concludes that the Fermi energies for all the three compounds are above the gap and are moving closer to it as  $x$  increases gradually from 5.07 to 5.13. The present calculations indicate that the thermoelectric properties and the resistivities of  $\text{Ba}_8\text{Au}_x\text{Si}_{46-x}$  alloys can be well described by the first-principles approach of this work.

### 5.6.2 $\text{Ba}_8\text{Cu}_x\text{Si}_{46-x}$ Clathrates

As for transport properties of  $\text{Ba}_8\text{Cu}_5\text{Si}_{41}$  two sets of calculations are made, namely for a geometrically fully relaxed structure and for a structure denoted as frozen- $\text{Ba}_8\text{Cu}_5\text{Si}_{41}$ , for which the high-symmetry structure corresponding  $\text{Ba}_8\text{Cu}_6\text{Si}_{40}$  was chosen and no relaxation was allowed. This procedure was chosen for testing the dependency of the results on structural and to critically analyze the comparison with experiment.

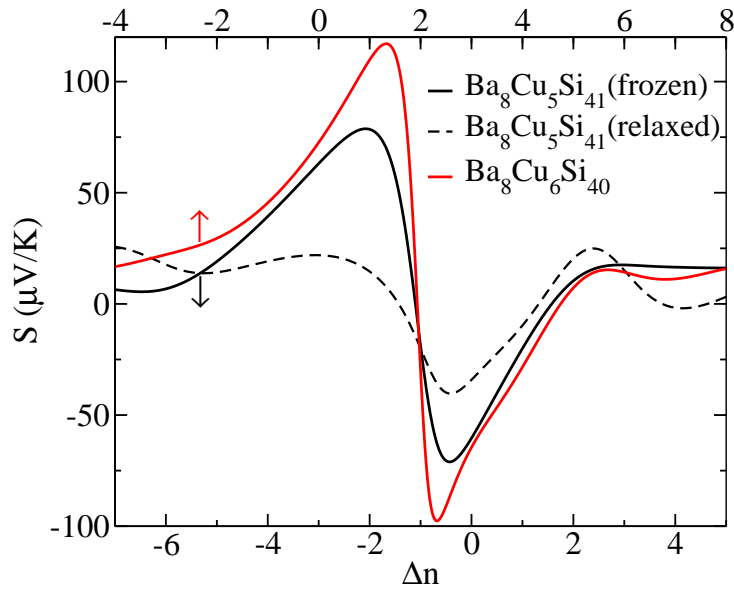


FIGURE 5.24: DFT derived Seebeck coefficient at 300 K for  $\text{Ba}_8\text{Cu}_5\text{Si}_{41}$  and  $\text{Ba}_8\text{Cu}_6\text{Si}_{40}$  as a function of doping  $\Delta n$ . A negative value corresponds to hole doping.

Figure 5.24 depicts the calculated Seebeck coefficients at 300 K vs. doping for relaxed- and frozen- $\text{Ba}_8\text{Cu}_5\text{Si}_{41}$ , and  $\text{Ba}_8\text{Cu}_6\text{Si}_{40}$ . It changes sign as the Fermi level crosses the gap, which is a clear indication of crossing the critical value for  $x_{gap}$ . There is a significant difference in the amplitudes of the Seebeck coefficient between the relaxed and frozen structures of  $\text{Ba}_8\text{Cu}_5\text{Si}_{41}$  revealing the influence of structural relaxation. The Seebeck coefficient of frozen- $\text{Ba}_8\text{Cu}_5\text{Si}_{41}$  resembles quite well that of  $\text{Ba}_8\text{Cu}_6\text{Si}_{40}$ , indicating that the rigid band approximation should be useful when varying  $x$  between 5 and 6, and when the structure should not be relaxed according to the experimental conditions. Both curves agree very well with each other except for the absolute values nearby the gap. However, the Seebeck coefficients are significantly different when comparing them with those of the fully relaxed structures. This is different to the comparison of Seebeck coefficients of  $\text{Ba}_8\text{Au}_5\text{Si}_{41}$  and  $\text{Ba}_8\text{Au}_6\text{Si}_{40}$  (or  $\text{Ba}_8\text{Ag}_5\text{Ge}_{41}$  and  $\text{Ba}_8\text{Ag}_6\text{Ge}_{40}$ ) with their fully relaxed structures, because they practically coincide. The difference may be due to atomic sizes of both dopant and framework atoms that atomic size effect on electronic structures is more significant in Ba-Cu-Si clathrates.

The difference in Seebeck coefficient between relaxed and frozen- $\text{Ba}_8\text{Cu}_5\text{Si}_{41}$  indicates the importance of ordering of Cu. As demonstrated in the previous work on Ba-Ag-Ge and Ba-Au-Si clathrates, starting with electronic structures of the fully relaxed structure of the reference compound, one can produce good agreement with experiments. This way is less valid when applied to Ba-Cu-Si clathrates by taking  $\text{Ba}_8\text{Cu}_5\text{Si}_{41}$  as the reference: Instead, freezing the five Cu atoms in  $\text{Ba}_8\text{Cu}_5\text{Si}_{41}$  to be in the same positions as those

in  $\text{Ba}_8\text{Cu}_6\text{Si}_{40}$  (the high symmetry structure) can produce reasonable agreement with experiments.

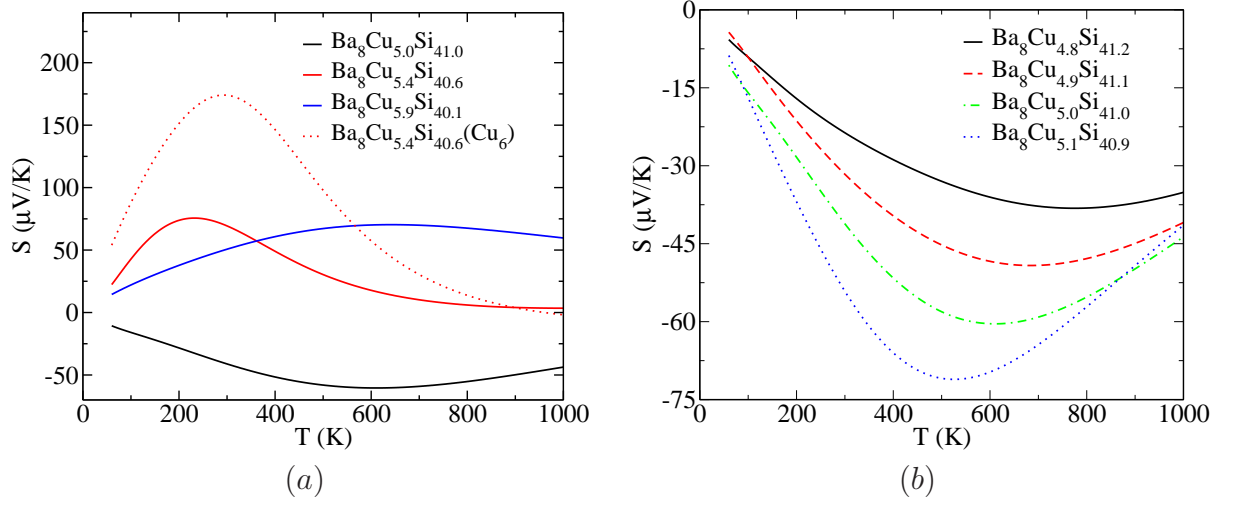


FIGURE 5.25: DFT derived  $S(T)$  for  $\text{Ba}_8\text{Cu}_x\text{Si}_{46-x}$  with (a)  $x = 5.0 - 5.9$  and (b)  $x = 4.8 - 5.1$  for fine scan as calculated within the rigid band approximation taking frozen- $\text{Ba}_8\text{Cu}_5\text{Si}_{41}$  as the reference. For  $\text{Ba}_8\text{Cu}_5\text{Si}_{41}$  the Seebeck coefficient derived by taking  $\text{Ba}_8\text{Cu}_6\text{Si}_{40}$  as the reference is also shown for comparison (dotted line).

Figure 5.25 depicts the calculated temperature dependent Seebeck coefficients  $S(T)$  for  $\text{Ba}_8\text{Cu}_x\text{Si}_{46-x}$ , which are obviously very sensitive to doping. Apparently,  $S(T)$  at low temperatures changes sign when the Cu concentration crosses the critical value of  $x_{gap} = 5.33$ . The change of sign can be understood in terms of the simplified Mott's formula, as already elaborated above. For comparison,  $S$  for  $\text{Ba}_8\text{Cu}_{5.4}\text{Si}_{40.6}$  was also calculated by taking  $\text{Ba}_8\text{Cu}_6\text{Si}_{40}$  as the reference. Although the  $S(T)$  as derived from the different references are qualitatively similar, there are significant differences concerning the magnitude and the position of the maximum. This suggests that care has to be taken when selecting the reference compound. Obviously, the rigid band approximation becomes less reliable the smaller the atomic sizes are, because then the overlap of the atomic wave functions is increased and changes in the local environment influence the resulting electronic structure stronger.

### 5.6.3 $\text{Ba}_8\text{Ni}_x\text{Si}_{46-x}$ clathrates

Figure 5.26 depicts the calculated temperature dependent Seebeck coefficients  $S(T)$  for  $\text{Ba}_8\text{Ni}_x\text{Si}_{46-x}$  with  $x$  varying from 3.3 to 3.8. The signs of the Seebeck coefficients are negative over the whole temperature range for because the compositions are away from the the critical value of  $x_{gap} = 4$  with  $n = 0$  for Ni. with the exception of  $S(T)$  for

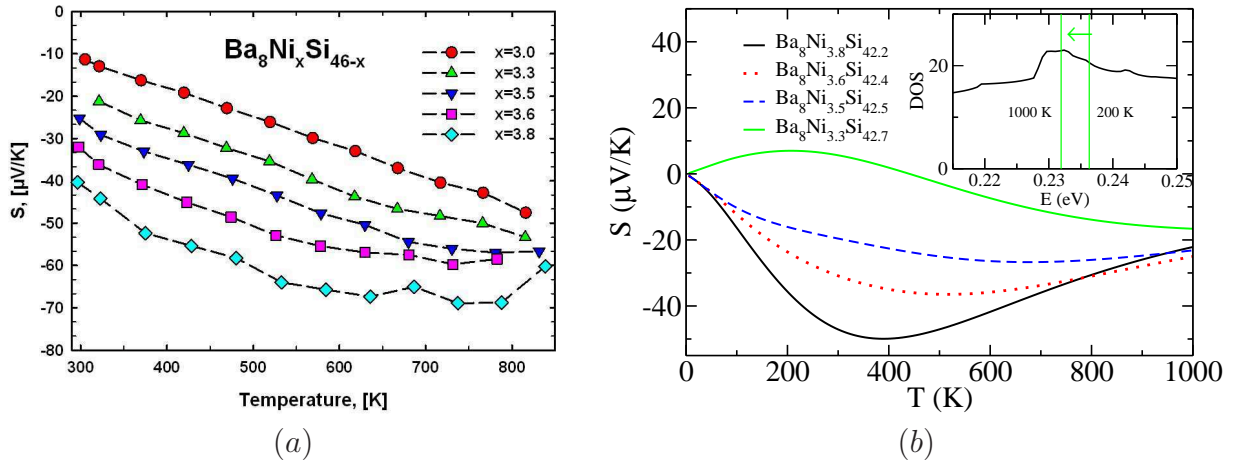


FIGURE 5.26: Experimental (a) and DFT derived (b) Seebeck coefficients of  $\text{Ba}_8\text{Ni}_x\text{Si}_{46-x}$ . Inset shows locations of the Fermi level of  $\text{Ba}_8\text{Ni}_{3.3}\text{Si}_{42.7}$  at 200 K and 1000 K, respectively. The arrow denoting the shifting direction of the Fermi level as temperature increases from 200 K and 1000 K.

$\text{Ba}_8\text{Ni}_{3.3}\text{Si}_{42.7}$ . Its positive sign at low temperatures can again be understood with help of the simplified Mott's relation in Eq.(B.15) together with location of the Fermi level. The inset shows the locations of the Fermi level at 200 K and 1000 K, respectively. At 200 K, one obtains a negative  $dN(E)/dE$  at  $E_F$  which consequently results in a positive Seebeck coefficient. The Fermi level moves towards lower energy to the top of a peak in the DOS as  $T$  increases from 200 K to 1000 K (inset of Fig.5.26(b)). During the temperature increase the delta-like Fermi function derivative, i.e.,  $df(E)/dE$ , broadens and therefore states at both sides of the peak are involved for the Seebeck coefficient according to Eq.(3.20). The left side has a steeper slope and therefore the corresponding integral in Eq.(3.20) yields a negative Seebeck coefficient. The global trend of the DFT results is similar to the experimental findings: in both cases the minimum of the Seebeck coefficient shifts towards lower temperature as  $x$  increases. Unlike the cases of  $\text{Ba}_8\text{Ag}_x\text{Ge}_{46-x}$  and  $\text{Ba}_8\text{Au}(\text{Cu})_x\text{Si}_{46-x}$ , where DFT calculations produce quantitative agreement with experiment, there are considerable discrepancies for  $\text{Ba}_8\text{Ni}_x\text{Si}_{46-x}$ . The measured data reveal no minimum of the Seebeck-coefficient up to 800 K for  $\text{Ba}_8\text{Ni}_{3.8}\text{Si}_{42.2}$ , whereas DFT predicts a minimum around 400 K.

Fig.5.27 shows the resistivity  $\rho(T)$  of  $\text{Ba}_8\text{Ni}_x\text{Si}_{46-x}$  with  $x = 3.3 - 3.8$ , using  $\text{Ba}_8\text{Ni}_4\text{Si}_{42}$  as a reference for the rigid band concept. The relaxation time  $\tau = 1.08 \times 10^{-14}$  was chosen to fit the calculated  $\rho(T)$  of  $\text{Ba}_8\text{Ni}_{3.3}\text{Si}_{42.7}$  to the experimental value at 600 K. Clearly, the calculations reproduce the experiment except for  $\text{Ba}_8\text{Ni}_{3.8}\text{Si}_{42.2}$ . The resistivities of  $\text{Ba}_8\text{Ni}_{3.3}\text{Si}_{42.7}$  and  $\text{Ba}_8\text{Ni}_{3.5}\text{Si}_{42.5}$  grow monotonically as the temperature increase.  $\text{Ba}_8\text{Ni}_{3.8}\text{Si}_{42.2}$  shows an anomalous behavior but still can be understood taking the location of the Fermi level into account, is elaborated above. Although for  $\text{Ba}_8\text{Ni}_x\text{Si}_{46-x}$  for

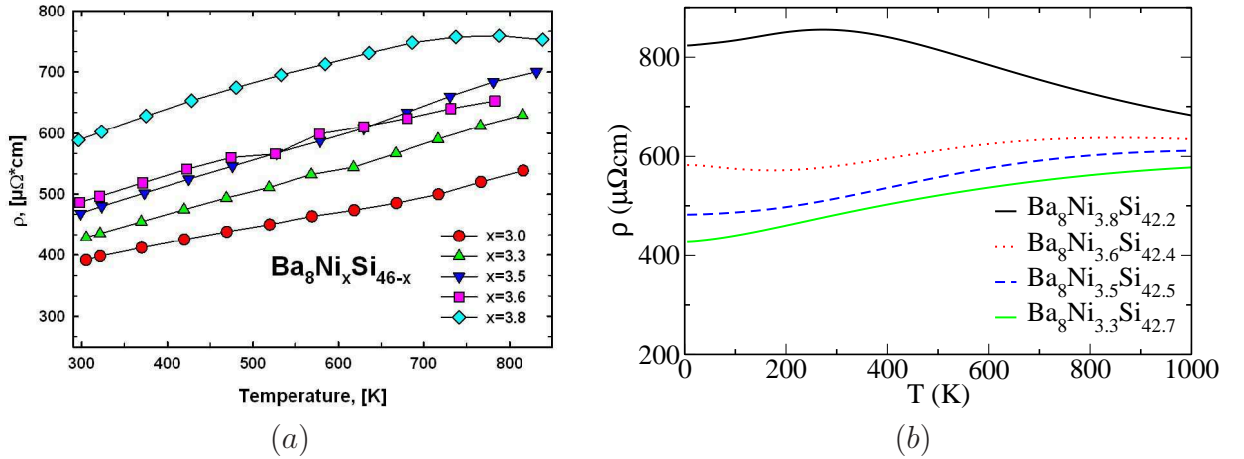


FIGURE 5.27: Experimental (a) and DFT derived (b) electrical resistivities of  $\text{Ba}_8\text{Ni}_x\text{Si}_{46-x}$ .

$x = 4$  there is no gap in the DOS, the Fermi level is located inside a minimum of the DOS and thus a temperature dependence similar to one with an existing gap is observed. As the Fermi level moves further away from the valley with decreasing Ni-content, the maximum in the electrical resistivity shifts to higher temperatures.

There are several possible reasons for the discrepancies between theory and experiment. The experimental uncertainties concerning the exact compositions are rather sizeable (namely about  $\Delta x \sim 0.2$ ), and the transport properties caused by small compositional differences within  $\Delta x = 0.5$  change significantly, as evidenced by Fig. 5.26 for the Seebeck coefficient. An important difference to the case of  $\text{Ba}_8\text{Ag}_x\text{Ge}_{46-x}$ , for which DFT simulations worked very well (also quantitatively!), consist in the atomic sizes: Both, Ag and Ge are larger than their counterparts Ni and Si. As the total volume and the atomic distances in  $\text{Ba}_8\text{Ni}_x\text{Si}_{46-x}$  are smaller and the overlap between the orbitals is larger, hybridization effects become stronger. Changes of the local environment therefore have a larger influence on the electronic structure. This also means that a rigid band approximation is less reliable in the present case than for  $\text{Ba}_8\text{Ag}_x\text{Ge}_{46-x}$ .

## 5.7 Lorenz Number and Electronic Thermal Conductivity

The electronic thermal conductivity  $\kappa_{el}$  is an important quantity, which affects the evaluation of ZT in two aspects. On one hand it determines ZT directly because it appears in the denominator of Eq. (1.1). On the other hand, experimentally it is used to extract thermal conductivity of phonons,  $\kappa_{ph}$ , which enters the numerator of ZT. None of both

thermal conductivities  $\kappa_{el}$  and  $\kappa_{ph}$  is directly measured. Usually,  $\kappa_{ph}$  is extracted by subtracting  $\kappa_{el}$  out from the total thermal conductivity, whereas  $\kappa_{el}$  is estimated by using the electrical conductivity according to the Wiedemann-Franz law [102, 121, 128], which is actually only valid for metals.

Rewriting Eq.(3.18), one obtains

$$\kappa_{el} = \frac{1}{T} [K_2 - \frac{K_1^2}{K_0}]. \quad (5.7)$$

The second term on the right hand side is negligible for metals (see Appendix D). If this is done,  $\kappa_{el}$  is just expressed by

$$\kappa_{el} = \frac{K_2}{T}. \quad (5.8)$$

From Eq.(B.3)- (B.7), one arrives at

$$K_2 = \frac{\pi^2 (k_B T)^2}{3} \sigma(\mu) \quad (5.9)$$

where  $\sigma(\mu)$  is given by Eq.(B.2). By substituting Eq.(5.9) into Eq.(5.8), one obtains

$$\kappa_{el} = \frac{K_2}{T} = \frac{\pi^2}{3} \left(\frac{k_B}{e}\right)^2 T \sigma \quad (5.10)$$

This is the Wiedemann-Franz law in the metallic limit that relates the electronic thermal conductivity to the electrical conductivity via the so called Lorenz number being the ratio  $\kappa_{el}/T\sigma$  [40]

$$L = \frac{\pi^2}{3} \left(\frac{k_B}{e}\right)^2 = 2.45 \times 10^{-8} \text{ W}\Omega/\text{K}^2 \quad (5.11)$$

Equation (5.11) indicates that the Lorenz number is a constant independent of charge carrier density and temperature. More generally, the Lorenz number is defined as

$$\kappa_{el} = LT\sigma. \quad (5.12)$$

Eq.5.12 indicates that L depends on the specific material because  $\kappa_{el}$  and  $\sigma$  are material dependent. Indeed, calculations reveal that L can deviate from the metallic limit significantly, in particular for lightly-doped semiconductors [129]. Since generally good TE materials are lightly doped semiconductors, thus the constant Lorenz number may cause severe discrepancies in the  $\kappa_{ph}$

It should be noted that the relaxation times of electron scatterings are required for calculating  $\sigma$  as well as  $\kappa_{el}$ , to which the constant relaxation time approximation has been applied in practical implementations. With this approximation, the relaxation time  $\tau$  disappears from the integrals  $K_n$  (Eq.(B.1)) by multiplication with  $\frac{1}{\tau}$ . Thus, the Lorenz

number can be obtained by

$$L = \frac{K_2}{T\sigma} = \frac{K_2}{\frac{T\sigma}{\tau}} \quad (5.13)$$

where  $K_2/(T\tau)$  and  $T\sigma/\tau$  are derived from transport calculations.

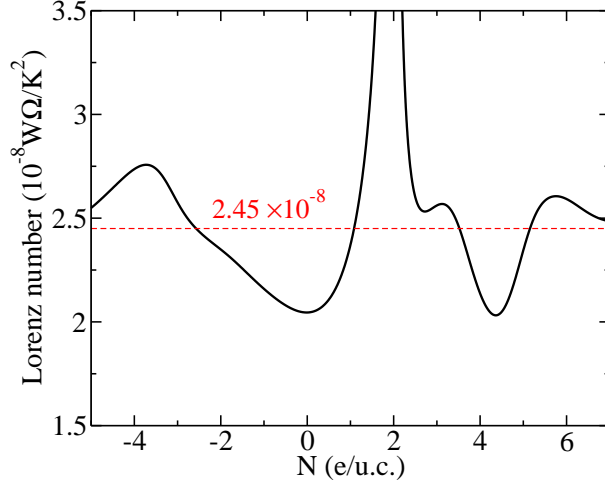


FIGURE 5.28: Lorenz number vs. charge doping for  $\text{Ba}_8\text{Au}_6\text{Ge}_{40}$  at 300 K. Negative(positive) values correspond to hole(electron) dopings.  $N = 2$  corresponds to a doping of 2 electrons that places the Fermi level into the middle of the gap according to the counting rule in Eq.(5.3).

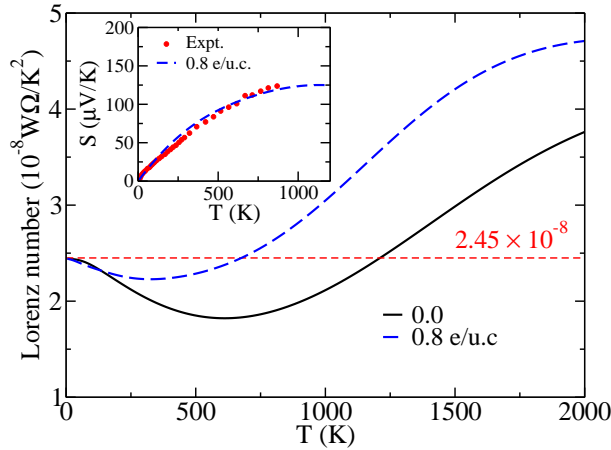


FIGURE 5.29: Lorenz number as a function of temperature for  $\text{Ba}_8\text{Au}_6\text{Ge}_{40}$  with doping of 0.0 (black solid line) and 0.8 electrons (blue dashed line), respectively. 0.8 electrons corresponds to  $N = 0.8$  in Fig.5.28. The reason for choosing the doping of 0.8 electrons is that the calculated Seebeck coefficient (inset) agrees well with the experiment for  $\text{Ba}_8\text{Au}_6\text{Ge}_{40}$  within the limits of the experimental error.

Turning now to realistic calculations, Figs.5.28 and 5.29 depict the Lorenz number as a function of charge doping (for 300K) and temperature for  $\text{Ba}_8\text{Au}_6\text{Ge}_{40}$  with a doping of 0.8 electrons, respectively. The doping by the rigid band approximation corresponds to

a chemical composition of  $\text{Ba}_8\text{Au}_6\text{Ge}_{40}$  within the limits of the experimental error[102]. The results indicate that the Lorenz number is charge-carrier-density- and temperature dependent, rather than a constant. In particular, a singularity arises when the Fermi level is in the gap, because the electrical conductivity becomes very small at low temperatures. This implies that lightly doped semiconductors violate the Wiedemann-Franz law. When the Fermi level is away from the gap, i.e. the system is metallic, the Lorenz number varies around  $2.45 \times 10^{-8} \text{ W}\Omega/\text{K}^2$ .

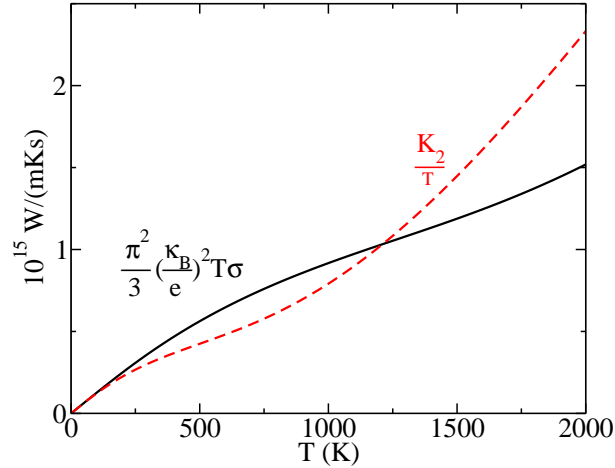


FIGURE 5.30: Temperature dependencies of  $\frac{K_2}{T}$  and  $\frac{\pi^2}{3} \left(\frac{k_B}{e}\right)^2 T \sigma$  for  $\text{Ba}_8\text{Au}_6\text{Ge}_{40}$  for zero doping.

Fig.5.29 shows that the Lorenz number approaches the metallic limit in the low temperature limit. However, it deviates from that and increases as temperature increases, which means that the Wiedemann-Franz law is only valid in the low temperature limit. The deviation originates from different temperature dependencies of  $\frac{K_2}{T}$  and  $T\sigma$  as shown in Fig.5.30. Moreover, Fig.5.29 demonstrates that the Lorenz number depends on the materials, i.e. the specific electronic structure of each material.

Fig.5.31 shows calculated electronic thermal conductivities  $\kappa_{el}$  of  $\text{Ba}_8\text{Au}_6\text{Ge}_{40}$  with a doping of 0.8 electrons, using Eq.(5.12) based on a measure electrical conductivity. The solid black line denotes the result derived by using a constant Lorenz number  $L_0$  and the dashed blue line a temperature-dependent Lorenz number derived from Eq.5.13. The results indicate that at higher temperatures, the Wiedemann-Franz law with a constant Lorenz number either underestimates or overestimates the electronic thermal conductivity significantly. These deviations become very significant at higher temperatures, depending on the doping.

In summary, in this section DFT calculations on the Lorenz number are performed which in general is a material and temperature dependent quantity rather than a constant value as it is usually derived from the metallic limit. Using the constant Lorenz number causes

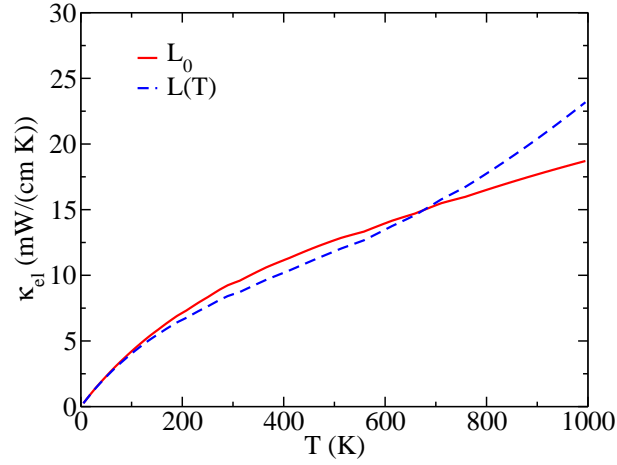


FIGURE 5.31: Electronic thermal conductivities  $\kappa_{el}$  for  $\text{Ba}_8\text{Au}_6\text{Ge}_{40}$  with a doping of 0.8 electrons. from the Wiedemann-Franz law using a constant Lorenz number  $L_0$  and a temperature-dependent Lorenz number derived from Eq.(5.13).

severe discrepancies which become significant at higher temperatures. The results of this Section suggest that one has to rethink the way of extracting both  $\kappa_{el}$  and  $\kappa_{ph}$  from experiment in the usual way. rather than simply using the constant Lorenz number for all materials over all temperatures. It is prosed proposed to combine -again- experiment and DFT theory now for the more precise evaluation of the thermal conductivity, which is very important for a reliable estimation of the figure of merit of a thermoelectric material.



# Chapter 6

## Summary and Outlook

The main goal of this work was the development and application of a first-principles approach for modeling thermoelectric properties of materials, which are promising for possible applications. Most of the results are directly compared to latest experimental measurements. In fact, a number of investigations were stimulated by experimental colleagues, with whom papers are already published or in preparation. The way to achieve this is to merge DFT electronic structures with the semi-classic Boltzmann transport theory. The calculations of the electronic structure was done with VASP, by which also the structural parameters were relaxed. For calculating the transport properties the program package BoltzTrap was taken. This package, which is available on the net, was substantially modified to significantly increase its feature such as varying the number of valence electrons, calculating Fermi velocities and deriving the Lorenz number, which is very important for thermal conductivity. This combination of the two packages provides a consistent description of thermoelectric properties from first principles provided the relaxation times, which may enter the expressions, are suitable chosen.

After the Introduction in chapter 2, which briefly discussed the basic mechanisms and quantities of thermoelectrics, the theoretical and methodological foundations of the DFT theory and calculations are presented. The electronic structure is given by the eigenvalues of the Kohn-Sham equations, which is calculated from first-principles by VASP. Furthermore, the first-principles LCPAO tight binding scheme is introduced, which is used for analyzing the VASP results within a simplified picture of structure and bonding. The corresponding program package needed to be adapted for the present purpose and is now available for all the users of the group. In chapter 3 an extensive discussion of the formalism and numerical implementation of Boltzmann's transport theory is made. It is important to understand the numerical intricacies because high accuracy, i.e. a dense  $\vec{k}$ -mesh and a sound interpolation method is needed for getting reliable numerical results.

The next two chapters deal with the two classes of materials, which are the focus of this thesis, namely skutterudites and clathrates. Chapter 4 is devoted to understanding the nature of rattling modes and bonding in Ge-based skutterudites and the role of band engineering in optimizing thermoelectric properties. Rattling modes are an often used concept for estimating the possible low thermal conductivity, which is important for increasing the figure of merit, the measure for the thermoelectric quality of a material. Phonon dispersion and densities of states are derived by a direct method employing force fields as calculated by highly accurate VASP calculations for filled skutterudites such as  $\text{MPt}_4\text{Ge}_{12}$  where  $M=\text{Ba, La, and Th}$  play the role of filler atoms, filling the large voids of the skutterudite structure. The three types of filler atoms, namely, Ba, La and Th, are chosen for studying the trend of information of rattling modes, because Ba and La have very similar atomic masses but with the different valence electron numbers 2 and 3, respectively, whereas the mass of Th is much heavier, and it provides 4 valence electrons. For the sake of analysis a simplified force constant model is then developed and applied to investigate the roles of the interaction between filler-atoms and the skutterudite framework, and the role of the atomic mass of the filler for the occurrence of rattling modes. In the phonon dispersion, in some cases rattling modes are observed: Ba modes are delocalized and therefore do not rattle, whereas La modes are localized but hybridized with framework modes. Th modes are further localized and lowered in frequency and become separated from the framework modes. On the basis of the localized phonon modes the specific heat of  $\text{ThPt}_4\text{Ge}_{12}$  can be modeled empirically which adds two Einstein-like modes to the Debye-like phonon DOS. Investigations of thermoelectric properties of  $\text{MPt}_4\text{Ge}_{12}$  were started with a test of the validity of Mott's relation and its simplified version that relates Seebeck coefficients to the electronic density of states. Although the Mott-based estimates are deviating from full calculations with increasing temperature, they show reasonable consistency with the full calculations in both magnitude and sign of the Seebeck coefficient in the low-temperature limit. Therefore, simplified Mott's relation is very useful for understanding the sign and magnitude of the Seebeck coefficient and may assist in guiding the design of thermoelectric materials with enhanced thermoelectric performance by means of a so-called band engineering. Calculations for the Ge-based skutterudites  $\text{MPt}_4\text{Ge}_{12}$  ( $M=\text{Ba, La and Th}$ ) reveal rather low Seebeck coefficients, which is anomalous for traditional pnictide skutterudites. Tight binding analysis indicates that a late transition element with a still open d-shell (such as Co, Ni, Pd, Pt) is crucial for the appearance of gaps in the electronic density of states, which are important for optimizing thermoelectric properties. The gap is a consequence of the p-d hybridization between the metal and pnictide atoms. The magic number of valence electrons for placing the Fermi energy in this hybridization gap is 24 per  $\text{TPn}_4$  unit (T: transition metal, Pn: pnictide) as it is the case for the prototypical compound  $\text{CoSb}_3$ . Combining this analysis with simplified Mott's relation for the Seebeck coefficient at low temperatures "band engineering" is employed for tuning the charge carrier concentration which is reflected by

the electronic structure close to Fermi energy. It is found that the Seebeck coefficients of  $\text{MPt}_4\text{Ge}_{12}$  skutterudites can be improved by two orders of magnitude by appropriate doping the Ge-sublattice by Sb.

In chapter 5, the comprehensive approach is applied extensively to understand and describe the experimental findings for  $\text{Ba}_8\text{M}_x\text{Pn}_{46-x}$  (M=Ni, Cu, Ag, Au; Pn=Ge, Si) clathrates. For these materials, the (large) gap is already formed at Fermi energy by the filler-free and metal-free pnictide framework, such as  $\text{Ge}_{46}$  (type-I clathrate) and  $\text{Ge}_{32}$  (type II clathrate). The same holds for the Si framework. Doping by metal atoms and adding Ba as a filler, still maintains the gap (in most cases), but may shifts Fermi energy according to the number of valence electrons away from the gap. Structural effects on the band gaps of the Ge isomers are explored by a tight binding analysis. Then, based on the occurrence of the gap at Fermi energy for the filler-free undoped clathrates and the derived DFT electronic structures, an electron counting rule for doping the clathrate and placing Fermi energy into the gap of the clathrates is presented. By this counting rule suitable chemical substitutions can be invented for placing the Fermi as close as possible to the gap. This of course, serves the purpose for, optimizing the Seebeck coefficients. Making use of this rule and the simplified Mott's relation, the observed sign and composition- and temperature-dependent magnitude of Seebeck coefficient of  $\text{Ba}_8\text{M}_x\text{Ge}_{46-x}$  is found to be closely related to locations of the Fermi level. The Fermi level of  $\text{Ba}_8\text{M}_x\text{Ge}(\text{Si})_{46-x}$  ( $x < 5.33$ ) is very close to the gap but at a higher energy. It slightly shifts toward lower energies as temperature increases, resulting in a small decrease in the electronic density of states at the Fermi level. This leads to a reduction in the charge carrier density, consequently resistivity is enhanced. States below the gap will involve electronic transport above a certain temperature due to the temperature broadening of the derivative of the Fermi function, and consequently a decrease in the resistivity occurs. Generally it is found that the Si-based clathrates - as investigated in this work- are less promising thermoelectric materials concerning the Seebeck coefficients. Nevertheless there is an extensive search for such Si-based materials because Si is much cheaper than Ge. Therefore, a variety of Si-based clathrates are also studied in the present work.

In a final smaller section being a part of the study on clathrates, the focus is put onto evaluation of lattice thermal conductivity, which enters the figure of merit in the denominator. Therefore, a reliable scheme for deriving these quantities is highly desirable, which is the aim of the last part. The Lorenz number is investigated to examine the validity of the Wiedemann-Franz law, which is used traditionally to separate thermal conductivities of electrons ( $\kappa_{el}$ ) and phonons ( $\kappa_{ph}$ ) based on the measured electrical conductivity. In contrast to the usual assumption which enter all these derivations as a constant, the Lorenz number may depend strongly on the charge carrier density and temperature. In particular a singularity occurs when the Fermi level is in the gap. The Wiedemann-Franz law may produce discrepancies of 25% and more at high temperatures for  $\kappa_{ph}$ , depending also

on the material. Therefore a better way of evaluating  $\kappa_{ph}$  is to combining experimental measurements and first-principles calculations, as exemplified in this work.

Despite the achievements of the approach merging first-principles methods and Boltzmann transport theory in modeling thermoelectric materials, it still faces a number of challenges. The major challenge, among others, is discrepancy in resistivity arising from the constant relaxation time approximation, which was used to avoid either expensive calculations or technique difficulties. Extending the DFT framework in order to produce parameter-free relaxation times of electrons may be the most important in the field.

Another -rather materials based- problem consists in the proper modelling of the experimental samples, which are fabricated at higher temperatures and rather rapidly cooled down. By that, metastable states are easily frozen in, which means, that it is not straightforward to compare the results of fully relaxed DFT calculations (strictly valid for  $T=0$ ) to the experiment. For example, substituted atoms may have several structural possibilities to get accommodated and at higher temperatures the real samples might be a (more or less) random mixture of occupations. The actual positions of the atoms have of course some influence on the electronic structure, in particular on the electronic structure around the gap. When doing DFT calculations one often takes the atomic configuration with the lowest total energy, although some kind of -yet not available- thermodynamic average might be more appropriate. Also of importance is the way how to treat small changes in stoichiometry. DFT calculations for solids require a unit cell, which for small variations in the stoichiometry, must be very large for a full modeling. Such an approach is not feasible in general and usually the so-called rigid band model is applied. This model assumes, that small variations of stoichiometry with respect to a reference system, do not change (significantly) the electronic structure but only shifts the Fermi energy according to the changed number of electrons. It is only required that this can be done in a certain range around Fermi energy (in which sizeable contributions to the transport integrals are made). Nevertheless, the rigid band model might be questionable depending on the material involved. In the present work on clathrates it was found, that if the atomic sizes are somewhat small (e.g.  $\text{Ba}_8\text{Ni}_x\text{Si}_{46-x}$ ) than the rigid band model is much worse than for systems such as  $\text{Ba}_8\text{Ag}_x\text{Ge}_{46-x}$ .

What is missing on a fundamental level all phonon-phonon and electron-phonon interactions, which are important for the thermal conductivity. The phonon-only is recently attracting quite some attention and the author of this thesis hopes, that he will get some opportunity to work on this hot topic in the near future, provided that a project -as submitted to the Asutrian Science foundation FWF- is granted.

# Appendix A

## V2Boltz Manual

### A.1 Files Used by V2Boltz

V2Boltz uses several input and output files:

INPUT	in	input parameters
STRUCT	in	the lattice geometry and point group elements
SYMOP	in	point group elements used for symmetrization
EIGENVAL	in	energy eigenvalues on a k-mesh
OUTPUT	out	general output, e.g., input data, $v_F$ , ...
trandos	in/out	DOS
sigxx	in/out	matrix elements of $\sigma(E)/\tau$ (second rank tensor)
sigxxx	in/out	matrix elements of $\nu(E)/\tau$ (third rank tensor)
engre	out	interpolated eigenvalues
tmp	out	symmetrized thermopower, i.e., Seebeck coefficient ( $\mu V/K$ )
elecond	out	symmetrized electrical resistivity ( $\mu\Omega cm$ )
condtens	out	electrical conductivity tensor
halltens	out	Hall conductivity tensor
chemipot	out	$E_F(T)$

### A.2 INPUT

**INPUT** is organized as several namelists which are :

&general_input:	general variables controlling the run
&band_control:	controlling shifting of bands
&dos_control:	restarting transport calculations from existing files

A sample of INPUT:

```
&general_input
neigen = 1,
ispin = 2,
lsorbit = .F.
eferm = 8.0628,
deltae = 0.0001,
ecut = 0.25,
nval = 96,
lpfac = 5,
tmax = 1000,
deltat = 5,
givenT = 600,
dosmethod = "TETRA",
seebtemp = .T.,
doping = 0.0
lsymref = .TRUE.
/
&band_control
band_shift = 0.0,
band_ref = 0.0
/
&dos_control
dos_old = .F.
/
```

**neigen** (*integer*): Number of eigenvalue files. In the case of more than one EIGENVAL files, they should be named as EIGENVAL*i*.

*Default: neigen = 1*

**ispin** (*integer*): ISPIN used in VASP calculations.

*Default: ispin = 1*

**lsorbit** (*logical*): LSORBIT used in VASP calculations.

*Default: lsorbit = .F.*

**eferm** (*real*): The Fermi energy (in eV) obtained from VASP eigenvalue calculations.

*No Default*

**deltae** (*real*): Energy step (in Ry) for integrations of transport coefficients.

*Default:* **deltae = 0.0005**

**ecut** (*real*): Energy window (in Ry) around the Fermi level for integrations of transport coefficients. The energy window is [eferm-ecut, eferm+ecut]

*Default:* **ecut = 0.25**

**nval** (*integer*): The total number of valence electrons of the system. It must be the same as NELECT in OUTCAR/EIGENVAL of VASP.

*No Default*

**lpfac** (*integer*): A factor used for expansion of k-mesh.

*Default:* **lpfac = 5**

**tmax** (*real*): Maximum temperature (in K) used for S(T) calculations. The temperature window for such calculations is [5, tmax].

*Default:* **tmax = 600**

**deltat** (*real*): Maximum temperature (in K) used for S(T) calculations.

*Default:* **deltat = 1**

**givenT** (*real*): The temperature for S( $\mu$ ) calculations.

*Default:* **givenT = 300**

**dosmethod** (*character*): Methods for DOS calculation used by **V2Boltz** but not by VASP. It is not necessary the same as that used in VASP calculations. It can be "TETRA" and "HISTO".

*Default:* **dosmethod = "TETRA"**

**seebtemp** (*logical*): Calculating S( $\mu$ ) or S(T).

*Default:* **seebtemp = .F.**

**doping** (*real*): The number of charges (n/u.c.) doped to the system. Negative(positive) means electron(hole) doping.

*Default:* **doping = 0.0**

**lsymref** (*logical*): Symmetrizing transport tensor or not.

*Default:* **lsymref = .F.**

**band\_shift** (*logical*): Shifting valence bands or not.

*Default:* **band\_shift = .F.**

**band\_ref** (*real*): Magnitude of shifting. Negative(positive) means shrink(enlarge) the gap.

*Default:* **band\_ref = 0.0**

**dos\_old** (*logical*): Restarting transport calculations using existing *trandos*, *sigxx*, *sigxxx*.

*Default:* **dos\_old = .F.**

**analy\_dos** (*logical*): Using parabolic bands.

*Default:* **analy\_dos = .F.**

## A.3 SYMOP

The file **SYMOP** contains symmetry operations of the space group of the system, which can be generated by adding following specifications into the main file of VASP, *main.F* and *main.f90*.

Firstly, find

```
OPEN(UNIT=70,FILE=DIR_APP(1:DIR_LEN)//'CHG',STATUS='UNKNOWN')
```

and add

```
OPEN(UNIT=175,FILE=DIR_APP(1:DIR_LEN)//'SYMOP',STATUS='UNKNOWN')
```

Secondly, find

```
! ... so take nosymm!
```

```
CALL NOSYMM
```

```
( ... )
```

```
END IF
```

add

```
do I=1,SYMM%NROT
```

```
write(175,'(3I2,f10.5)')ISYMOP(1,1:3,I),GTRANS(1,I)
```

```
write(175,'(3I2,f10.5)')ISYMOP(2,1:3,I),GTRANS(2,I)
```

```
write(175,'(3I2,f10.5)')ISYMOP(3,1:3,I),GTRANS(3,I)
```

```
write(175,'(I8)')I
```

```
enddo
```

For the use of symmetrization, one need to generate **SYMOP** for the desired highly symmetrical structure.

## A.4 STRUCT

To construct file **STRUCT**, one needs to copy the header of **POSCAR** (the first five lines) into file **STRUCT** followed by the number of symmetry operations and symmetry operations contained in **SYMOP**.

## A.5 EIGENVAL

**V2Boltz** needs some **EIGENVAL** files from VASP calculations. In the case that one just has one **EIGENVAL** file, i.e. `neigen = 1`, nothing needs to do on the **EIGENVAL** file. However, very often we need a very dense k-mesh for transport coefficient calculations, which requires **EIGENVAL** on a very dense k-mesh. Generally one may use a k-mesh of  $25 \times 25 \times 25$ . However, such a dense k-mesh would make the calculations hard to be proceeded with reasonable computer nodes and time expenses when the system is not small. In this case, one alternatively splits the task into many small tasks so that each involves a much less number k-points. In this way one can run eigenvalue calculations separately and each job just requires a few processes. Finally collecting all the **EIGENVAL** files and naming them as **EIGENVAL\_1**, **EIGENVAL\_2** ...



# Appendix B

## Mott's Relation and Its Simplified Version

This appendix is to illustrate derivation of Mott's relation, which relates the Seebeck coefficient to the electrical conductivity tensor. Further efforts were done by the author to relate the Seebeck coefficient to DOS and edges of band gap for guiding optimizing TE properties of materials based on electronic structure calculations.

### B.1 Mott's Relation

The integrals  $K_n$  involves the energy derivative of the Fermi function which becomes a delta-like peak as temperature decreases vanishing except within a few  $k_B T$  of  $E = \mu$ .  $K_n$  can be written as

$$K_n = \int_{-\infty}^{\infty} \sigma(E)(E - \mu)^n \left(-\frac{\partial f^0}{\partial E}\right) dE \quad (\text{B.1})$$

where

$$\sigma(E) = \frac{1}{4\pi^3 \hbar} \iint \mathbf{v}(\mathbf{k}) \mathbf{v}(\mathbf{k}) \tau(\mathbf{k}) \frac{dS}{\nabla_{\mathbf{k}} E} \quad (\text{B.2})$$

$\sigma(E)$  is related to  $\sigma$  through Eqs.(3.16) and (B.1). A smooth function  $F(E) = \sigma(E)(E - \mu)^n$  can be expanded by Taylor's theorem[130],

$$F(E) = F(\mu) + (E - \mu)F'(\mu) + \frac{1}{2}(E - \mu)^2 F''(\mu) + \dots, \quad (\text{B.3})$$

and obtain from Eq.(B.1)

$$I = C_0 F(\mu) + C_1 F'(\mu) + C_2 F''(\mu) + \dots, \quad (\text{B.4})$$

$$C_0 = - \int_{-\infty}^{\infty} \frac{\partial f^0}{\partial E} dE = 1 \quad (\text{B.5})$$

$$C_1 = - \int_{-\infty}^{\infty} (E - \mu) \frac{\partial f^0}{\partial E} dE = 0 \quad (\text{B.6})$$

$$C_2 = - \frac{1}{2} \int_{-\infty}^{\infty} (E - \mu)^2 \frac{\partial f^0}{\partial E} dE \simeq \frac{\pi^2}{6} (k_B T)^2 \quad (\text{B.7})$$

If terminating the expansion up to the second-order term, then one obtains

$$K_1 = \frac{\pi^2}{3} (k_B T)^2 \left[ \frac{\partial \sigma(E)}{\partial E} \right]_{E=\mu} \quad (\text{B.8})$$

Substituting Eqs.(3.16) and (B.8) into Eq.(3.20), one obtains

$$S = \frac{\pi^2 k_B^2 T}{3e} \left[ \frac{\partial \ln \sigma(E)}{\partial E} \right]_{E=\mu} \quad (\text{B.9})$$

Equation (B.9) is known as Mott's relation[130].

## B.2 Simplified Mott's Relation

Nowadays accurate electronic structures (electron density of states and band structures) of many materials can be easily derived from the state-of-art ab initio methods. On the basis of these results one finds relations between the Seebeck coefficient and electronic structures at qualitative and quantitative useful level comparable to the experimental results. Of course, one has to keep in mind that only the electronic contributions to the TE as described by a quasiparticle picture (namely the Kohn-Sham equations) are considered. Nevertheless, such an approach via the electronic structure can be quite useful also for the experimentalists searching for large Seebeck coefficients. Searching for easier and simplified formulations one rewrites Eq.(B.2)

$$\sigma(E) = \frac{1}{4\pi^3 \hbar} \iint \mathbf{v}(\mathbf{k}) \mathbf{v}(\mathbf{k}) \tau(\mathbf{k}) \frac{dS}{\nabla_{\mathbf{k}} E} \quad (\text{B.10})$$

DOS  $N(E)$  is given by Eq.(8.63) in *Ashcroft and Mermin* [131]

$$N(E) = \frac{1}{4\pi^3 \hbar} \iint \frac{dS}{\nabla_{\mathbf{k}} E} \quad (\text{B.11})$$

Similar to DOS,  $\sigma(E)$  can be expressed as

$$\sigma(E) = \mathbf{v}(E) \mathbf{v}(E) N(E) \tau(E) \quad (\text{B.12})$$

Assuming one is dealing with an isotropic system

$$\sigma_{ij}(E) = \sigma_{xx}(E)\delta_{ij} \quad (\text{B.13a})$$

$$S_{ij} = S_{xx}\delta_{ij} \quad (\text{B.13b})$$

$$i, j = x, y, z \quad (\text{B.13c})$$

thus there is only one independent element in S. Substituting Eq.(B.12) back to Eq.(B.9), one obtains

$$S = \frac{\pi^2 k_B^2 T}{3 e} \left\{ \frac{1}{N(E)} \frac{dN(E)}{dE} + \frac{1}{v^2(E)} \frac{dv^2(E)}{dE} + \frac{1}{\tau(E)} \frac{d\tau(E)}{dE} \right\}_{E=\mu} \quad (\text{B.14})$$

Assuming that  $v^2(E)\tau(E)$  remains constant or varies slowly close to the Fermi level and focusing on the contribution of the DOS,

$$S = -\frac{\pi^2 k_B^2 T}{3 |e|} \left\{ \frac{1}{N(E)} \frac{dN(E)}{dE} \right\}_{E=\mu} \quad (\text{B.15})$$

where the sign of charge is given by  $-|e|$ . Equation (B.15) directly links the Seebeck coefficient to the electronic DOS. By that it is obvious that maximizing the Seebeck coefficient requires a large slope of the DOS and a small DOS at the Fermi level. From Eq.(B.15) one learns that weakly doped semiconductors are inherently ideal candidates of thermoelectric materials. To optimize the thermoelectric performance of materials by improving the Seebeck coefficient, the Fermi level of systems should be close to the gap. In particular, a significant enhancement of Seebeck coefficient can be achieved if highly localized states such as f states constitute the states of gap-edge where the Fermi level is located as shown in Fig.B.1. This leads to a delta-like transport distribution, i.e.,  $\sigma(E)$  in Eq.(B.12), favoring a high ZT according to Mahan's statement[98].

Equation (B.15) also shows that the sign of the Seebeck coefficient is determined by the energy derivative of the DOS at the Fermi energy, which results in an opposite sign of Seebeck coefficient and slope of the DOS at  $E_F$ .

For most TE materials are doped semiconductors, one can relates the Seebeck coefficient to edges of band gap. Assuming one is dealing with a n-type semiconductor

$$E = \frac{\hbar^2 k^2}{2m^*} + E_c \quad (\text{B.16a})$$

$$v^2(E) = 2m^*(E - E_c) \quad (\text{B.16b})$$

Relaxation time in general is a function energy and is sometimes approximated as

$$\tau(E) = \tau_0(E - E_c)^\gamma \quad (\text{B.17})$$

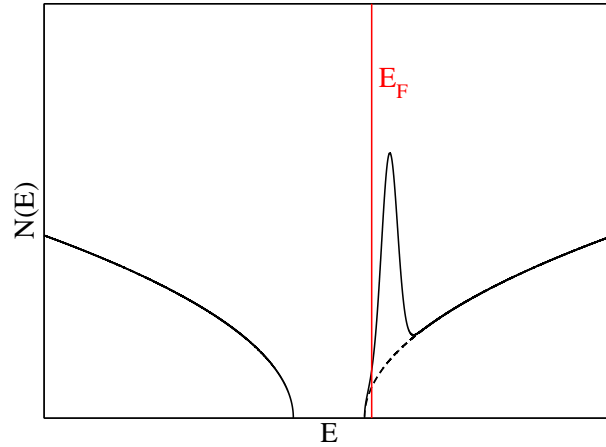


FIGURE B.1: Illustration of the density of states and location of the Fermi level which favor a high Seebeck coefficient.

where  $\gamma$  is an empirical parameter accounting for scattering mechanisms. [132] Equation (B.14) then can be written as

$$S = \frac{\pi^2 k_B^2 T}{3 e} \left\{ \frac{1}{2\sqrt{E - E_c}} + \frac{1 + \gamma}{E - E_c} \right\}_{E=E_F} \quad (\text{B.18})$$

In the approximation of constant relaxation time, Eq.(B.18) becomes

$$S = \frac{\pi^2 k_B^2 T}{3 e} \left\{ \frac{1}{2\sqrt{E - E_c}} \right\}_{E=E_F} \quad (\text{B.19})$$

Both Eqs.(B.18) and (B.19) indicate that a giant Seebeck coefficient can be produced when the Fermi level close to  $E_c$ . Therefore to maximize  $S$  the Fermi level should be close to the edges of band gap.

# Appendix C

## Atomic Displacement Parameters

In this appendix the relation between atomic displacement parameters (ADPs) and PH-DOS is derived. In the isotropic case, ADPs is given by

$$U_{iso}(T) = \frac{1}{3} \langle \mathbf{u}_l^2(T) \rangle = \frac{1}{3} \sum_{\alpha=1}^3 \langle \mathbf{u}_{l\alpha}^2(T) \rangle \quad (\text{C.1})$$

where  $\langle \mathbf{u}_l^2(T) \rangle$  is the mean square displacement amplitude. Our goal is to derive a formula for  $\langle \mathbf{u}_l^2(T) \rangle$ . The displacement  $\mathbf{u}_l$  is expressed in terms of normal coordinates, which in one-dimensional case is

$$\mathbf{u}_l = \frac{1}{\sqrt{NM_l}} \sum_{\mathbf{q},\sigma} \mathbf{Q}_{\mathbf{q},\sigma} \mathbf{e}_{\mathbf{q},\sigma} e^{i\mathbf{q}\cdot\mathbf{R}_l} \quad (\text{C.2})$$

where  $\mathbf{Q}_{\mathbf{q},\sigma}$  is the normal coordinate at wave vector  $\mathbf{q}$  with polarization  $\sigma$ . Since the  $\mathbf{u}_l$  must be real, we have

$$\mathbf{e}_{\mathbf{q},\sigma}^* \mathbf{Q}_{\mathbf{q},\sigma}^* = \mathbf{e}_{-\mathbf{q},\sigma} \mathbf{Q}_{-\mathbf{q},\sigma} \quad (\text{C.3})$$

We satisfy this by the requirements

$$\mathbf{e}_{\mathbf{q},\sigma}^* = \mathbf{e}_{-\mathbf{q},\sigma} \quad (\text{C.4a})$$

$$\mathbf{Q}_{\mathbf{q},\sigma}^* = \mathbf{Q}_{-\mathbf{q},\sigma} \quad (\text{C.4b})$$

Using Eq.(C.2)

$$\begin{aligned}
 \sum_l M_l \mathbf{u}_l^2 &= \sum_l M_l \mathbf{u}_l \cdot \mathbf{u}_l \\
 &= \frac{1}{N} \sum_l \sum_{\mathbf{q}, \sigma} \sum_{\mathbf{q}', \sigma'} (\mathbf{Q}_{\mathbf{q}, \sigma} \mathbf{Q}_{\mathbf{q}', \sigma'}) (\mathbf{e}_{\mathbf{q}, \sigma} \cdot \mathbf{e}_{\mathbf{q}', \sigma'}) e^{i(\mathbf{q} + \mathbf{q}') \cdot \mathbf{R}_l} \\
 &= \sum_{\mathbf{q}, \sigma} \sum_{\sigma'} (\mathbf{Q}_{\mathbf{q}, \sigma} \mathbf{Q}_{-\mathbf{q}, \sigma'}) (\mathbf{e}_{\mathbf{q}, \sigma} \cdot \mathbf{e}_{-\mathbf{q}, \sigma'}) \\
 &= \sum_{\mathbf{q}, \sigma} \mathbf{Q}_{\mathbf{q}, \sigma}^* \mathbf{Q}_{-\mathbf{q}, \sigma}
 \end{aligned} \tag{C.5}$$

where we have used

$$\frac{1}{N} \sum_l e^{i(\mathbf{q} + \mathbf{q}') \cdot \mathbf{R}_l} = \delta_{\mathbf{q}, -\mathbf{q}} \tag{C.6}$$

Eq.(C.4) and

$$\sum_{\sigma, \sigma'} \mathbf{e}_{\mathbf{q}, \sigma}^* \mathbf{e}_{\mathbf{q}, \sigma'} = \delta_{\sigma, \sigma'} \tag{C.7}$$

The  $\mathbf{Q}_{\mathbf{q}, \sigma}$  has the form

$$\mathbf{Q}_{\mathbf{q}, \sigma} = \sqrt{\frac{\hbar}{2\omega_{\mathbf{q}, \sigma}}} (a_{\mathbf{q}, \sigma} + a_{-\mathbf{q}, \sigma}^+) \tag{C.8}$$

Substituting Eq.(C.8) into Eq.(C.5), we have

$$\sum_l M_l \mathbf{u}_l^2 = \sum_{\mathbf{q}, \sigma} \frac{\hbar}{2\omega_{\mathbf{q}, \sigma}} (a_{\mathbf{q}, \sigma} + a_{-\mathbf{q}, \sigma}^+) (a_{\mathbf{q}, \sigma}^+ + a_{-\mathbf{q}, \sigma}) \tag{C.9}$$

The mean value of  $\sum_l M_l \mathbf{u}_l^2$  is given by

$$\begin{aligned}
 \langle \sum_l M_l \mathbf{u}_l^2 \rangle &= \sum_{\mathbf{q}, \sigma} \frac{\hbar}{2\omega_{\mathbf{q}, \sigma}} (\langle a_{\mathbf{q}, \sigma}^+ a_{\mathbf{q}, \sigma} \rangle + \langle a_{-\mathbf{q}, \sigma} a_{-\mathbf{q}, \sigma}^+ \rangle) \\
 &= \sum_{\mathbf{q}, \sigma} \frac{\hbar}{2\omega_{\mathbf{q}, \sigma}} (2 \langle a_{\mathbf{q}, \sigma}^+ a_{\mathbf{q}, \sigma} \rangle + 1) \\
 &= \sum_{\mathbf{q}, \sigma} \frac{\hbar}{2\omega_{\mathbf{q}, \sigma}} (2n(\omega_{\mathbf{q}, \sigma}) + 1)
 \end{aligned} \tag{C.10}$$

where  $n$  is the Bose-Einstein function,

$$n(\omega) = \frac{1}{e^{\frac{\hbar\omega}{k_B T}} - 1} \tag{C.11}$$

Projecting Eq.(C.10) into  $\omega$  representation and using the definition of phonon DOS

$$g(\omega) = \sum_{\mathbf{q},\sigma} \delta(\omega - \omega_{\mathbf{q},\sigma}) = \sum_l g_l(\omega) \quad (\text{C.12})$$

where  $g_l$  is the partial phonon DOS of  $l$ th atom, we have

$$\langle \sum_l M_l \mathbf{u}_l^2 \rangle = \sum_l \frac{\hbar}{2} \int \frac{g_l(\omega)}{\omega} \coth\left(\frac{\hbar\omega}{2k_B T}\right) \quad (\text{C.13})$$

And finally for  $\langle \mathbf{u}_l^2 \rangle$  we obtain

$$\langle \mathbf{u}_l^2 \rangle = \frac{\hbar}{2M_l} \int \frac{g_l(\omega)}{\omega} \coth\left(\frac{\hbar\omega}{2k_B T}\right) \quad (\text{C.14})$$

For three-dimensional case, we have

$$\langle \mathbf{u}_l^2 \rangle = \frac{3\hbar}{2M_l} \int \frac{g_l(\omega)}{\omega} \coth\left(\frac{\hbar\omega}{2k_B T}\right) \quad (\text{C.15})$$

Substituting Eq.(C.15) into Eq.(C.1), we have

$$U_{iso}(T) = \frac{\hbar}{2M_l} \int \frac{g_l(\omega)}{\omega} \coth\left(\frac{\hbar\omega}{2k_B T}\right) \quad (\text{C.16})$$



# Appendix D

## An Approximation to The Electronic Thermal Conductivity

This appendix provide the proof that the second term in the electronic thermal conductivity (Eq.(3.18) or (5.7)) is negligible in the metallic limit. Rewriting Eq.(3.18) gives

$$\kappa_{el} = \frac{1}{T} [K_2 - \frac{K_1^2}{K_0}] \quad (\text{D.1})$$

In the low temperature limit  $K_1$  and  $K_2$  are approximated as Eqs.(B.8) and (5.9) by the expansions Eqs.(B.3) and (B.7), respectively. Rewriting them, one has

$$K_1 = \frac{\pi^2(k_B T)^2}{3} \left[ \frac{\partial \sigma(E)}{\partial E} \right]_{E=\mu} \quad (\text{D.2})$$

and

$$K_2 = \frac{\pi^2(k_B T)^2}{3} \sigma(\mu) \quad (\text{D.3})$$

where  $\sigma(E)$  is given by Eq.(B.2), which in energy representation is given by Eq.(B.12).  $\mu$  is the chemical potential. Rewriting it

$$\sigma(E) = \frac{1}{4\pi^3 \hbar} v^2(E) N(E) \tau(E) \quad (\text{D.4})$$

According to Eqs.(D.3) and (D.4)  $K_2$  is nonzero at finite temperature unless the system is an insulator.

Now taking a look at the contribution of the second term relative to that of the first one in Eq.(D.1). Thus the ration of  $K_1^2/K_0$  to  $K_2$  is

$$\frac{K_1^2}{K_0 K_2} = \frac{\pi^2(k_B T)^2}{3} \left[ \frac{\partial \sigma(E)}{\sigma(E)} \right]^2 \Big|_{E=\mu} \quad (\text{D.5})$$

In the low temperature limit  $\tau(E) = \tau_0 E^{-\frac{1}{2}}$ , together with assumption that we are dealing with parabolic bands,

$$\sigma(E) \sim E \tag{D.6}$$

Consequently, Eq.(D.5) can be written as

$$\frac{K_1^2}{K_0 K_2} = \frac{\pi^2 (k_B T)^2}{3} \left[ \frac{1}{\mu} \right]^2 \tag{D.7}$$

$k_B$  is  $8.62 \times 10^{-5}$  eV/K. For general metals  $\mu$  has a value of a few eV, thus the ratio is in the order of about  $10^{-10}$  in the low temperature limit, which means  $K_1^2/K_0$  is negligible as compared to  $K_2$ .

# Bibliography

- [1] G. A. Slack, in *CRC Handbook of Thermoelectrics*, edited by D. Rowe (CRC Press, 1995) pp. 407–440.
- [2] R. Venkatasubramanian, E. Siivola, T. Colpitts, and B. O’Quinn, [Nature](#) **413**, 597 (2001).
- [3] H. Beyer, J. Nurnus, H. Bttner, A. Lambrecht, T. Roch, and G. Bauer, [Applied Physics Letters](#) **80**, 1216 (2002).
- [4] J. C. Caylor, K. Coonley, J. Stuart, T. Colpitts, and R. Venkatasubramanian, [Applied Physics Letters](#) **87**, 023105 (2005).
- [5] H. Bttner, G. Chen, and R. Venkatasubramanian, [MRS Bulletin](#) **31**, 211 (2006).
- [6] J. S. Dyck, W. Chen, C. Uher, L. Chen, X. Tang, and T. Hirai, [Journal of Applied Physics](#) **91**, 3698 (2002).
- [7] A. Saramat, G. Svensson, A. E. C. Palmqvist, C. Stiewe, E. Mueller, D. Platzek, S. G. K. Williams, D. M. Rowe, J. D. Bryan, and G. D. Stucky, [Journal of Applied Physics](#) **99**, 023708 (2006).
- [8] D. T. Morelli and G. P. Meisner, [Journal of Applied Physics](#) **77**, 3777 (1995).
- [9] B. C. Sales, D. Mandrus, and R. K. Williams, [Science](#) **272**, 1325 (1996).
- [10] G. S. Nolas, G. A. Slack, D. T. Morelli, T. M. Tritt, and A. C. Ehrlich, [Journal of Applied Physics](#) **79**, 4002 (1996).
- [11] B. C. Sales, B. C. Chakoumakos, and D. Mandrus, [Physical Review B](#) **61**, 2475 (2000).
- [12] G. S. Nolas, M. Kaeser, R. T. Littleton, and T. M. Tritt, [Applied Physics Letters](#) **77**, 1855 (2000).
- [13] G. S. Nolas, D. T. Morelli, and T. M. Tritt, [Annual Review of Materials Science](#) **29**, 89 (1999).

- [14] G. A. Lamberton, S. Bhattacharya, R. T. Littleton, M. A. Kaeser, R. H. Tedstrom, T. M. Tritt, J. Yang, and G. S. Nolas, [Applied Physics Letters](#) **80**, 598 (2002).
- [15] X. Shi, H. Kong, C. P. Li, C. Uher, J. Yang, J. R. Salvador, H. Wang, L. Chen, and W. Zhang, [Applied Physics Letters](#) **92**, 182101 (2008).
- [16] G. S. Nolas, J. L. Cohn, G. A. Slack, and S. B. Schujman, [Applied Physics Letters](#) **73**, 178 (1998).
- [17] B. B. Iversen, A. E. Palmqvist, D. E. Cox, G. S. Nolas, G. D. Stucky, N. P. Blake, and H. Metiu, [Journal of Solid State Chemistry](#) **149**, 455 (2000).
- [18] V. L. Kuznetsov, L. A. Kuznetsova, A. E. Kaliazin, and D. M. Rowe, [Journal of Applied Physics](#) **87**, 7871 (2000).
- [19] Y. Mudryk, P. Rogl, C. Paul, S. Berger, E. Bauer, G. Hilscher, C. Godart, and H. Nol, [Journal of Physics: Condensed Matter](#) **14**, 7991 (2002).
- [20] B. Chakoumakos, B. Sales, D. Mandrus, and G. Nolas, [Journal of Alloys and Compounds](#) **296**, 80 (2000).
- [21] M. M. Koza, M. R. Johnson, R. Viennois, H. Mutka, L. Girard, and D. Ravot, [Nat Mater](#) **7**, 805 (2008).
- [22] A. Bentien, S. Johnsen, G. K. H. Madsen, B. B. Iversen, and F. Steglich, [Europhysics Letters \(EPL\)](#) **80**, 17008 (2007).
- [23] P. Sun, N. Oeschler, S. Johnsen, B. B. Iversen, and F. Steglich, [Physical Review B](#) **79**, 153308 (2009).
- [24] P. Sun, N. Oeschler, S. Johnsen, B. B. Iversen, and F. Steglich, [Applied Physics Express](#) **2**, 091102 (2009).
- [25] P. Sun, N. Oeschler, S. Johnsen, B. B. Iversen, and F. Steglich, [Dalton Transactions](#) **39**, 1012 (2010).
- [26] A. Herzog, M. Marutzky, J. Sichelschmidt, F. Steglich, S. Kimura, S. Johnsen, and B. B. Iversen, [Physical Review B](#) **82**, 245205 (2010).
- [27] P. Sun, N. Oeschler, S. Johnsen, B. B. Iversen, and F. Steglich, [Journal of Physics: Conference Series](#) **150**, 012049 (2009).
- [28] J. M. Tomczak, K. Haule, T. Miyake, A. Georges, and G. Kotliar, [Physical Review B](#) **82**, 085104 (2010).

- 
- [29] P. Sun, M. Sondergaard, Y. Sun, S. Johnsen, B. B. Iversen, and F. Steglich, [Applied Physics Letters](#) **98**, 072105 (2011).
- [30] D. J. Singh and W. E. Pickett, [Physical Review B](#) **50**, 11235 (1994).
- [31] D. J. Singh and I. I. Mazin, [Physical Review B](#) **56**, R1650 (1997).
- [32] S. Kim, I. I. Mazin, and D. J. Singh, [Physical Review B](#) **57**, 6199 (1998).
- [33] M. Fornari and D. J. Singh, [Physical Review B](#) **59**, 9722 (1999).
- [34] R. W. Nunes, I. I. Mazin, and D. J. Singh, [Physical Review B](#) **59**, 7969 (1999).
- [35] G. K. H. Madsen, K. Schwarz, P. Blaha, and D. J. Singh, [Physical Review B](#) **68**, 125212 (2003).
- [36] J. Androulakis, P. Migiakis, and J. Giapintzakis, [Applied Physics Letters](#) **84**, 1099 (2004).
- [37] M. S. Green, [The Journal of Chemical Physics](#) **22**, 398 (1954).
- [38] R. Kubo, [Journal of the Physical Society of Japan](#) **12**, 570 (1957).
- [39] J. M. Ziman, *Electrons and Phonons: The Theory of Transport Phenomena in Solids* (Oxford University Press, USA, 2001).
- [40] T. M. Tritt, *Thermal conductivity: theory, properties, and applications* (Springer, 2004).
- [41] D. Rowe, in *Thermoelectrics Handbook*, edited by D. Rowe (CRC Press, 2005) pp. 1-1-1-14.
- [42] M. Born and R. Oppenheimer, [Annalen der Physik](#) **389**, 457 (1927).
- [43] P. Hohenberg and W. Kohn, [Physical Review](#) **136**, B864 (1964).
- [44] W. Kohn and L. J. Sham, [Physical Review](#) **140**, A1133 (1965).
- [45] J. P. Perdew, [Physical Review B](#) **33**, 8822 (1986).
- [46] J. P. Perdew and W. Yue, [Physical Review B](#) **33**, 8800 (1986).
- [47] G. Kresse and J. Furthmüller, [Computational Materials Science](#) **6**, 15 (1996).
- [48] G. Kresse and J. Furthmüller, [Physical Review B](#) **54**, 11169 (1996).
- [49] P. E. Blchl, [Physical Review B](#) **50**, 17953 (1994).

- [50] G. Kresse and D. Joubert, [Physical Review B](#) **59**, 1758 (1999).
- [51] D. M. Ceperley and B. J. Alder, [Physical Review Letters](#) **45**, 566 (1980).
- [52] J. P. Perdew, K. Burke, and M. Ernzerhof, [Physical Review Letters](#) **77**, 3865 (1996).
- [53] J. C. Slater and G. F. Koster, [Physical Review](#) **94**, 1498 (1954).
- [54] W. J. Hehre, R. F. Stewart, and J. A. Pople, [The Journal of Chemical Physics](#) **51**, 2657 (1969).
- [55] N. Marzari and D. Vanderbilt, [Physical Review B](#) **56**, 12847 (1997).
- [56] O. K. Andersen and T. Saha-Dasgupta, [Physical Review B](#) **62**, R16219 (2000).
- [57] T. S. D. Nguyen-Manh, [Bulletin of Materials Science](#), v.26, 27-32 (2003) [urn:ISSN:0250-4707](#).
- [58] T. Ozaki and H. Kino, [Physical Review B](#) **69**, 195113 (2004).
- [59] T. Ozaki, “[Openmx](#),” (2009).
- [60] M. Born and K. Huang, *Dynamical theory of crystal lattices* (Clarendon Press, 1998).
- [61] O. Madelung, *Introduction to solid-state theory* (Springer, 1996).
- [62] G. Kresse, J. Furthmüller, and J. Hafner, [Europhysics Letters \(EPL\)](#) **32**, 729 (1995).
- [63] K. Parlinski, Z. Q. Li, and Y. Kawazoe, [Physical Review Letters](#) **78**, 4063 (1997).
- [64] D. Alf, G. D. Price, and M. J. Gillan, [Physical Review B](#) **64**, 045123 (2001).
- [65] A. Dario, [Computer Physics Communications](#) **180**, 2622 (2009).
- [66] Y. Yao, L. Kleinman, A. H. MacDonald, J. Sinova, T. Jungwirth, D.-s. Wang, E. Wang, and Q. Niu, [Physical Review Letters](#) **92**, 037204 (2004).
- [67] D. G. Shankland, in *Computational Methods in Band Theory*, edited by P. Marcus, J. Janak, and A. Williams (Plenum, New York, 1971) p. 362.
- [68] D. Koelling and J. Wood, [Journal of Computational Physics](#) **67**, 253 (1986).
- [69] W. Pickett, [Physical Review B](#) **38**, 2721 (1988).
- [70] G. K. Madsen and D. J. Singh, [Computer Physics Communications](#) **175**, 67 (2006).

- 
- [71] I. I. Mazin, [Physical Review Letters](#) **83**, 1427 (1999).
- [72] J. He, M.-X. Chen, X.-Q. Chen, and C. Franchini, Submitted to [Physical Review Letters](#) (2012).
- [73] G. S. Nolas, J. L. Cohn, and G. A. Slack, [Physical Review B](#) **58**, 164 (1998).
- [74] V. L. Kuznetsov, L. A. Kuznetsova, and D. M. Rowe, [Journal of Physics: Condensed Matter](#) **15**, 5035 (2003).
- [75] L. Xi, J. Yang, W. Zhang, L. Chen, and J. Yang, [Journal of the American Chemical Society](#) **131**, 5560 (2009).
- [76] Y. Wang, X. Xu, and J. Yang, [Physical Review Letters](#) **102**, 175508 (2009).
- [77] M. Zebarjadi, K. Esfarjani, J. Yang, Z. F. Ren, and G. Chen, [Physical Review B](#) **82**, 195207 (2010).
- [78] X. Shi, J. Yang, J. R. Salvador, M. Chi, J. Y. Cho, H. Wang, S. Bai, J. Yang, W. Zhang, and L. Chen, [Journal of the American Chemical Society](#) **133**, 7837 (2011).
- [79] G. A. Slack and V. G. Tsoukala, [Journal of Applied Physics](#) **76**, 1665 (1994).
- [80] M. Christensen, A. B. Abrahamsen, N. B. Christensen, F. Juranyi, N. H. Andersen, K. Lefmann, J. Andreasson, C. R. H. Bahl, and B. B. Iversen, [Nat Mater](#) **7**, 811 (2008).
- [81] J. L. Feldman, D. J. Singh, C. Kendziora, D. Mandrus, and B. C. Sales, [Physical Review B](#) **68**, 094301 (2003).
- [82] G. J. Long, R. P. Hermann, F. Grandjean, E. E. Alp, W. Sturhahn, C. E. Johnson, D. E. Brown, O. Leupold, and R. Rffer, [Physical Review B](#) **71**, 140302 (2005).
- [83] C. H. Lee, I. Hase, H. Sugawara, H. Yoshizawa, and H. Sato, [Journal of the Physical Society of Japan](#) **75**, 123602 (2006).
- [84] S. Tsutsui, H. Kobayashi, D. Ishikawa, J. P. Sutter, A. Q. R. Baron, T. Hasegawa, N. Ogita, M. Udagawa, Y. Yoda, H. Onodera, D. Kikuchi, H. Sugawara, C. Sekine, I. Shirovani, and H. Sato, [Journal of the Physical Society of Japan](#) **77**, 033601 (2008).
- [85] D. Wee, B. Kozinsky, N. Marzari, and M. Fornari, [Physical Review B](#) **81**, 045204 (2010).

- [86] T. Hasegawa, Y. Takasu, N. Ogita, and M. Udagawa, *Journal of the Physical Society of Japan* **77**, 248 (2008).
- [87] C. P. Yang, H. Wang, K. Iwasa, M. Kohgi, H. Sugawara, and H. Sato, *Applied Physics Letters* **90**, 102503 (2007).
- [88] M. M. Koza, L. Capogna, A. Leithe-Jasper, H. Rosner, W. Schnelle, H. Mutka, M. R. Johnson, C. Ritter, and Y. Grin, *Physical Review B* **81**, 174302 (2010).
- [89] E. Bauer, A. Grytsiv, X. Chen, N. Melnychenko-Koblyuk, G. Hilscher, H. Kaldarar, H. Michor, E. Royanian, G. Giester, M. Rotter, R. Podlucky, and P. Rogl, *Physical Review Letters* **99**, 217001 (2007).
- [90] E. Bauer, X. Chen, P. Rogl, G. Hilscher, H. Michor, E. Royanian, R. Podlucky, G. Giester, O. Sologub, and A. P. Goncalves, *Physical Review B* **78**, 064516 (2008).
- [91] R. Gumeniuk, W. Schnelle, H. Rosner, M. Nicklas, A. Leithe-Jasper, and Y. Grin, *Physical Review Letters* **100**, 017002 (2008).
- [92] M. Toda, H. Sugawara, K.-i. Magishi, T. Saito, K. Koyama, Y. Aoki, and H. Sato, *Journal of the Physical Society of Japan* **77**, 124702 (2008).
- [93] R. Gumeniuk, H. Borrmann, A. Ormeci, H. Rosner, W. Schnelle, M. Nicklas, Y. Grin, and A. Leithe-Jasper, *Zeitschrift fr Kristallographie* **225**, 531 (2010).
- [94] R. Gumeniuk, M. Schneich, A. Leithe-Jasper, W. Schnelle, M. Nicklas, H. Rosner, A. Ormeci, U. Burkhardt, M. Schmidt, U. Schwarz, M. Ruck, and Y. Grin, *New Journal of Physics* **12**, 103035 (2010).
- [95] M. Nicklas, R. Gumeniuk, W. Schnelle, H. Rosner, A. Leithe-Jasper, F. Steglich, and Y. Grin, *Journal of Physics: Conference Series* **273**, 012118 (2011).
- [96] E. Bauer, (2007), thermoelectric properties of Ge-based skutterudites.
- [97] V. H. Tran, D. Kaczorowski, W. Miiller, and A. Jezierski, *Physical Review B* **79**, 054520 (2009).
- [98] G. D. Mahan and J. O. Sofo, *Proceedings of the National Academy of Sciences* **93**, 7436 (1996).
- [99] J. P. Heremans, V. Jovovic, E. S. Toberer, A. Saramat, K. Kurosaki, A. Charoengphakdee, S. Yamanaka, and G. J. Snyder, *Science* **321**, 554 (2008).
- [100] S. K. Mishra, S. Satpathy, and O. Jepsen, *Journal of Physics: Condensed Matter* **9**, 461 (1997).

- 
- [101] J. Yang, T. Aizawa, A. Yamamoto, and T. Ohta, *Journal of Alloys and Compounds* **312**, 326 (2000).
- [102] I. Zeiringer, N. Melnychenko-Koblyuk, A. Grytsiv, E. Bauer, G. Giester, and P. Rogl, *Journal of Phase Equilibria and Diffusion* **32**, 115 (2011).
- [103] H. Zhang, H. Borrmann, N. Oeschler, C. Candolfi, W. Schnelle, M. Schmidt, U. Burkhardt, M. Baitinger, J. Zhao, and Y. Grin, *Inorg. Chem.* **50**, 1250 (2011).
- [104] M. O’Keeffe and B. G. Hyde, *Acta Crystallographica Section B Structural Crystallography and Crystal Chemistry* **33**, 3802 (1977).
- [105] M. Llunell, S. Alvarez, and P. Alemany, *J. Chem. Soc., Dalton Trans.* , 1195 (1998).
- [106] J. C. Smith, S. Banerjee, V. Pardo, and W. E. Pickett, *Physical Review Letters* **106**, 056401 (2011).
- [107] M.-X. Chen, Unpublished data (2010).
- [108] J. Dong, O. F. Sankey, G. K. Ramachandran, and P. F. McMillan, *Journal of Applied Physics* **87**, 7726 (2000).
- [109] A. Junod, T. Jarlborg, and J. Muller, *Physical Review B* **27**, 1568 (1983).
- [110] T. Ozaki and H. Kino, *Physical Review B* **72**, 045121 (2005).
- [111] Y. Mudryk, P. Rogl, C. Paul, S. Berger, E. Bauer, G. Hilscher, C. Godart, H. Nol, A. Saccone, and R. Ferro, *Physica B: Condensed Matter* **328**, 44 (2003).
- [112] K. KISHIMOTO, N. IKEDA, K. AKAI, and T. KOYANAGI, *Applied physics express* **1** (2008).
- [113] G. B. Adams, M. O’Keeffe, A. A. Demkov, O. F. Sankey, and Y. Huang, *Physical Review B* **49**, 8048 (1994).
- [114] D. Conntable, *Physical Review B* **82**, 075209 (2010).
- [115] J. Dong and O. F. Sankey, *Journal of Physics: Condensed Matter* **11**, 6129 (1999).
- [116] J. Zhao, A. Buldum, J. Ping Lu, and C. Y. Fong, *Physical Review B* **60**, 14177 (1999).
- [117] C. Kittel, *Introduction to solid state physics* (Wiley, 2005).
- [118] X. Blase, *Physical Review B* **67**, 035211 (2003).
- [119] H. J. Monkhorst and J. D. Pack, *Physical Review B* **13**, 5188 (1976).

- [120] C. Candolfi, U. Aydemir, A. Ormeci, M. Baitinger, N. Oeschler, F. Steglich, and Y. Grin, [Physical Review B \*\*83\*\*, 205102 \(2011\)](#).
- [121] I. Zeiringer, M. Chen, I. Bednar, E. Royanian, E. Bauer, R. Podloucky, A. Grytsiv, P. Rogl, and H. Effenberger, [Acta Materialia \*\*59\*\*, 2368 \(2011\)](#).
- [122] D. Shu-Kang, T. Xin-Feng, and T. Run-Sheng, [Chinese Physics B \*\*18\*\*, 3084 \(2009\)](#).
- [123] X. Yan, M. X. Chen, S. Laumann, E. Bauer, P. Rogl, R. Podloucky, and S. Paschen, [arXiv:1111.3278 \(2011\)](#).
- [124] I. Zeiringer, (2010).
- [125] X. Yan, A. Grytsiv, G. Giester, E. Bauer, P. Rogl, and S. Paschen, [Journal of Electronic Materials \*\*40\*\*, 589 \(2010\)](#).
- [126] X. Yan, G. Giester, E. Bauer, P. Rogl, and S. Paschen, [Journal of Electronic Materials \*\*39\*\*, 1634 \(2010\)](#).
- [127] U. Aydemir, C. Candolfi, A. Ormeci, Y. Oztan, M. Baitinger, N. Oeschler, F. Steglich, and Y. Grin, [Physical Review B \*\*84\*\*, 195137 \(2011\)](#).
- [128] I. Zeiringer, M. Chen, A. Grytsiv, E. Bauer, R. Podloucky, H. Effenberger, and P. Rogl, *Acta Materialia* **xx**, xxx (2012).
- [129] L. Chaput, P. Pcheur, J. Tobola, and H. Scherrer, [Physical Review B \*\*72\*\*, 085126 \(2005\)](#).
- [130] S. N. F. Mott and H. Jones, *The theory of the properties of metals and alloys* (Courier Dover Publications, 1958).
- [131] N. W. Ashcroft and N. D. Mermin, *Solid State Physics*, 1st ed. (Brooks Cole, 1976).
- [132] F. J. Blatt, *Physics of electronic conduction in solids* (McGraw-Hill, 1968).

# List of Publications and Manuscripts

1. I. Zeiringer, M.-X. Chen, I. Bednar, E. Royanian, E. Bauer, R. Podlucky, A. Grytsiv, P. Rogl, and H. Effenberger,  
*Phase equilibria, crystal chemistry, electronic structure and physical properties of AgBaGe clathrates,*  
Acta Materialia **59**, 2368-2384 (2011).
2. I. Zeiringer, M.-X. Chen, A. Grytsiv, E. Bauer, R. Podlucky, H. Effenberger and P. Rogl,  
*The ternary system AuBaSi: Clathrate solution, electronic structure, physical properties, phase equilibria and crystal structures,*  
Acta Materialia in press (2012).
3. J. He, M.-X. Chen, X.-Q. Chen, and C. Franchini  
*Structural transitions and transport-half-metallic ferromagnetism in LaMnO<sub>3</sub> at elevated pressure*  
submitted to Phys. Rev. Lett.
4. X. Yan, M.-X. Chen, S. Laumann, E. Bauer, P. Rogl, R. Podlucky, and S. Paschen  
*Thermoelectric properties of Ba-Cu-Si clathrates,*  
arXiv:1111.3278 (2011), submitted to Phys. Rev. B.
5. M. Falmbigl, M.-X. Chen, A. Grytsiv, P. Rogl, E. Royanian, H. Michor, E. Bauer, R. Podlucky, and G. Giester,  
*Type-I clathrate Ba<sub>8</sub>Ni<sub>x</sub>Si<sub>46-x</sub>: phase relations, crystal chemistry and thermoelectric properties,*  
submitted to Dalton Transactions.
6. M.-X. Chen and R. Podlucky,  
*First-principles study of rattling modes in MPt<sub>4</sub>Ge<sub>12</sub> skutterudites,*  
to be submitted to Phys. Rev. B.

7. M.-X. Chen and R. Podloucky,  
*Enhanced thermoelectric properties of filled  $Pt_4(Sb_xGe_{12-x})$  skutterudites: band engineering for thermoelectrics*,  
to be submitted to Phys. Rev. Lett.
8. M.-X. Chen and R. Podloucky,  
*Origin of wide-band-gap of Clathrates*, in preparation.
9. M. X. Chen and R. Podloucky, *Lorenz number for evaluating lattice thermal conductivity*, in preparation.

# Curriculum Vitae

## Personal Data

Name: Mingxing Chen  
Place of Birth: Hunan, China  
Date of Birth: August, 23, 1981  
Citizenship: Chinese

## Education and Experience

M.S., 2007 Xiangtan University (Hunan, China)  
B.S., 2004 Xiangtan University (Hunan, China)

06/2005 - 06/2007 Graduate Student Research Assistant, Nanjing University of Aeronautics and Astronautics (Jiangsu, China), Supervisor Prof. Dr. Xiaohong Yan.  
07/2007 - 09/2008 Projector Research Assistant, Nanjing University of Aeronautics and Astronautics (Jiangsu, China).  
10/2008 - 03/2012 PhD studies in the field of computational materials science, University of Vienna (Austria), Supervisor Prof. Dr. Raimund Podlousky.